

Biologically-Inspired Systems

Feodor M. Borodich
Xiaoqing Jin *Editors*



Contact Problems for Soft, Biological and Bioinspired Materials

 Springer

Biologically-Inspired Systems

Volume 15

Series Editor

Stanislav N. Gorb, Department of Functional Morphology and Biomechanics,
Zoological Institute, Kiel University, Kiel, Germany

Motto: Structure and function of biological systems as inspiration for technical developments.

Throughout evolution, nature has constantly been called upon to act as an engineer in solving technical problems. Organisms have evolved an immense variety of shapes and structures from macro down to the nanoscale. Zoologists and botanists have collected a huge amount of information about the structure and functions of biological materials and systems. This information can be also utilized to mimic biological solutions in further technical developments. The most important feature of the evolution of biological systems is multiple origins of similar solutions in different lineages of living organisms. These examples should be the best candidates for biomimetics. This book series will deal with topics related to structure and function in biological systems and show how knowledge from biology can be used for technical developments in engineering and materials science. It is intended to accelerate interdisciplinary research on biological functional systems and to promote technical developments. Documenting of the advances in the field will be important for fellow scientists, students, public officials, and for the public in general. Each of the books in this series is expected to provide a comprehensive, authoritative synthesis of the topic.

More information about this series at <https://link.springer.com/bookseries/8430>

Feodor M. Borodich • Xiaoqing Jin
Editors

Contact Problems for Soft, Biological and Bioinspired Materials

 Springer

Editors

Feodor M. Borodich
Cardiff University
Cardiff, UK

Xiaoqing Jin
Chongqing University
Chongqing, China

National Natural Science Foundation of China
X. Jin is funded by National Science Foundation of China.

ISSN 2211-0593 ISSN 2211-0607 (electronic)
Biologically-Inspired Systems
ISBN 978-3-030-85174-3 ISBN 978-3-030-85175-0 (eBook)
<https://doi.org/10.1007/978-3-030-85175-0>

© Springer Nature Switzerland AG 2022

This work is subject to copyright. All rights are reserved by the Publisher, whether the whole or part of the material is concerned, specifically the rights of translation, reprinting, reuse of illustrations, recitation, broadcasting, reproduction on microfilms or in any other physical way, and transmission or information storage and retrieval, electronic adaptation, computer software, or by similar or dissimilar methodology now known or hereafter developed.

The use of general descriptive names, registered names, trademarks, service marks, etc. in this publication does not imply, even in the absence of a specific statement, that such names are exempt from the relevant protective laws and regulations and therefore free for general use.

The publisher, the authors and the editors are safe to assume that the advice and information in this book are believed to be true and accurate at the date of publication. Neither the publisher nor the authors or the editors give a warranty, expressed or implied, with respect to the material contained herein or for any errors or omissions that may have been made. The publisher remains neutral with regard to jurisdictional claims in published maps and institutional affiliations.

This Springer imprint is published by the registered company Springer Nature Switzerland AG
The registered company address is: Gewerbestrasse 11, 6330 Cham, Switzerland

*This book is dedicated to the memory of
Professor Leon M. Keer
who inspired our research in Solid
Mechanics and Tribology
during our stay at Northwestern University
and many years after we left it.*

Feodor M. Borodich and Xiaoqing Jin

Preface

This book contains contributions from leading researchers in biomechanics, nanomechanics, tribology, contact mechanics and materials science, and applications of various experimental techniques including atomic force microscopy (AFM) for studying soft, biomimetic, and biological materials and objects. Biologists, physicists, and researchers applying methods of contact mechanics and researchers testing materials using indentation techniques along with many other applied scientists will find this book a useful addition to their libraries. Moreover, several reviews in this book are written as introductions to several important and rather sophisticated research areas such as depth-sensing indentation, studying of biological cells by AFM probes, mechanics of adhesive contact, and contact between viscoelastic (hereditary elastic) solids. This book, containing new theoretical models, results of experimental studies, and numerical simulations, along with reviews of above-mentioned areas of contact mechanics in application to biological systems, would be beneficial for researchers in many areas of biology, medicine, engineering, mechanics, and biomimetics.

This book is dedicated to Professor Leon M. Keer (1934–2021). He was a great university teacher and prolific researcher famous for his results in tribology, and contact and fracture mechanics. Leon Keer earned his bachelor's degree in engineering and master's degree in mechanical engineering from the California Institute of Technology, and his PhD in aeronautics and engineering mechanics from the University of Minnesota. After serving as a NATO postdoctoral fellow at Newcastle University in England in 1962, Leon Keer spent a year at Columbia University as a preceptor. In 1964, he joined the McCormick School of Engineering as an assistant professor of civil engineering. From 1970 he worked as a professor, and from 1994 as Walter P. Morphy Professor in Civil Engineering. He received multiple awards including the Daniel C. Drucker Medal (2003), the Mayo D. Hersey Award, the ASME's Tribology Division Innovative Research Award (2008), and Raymond D. Mindlin Medal (2011). He was elected to the National Academy of Engineering in 1997, and he was a fellow of the American Academy of Mechanics, the John Simon Guggenheim Memorial Foundation, the American Society of

Mechanical Engineers (ASME), the American Society of Civil Engineers, and the Acoustical Society of America.

Leon Keer's colleague, Professor Julio M. Ottino (Northwestern University), gave him a very precise characteristic: "Leon was one of the giants in the field of elasticity and mechanics and made many significant contributions to our community as a researcher, teacher, and administrator. He was also one of the kindest colleagues I have ever met and was incredibly supportive of young faculty. He was always at peace with himself, which made him beloved by so many." Leon inspired many researchers and contributed himself to discovery of new phenomena of nature, as an example we can mention his discovery of the Polonsky-Keer effect for crystalline solids saying that "plastic deformation at an asperity micro-contact becomes difficult and then impossible when the asperity size decreases below a certain threshold value on the order of the microstructural length," which is of crucial importance for modern nanotribology.

In 2001, the editors of this book met each other at Leon Keer's research group when one of them (XJ) was a PhD student at the Technological Institute of Northwestern University and another one (FB) arrived there as a visiting scholar.

FB learnt about Keer's group from Professor K.L. Johnson in 1991. That time, Professor Johnson worked the last year at Cambridge before his retirement, hence he was not able to invite FB and advised to contact Professor Keer. Unfortunately, there was no vacancy at the group; however, FB was very lucky, and Professor John R. Willis invited him to DAMTP at the University of Cambridge. In 2000, FB learnt from Dr. Igor Polonsky that there is a vacancy at Keer's group and his second attempt to join the group was successful.

Leon Keer was a very delicate person and he created wonderful working atmosphere at his group. Let us give an example of his incredible support. One of the main topics that FB had to study at the group was tribology of carbon-based coatings, in particular diamond-like coatings. At his arrival, FB had just a very general knowledge about this area and he studied the topic during first 2 months having just very friendly and inspiring discussions with Leon. During these discussions, FB learnt about very impressive experimental observations of Dr. Steve J. Harris (that time at Ford Research Laboratory). After some time, FB approached Leon and proposed to give a theoretical explanation to these observations. Leon and FB had several very fruitful discussions that involved Dr. Harris, and these discussions led to preparation of the first paper on self-similarity in abrasiveness of hard carbon-containing coatings. After this, without any preliminary discussion with FB, Leon organized for FB a very prestigious Northwestern Technological Institute seminar. In addition, Leon's colleagues elected FB to serve as visiting professor at their Institute. These 3 years of stay at Keer's group (2001–2003) were the most productive years of FB's career.

In 1998, XJ went to Northwestern University and embarked on contact mechanics, fracture mechanics, micromechanics, and tribology under Prof. Keer's guidance. Since then, they have successfully collaborated on a series of research projects through 2021. Among more than 50 PhD students that Leon has mentored, XJ has collaborated the greatest number of papers with him. Leon has always been

supportive of XJ's academic career. After XJ joined Chongqing University as a faculty member in 2013, Leon has visited Chongqing University twice. Each time the octogenarian was enthusiastic to talk to young mechanicians in China and delivered wonderful seminars. In 2018, XJ was invited to attend the 3rd CARBTRIB International Workshop organized by FB. In return, FB visited XJ at Chongqing University in 2019, and this book has originated from many pleasant conversations thereafter. We hope that the present book would be very much in spirit of Leon and many parts of it will bring readers back to original ideas inspired by him.

Contact mechanics is an old branch of solid mechanics that studies interactions between surfaces of solids loaded by external forces. Mathematical formulation of contact mechanics was born in classic works by H. Hertz (1882) and J.V. Boussinesq (1885) dedicated to contact between elastic solids. Later the theory of contact interactions was developed in enormous number of research papers and various models of contacting materials were employed, including models of elastic, plastic, viscoelastic, and creeping materials. However, these studies were mainly applied to quite stiff materials used in various areas of engineering, especially in mechanical engineering and tribology. In addition, these contact models had not taken into account the molecular attractions between contacting solids until the pioneering papers describing adhesive contact between elastic solids were published by B.V. Derjaguin in 1934. Derjaguin and his research group continued his studies of effects of adhesion in many other excellent works. These studies were a trigger for studies of mechanics of adhesive contact by many other researchers, and the most impressive results were achieved in works by K.L. Johnson, K. Kendall, A.D. Roberts, and D. Maugis and their colleagues. The JKR (Johnson-Kendall-Roberts) and DMT (Derjaguin-Muller-Toporov) theories, and a united point of view on these theories by Maugis are now classic. However, even the most cited JKR theory presented in 1971 was rather rarely employed in practical applications for the first 20 years. According to Web of Science, the JKR theory was cited 226 times in the 1971–1990 period, while it has currently about 5700 citations. The situation changed drastically with development of nanoscience, biomechanics, and introduction of the atomic force microscope (AFM) by G. Binnig, C. Quate, and Ch. Gerber in 1986. Another very important step in popularization of contact mechanics in biological applications was the publication of a book on biological micro and nanotribology by M. Scherge and S.N. Gorb in 2000. In the next 20 years, this field has been considerably developed, and therefore there is a need of a description of recent results related to problems of indentation, contact, and AFM probing of soft, biological, and bioinspired materials.

Since the research areas related to contact problems and contact probing of biological objects and structures are at the crossroads of nanoscience, physics, biology, and engineering, the book can attract experts in biology whose research interests include studies of mechanical and physical properties of biological objects and materials by nano/micro indentation techniques, and experts in mechanics and materials science who intend to learn more about specific features of biological objects and novel results in contact mechanics. The book is also well suited for

graduate students who want to become active in the above-mentioned areas of the interdisciplinary research.

The first three chapters are dedicated to contact problems and AFM studies of living cells. The field is introduced in the first chapter. Here several topics are covered: (i) microscopy, (ii) theoretical basis of depth-sensing indentation (DSI) techniques, (iii) physical mechanisms of adhesion between biological cells and van der Waals forces, (iv) adhesive contact problems and experimental evaluation of cell characteristics, and (v) evaluation of elastic and adhesive characteristics of cells. The review is not targeted to narrow experts in the field, but rather for beginners. Another specific feature of the review is that it explains historically achievements of researchers of the former Soviet Union and Germany that are rather seldom mentioned in the scientific literature. It is argued that the classic theories such as Johnson-Kendall-Roberts and Derjaguin-Muller-Toporov should be modified in order to reflect the initial stresses in cell membranes. Finally, the DSI methods that may be used for extraction of adhesive and mechanical properties of cell membranes are discussed. Chapter 2 shows how to deal with a rather non-trivial problem of contact probing of realistic soft, biological, and bioinspired materials whose samples do not have ideally well-defined interfaces, but they have either intrinsically rough interface and/or the presence of large molecules covering the interface. As an example, it describes in detail the process of AFM indentation of biological cells. Chapter 3 provides descriptions of AFM techniques and characteristics of cells that may be used in medicine for establishing the relationship between the nanomechanical parameters measured by AFM and the state of the cell or its components. The effectiveness of using the AFM parameters for characterization of the type and state of cells is illustrated by the example of erythrocytes in hereditary spherocytosis, epithelial cells, and fibroblasts.

The next four chapters are dedicated to various models of adhesive contact and adhesive effects. Chapter 4 presents recent results related to theoretical modeling of capillary adhesion between a soft elastic half-space and an axisymmetric asperity or a periodic system of asperities. The asperity shapes are described as power-law functions. The results obtained are used to analyze the effects of fluid volume in a meniscus, surface tension of fluid, elastic properties of the half-space, shape of an asperity, and mutual influence of neighbor asperities on the contact characteristics. It is shown that the load-distance dependencies have hysteresis, and the corresponding energy dissipation in an approach-retraction cycle is calculated and analyzed depending on the fluid volume, its surface tension, elastic properties of contacting bodies, and shape of the asperity. Chapter 5 studies adhesion between a macroscopically flat-ended rigid cylinder having a short wave-length waviness. The waviness may be considered as a simple model for roughness of an elastic body coated with a soft elastic layer. The critical thickness of the surface soft layer for achieving the maximum adhesive strength of the contact is calculated. It is found that the properties of adhesive contact do not depend continuously on the thickness of the layer and the corresponding adhesive contact problem is analyzed. Chapter 6 presents a review of asymptotic models for analysis of bioinspired fibrillar adhesive interfaces. It is argued that asymptotic modeling provides a clear scheme

for analysis of both multi-parametric and multi-scale problems with application to multiple elastic contact at bio-inspired fibrillar adhesive interfaces. Chapter 7 presents experimental and theoretical analysis of contact problems for red caviar cells. The difficulties in both modeling of the contact interactions by Hertz and JKR theories, and experimental studies of cells having fast drying surfaces along with varying adhesive properties of cells are discussed. It is argued that the results can be used for modeling interactions between collagen-based shells and other materials.

The next two chapters are dedicated to nanoindentation studies of materials. Chapter 8 explains how one can study the mechanical behavior of polymeric and soft materials through combined computational and experimental nanoindentation approach. This study helps to identify the mechanical characteristics of soft materials that may exhibit time-dependent or a very large non-linear strain behavior known as viscoelasticity/viscoplasticity. Chapter 9 is dedicated to theoretical aspects of indentation tests of biological materials. A review of results, related to DSI tests of rather different biomaterials such as bones, snake skins, cartilages, resilin, and elastin-based materials, is given. It is stressed that although the depth-sensing indentation is a valuable tool for studying mechanical properties of biomaterials, one should be aware that the theoretical models used for justification of modern nanoindentation tests are based on non-adhesive contact, while the influence of adhesive interactions increases as the scale of samples goes down to micro and nanoscales.

The last three chapters of the book are dedicated to contact problems for soft materials and their applications. Chapter 10 presents new results on quasi-static contact problem for a rigid smooth slider and a two layered half-space with rheological properties of a layer or a substrate. A method is proposed to study two cases: a viscoelastic layer bonded to a rigid base, and a rigid bending layer on a viscoelastic half-space. The dependence of the coefficient of friction arising due to imperfect elasticity on the sliding velocity for different values of the layer thickness is analyzed. Chapter 11 is dedicated to estimations of bluntness of AFM tip probes. The bluntness may affect the precision of AFM measurements of surface topography and accuracy of AFM nanomachining of solid surfaces. Both tips are considered: (i) the intact tips as received from factory and (ii) worn tips. The tip bluntness is studied in both vertical position of the probes and in working position when the AFM cantilever is inclined by 12° to the horizontal plane. It is suggested to describe the tips as power-law functions, whose exponent d is used as a characteristic of tip bluntness. It is argued that the load displacement curve of an experimental DSI test may be used to extract the quantitative measure of the AFM tip bluntness. Chapter 12 reviews the history of development of the JKR theory of adhesive contact, its recent generalizations, and application of the JKR formalism to various non-classic problems. It is argued that the JKR formalism may be applied to many elastic materials and structures if the contact problem formulation is geometrically linear and it is possible to superpose solutions to Hertz-type and Boussinesq-type non-adhesive contact problems.

Many questions described in this book were discussed during workshops of the international Networks ADHESINT: Adhesive interactions between particles and

surface at micro/nanometer scales (2007–2010) and CARBTRIB: Nano-phenomena and functionality of modern carbon-based tribo-coatings (2016–2018) supported by grants of the Leverhulme Trust. The research collaboration between the editors was supported by a grant of Chongqing University (China). The research collaboration between NanoScience and NanoEngineering cross-disciplinary Group (NANOSNEG) at Cardiff University and the Department of Functional Morphology and Biomechanics at Christian-Albrechts-Universität zu Kiel was supported by the Alexander von Humboldt Foundation. We would like to thank The Leverhulme Trust for financial support of International Networks ADHESINT and CARBTRIB. We are grateful to Chongqing University for its financial support of collaboration between the editors. One of editors (FB) is grateful to Alexander von Humboldt Foundation for its support of his collaboration with the Department Functional Morphology and Biomechanics of Christian-Albrechts-Universität zu Kiel.

Cardiff, UK

Feodor M. Borodich

Chongqing, China
April 2021

Xiaoqing Jin

Contents

1	Adhesion of Living Cells: Mechanisms of Adhesion and Contact Models	1
	Feodor M. Borodich, Boris A. Galanov, Leon M. Keer, and Maria M. Suarez-Alvarez	
2	Contact Problem in Indentation Measurements of Soft, Biological and Bioinspired Materials	31
	Igor Sokolov	
3	Mechanical Properties of the Cell Surface Layer Measured by Contact Atomic Force Microscopy	51
	Maria N. Starodubtseva	
4	Capillary Adhesion Effect in Contact Interaction of Soft Materials ..	73
	I. G. Goryacheva and Yu. Yu. Makhovskaya	
5	Influence of a Soft Elastic Layer on Adhesion of Rough Surfaces	93
	Q. Li, I. A. Lyashenko, R. Pohrt, and V. L. Popov	
6	Asymptotic Modeling Scheme for Analysis of Bio-inspired Fibrillar Adhesive Interfaces: A Short Review	103
	Ivan Argatov	
7	Spreading of Red Caviar Cells: The Knife-Cell and the Cell-Cell Adhesive Interactions	117
	Feodor M. Borodich and Stanislav N. Gorb	
8	Mechanical Characterisation of Polymeric Materials Using Nanoindentation	139
	Hassan Gonabadi, Arti Yadav, and Steve Bull	
9	Indentation Tests of Biological Materials: Theoretical Aspects	181
	Xiaoqing Jin, Pu Li, and Feodor M. Borodich	

10 Effect of Viscoelasticity in Sliding Contact of Layered Solids 199
Elena V. Torskaya and Fedor I. Stepanov

11 Characterisation of an AFM Tip Bluntness Using Indentation of Soft Materials..... 221
Sameeh Baqain, Feodor M. Borodich, and Emmanuel Brousseau

12 The JKR Formalism in Applications to Problems of Adhesive Contact 243
Feodor M. Borodich

Chapter 1

Adhesion of Living Cells: Mechanisms of Adhesion and Contact Models



Feodor M. Borodich, Boris A. Galanov, **Leon M. Keer**,
and Maria M. Suarez-Alvarez

Abstract All known biological organisms consist of cells. Contact probing of cells is one of the preferred methods of studying cells' mechanical properties. Here we discuss various questions related to nanotechnology and contact probing of cells. The main goals of the review are twofold: (1) to explain some specific features of nanoscale mechanics and modern experimental techniques used in modern nanotechnology to experts in theoretical aspects of classical solid mechanics; and (2) to describe the main assumptions and approaches employed in mechanics of adhesive contacts, in particular in applications to contact probing of living cells, to experts in experimental biology. First, historical overview of the methods for studying cells are given, these include methods of microscopy and contact mechanics. Then the mechanisms of adhesion between cells are described. It is shown that adhesive interactions between cells may be caused by various physical and chemical mechanisms. Although all these mechanisms have the same electromagnetic nature, their manifestations may be rather different. Theories of adhesive contact between elastic spheres are discussed. It is argued that the classic theories such as Johnson-Kendall-Roberts and Derjaguin-Muller-Toporov should be modified in order to reflect the initial stresses in cell membranes. After these models may be applied to cells assuming that the cell surfaces may be locally approximated by spherical surfaces. Finally, we discuss the depth-sensing indentation methods that may be used for extraction of adhesive and mechanical properties of cell membranes.

F. M. Borodich (✉) · M. M. Suarez-Alvarez
School of Engineering, Cardiff University, Cardiff, UK
e-mail: BorodichFM@cardiff.ac.uk

B. A. Galanov
Institute for Problems in Materials Science, National Academy of Sciences of Ukraine, Kiev,
Ukraine

L. M. Keer (✉) (Deceased)
Department of Mechanical Engineering, Northwestern University, Evanston, IL, USA

Keywords Contact between cells · Adhesion · JKR theory · DMT theory · Mechanical properties of cells

1 Introduction

The term ‘cell’ for a basic unit of all known biological organisms was introduced by Robert Hooke in 1665. Observing a smooth section of a cork sample (Hooke, 1665), he wrote in the Chapter “Of the Schematisme or Texture of Cork, and of the Cells and Pores of some other such frothy Bodies”: “. . . in that these pores, or cells, were not very deep, but consisted of a great many little Boxes, separated out of one continued long pore, by certain Diaphragms, as is visible by the Figure B, which represents a sight of those pores split the long-ways. The famous book by R. Hooke along with discoveries of bacteria, red blood cells, and many unicellular organisms by Leewenhoek (1677) gave a start to microbiology and studies of living cells.

Using very impressive expressions from a talk given by Richard P. Feynman in 1959 (see, Feynman 1992), we can say that Hooke and Leeuwenhoek made the first steps to the bottom. Following a very wise observation by Kendall (2001), we can say that Hooke and Leeuwenhoek made a breakthrough to the Sticky Universe. Indeed, bodies are very sticky at micro and nanoscales, in spite of effects of adhesion not being as evident at the macroscale as they are at the nanoscale.

Comment Unfortunately, the predictions of scientific experts are often noticed only after their predictions have become a reality. For example, in 1974 A.D. Sakharov predicted the creation of Word Information System (Sakharov 1974), however this prediction did not affect the creation of Internet. The same is regarded to Feynman’s talk; it started to be cited only after the main ideas of nanotechnology were developed, see a discussion by Ball (2009).

Effects of adhesion should not be forgotten when one is discussing nanotechnology. Indeed, discussing the idea of nanorobots (nanobots), R. Smalley wrote: “*How soon will we see the nanometer-scale robots . . . ? The simple answer is never . . . Manipulator fingers on the hypothetical self-replicating nanobot are not only too fat; they are also too sticky. Both these problems are fundamental, and neither can be avoided*” (Smalley 2001). Thus, our experience gained at the macroscale cannot be transferred directly to the nanoscale world.

This chapter will be devoted to a reviewing of several interrelated topics: (1) technologies and devices that enabled the researchers to study micro- and nano-sized bodies and structures, with the emphasis on methodologies based on contact mechanics, (2) physical and chemical mechanisms of adhesion between biological cells, (3) models of adhesive contact between bodies having spherical shapes, and (4) some methods of evaluation of mechanical and adhesive characteristics of the cells by probing the cell by indenters. The main goals of the review are twofold: (1) to explain some specific features of nanoscale mechanics and modern experimental techniques used in modern nanotechnology to experts in theoretical aspects of

classical solid mechanics; and (2) to describe the main assumptions and approaches employed in mechanics of adhesive contacts, in particular in applications to contact probing of living cells, to experts in experimental biology. We believe that the authors are able to provide reliable information about the key concepts of modern nanomechanics and nanotechnology in their historical development based not only on literature available in English, but also based on sources published in German and Russian. The later sources are rarely mentioned in modern literature.

2 Preliminaries. The Long Way to the Bottom

Let us discuss some scientific achievements and technologies that allowed the researchers to develop nanoscience.

2.1 *Light and Electron Microscopy*

It is well known that ‘Seeing is Believing’. The great figures of the first ever scientific bestseller by Hooke (1665) supported by Leeuwenhoek’s discoveries (Leeuwenhoek 1677) opened the way to the wonder land of microscale. R. Hooke used a compound microscope, while A. van Leeuwenhoek observed the objects by a single-lens microscope, i.e. by a magnifying lens (a loupe). For many years, the only way to study biological cells was to employ light microscopy. During centuries the optical microscopy techniques were greatly improved by efforts of Carl Zeiss, Ernst Abbe, Otto Schott, August Koehler (Köhler) and other researchers (see, e.g. a discussion by Murphy 2001). Development of photography and its use in optical microscopy was an important step in the development of techniques for microscopy image processing. If the microscopic images are obtained by photography, then one does not need to be an artist like R. Hooke or S. Ramon y Cajal, who could produce excellent drawings, in order to describe the images observed.

The next important step in passing from microscale to nanoscale studies was an introduction of transmission electron microscopy (TEM). The development of TEM techniques is usually connected with names of Max Knoll, Ernst Ruska, Bodo von Borries, Vladimir K. Zworykin and others (see, e.g. Borries and Ruska 1933, and a discussion by Gorkom et al. 2018). The first TEMs in the Soviet Union were built by Alexander A. Lebedev (Lebedeff). According to Wikipedia, the resolution of his TEM built in 1940 was 40 nm, while his microscope of 1943 had resolution 10 nm. In 1946 this type of TEM was customized. In 1947 A.A. Lebedev was awarded the USSR State prize for the creation of the Soviet electron microscope. It is interesting to note that as early as in 1931, during his work as a visitor at Laboratory led by Prof. William Henry Bragg (Royal Institution, London), he published a note describing a scheme of his device for producing electron diffraction patterns. He presented also

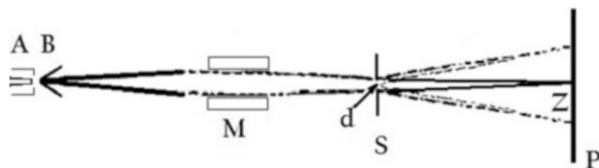


Fig. 1.1 Lebedeff's device for focusing electron beams by magnetic lenses: (A) a spiral for emitting of electrons; (B) a hollow metal cone; (M) is a coil (magnetic lens); (S) the specimen of diameter d ; (P) photographic plate or fluorescent screen; (Z) a point of convergence of the of the rays (after Lebedeff 1931)

the photographs of patterns that he obtained after transmission of an electron beam focused by magnetic lenses through thin specimens (Fig. 1.1).

He studied sodium chloride, gold leaf, paraffin and a gold film produced by cathodic sputtering. The electrons transmitted were focused on the specimen by a magnetic lens and the diffraction images were either observed on a fluorescent screen or fixed by photographic plates (Lebedeff 1931).

The development of TEM was very important for nanoscience and led to many discoveries. For example, using TEM, carbon nanotubes were discovered by Radushkevich and Lukyanovich (1950), Radushkevich and Lukyanovich (1952) at Institute of Physical Chemistry, USSR Academy of Sciences. Studies of carbon based materials at this Institute were led mainly by Derjaguin who focused on studying these materials around 1950. He introduced the Chemical Vapor Deposition and suggested the synthesis of diamond from gases at low pressure. These and many other results related to the studies of diamonds, carbon whiskers and hollow whiskers (carbon nanotubes) were presented by Derjaguin and Fedoseev (1975), Derjaguin and Fedoseev (1977). In particular, using the diffraction studies of the hollow whiskers, they reported that the whiskers are made from pure carbon and there are no metallic inclusions. Derjaguin and Fedoseev (1977) concluded that the graphite planes elongated along the hollow whiskers (carbon nanotubes) and this fact may explain the high tensile strength of the hollow carbon whiskers.

Using TEM, single and multiwall biological nanotubes were discovered by Kiselev et al. (1967), Kiselev et al. (1968). Indeed, in 1967 Kiselev, Spitzberg and Vainshtein published the results of their studies of the catalase of beef liver and human erythrocytes using electron microscopy. The catalase is a very common enzyme that can be found in many living organisms; it catalyzes the decomposition of hydrogen peroxide to water and oxygen. Catalase can be crystallized. Kiselev et al. (1967) discovered that the catalase of both the erythrocytes and beef liver can form single wall nanotubes. It was measured that tubes of catalase from erythrocytes have external diameter of about 42 nm and the wall thickness of 6.5 nm, while the dimensions of the catalase tubes from beef liver were respectively 31 ± 1.5 nm and the wall thickness of about 6.5 nm. They concluded that the packing unit in both kinds of catalase tubes are the same and described the crystals of the tubes as structures having helical packing. Later Kiselev et al. (1971) published results

of similar studies of muscle phosphorylase *b* prepared from rabbit muscle. It was found that it shows three types of crystal formations: plane monolayers of particles, tubes and three-dimensional crystals. It was reported again that both single-walled and multiwalled nanotubes of phosphorylase were observed.

The next important technology for studying micro/nano scale objects was the Scanning Electron Microscopy (SEM). It was invented by Max Knoll and developed further by Manfred von Ardenne (Knoll 1935; Ardenne 1938, 1939). SEMs are capable of producing high-resolution images of a sample surface such that the images have three-dimensional appearance. For example, Lin et al. (2004) used TEM images for initial identification of the coronavirus, SARS-CoV. However, to obtain three-dimensional appearance of SARS-CoV at greater morphological detail, they used ultra-high SEM. In particular, SEM images allowed to observe the trimeric structure of the 10–20 nm spikes on the coronavirus surface.

Comment One can say that the idea of self-replication is realized in Nature as oligomers (the word means in Greek consisting of a few parts). A few small identical molecules connect to each other and create an oligomer. It is known that oligomeric spike (S) proteins extend from coronavirus membranes. In fact, the coronavirus spikes consist of two noncovalently associated subunits (S1 and S2). According to Lewicki and Gallagher (2002), once on the surface of infected cells and virions, peripheral S1 units bind carcinoembryonic antigen-related cell adhesion molecule (CEACAM) receptors, and this triggers membrane fusion reactions mediated by integral membrane S2 units.

The device Topografiner by Young et al. (1972) and Scanning Tunneling Microscope (STM) by Binnig et al. (1982) gave much higher resolution of surface topography than all previous devices. Using STM one can detect the quantum tunneling current between a tip and a surface. Putting the data into a computer, one can produce a map of the sample surface atom by atom.

2.2 *Surface Force Apparatus and Adhesion Meter*

All previously mentioned devices allowed researchers to get some images of surface topography and same internal structure of the samples. However, these devices did not provide information about forces acting between surfaces and their mechanical properties. The first direct measurements of forces of molecular attraction between solids was fulfilled by Abrikosova and Derjaguin (1951). They suggested to build a special scale having a feedback mechanism that measures directly the interaction force of two surfaces. The schematic diagrams of both the Derjaguin and Abrikosova apparatus and the Derjaguin, Rabinovich and Churaev apparatus for measuring molecular attraction forces in air and vacuum are given by Derjaguin et al. (1978), see, further Derjaguin et al. (1954), Derjaguin et al. (1956), Derjaguin et al. (1958). Currently such a device is called the Surface Force Apparatus (SFA). The technique was developed further by Tabor and Winterton (1969). The SFA may measure

the surface separation by multiple beam interferometry with accuracy ± 0.1 nm (Israelachvili 1991).

The Adhesion Meter (AM) device introduced and built by Myshkin et al. (2004), Myshkin et al. (2005a) has a vertical torsion balance with the negative feedback. As it has been noted by Myshkin et al. (2005b) this design scheme eliminates the problems with balancing and errors caused by friction in the balance support. Using the AM one can measure the force interaction of surfaces in two regimes: (1) separation of surfaces (pull-off force is used for measurement of the strength of adhesive bonds); and (2) approach to and contact between solids (one can study adhesive contact). Using the contact AM, the surface energy of various coatings on a silicone plate was measured, including a 3 nm thick organic self-assembled monolayer (SAM) made of octadecyltrichlorosilane (OTS). Such organic OTS-SAM may be effectively used in application to tooth surfaces of silicon-based micro-electro-mechanical systems (MEMS) microgears (see, e.g. Almuramy et al. 2019).

2.3 Depth-Sensing Indentation Techniques

The depth-sensing indentation (DSI) techniques were introduced by Kalei (1967) in his PhD thesis prepared under supervision of M.M. Khrushchov (1890–1972). The technique assumes that a smooth material sample is probed by an indenter and the load (the compressive force P) acting on the indenter and the displacement h (an alternative notation is δ that we will use further) of the indenter, i.e. the approach between the indenter and the sample, are continuously recorded. The first paper describing DSI techniques was published by Kalei (1968). Kalei used a standard PMT-3 microhardness tester built by Khrushchov and Berkovich. This indenter was equipped by a four-side pyramid probe.

Later Bulychev et al. (1975), Bulychev et al. (1976) suggested to estimate the contact modulus of materials using the unloading branch of the $P - \delta$ curve. They noted that for some axisymmetric indenters, the slope of the $P - \delta$ curve calculated in the framework of the Hertz contact theory satisfies the exact expression

$$\frac{dP}{d\delta} = 2E^*a, \quad (1.1)$$

where E^* is the contact reduced modulus and a is the contact radius.

The Hertz contact theory assumes that both solids may be approximated as elastic half-spaces. If an isotropic linear elastic half-space is characterized by the Young's modulus E and the Poisson ratio ν then its contact modulus E^* is defined as

$$E^* = \frac{E}{1 - \nu^2}. \quad (1.2)$$

The problem of contact between two elastic bodies having contact moduli E_1^* and E_2^* respectively, is mathematically equivalent to the problem of contact between an isotropic elastic half-space with contact modulus E_I^*

$$\frac{1}{E_I^*} = \frac{1}{E_1^*} + \frac{1}{E_2^*} \quad (1.3)$$

and a curved rigid body whose effective shape function f is equal to the initial distance between the surfaces.

Comment Let one consider two polar systems of coordinates having the same origin at the point of initial contact. The systems differ from each other just by direction of the vertical axes (z_1 and z_2). The axis for each of the solids is directed inside the solid. Then $f = f_1 + f_2$. Here f_1 and f_2 are the shape functions of the solids. If one considers two spheres of radii R_1 and R_2 , then in the Hertz approximation, they are described as paraboloids of revolution

$$f_1(r) = \frac{1}{2R_1}r^2, \quad f_2(r) = \frac{1}{2R_2}r^2.$$

In this case the effective shape function f is an effective sphere of radius R_{ef}

$$f(r) = \frac{1}{2R_{ef}}r^2, \quad \frac{1}{R_{ef}} = \frac{1}{R_1} + \frac{1}{R_2}. \quad (1.4)$$

Formally, the radius of curvature of sharp conical indenters is zero and, therefore (1.3) is not applicable. However, if the indenter is much stiffer than the material of the sample, i.e. $E_2^* \gg E_1^*$ then one can put $E_2 = \infty$ and $E_I^* = E_1^*$.

If contacting materials are non-linear elastic having homogeneous prestress, or they are transversely isotropic ones, then one needs to use the corresponding effective contact modulus K_I^* instead of E_I^* (see, e.g. Borodich 1990, 2014).

Bulychev et al. (1975), Bulychev et al. (1976) argued that if (1.1) re-write as the following approximate expression (the BASH formula)

$$\frac{dP}{d\delta} = 2E^* \sqrt{\frac{A}{\pi}} \quad (1.5)$$

where A is the contact area, then (1.5) can be applied not only to axisymmetric indenters as but also to pyramidal indenters and that the error will be small. This formula is the corner stone of interpretation of results of nanoindentation tests. A review of applications of the DSI techniques based on the use of the BASH formula is given by Jin et al. (2022). It was noted that the theoretical background of the DSI techniques in application to sharp indenters suffers from the lack of rigorous background (Jin et al. 2022). In particular, the current interpretations of results of nanoindentation by sharp indenters neglect residual stresses in materials after their

plastic deformations. On the other hand, DSI techniques based on employment of the spherical indenters along with the so-called BG method (Borodich and Galanov 2008) may be justified by the use of the well-established theories of adhesive contact. The BG method will be discussed in this Chapter.

2.4 Atomic Force Microscopy and Devices Based on the Use of Elastic Cantilevers

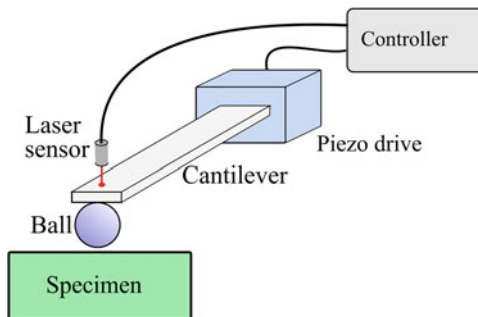
The atomic force microscope (AFM) is a device that enables researchers to obtain a very high-resolution map of surface topography. The inventors of the AFM (Binnig et al. 1986) argued that the capability of such instruments to measure inter-atomic scale forces opens the door to a variety of applications. Indeed, the use of AFM allows researchers not only to characterize the topography of sample surfaces (Sánchez Quintanilla 2013; Podestà 2013), but also to manipulate the nanoscale objects (Chen et al. 2003), to tailor surface nanostructures by AFM tip-based nanomachining (Al-Musawi et al. 2016), to measure nanometre-scale frictional properties (Mate et al. 1987), and to estimate the elastic properties of objects (Kuznetsova et al. 2007; Acerbi et al. 2012). AFM tests are also actively used in various areas, including applications to biological objects (see, e.g. Scherge and Gorb 2001), in particular to biological cells (see, e.g. Sokolov 2022; Starodubtseva 2022).

Roughly speaking, it can be described as an elastic cantilever beam having a feedback mechanism. A tip (probe) is attached to the free end of the cantilever. The tip is moving along the sample surface, while an AFM detector records continuously the deflection and motion of the cantilever. Contact mode is the most common method of operation of the AFM. This means that the AFM tip and sample remain in close contact during scanning of the surface. Here, the term ‘contact’ means that the surface and the probe are in the repulsive regime of the inter-molecular force curve. The tips can be a sharp pyramid (Starodubtseva 2022), a sphere (Sokolov 2022), or a flat-ended cylinder (Acerbi et al. 2012). An AFM may also have no tip (Benoit et al. 2000; Weder et al. 2009).

There are many papers devoted to DSI studies of cells using AFMs. However, contrary to DSI by nanoindenters, AFM probing involves not only indentation but also retraction (the probe sticks to the surface due to adhesion). As an example of a very useful application of DSI of cells by AFM, one can mention cells with brush layers. The layers consist mainly of microvilli, microridges and cilia. AFM with a spherical probe may detect the difference in the surface brush of normal and cancerous cells (Sokolov 2007; Iyer et al. 2009). Good reviews of other AFM studies of cells have been given by Kuznetsova et al. (2007) and Starodubtseva (2022).

There are also other devices that are based on the use of elastic cantilevers. For example, the force tester (Tetra GmbH, Germany) consists of a sapphire ball attached to the double-leaf cantilever spring of known spring constant (Fig. 1.2). The

Fig. 1.2 Schematic setup of the force measurement device Basalt-1



custom made force measurement device Basalt-1 (Tetra GmbH, Ilmenau, Germany) was used for DSI experiments of many soft materials, see, e.g. Gorb et al. (2000), Borodich et al. (2013) and Perepelkin et al. (2019), Perepelkin et al. (2021).

During indentation, the deflection of the spring is continuously monitored by fiber-optical-sensor. If a sample is elastic then the loading and unloading branches of the force-displacement curve are very close to each other. Since the surface asperities are squashed during loading, only unloading branches are normally studied, where the classic models of smooth adhesive contact may be used applicable. The interacting force between the sphere and the sample is recorded as a force versus time curve. One can find a detailed description of the device in papers by Gorb et al. (2000) and Perepelkin et al. (2019).

3 Mechanisms of Adhesion Between Biological Cells

A property of molecules to attract each other was discovered by van der Waals in 1873. As he noted, “*attraction of the molecules decreases extremely quickly with distance, indeed that the attraction only has an appreciable value at distances close to the size of the molecules*” (van der Waals, 1910). Maxwell (1874) read the thesis written in Dutch by van der Waals and gave a very high appraisal of the results. Maxwell made a very important prediction: although molecules attract each other at short distances, they repel each other at a closer approach. Qualitatively these effects are reflected in the Lennard-Jones potential and other potentials used in Molecular Mechanics.

3.1 Physical Mechanisms of the vdW Forces

Peter N. Lebedev (Lebedew) and B.B. Golitzin gave the first electromagnetic explanation of molecular forces (see references in Derjaguin et al. 1958). In particular, Lebedew (1894) wrote: “Interpretation of light vibrations by Hertz as

electromagnetic processes conceals one more, thus far untouched, problem that of radiation sources and processes proceeding in a molecular vibrator when it gives up light energy to the surrounding space. This problem leads, on the one hand, to spectroscopic analysis and, on the other hand, quite unexpectedly, to one of the most complicated problems of modern physics, i.e., the theory of molecular forces. The latter ensues from the following considerations: from the standpoint of the electromagnetic theory of light, we have to recognize the existence of ponderomotive forces between two light-emitting molecules as between two vibrators in which electromagnetic vibrations are excited; these forces arise from electrodynamic interactions between variable electric currents flowing in molecules (in accordance with Ampere's laws) or between variable charges in them (in accordance with the Coulomb laws). Therefore, we must assert that in this case molecular forces exist between molecules closely linked to radiative processes. . .".

The modern interpretation of the vdW forces appeared after the introduction of quantum mechanics by M. Planck. Indeed, the various kinds of attractive forces were described by Keesom (the Keesom force of attraction is caused by two permanent dipoles), by Debye (the Debye force of attraction is caused by a permanent dipole and a corresponding induced dipole), and by London (the London dispersion force is caused by two instantaneously induced dipoles), see, e.g. Derjaguin et al. 1958. These three attractive forces are collectively called van der Waals forces.

The common models of vdW forces may explain many physical phenomena. However, there are cases that need further investigations. For example, Lessel et al. (2013) studied the impact of vdW interactions on a single asperity friction sliding along *Si* wafers having variable *SiO₂* layer thickness. It was found that on thin (1 nm) *SiO₂* layers, higher friction and jump-off forces were observed than on the thick (150 nm) layers. It was shown that the effects of different elastic moduli, electrostatic effects, triboelectrification of the tip and surface, and effects of surface charges can be ruled out as an origin for the observed differences. Indeed, electrostatic forces cause very high jump-off forces, which were not observed during the experiments. The difference was explained by the influence of vdW interactions. Although it was suggested to describe the experimental data by calculations employing a combination of the effective interface potentials along with the Derjaguin-Muller-Toporov (DMT) model, the distance of influence of vdW forces is larger than the distances commonly considered in models of friction (see, e.g. a review by Borodich and Savencu, 2017). In fact, the description of vdW interactions and adhesion between solids are still actively discussed. For example, it was argued that a qualitatively correct description of the vdW interactions between polarizable nanostructures over a wide range of finite distances can only be attained by accounting for the wavelike nature of charge density fluctuations (Ambrosetti et al. 2016).

3.2 *Physical Mechanisms of Cell Adhesion*

It is known (see, e.g. Maitre and Heisenberg 2011) that adhesion of cells is a key biological property for maintaining multicellular structures. The physical and chemical mechanisms of adhesion between solids may be roughly subdivided into four classes: chemical bonding, intermolecular bonding, electrostatic interactions, and capillary forces (see, e.g. Meng 2013). Although capillary adhesion may significantly affect contact between soft materials or some biological systems (see, e.g. Creton and Gorb 2007; Goryacheva and Makhovskaya 2022), they are less important for modelling adhesive contact between cells because cells interfaces are normally immersed in aqueous solution (Sokolov 2022).

As we have mentioned in our recent paper (Borodich et al. 2021), there are different opinions about the sources of cell adhesion. The common opinion of biologists is that adhesive binding of a cell to a surface or another cell is due to actions of complex proteins such as selectins, integrins, and cadherins (named for “calcium-dependent adhesion”), called collectively as cell adhesion molecules (adhesins), i.e. the main determinants of adhesion energy at the cell contact are the adhesins. Assuming selective adhesion of cell adhesins, the so-called ‘lock-and-key’ mechanism is accepted (see, e.g. Maitre and Heisenberg 2011).

On another hand, Kendall and his co-workers (see, Kendall et al. 2011; Kendall and Roberts 2015) stated that the lock-and-key molecules are not the dominant mechanism of cell adhesion. They argued that the key cause of adhesion are vdW forces and demonstrated that effects from geometry, elasticity and surface molecules must all add on to the basic cell attractive force. This opinion is in agreement with calculations by Sivasankar et al. (1999) that show that vdW interactions between cadherins could be the main physical mechanism for the measured adhesion, even if the cell-cell adhesion in soft biological materials involves interactions among special proteins. The lock-and-key mechanism is important only if there are such molecules (adhesins) present on the cell membrane (their distribution is very specific and varies depending on the cell types) and their adhesive action depends not only on vdW, but also on chemical bonds.

Derjaguin and his co-workers did not discuss adhesion of cells. However, they studied adhesion of many materials including polymer films and colloidal particles (Derjaguin et al. 1973). They argued that in many cases electrical phenomena are the most important factor in determining the resistance of a film to detachment. They wrote: “*Electrical phenomena not only accompany film peeling, as has been known for some time, but in a great many instances are the most important factor in determining the resistance of a film to detachment, both in cases of purely adhesive failure (i.e., when the separation surface lies between the substrate and the film, so that no part of the film remains on the substrate) and in cases of mixed-type failure, not purely cohesive (i.e., when the separation plane is in the space-charge zone of the double layer)*”. Studying the forces of interactions between surfaces separated by liquid films, Derjaguin (1940) demonstrated effects that were caused by forces having neither of the nature of vdW forces nor of the nature of dipole

forces. The further studies led to the DLVO theory (Derjaguin 1940; Derjaguin and Landau 1941; Verwey and Overbeek 1948). According to the DLVO theory, the potential of interactions between colloidal particles is the combination of an attractive vdW potential and a repulsive electrostatic potential (the latter is due to the repulsion between the electrical double layers formed at the surface). Hence, there is a potential energy barrier between particles that prevents the proximity of the particles. The importance of this source of adhesion is also found in cell adhesion. For example, Hermansson (1999) argued that adhesion of microorganisms to various interfaces may be explained by the classical DLVO theory of colloid stability. Further, electric double layer interactions play also an important role in bacterial adhesion to surfaces, see a review by Poortinga et al. (2002).

As it was noted by Derjaguin et al. (1973): *“Absolutely irrespectively to the nature and the value of the forces carrying out the adhesive connection, to make the adhesive seam to be strong enough one needs to increase maximum possible the area of the true contact. Since the real surfaces have rather sophisticated jagged profile, the simplest way to create a quite good contact is to cover a solid material by another being in a liquid phase. If both materials are in solid state then a good contact can be made only if a rather high external pressure is applied.”* This observation was confirmed experimentally (Purtov et al. 2013) and explained by a combination of a theoretical model by Galanov (2011) along with statistical analysis of surface roughness and the contact area between a hard rough surface and a soft indenter (Pepelyshev et al. 2018). It was observed that a surface with a relatively small roughness contacting a soft sphere may show higher values of the adhesive force than a smooth surface because the area of with the former surface is heier than the contact area with the latter one.

In fact, biological cells are not smooth spheres. They are often covered by brash-like protein structures (Sokolov 2022). The protein structures may be rather complicated. Fortoul et al. (2015) argued that the soluble *n*-ethylmaleimide-sensitive-factor attachment protein receptor (SNARE) complexes are “the core protein machinery involved in synaptic vesicle docking and fusion”. They developed a model that combines the mechanics of vesicle/membrane deformation with a coarse-grained model of the SNARE complex. According to their vision, the docking and fusion process for a synaptic vesicle (a nearly spherical lipid bilayer shell) may be described in the following way. The shell is “brought in proximity to the plasma membrane (a nearly flat lipid bilayer), under the influence of the attractive forces exerted by the SNARE complex” that allows to overcome the long-range repulsion between the vesicle and membrane. These interactions may be described by a system of modified Lennard-Jones potentials.

Let us use an analogy between adhesion of biological cells and polymer materials (Myshkin and Kovalev 2018). They argued that a polymer surface operates with a counterbody mainly through vdW and electrostatic interactions along with the chemisorption of polymer chains. The cell surfaces have flexible proteins that have a similar function as chains of macromolecules in polymers. As it was noted by Shull (2002), if the molecule is stretched to the point of failure, the force required to break a bond along the molecule can be measured. By carefully tailoring the experiment

so that one knows which type of bond is actually breaking, it is possible to measure the force required to break an isolated bond. The experimentally observed discrete reduction of the adhesive force at separation of an indenter and living cells (Kadem et al. 2016) may be explained by failure of single protein chains.

Thus, the adhesion between biological cells may be caused by different mechanisms. However, if one would like to employ the well-established models of adhesive contact without their cordial modifications, then all these forces should be considered just as parts contributing to work of adhesion w of the contacting bodies.

4 Adhesive Contact Problems and Experimental Evaluation of Cell Characteristics

The contact probing of biological materials is a very popular approach for evaluating mechanical and adhesive properties of the materials. However, to extract these characteristics from experimental $P - \delta$ curves, one needs to employ a proper model of contact.

Theoretical studies of contact problems started from pioneering works by Hertz (1882) and Boussinesq (1885). There are many books dedicated to modern adhesive contact mechanics (see, e.g. Argatov and Mishuris 2018; Kendall 2001; Popov 2010; Sviridenok et al. 1990). Using the Hertz contact theory, one can consider various problems for smooth blunt solids, in particular for a spherical probe that is approximated as a paraboloid of revolution according to Hertz contact theory. To apply the classic contact theories one needs to know the contact modulus K_I^* (or E_I^* in the case of isotropic linear elastic material) and if contact is adhesive, then one needs to know also the work of adhesion w . The work w is defined as the energy per unit area needed to separate two dissimilar surfaces from contact to infinity. Thus, one needs to use a proper contact theory and a proper mechanical models of cells in order to interpret experimental data obtained by AFM indentation (see, e.g. Borodich 2014; Perepelkin et al. 2021; Borodich et al. 2021).

4.1 Adhesive Contact Problems

Reviews on history of mechanics of adhesive contact start usually by citing the paper by Bradley (1932). However, there is a confusion related to this paper because he did not consider any contact problem. In fact, he considered attraction between two rigid spheres. Taking into account only one of components of the vdW forces, namely the London dispersion force, he calculated the attraction of each point of one of the spheres to all points of another sphere. Then he integrated the obtained values, assuming additivity of the London forces. As the result of rather lengthy

calculations, he derived the value of the force of attraction between two spheres of radii R_1 and R_2 respectively, is

$$P_{adh} = 2\pi w R_{ef}. \quad (1.6)$$

A very good and popular paper by Johnson and Greenwood (1997) contributed to the above confusion. Indeed, they presented a map of applicability of adhesive contact theories and included in the map a region where Bradley's result should be applied, while as it has been mentioned above, Bradley (1932) did not consider contact between deformable bodies. Although Hamaker (1937) paper considered a more general formulation of the problem of attraction between spheres, he used the same assumptions as Bradley (1932), i.e. the bodies are rigid and calculations should be pointwise. Some authors believe that these point-wise calculations describe better the attraction between solids. For example, Soldatenkov (2013) treats the contact problem with the bulk application of intermolecular interaction forces as problems having a refined formulation. In fact, this approach suffers from the lack of *physical rigour*. Indeed, as Derjaguin et al. (1958) wrote: "*Strictly speaking, the additivity of London forces for condensed bodies has neither theoretical nor experimental substantiation ... Moreover, atomic and molecular characteristics, ... are altered in condensed systems compared with the properties of isolated atoms and molecules due to the mutual influence of neighboring particles. For this reason, the contribution to the molecular interaction from individual molecules depends on their coordination and concentration; for surface molecules, it depends on the number of neighbors.*"

Overwhelming majority of models of adhesive contact are based on explicit or implicit employment of Derjaguin (1934) approximation that may be formulated as the following three statements (Borodich 2014): (1) instead of the pairwise summation of the interactions between the elements of solids, the volume molecular attractions are reduced to surface interactions; (2) the surface interactions are taken into account only between the closest elements of the surfaces lying on vertical straight lines; and (3) the interaction energy per unit area between small elements of curved surfaces connected by vertical straight lines is the same as the interaction energy per unit area energy between two parallel infinite planar surfaces. The questions of transition between formulations of problems of adhesive contact with volumetric distributions of intermolecular forces and with surface distributions of the forces were discussed by Argento et al. (1997) and Jagota and Argento (1997). They provided new surface formulation of the problems based on the use of a new concept: *the inter-surface stress tensor*. They argued that this new surface formulation eliminates the geometrical restrictions associated with the commonly used Derjaguin approximation.

Using the Derjaguin approximation, one can calculate a force of attraction between two rigid spheres and get the Bradley (1932) result writing just one or two lines of calculations. Derjaguin (1934) was the first who suggested to take into account deformations of solids in order to estimate the attraction between them. He tried also to calculate the force of adhesion between three-dimensional bodies

using the Hertzian approximation of their surfaces. Unfortunately, his calculations had some errors.

Derjaguin (1934) suggested to calculate the total energy of contact between solids. Using this idea, Sperling (1964) developed a model of adhesion between solids. Formally, the final expressions derived by Sperling (1964) for $P-a$ and $\delta-a$ relations are the same as those independently derived by Johnson et al. (1971), i.e. the JKR theory of adhesive contact (this is the reason that K.L. Johnson sometimes referred to this theory as JKRS theory). However, the JKR formalism that suggests superposition of the Hertz and Boussinesq solutions for spherical and flat-ended cylindrical indenters (the main idea of this formalism may be traced back to Johnson 1958), provides huge opportunities for further development of the JKR theory (see a discussion by Perepelkin and Borodich 2021). One can even say that the JKR formalism is in some sense universal for problems of contact probing of biological materials (Borodich 2022).

According to Kendall (2001, pages 185–186), the JKR theory historically was developed in the following steps. In 1970 Kendall and Roberts discussed the experimental observations of the contact spots that were larger than expected from the Hertz equation. They found that the answer lay in applying Derjaguin’s method . . . to Johnson’s stress distribution. Johnson presented a mathematical realization of this idea an evening later. Thus, Johnson et al. (1971) applied the idea to equate the work done by the surface attractions against the work of deformation in the elastic spheres (Derjaguin 1934), to stress superposition (Johnson 1958). The JKR approach is based on the use of a geometrically linear formulation of the contact problem, and a combination of both the Hertz contact problem for two elastic spheres and the Boussinesq relation for a flat ended cylindrical indenter. If there were no surface forces of attraction, the radius of the contact area under a punch subjected to the external load P could be found by solving the Hertz-type contact problem. However, in the presence of the forces of molecular adhesion, the equilibrium contact radius is greater than the radius calculated according to the Hertz theory under the same load.

It follows from the JKR theory that the relation between the external load P and the adhesive contact radius a is

$$P = (4E^*/3R_{ef})a^3 - \sqrt{8\pi w E^* a^3} \quad (1.7)$$

while the approach between the spheres is

$$\delta = a^2/R_{ef} - \sqrt{2\pi w (E^*)^{-1} a}. \quad (1.8)$$

The well established classic theories of adhesive contact such as JKR and DMT theories, and the Maugis transition solution between the JKR and DMT theories, propose methodologies to predict the adhesion force between surfaces.

It follows from (1.7) and (1.8) that the separation load that is equal to the instability point P_{sep} of a $P - \delta$ curve is at the point where $dP/d\delta = 0$, i.e.

$$P_{sep}^{JKR} = -(3/2)\pi w R_{ef}. \quad (1.9)$$

One can see that the separation load is negative, i.e. one needs to apply tensile load to separate the indenter and the sample stuck to the indenter surface.

According to an alternative theory of adhesive contact introduced by Derjaguin et al. (1975) the separation load is

$$P_{sep}^{DMT} = -2\pi w R_{ef}. \quad (1.10)$$

This load is in accordance with rigid body limit (1.6).

Initially, the JKR approach was criticized by B.V. Derjaguin. Later Derjaguin et al. (1975) published an alternative theory of adhesive contact (the DMT theory). It is assumed by Johnson et al. (1971) that adhesive forces act only within the contact region, while Derjaguin (1934) assumed that the adhesive forces act outside the contact region and they should not be taken into account within the contact region. The same assumptions are taken by Derjaguin et al. (1975).

Comment We may only guess that one of the causes for his critics was that none of his numerous papers dedicated to various aspects of the phenomenon of adhesion were cited by Johnson et al. (1971). In 1995 Prof. K.L. Johnson told one of the authors (FB) during one of their meetings that he knew neither German nor Russian. Therefore, he could not read the paper by Derjaguin (1934) published in German. In fact, Kendall cited one of Derjaguin's papers in another paper (Kendall 1971) where he considered a wide spectrum of adhesive contact problems including the Boussinesq-Kendall contact problem for a flat-ended cylindrical indenter. Thus, it is evident that references to Derjaguin papers were omitted by Johnson et al. (1971) by an unfortunate accident.

The main critical point by Derjaguin was that P_{sep}^{JKR} does not go to the rigid body limit (1.6) as materials of the contacting solids become harder. Indeed, P_{sep}^{JKR} does not depend on the elastic modulus of the material and formally the theory could be applied to the case of very hard materials.

The commonly accepted point of view is that this seeming paradox was resolved by Tabor (1977) who assumed that the pull-off (separation) force has the form

$$F_{sep} = 1.5\pi R_{ef} w \Phi(R_{ef} w^2 / (4E^2 z_0^3))$$

where the function $\Phi(R_{ef} w^2 / E^2 z_0^3)$ tends to $4/3$ as $(R_{ef} w^2 / E^2 z_0^3)^{1/3}$ approaches unity. This is interpreted as Tabor introduced the parameter μ

$$\mu = \left(\frac{R_{ef} w^2}{(E^*)^2 z_0^3} \right)^{1/3}$$

such that if $\mu > 1$ then the JKR model is applicable, while if $\mu \leq 1$ then one needs to use the DMT theory. Here z_0 is the equilibrium separation of the surfaces (usually its values are in the range of 0.3–0.5 nm). Nowadays it is usually accepted that the JKR model is valid if $\mu > 5$.

The Tabor arguments were accepted by Derjaguin's group. Muller et al. (1980) presented results of numerical analysis based on the use of a Lennard-Jones potential that confirmed the point of view of Tabor. They used another parameter that was quite close to the Tabor one. Unfortunately, there were other problems that showed that the original DMT analysis should be corrected (see Muller et al. 1983 along with discussions by Greenwood 2007, and Barthel 2008). However, the analysis by Maugis (1992, 2000) provided an analytical interpretation of the DMT theory, confirmed the point of view by Tabor (1977) and presented a new theory of adhesive contact based on ideas of fracture mechanics and using piecewise-constant approximations of the Lennard-Jones potential near the border of the contact region.

If a theory of adhesive contact is represented by a functional, then it is quite convenient to write it in a dimensionless form. To do this one needs to write new 'units' or scales for forces and displacements using the problem governing parameters R_{ef} , w , and E^* . It was suggested by Borodich and Galanov (2008) to use $P_c > 0$ and $\delta_c > 0$ as characteristic scales of the contact problem for the force and the displacement respectively at low loads and small displacements

$$P_c = \frac{3}{2}\pi w R_{ef} > 0, \quad \delta_c = \frac{3}{4} \left(\frac{\pi^2 w^2 R_{ef}}{(E^*)^2} \right)^{1/3} > 0. \quad (1.11)$$

If one employs the classic JKR theory then P_c and δ_c have a very clear physical meaning: $P_c = -P_{sep}^{JKR} > 0$, i.e. $dP/d\delta = 0$ at $P = -P_c$ and $dP/d\delta = \infty$ at $\delta = \delta_c$.

Let us use the Maugis notation $\chi = \sqrt{1 + \frac{P}{P_c}}$.

For the DMT model, the functional expression has the following forms

$$F\left(\frac{P}{P_c}, \frac{\delta}{\delta_c}\right) \equiv \frac{P}{P_c} - \frac{1}{\sqrt{3}} \left(\frac{\delta}{\delta_c}\right)^{3/2} + \frac{4}{3} = 0 \quad (1.12)$$

and for the JKR model, the functional expression is

$$F\left(\frac{P}{P_c}, \frac{\delta}{\delta_c}\right) \equiv \begin{cases} (3\chi - 1) \left(\frac{1+\chi}{9}\right)^{1/3} - \frac{\delta}{\delta_c} = 0, \\ -(3\chi + 1) \left(\frac{1-\chi}{9}\right)^{1/3} - \frac{\delta}{\delta_c} = 0, \end{cases} \quad (1.13)$$

where the former expression is used if $\chi \geq 0$ and $\delta/\delta_c \geq -3^{-2/3}$, while the latter expression is applied if $\frac{2}{3} \geq \chi \geq 0$, and $-1 \leq \delta/\delta_c < -3^{-2/3}$.

It was suggested by Borodich and Galanov (2008) to fit the experimental $P - \delta$ relations by (1.13) or (1.12) with checking of applicability of these models by

calculating the Tabor parameter using the estimated values of E^* and w . This so-called BG method is discussed in this Chapter later.

4.2 Evaluation of Elastic and Adhesive Characteristics of Cells

As it has been mentioned, the contact probing of biological materials is used to evaluate mechanical and adhesive properties of the materials. Currently the indentation of materials by sharp indenters is the most popular method for evaluation of the contact modulus of materials (see, Wahl et al. 2006; Ebenstein and Wahl 2006, and also reviews by Borodich 2014; Gonabadi et al. 2022; Jin et al. 2022). However, the methods based on the use of sharp indenters have several drawbacks (see, discussions by Chaudhri and Lim 2007; Borodich 2014, and Perepelkin et al. 2019). Hence, Chaudhri and Lim (2007) suggested to determine elastic contact modulus using the classic Hertz theory in application to the initial elastic stage of the force-displacement curves when the material samples are loaded by spherical indenters.

To model interactions between the AFM tip and a cell membrane, various known problems of contact theory were used, see a discussion by Wang and Discher (2007). In particular, these include Hertzian problems of contact for spherical probes and other non-adhesive contact problems. Approaches that were in accordance with the above mentioned suggestion by Chaudhri and Lim (2007), i.e. to use the classic non-adhesive contact mechanics in application to indentation of spherical indenters, was suggested by Dimitriadis et al. (2002) and other researchers.

We would like to underline that the expression (1.1) for axisymmetric Hertzian contact is exact. The same is valid for the BASH relation in application to contact between a spherical indenter and a linear elastic isotropic sample. If one assumes that there is no-slip within the contact region among the material points of the sample and the indenter surface instead of the usual frictionless boundary conditions then as it was shown by Borodich and Keer (2004a), Borodich and Keer (2004b), the BASH relation should be modified by introduction of a coefficient $C_{NS}(\nu)$ that depends on the material Poisson's ratio ν . They showed that $C_{NS}(0.5) = 1$ and $C_{NS}(0) < 1.1$. This means that usually friction between the sample and the indenter has negligible effect on the experimental $P - \delta$ curves. As it was shown by Borodich et al. (2014a), the same statement is valid in an extension of the JKR theory to the no-slip boundary conditions. On the other hand, it was shown by Borodich and Galanov (2018) employing the classic JKR theory of adhesive contact (Johnson et al. 1971) that for spherical probe of radius R , the for the slope $S = dP/d\delta$ is

$$\frac{dP}{d\delta} = 2aE^* \left[\frac{1 - 3\sqrt{(\pi R^2 w)/(8E^* a^3)}}{1 - \sqrt{(\pi R^2 w)/(8E^* a^3)}} \right].$$

The above expression may be expressed explicitly not as a function of the contact radius but as a function of the force P or the displacement δ . Evidently, if $w = 0$ then the above expression reduces to the classic BASH formula. Thus, the use of the original BASH formula may lead to wrong estimations of the contact modulus. The above adhesive corrections are especially important for sticky soft and biological materials. Hence, in application to these materials, it is more reasonable to use theories of adhesive contact. However, usually adhesive and mechanical characteristics of contacting solids are evaluated employing two independent and rather different indentation tests: (1) DSI by sharp pyramidal indenters for extraction of the effective contact modulus E_I^* from the unloading branch of the $P - \delta$ curve; and (2) extraction of the work of adhesion w from direct measurements of the pull-off force of a spherical indenter from the material sample and application of the JKR theory

$$w = \frac{2P_c}{3\pi R_{ef}}. \quad (1.14)$$

Sometimes several points of the $P - \delta$ curve are used for estimation of w (see, Wahl et al. 2006; Ebenstein and Wahl 2006). These approaches are not very reliable. As it has been mentioned above, the DSI methods in application to sharp indenters have several drawbacks, hence, there is no reliable theoretical background supporting these approaches. Concerning the direct methods of estimations of the adhesive characteristics of materials, Borodich and Galanov (2008) wrote that they are not reliable due to instability of the experimental $P - \delta$ curves for ultra-low tensile forces. Indeed, even slight damage of the contact due to surface irregularities or surface contamination leads to contact breakage (Gorb and Gorb 2009). To the best of our knowledge, the BG method is currently the unique method that may estimate both the contact modulus and the work of adhesion from the stable part of the $P - \delta$ curves, e.g. from the compressive part of the unloading branch of the curve.

Because adhesion is important when the contacting bodies are sufficiently small or sufficiently compliant (Shull 2002) and living cells belong to both groups, adhesion of cells is of crucial importance for their proper modelling. Chu et al. (2005) argued that the JKR theory may be used to model adhesion of living cells. Actually, they argued that if the cytoskeleton of the cells has a complete 3-D structure of approximately spherical shape, then JKR theory is applicable to relate the separation force to the adhesion energy (see, (1.14)). It is important to note that although the original JKR model was used for describing adhesion of two cells (see, e.g. Korayem et al. 2012), the original model is valid only for contact of isotropic linearly elastic spheres. Therefore, the JKR theory should be modified to take into account some specific features of cell membranes and to model their contact properties. It is known that the JKR theory for a spherical indenter may be extended to transversely isotropic (Espinasse et al. 2010; Borodich et al. 2014b) and prestressed materials (Borodich 2014). Hence, it is possible to take into account the prestress of cell membranes.

4.3 Adhesive Contact Problem for a Prestressed Neo-Hookean Material

Dao et al. (2003) argued that the cell membranes may be described as a composite material of the neo-Hookean type having the same effective properties as the membranes. It is assumed further that the effective properties of the cell are described as neo-Hookean material; the cell membrane has initial stresses, and the principal stretches of the cell satisfy the condition of incompressibility. Although the membrane is incompressible, its thickness may vary. It is assumed that the cell shape may be locally described as a sphere of radius R_1 and it is in contact with a rigid indenter of radius R_2 . During contact with a probe or another cell, the stress field arises that is just a small perturbation of the large initial stresses. In addition, it is assumed the initial stress field can be considered as homogeneous. The full formulation of the contact problem for a prestressed cell is described by Borodich et al. (2021).

The potential for a hyperelastic material of neo-Hookean type may be written as

$$W = \frac{1}{2}G(\lambda_1^2 - 1 + \lambda_2^2 - 1 + \lambda_3^2 - 1), \quad (1.15)$$

where λ_i is the extension ratio in the x_i direction, G is the initial shear modulus of the material of the natural unstressed state.

It is assumed that the material in its natural unstressed state is isotropic and the shear modulus is $G = E/2(1 + \nu)$. For an incompressible material, one has $\nu = 0.5$ and

$$\lambda_1 \lambda_2 \lambda_3 = 1. \quad (1.16)$$

Because the initial prestress of the cell is homogeneous, there are the following conditions for a stretch λ of the membrane

$$\lambda_1 = \lambda_2 = \lambda, \quad \lambda_3 = \lambda^{-2}. \quad (1.17)$$

The linearized boundary value problems of contact between the cell and a spherical probe satisfy the condition of rotational symmetry of elastic properties for small perturbations of the stress field due to conditions of homogeneous prestress of the membrane (1.17). For homogeneously prestressed solids, the non-adhesive contact problem can be solved just by replacing the contact modulus E^* by the corresponding contact modulus that depends on the prestress of the material (see, e.g. Borodich 1990). The contact problems for incompressible materials of the neo-Hookean type were solved independently by Filippova (1978), and by Dhaliwal and Singh (1978). It was shown that the solution of the Boussinesq problem for a concentrated load P acting on an elastic half-space whose properties and prestress

are described by (1.15) and (1.17) respectively, may be written as

$$u_3(r, 0) = \frac{P}{4\pi Gr} N(\lambda) \quad (1.18)$$

where r is the radius of polar coordinates, u_3 is the vertical displacement of the surface, and the coefficient N is

$$N(\lambda) = \frac{2\lambda^4(1 + \lambda^3)}{\lambda^9 + \lambda^6 + 3\lambda^3 - 1}. \quad (1.19)$$

Because for incompressible solids $\nu = 0.5$, (1.18) can be written as

$$u_3(r, 0) = \frac{P}{E^* \pi r} N(\lambda) = \frac{P}{4G\pi r} N(\lambda). \quad (1.20)$$

Hence, the integral equation of an arbitrary contact problem for equally and uniformly prestressed solids differs from the integral equation of the corresponding classic contact problem only by a constant coefficient $N(\lambda)$. For a non-linear elastic homogeneously prestressed half-space, the contact modulus E_{PS}^* is

$$E_{PS}^* = E_I^*/N(\lambda) = 4G/N(\lambda) \quad (1.21)$$

where $N(\lambda)$ depends on the initial deformations λ within x_1x_2 plane and the non-linear strain potential of the material. For neo-Hookean materials, the expression of multiplier $N(\lambda)$ is given by (1.19).

Thus, an extension of the JKR theory in application to AFM probing of cells leads to the following relation between the external load P acting on the spherical probe and the adhesive contact radius a

$$P = (4E_{PS}^*/3R_{ef})a^3 - \sqrt{8\pi w E_{PS}^*} a^3 \quad (1.22)$$

and

$$\delta = a^2/R_{ef} - \sqrt{2\pi w (E_{PS}^*)^{-1}} a \quad (1.23)$$

where

$$E_{PS}^* = 4G/N(\lambda). \quad (1.24)$$

For a spherical indenter, the (1.22) and (1.23) relations can be united as an explicit $P(\delta)$ relation.

4.4 The Extended BG Method (eBG)

As it has been explained above, the BG method provides a methodology for estimations of the elastic moduli along with estimations of the work of adhesion of the contacting pair in a single experiment using the experimental DSI data for spherical indenters. The method assumes optimal fitting of the experimental points of the load-displacement curves using a dimensionless expression of an appropriate theory of adhesive contact. The BG method is based on a non-direct approach, i.e. on solving an inverse problem of determination of seeking parameters without direct measurements of the adhesive force. Earlier numerical simulations showed that the BG method was robust (Borodich et al. 2013).

It is argued that the values of the effective contact modulus for two cells or between a cell and material of the probe and the work of adhesion for the same pairs may be quantified from a single test using a simple and robust BG method Borodich and Galanov (2008) and Borodich et al. (2013) or its extension (Perepelkin et al. 2019, 2020, 2021). The method is based on an inverse analysis of a stable region of the force-displacements curve obtained from the depth-sensing indentation of a sphere into an elastic sample. Of course, the results for the effective contact modulus depend on the employed model of non-linear elasticity. As it has been shown, if the cell membranes are described as materials of the neo-Hookean type, then the solutions may be given explicitly as a function of prestress of the membrane.

A real experiment presents results of measurements of the $P - \delta$ curve as a set of points (P_i, δ_i) , where $i = 1, \dots, N$ and N is the number of measurements. These measurements are contaminated by experimental errors. If the contamination is not very strong then one may use the least square method for fitting the data and extraction of the seeking parameters. Because the BG method uses a fitting curve written in dimensionless form, this allows to treat quantities of different orders of magnitude in the same way. After the values of the scale characteristics P_c , and δ_c have been extracted from the reliable data, other mechanical and adhesive characteristics are calculated. In particular, w and E^* can be obtained from the following formulae

$$w = \frac{2P_c}{3\pi R}, \quad E^* = \frac{P_c}{4} \sqrt{\frac{3}{R\delta_c^3}}. \quad (1.25)$$

Recently the original BG method has been modified by Perepelkin et al. (2019), Perepelkin et al. (2020), Perepelkin et al. (2021). It has been suggested to use a two-stage fitting of the theoretical DSI dependency to the experimental data. In addition, a new objective functional has been introduced which minimizes the squared norm of the difference between the theoretical curve and the one used in preliminary data fitting.

The main steps of the method are the following. First, the experimental data is approximated by an auxiliary piecewise linear curve (a polygonal chain with relatively small number of segments). The curve acts as a simple yet effective low-

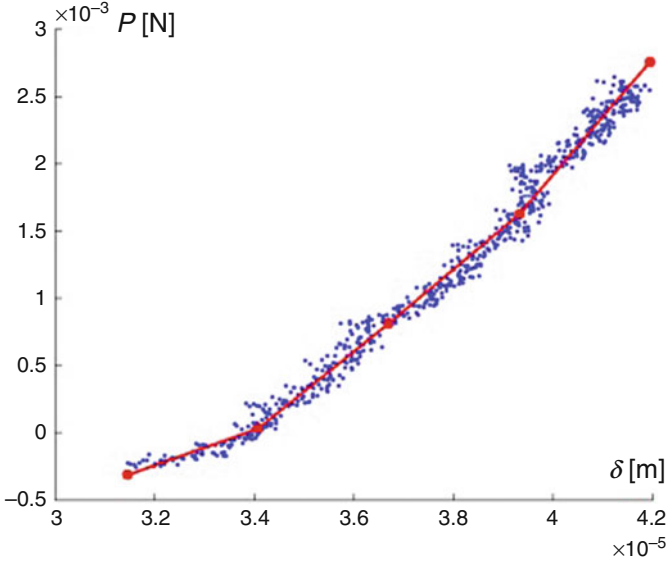


Fig. 1.3 An example result of the first stage fitting procedure of the eBG method. The experimental load-displacement data points are fitted with an auxiliary piecewise linear curve (a polygonal chain with relatively small number of segments)

pass filter, smoothing the data considerably (see Fig. 1.3). On this step the data has been normalized by intervals of the available experimental values. The fitting is based on minimization of the sum of squares of orthogonal distances from the polygonal chain to the normalized data points (the so-called orthogonal distance fitting concept).

Then the fitting procedure of the theoretical load-displacement curve to the auxiliary one is applied (both curves are dimensionless). The second fitting is done via minimization of the squared L^2 norm of the difference of the two functions, the theoretical load-displacement curve and the auxiliary (the polygonal chain) one. Minimization is done by means of varying the scale characteristics P_c , and δ_c . Having found the optimal values of P_c and δ_c one should use (1.25) to obtain E_{pS}^* and w . Please refer to Perepelkin et al. (2019), Perepelkin et al. (2021) for further details. The latter work (Perepelkin et al. 2021) contains an in-depth mathematical discussion of the approach.

Thus, the eBG method can be applied to extract E_{pS}^* and w from $P - \delta$ curves obtained by probing of cell membranes by a spherical indenter. It is clear that the results will depend on the prestress of the membrane. If a cell has large deformations and cannot be approximated by a sphere, then the described procedure cannot be applied.

5 Conclusion

We have presented a review of several questions related to studies of biological cells, materials and other objects of nanotechnology. First we have reviewed methods of microscopy and contact methods for studying micro/nanoscale objects and interactions between their surfaces. Then we have discussed the physical background of van der Waals interactions and mechanisms of adhesion between biological cells. We have also reviewed some contact theories including the JKR and DMT theories of adhesive contact. Evidently, we have not covered all problems related to the topic, we have just selected several questions that are of interest for goals formulated in the Introduction.

It is argued, that the JKR theory should be modified to reflect specific features of membranes of biological cells, in particular the initial stresses of the membranes should be taken into account. If a cell membrane is treated as a prestressed non-linear material of the neo-Hookean type and the prestress is homogeneous, then the JKR theory may be easily modified. The corresponding formulae presented in an exact form.

It has been argued that the eBG method may be applied for the extraction of mechanical and adhesive properties of the membranes. It has been shown that the obtained values of the effective contact modulus would depend on the initial prestress of the membrane.

Acknowledgments The authors are grateful to Professor K.R. Shull (Northwestern University, USA) for his valuable comments on mechanics of cell adhesion.

The authors are also grateful to Dr. N.V. Perepelkin (currently at Leeds Beckett University, UK) for discussing problems of adhesive contact and for providing illustrative material for the eBG method.

References

- Abrikosova II, Derjaguin BV (1951) Measurements of molecular forces of attraction between two solids. *Zhurnal Eksperimentalnoi i Teoreticheskoi Fiziki. J Exp and Theoret Phy* 21:945–955 (Russian)
- Acerbi I, Luque T, Giménez A, Puig M, Reguart N, Farré, R, Navajas D, Alcaraz J (2012) Integrin-specific mechanoresponses to compression and extension probed by cylindrical flat-ended AFM tips in lung cells. *PLoS One* 7:e32261
- Almuramady N, Borodich FM, Goryacheva IG, Torskaya EV (2019) Damage of functionalized self-assembly monomolecular layers applied to silicon microgear MEMS. *Tribology Int* 129:203–212
- Al-Musawi RSJ, Brousseau EB, Geng Y, Borodich FM (2016) Insight into mechanics of AFM tip-based nanomachining: bending of cantilevers and machined grooves. *Nanotechnology* 27:385302
- Ambrosetti A, Ferri N, DiStasio RA, Tkatchenko A (2016) Wavelike charge density fluctuations and van der Waals interactions at the nanoscale. *Science* 351:1171–1176
- Ardenne von M (1938) Das Elektronen-Rastermikroskop. *Praktische Ausführung. Zeitschrift für technische Physik* 19:407–416

- Ardenne von M (1939) Das Elektronen-Rastermikroskop. Theoretische Grundlagen. *Zeitschrift für Physik* 108:553–572
- Argatov I, Mishuris G (2018) Indentation testing of biological materials. Springer, Berlin
- Argento C, Jagota A, Carter WC (1997). Surface formulation for molecular interactions of macroscopic bodies. *J Mech Phys Solids* 45:1161–1183
- Ball F (2009) Feynman’s fancy. *Chem World* 6:58–62
- Barthel E (2008) Adhesive elastic contacts: JKR and more. *Phys D Appl Phys* 41:163001
- Benoit M, Gabriel D, Gerisch G, Gaub HE (2000) Discrete interactions in cell adhesion measured by single-molecule force spectroscopy. *Nat Cell Biol* 2:313–317
- Binnig G, Rohrer H, Gerber Ch, Weibel E (1982) Surface studies by scanning tunneling microscopy. *Phys Rev Lett* 49:57–61
- Binnig G, Quate CF, Gerber C (1986) Atomic force microscope. *Phys Rev Lett* 56:930–933
- Borodich FM (1990) Hertz contact problems for an elastic anisotropic half-space with initial stresses. *Soviet Appl Mech* 26:126–132
- Borodich FM (2014) The Hertz-type and adhesive contact problems for depth-sensing indentation. *Adv Appl Mechan* 47:225–366
- Borodich FM (2022) Chapter 12: The JKR formalism in applications to problems of adhesive contact. In: Borodich FM, Jin X (eds) *Contact problems for soft, biological and bioinspired materials*. Springer, Berlin, pp 243–287
- Borodich, FM, Galanov BA (2008) Non-direct estimations of adhesive and elastic properties of materials by depth-sensing indentation. *Proc R Soc A* 464:2759–2776
- Borodich, FM, Galanov BA (2018) Interpretation of nanoindentation tests using mechanics of adhesive contact. In: *Abstracts of 10th European solid mechanics conference, July 2–6, 2018 Bologna*
- Borodich FM, Keer LM (2004a) Evaluation of elastic modulus of materials by adhesive (no-slip) nanoindentation. *Proc R Soc Ser A* 460:507–514
- Borodich FM, Keer LM (2004b) Contact problems and depth-sensing nanoindentation for frictionless and frictional boundary conditions. *Int J Solids Struct* 41:2479–2499
- Borodich FM, Savencu O (2017) Hierarchical models of engineering rough surfaces and bioinspired adhesives. In: Heepe L, Xue L, Gorb SN (eds) *Bio-inspired structured adhesives: biological prototypes, fabrication, tribological properties, contact mechanics, and novel concepts*, Ch 10. Springer International Publishing, Cham, pp 179–219. https://doi.org/10.1007/978-3-319-59114-8_10
- Borodich FM, Galanov BA, Gorb SN, Prostov MY, Prostov YI, Suarez-Alvarez MM (2013) Evaluation of adhesive and elastic properties of polymers by the BG method. *Macromolec Reaction Eng* 7:555–563
- Borodich FM, Galanov BA, Suarez-Alvarez MM (2014a) The JKR-type adhesive contact problems for power-law shaped axisymmetric punches. *J Mech Phys Solids* 68:14–32
- Borodich FM, Galanov BA, Keer LM, Suarez-Alvarez MM (2014b) The JKR-type adhesive contact problems for transversely isotropic elastic solids. *Mech Mater* 75:34–44
- Borodich FM, Galanov BA, Keer LM, Suarez-Alvarez MM (2021) Contact probing of prestressed adhesive membranes of living cells. *Phil Trans R Soc A* 379:20200289. <https://doi.org/10.1098/rsta.2020.0289>
- Borries Bv, Ruska E (1933) Die Abbildung durchstrahlter Folien im Elektronenmikroskop. *Z Physik* 83:187–193
- Boussinesq J (1885) *Applications des potentiels ‘a l’Étude de l’équilibrium et du Mouvement des Solides Élastique*. Gauthier-Villars, Paris
- Bradley RS (1932) The cohesive force between solid surfaces and the surface energy of solids. *Philosoph Mag* 13:853–862
- Bulychev SI, Alekhin VP, Shorshorov MK, Ternovskii AP, Shnyrev GD (1975) Determination of Young’s modulus according to indentation diagram. *Ind Labor* 41:1409–1412
- Bulychev SI, Alekhin VP, Shorshorov MKh, Ternovskii AP (1976) Mechanical properties of materials studied from kinetic diagrams of load versus depth of impression during microimpression. *Strength Mater* 8:1084–1089

- Chaudhri MM, Lim YY (2007). Nanoindentation techniques: a critical assessment of the current methods of data analysis. *Key Eng Mater* 345–346:1107–1114
- Chen X, Zhang S, Dikin DA, Ding W, Ruoff RS, Pan L, Nakayama Y (2003) Mechanics of a carbon nanocoil. *Nano Lett* 3:1299–1304
- Chu YS, Dufour S, Thiery JP (2005) Johnson-Kendall-Roberts theory applied to living cells. *Phys Rev Lett* 94:028102
- Creton C, Gorb SN (2007) Sticky feet: from animals to materials. *MRS Bulletin* 32:466–468
- Dao M, Lim CT, Suresh S (2003) Mechanics of the human red blood cell deformed by optical tweezers. *JMPS* 51:2259–2280
- Derjaguin B (1934) Untersuchungen über die Reibung und Adhäsion, IV. Theorie des Anhaftens kleiner Teilchen. *Kolloid Zeitschrift* 69:155–164
- Derjaguin B (1940) On the repulsive forces between charged colloid particles and on the theory of slow coagulation and stability of lyophobic sols. *Trans Faraday Soc* 35:203–215
- Derjaguin BV, Fedoseev DV (1975) The synthesis of diamond at low pressure. *Sci Amer* 233:102–109
- Derjaguin BV, Fedoseev DV (1977) Growth of diamond and graphite from the gas phase. Nauka, Moscow (Russian)
- Derjaguin B, Landau L (1941) The theory of stability of highly charged lyophobic sols and coalescence of highly charged particles in electrolyte solutions. *Acta Physicochimica URSS* 14:633–662
- Derjaguin BV, Titiyevskaya AS, Abrikosova II, Malkina AD (1954). Investigations of the forces of interaction of surfaces in different media and their application to the problem of colloidal stability. *Discuss Faraday Soc* 18:24–41
- Derjaguin BV, Abrikosova II, Lifshitz EM (1956). Direct measurement of molecular attraction between solids separated by a narrow gap. *Quarterly Rev Chem Soc* 103:295–329
- Derjaguin BV, Abrikosova II, Livshitz EM (1958) Molecular attraction of condensed bodies. *Uspekhi Fiz Nauk* 64:493–528 (English transl. Derjaguin BV, Abrikosova II, Livshitz EM (2015) Molecular attraction of condensed bodies. *Physics – Uspekhi* 58:906–924)
- Derjaguin BV, Krotova NA, Smilga VP (1973) *Adhesiya Tverdykh Tel*. Nauka, Moscow (Russian). (English transl. Deryagin BV, Krotova NA, Smilga VP (1978) *Adhesion of solids*. Consultants Bureau, New York)
- Derjaguin BV, Muller VM, Toporov YP (1975) Effect of contact deformations on adhesion of particles. *J Colloid Interface Sci* 53:314–326
- Derjaguin BV, Rabinovich YI, Churaev NV (1978). Direct measurement of molecular forces. *Nature* 272:313–318
- Dhaliwal RS, Singh BM (1978) The axisymmetric Boussinesq problems of an initially stressed neo-Hookean half-space for a punch of arbitrary profile. *Int J Engng Sci* 16:379–385
- Dimitriadis EK, Horkay F, Maresca J, Kachar B, Chadwick RS (2002) Determination of elastic moduli of thin layers of soft material using the atomic force microscope. *Biophysical J* 82:2798–2810
- Ebenstein DM, Wahl KJ (2006) A comparison of JKR-based methods to analyze quasi-static and dynamic indentation force curves. *J Colloid Interface Sci* 298:652–662
- Espinasse L, Keer L, Borodich F, Yu H, Wang J (2010) A note on JKR and DMT theories of contact on a transversely isotropic half-space. *Mech Mater* 42:477–480
- Feynman RP (1992) There's plenty of room at the bottom. *J Microelectromech Syst* 1:60–66
- Filippova LM (1978) Three-dimensional contact problem for a prestressed elastic body. *PMM J Appl Math Mech* 42:1183–1188
- Fortoul N, Singh P, Hui C-Y, Bykhovskaia M, Jagota A (2015) Coarse-grained model of SNARE-mediated docking. *Biophysical J* 108:2258–2269
- Galanov BA (2011) Models of adhesive contact between rough elastic bodies. *Int J Mech Sci* 53:968–977
- Gonabadi H, Yadav A, Bull S (2022) Chapter 8: Mechanical characterisation of polymeric materials using nanoindentation In: Borodich FM, Jin X (eds) *Contact problems for soft, biological and bioinspired materials*. Springer, Berlin, pp 139–180

- Gorb EV, Gorb SN (2009) Contact mechanics at the insect-plant interface. How do insects stick and how do plants prevent this? In: Borodich FM (ed) *Scaling in solid mechanics*. Springer, Berlin
- Gorb SN, Jiao Y, Scherge M (2000) Ultrastructural architecture and mechanical properties of attachment pads in *Tettigonia viridissima* (Orthoptera Tettigoniidae) *J Comp Physiol A* 186:821–831
- Gorkom J, van Delft D, van Helvoort T (2018) Chapter one - the early electron microscopes: A critical study *Adv Imag Electron Phys* 205:1–137
- Goryacheva IG, Makhovskaya YY (2022) Chapter 4: Capillary adhesion effect in contact interaction of soft materials. In: Borodich FM, Jin X (eds) *Contact problems for soft, biological and bioinspired materials*. Springer, Berlin, pp 73–92
- Greenwood JA (2007) On the DMT theory. *Tribol Lett* 26:203–211
- Hamaker HC (1937) The London - van der Waals attraction between spherical particles. *Physica* 4:1058–1072
- Hermanson M (1999) The DLVO theory in microbial adhesion. *Colloids Surfaces B Biointerfaces* 14:105–119
- Hertz H (1882) Ueber die Berührung fester elastischer Körper. *J reine angewandte Mathematik* 92:156–171 (English transl. Hertz H (1896) On the contact of elastic solids. In: Jones DE, Schott GA (eds) *Miscellaneous papers by H. Hertz*, pp 146–162. Macmillan, London)
- Hooke R (1665) *Micrographia: or some Physiological Descriptions of Minute Bodies made by Magnifying Glasses with Observations and Inquiries thereupon*. London, John Martin and James Allestry, Printers to the Royal Society.
- Israelachvili JN (1991) *Intermolecular and surface forces*. Academic, London
- Iyer S, Gaikwad RM, Subba-Rao V, Woodworth CD, Sokolov I (2009) Atomic force microscopy detects differences in the surface brush of normal and cancerous cells. *Nat Nanotechnol* 4:389–393
- Jagota A, Argento C (1997) An intersurface stress tensor. *J Colloid Interf Sci* 191:326–336
- Jin X, Li P, Borodich FM (2022) Chapter 9: Indentation tests of biological materials: Theoretical aspects. In: Borodich FM, Jin X (eds) *Contact problems for soft, biological and bioinspired materials*. Springer, Berlin, pp 181–198
- Johnson KL (1958) A note on the adhesion of elastic solids. *Brit J Appl Phys* 9:199–200
- Johnson KL, Greenwood JA (1997) An adhesion map for the contact of elastic spheres. *J Colloid Interf Sci* 192:326–333
- Johnson KL, Kendall K, Roberts AD (1971) Surface energy and the contact of elastic solids. *Proc R Soc Lond A* 324:301–313
- Kadem LF, Holz M, Suana KG, Li Q, Lamprecht C, Herges R, Selhuber Unkel C (2016) Rapid reversible photoswitching of integrin mediated adhesion at the single cell level. *Adv Mater* 28:1799–1802
- Kalei GN (1967) Investigations of methods for determining microhardness (with a measurement of the indentation across a diagonal and along the depth). Candidate's Dissertation. Moscow
- Kalei GN (1968) Some results of microhardness test using the depth of impression. *Mashinovedenie* 4(3):105–107 (Russian)
- Kendall K (1971) The adhesion and surface energy of elastic solids *J Phys D Appl Phys* 4:1186–1195
- Kendall K (2001) *Molecular adhesion and its applications*. Kluwer Academic/Plenum Publishers, New York
- Kendall K, Roberts AD (2015) van der Waals forces influencing adhesion of cells. *Phil Trans R Soc B* 370:20140078
- Kendall K, Kendall M, Rehfeldt F (2011) *Adhesion of cells, viruses and nanoparticles*. Springer, Dordrecht
- Kiselev NA, Shpitzberg CL, Vainshtein BK (1967) Crystallization of catalase in the form of tubes with monomolecular walls. *J Molec Biol* 25:433–441
- Kiselev NA, De Rosier DJ, Klug A (1968) Structure of the tubes of catalase: analysis of electron micrographs by optical filtering. *J Molec Biol* 35:561–566

- Kiselev NA, Lerner FY, Livanova NB (1971) Electron microscopy of muscle phosphorylase B. *J Molec Biol* 62:537–549
- Knoll M (1935) Aufladepotential und Sekundäremission elektronenbestrahlter Körper. *Zeitschrift für technische Physik* 16:467–475
- Korayem MH, Rastegar Z, Taheri M (2012) Application of Johnson-Kendall-Robers model in nanomanipulation of biological cell: air and liquid environment. *Micro Naono Lett* 7:576–580
- Kuznetsova TG, Starodubtseva MN, Yegorenkov NI, Chizhik SA, Zhdanov RI (2007) Atomic force microscopy probing of cell elasticity. *Micron* 38:824–833
- Lebedeff AA (1931) A focusing method for producing electron diffraction patterns. *Nature* 128(3339):491
- Lebedew P (1894) Ueber die mechanische Wirkung der Wellen auf ruhende Resonatoren. I. Electromagnetischen Wellen. *Annalen der Physik* 288:621–640
- Lessel M, Loskill P, Hausen F, Gosvami NN, Bennewitz R, Karin J (2013) Impact of van der Waals interactions on single asperity friction. *Phys Rev Lett* 111:035502
- Leewenhoeck A (1677) Observation, communicated to the publisher by Mr. Antony van Leewenhoeck, in a Dutch letter of the 9 Octob. 1676 here English'd: concerning little animals by him observed in rain-well-sea and snow water; as also in water wherein pepper had lain infused. *Phil Trans* 12:821–831. <https://doi.org/10.1098/rstl.1677.0003>
- Lewicki DN, Gallagher TM (2002) Quaternary structure of coronavirus spikes in complex with carcinoembryonic antigen-related cell adhesion molecule cellular receptors. *J Biol Chem* 277:19727–19734
- Lin Y, Yan X, Cao W, Wang C, Feng J, Duan J, Xie S (2004) Probing the structure of the SARS coronavirus using scanning electron microscopy. *Antivir Ther* 9:287–289
- Maitre JL, Heisenberg CP (2011) The role of adhesion energy in controlling cell-cell contacts. *Curr Opin Cell Biol* 23:508–514
- Mate CM, McClelland GM, Erlandsson R, Chiang S (1987) Atomic-scale friction of a tungsten tip on a graphite surface. *Phys Rev Lett* 59:1942–1945
- Maugis D (1992) Adhesion of spheres: the JKR-DMT transition using a Dugdale model. *J Colloid Interf Sci* 150:243–269
- Maugis D (2000) Contact, adhesion and rupture of elastic solids. Springer, Berlin
- Maxwell JC (1874) Van der Waals on the continuity of gaseous and liquid states. *Nature* 10:477–480
- Meng Y (2013) Electrostatic field effects on adhesion. In: Wang QJ, Chung Y-W (eds) *Encyclopedia of tribology*. Springer, Berlin, pp 951–956
- Muller VM, Yuschenko VS, Derjaguin BV (1980) On the influence of molecular forces on the deformation of an elastic sphere and its sticking to a rigid plane. *J Colloid Interf Sci* 77:91–101
- Muller VM, Derjaguin BV, Toporov YuP (1983) On two methods of calculation of the force of sticking of an elastic sphere to a rigid plane. *Colloids Surf* 7:251–259
- Murphy DB (2001) *Fundamentals of light microscopy and electronic imaging*. Wiley-Liss, Hoboken
- Myshkin N, Kovalev A (2018) Adhesion and surface forces in polymer tribology – a review. *Friction* 6:143–155
- Myshkin NK, Grigoriev AYa, Dubravin AM, Komkov OYu, Spencer ND, Tosatti M (2004) Experimental equipment for interfacial force and friction measurements of micro scale samples. *Tribology and lubrication engineering*. In: 14th international colloquium tribology. Esslingen, pp 73–78
- Myshkin NK, Grigoriev AYa, Dubravin AM, Komkov OYu, Kovalev AV (2005a) Instruments for adhesion and friction measurements at micro/nano scale. In: *Proceedings of the international conference on “Viennano”*, Vienna, pp 213–218
- Myshkin NK, Petrokovets MI, Kovalev AV (2005b) Tribology of polymers: Adhesion, friction, wear, and mass-transfer. *Tribol Int* 38:910–921
- Pepelyshev A, Borodich FM, Galanov BA, Gorb EV, Gorb SN (2018) Adhesion of soft materials to rough surfaces: experimental studies, statistical analysis and modelling. *Coatings* 8(10):350

- Perepelkin NV, Borodich FM (2021) Explicit transition between solutions to non-adhesive and adhesive contact problems by means of the classical Johnson-Kendall-Roberts formalism. *Phil Trans R Soc A* 379:20200374. <https://doi.org/10.1098/rsta.2020.0374>
- Perepelkin NV, Kovalev AE, Gorb SN, Borodich FM (2019) Estimation of the elastic modulus and the work of adhesion of soft materials using the extended Borodich-Galanov (BG) method and depth sensing indentation. *Mech Mater* 129:198–213
- Perepelkin NV, Borodich FM, Kovalev AE, Gorb SN (2020) Depth-sensing indentation as a micro- and nanomechanical approach to characterisation of mechanical properties of soft, biological, and biomimetic materials. *Nanomaterials* 10:15. <https://doi.org/10.3390/nano10010015>
- Perepelkin NV, Argatov II, Borodich FM (2021) Evaluation of elastic and adhesive properties of solids by depth-sensing indentation. *J Adhesion* 97:569–610. <https://doi.org/10.1080/00218464.2019.1686981>
- Podestà A (2013) Surface analysis using dynamic AFM. In: Wang QJ, Chung Y-W (eds) *Encyclopedia of tribology*. Springer, Berlin, pp 3411–3418
- Poortinga AT, Bos S, Norde W, Busscher HJ (2002) Electric double layer interactions in bacterial adhesion to surfaces. *Surface Sci Rep* 47:1–32
- Popov VL (2010) *Contact mechanics and friction*. Springer, Heidelberg
- Purtov J, Gorb EV, Steinhart M, Gorb SN (2013) Measuring of the hardly measurable: adhesion properties of anti-adhesive surfaces. *Appl Phys A* 111:183–189
- Radushkevich LV, Lukyanovich VM (1950) Structure of sorbents owing by the evidence provided by an electron microscopy study. *Zhurnal Fizicheskoi Khimii* 24:21–42 (in Russian)
- Radushkevich LV, Lukyanovich VM (1952) Structure of the carbon produced in the thermal decomposition of carbon monoxide on an iron catalyst. *Zhurnal Fizicheskoi Khimii* 26:88–95 (in Russian)
- Sakharov AD (1974) Tomorrow: the view from red square. *Saturday Rev* 14–20:12–14 108
- Sánchez Quintanilla MA (2013) Surface analysis using contact mode AFM. In: Wang QJ, Chung Y-W (eds) *Encyclopedia of tribology*. Springer, Berlin, pp 3401–3411
- Scherge M, Gorb SN (2001) *Biological micro- and nanotribology: nature's solutions*. Springer, Berlin
- Shull KR (2002) Contact mechanics and the adhesion of soft solids *Mater Sci Eng Rep* 36:1–45
- Sivasankar S, Briehner W, Lavrik N, Gumbiner B, Leckband D (1999) Direct molecular force measurements of multiple adhesive interactions between cadherin ectodomains. *Proc Natl Acad Sci USA* 96:11820–11824
- Smalley RE (2001). Of chemistry, love and nanobots. *Sci Amer* 285:76–77
- Sokolov I (2007) Atomic force microscopy in cancer cell research. In: Nalwa HS, Webster T (eds) *Cancer nanotechnology*. American Scientific Publisher, Valencia, pp 1–17
- Sokolov I (2022) Chapter 2: Contact problem in indentation measurements of soft, biological and bioinspired materials. In: Borodich FM, Jin X (eds) *Contact problems for soft, biological and bioinspired materials*. Springer, Berlin, pp 31–50
- Soldatenkov IA (2013) The contact problem with the bulk application of intermolecular interaction forces (a refined formulation). *PMM J Appl Math Mech* 77:629–641
- Sperling G (1964) *Eine Theorie der Haftung von Feststoffteilchen an festen Körpern*. Unpublished doctoral dissertation, Technische Hochschule Karlsruhe
- Starodubtseva MN (2022) Chapter 3: Mechanical properties of the cell surface layer measured by contact atomic force microscopy. In: Borodich FM, Jin X (eds) *Contact problems for soft, biological and bioinspired materials*. Springer, Berlin, pp 51–72
- Sviridenok AI, Chizhik SA, Petrokovets MI (1990) *Mechanics of Discrete Frictional Contact*. Minsk. Navuka i Tekhnika
- Tabor D (1977) Surface forces and surface interactions. *J Colloid Interf Sci* 58:2–13
- Tabor D, Winterton RHS (1969) The direct measurement of normal and retarded van der Waals forces. *Proc R Soc A Math Phys Eng Sci* 312:435–450
- Verwey EJW, Overbeek, JThG (1948) *Theory of the stability of lyophobic colloids*. Elsevier, Amsterdam

- Wahl KJ, Asif SAS, Greenwood JA, Johnson KL (2006) Oscillating adhesive contacts between micron-scale tips and compliant polymers. *J Colloid Interf Sci* 296:178–188
- Wang YL, Discher DE (Eds) (2007) *Methods in cell biology*, vol 83. Cell mechanics. Elsevier, Amsterdam
- van der Waals JD (1910) The equation of state for gases and liquids. Nobel lectures (physics) 1901–1921. Academic Press (1975), pp 254–265
- Weder G, Vörös J, Giazoni M, Matthey N, Heinzelmann H, Liley M (2009) Measuring cell adhesion forces during the cell cycle by force spectroscopy. *Biointerphases* 4:27–34
- Young R, Ward J, Scire F (1972) The topografiner: an instrument for measuring surface microtopography. *Rev Sci Instrum* 43:999–1011

Chapter 2

Contact Problem in Indentation Measurements of Soft, Biological and Bioinspired Materials



Igor Sokolov

Abstract Realistic soft, biological, and bioinspired materials do not have an ideally well-defined interface. As a result, the contact problem becomes rather non-trivial because of the existence of either intrinsically rough interface and/or the presence of large molecules covering the interface. As a result, the bulk material deformation precedes the physical contact between the indenter and the interface. Here we describe how to deal with such a contact problem. We describe in detail an example of biological cells indented with an atomic force microscopy probe. The self-consistency of the described contact model is experimentally verified.

Keywords Contact problem · Atomic force microscopy · Contact roughness · Molecular brush

1 Introduction

Contact problems occur when various probe techniques are used so study interfaces of materials. When a probe and a sample are put in contact, the contact problem is typically reduced to the analysis of mechanical deformations and stresses. Scanning probe techniques are the most promising in the study of interfaces of soft materials (Sokolov et al. 1996; Hansma et al. 2004; Fritz et al. 1995; Colton et al. 1991). In these techniques, a relatively sharp probe is deforming a sample of interest while the forces between the probe and sample are recorded. The mechanical and geometrical properties of the interface are derived through the analysis of these forces. The contact problem arises in the analysis of these forces. Because of high interest in the

I. Sokolov (✉)

Department of Mechanical Engineering, Tufts University, Medford, MA, USA

Department of Biomedical Engineering, Tufts University, Medford, MA, USA

Department of Physics, Tufts University, Medford, MA, USA

e-mail: igor.sokolov@tufts.edu

© Springer Nature Switzerland AG 2022

F. M. Borodich, X. Jin (eds.), *Contact Problems for Soft, Biological and Bioinspired Materials*, Biologically-Inspired Systems 15,

https://doi.org/10.1007/978-3-030-85175-0_2

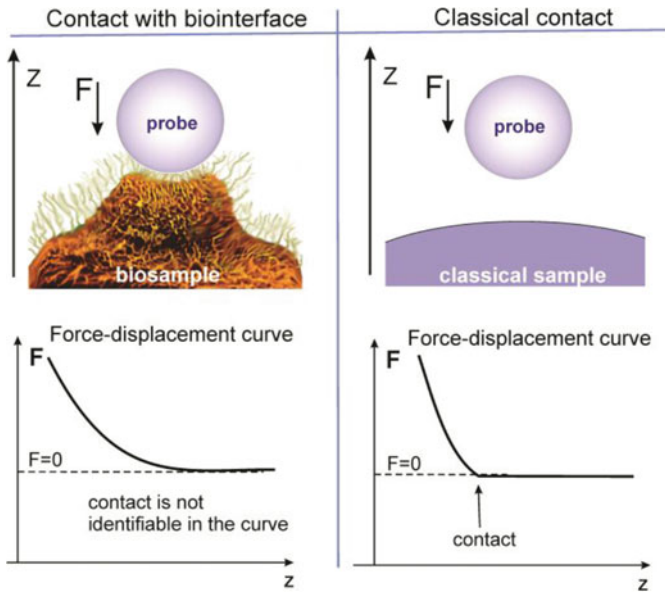


Fig. 2.1 Demonstration of the complexity of the contact problem in the case of biointerfaces. Top row: Schematics of a typical biointerface and a classical contact geometry, which are deformed by a spherical rigid indenting probe. The biointerface is typically rough and may be covered with various molecules and molecular formations. Bottom row: The force-vertical displacement curves are shown for both cases. The moment of contact is practically not identifiable in the force-displacement curve measured above the biointerface, whereas such contact is clearly seen for the classical contact force curve

study of materials at a small scale, in this chapter, we will focus on the indentation technique at the sub-micron and nanoscale.

Contact problem in indentation measurements of soft, biological and bioinspired materials is complicated due to the fact that the interface is not smooth and flat. It is typically rough and covered with various molecules, molecular bundles, gels, mucus. Because practically all interfaces are well defined only in aqueous solutions, it should be stressed that the contact problem considered here is for the contact between bodies immersed in aqueous solution, for example, physiological solution. Figure 2.1 shows schematics of a typical biointerface and a classical contact geometry, which are deformed by a spherical rigid indenting probe. Besides the need to take into account the interface roughness and steric repulsion due to the presence of molecular layer and the biointerface, it is virtually impossible to identify the point of contact in the force indentation curve because the indenting probe first experiences small forces due to the molecular coat and the surface roughness, and only then, it starts to develop the actual contact with the sample body. This adds more complexity to the analysis of these curves.

In most cases, the contact problem on biointerfaces can bring information not only about the mechanical properties of the contact but also about the physical properties of the interface (like the information about molecular coating or interface

roughness) (Dokukin et al. 2016). This information is of fundamental interest in the study of the interface of soft biological and bioinspired materials. For example, all eukaryotic and the majority of prokaryotic biological cells are covered with a thick layer of polysaccharides and various glycoproteins, so-called pericellular coat layer (Cohen et al. 2003; Jones et al. 1995). The pericellular coat plays an important role in many cell functions. Cells interact with the environment through this layer. This layer defines the flow of various nutrients and cytokines. It influences cell adhesion, migration, differentiation, and proliferation (Toole 1982; Zimmerman et al. 2002). The molecular size of the pericellular layer correlates with the degree of invasiveness of cancer (Jones et al. 1995; Zhang et al. 1995). Multiple medical implants are also coated with a molecular layer to minimize interaction with the organismal defense system, to prevent biomineralization and blood clogging.

When a probe and a sample comprise smooth linear elastic homogenous and isotropic materials, the contact problem is relatively simple. In the case of biological materials, which are typically soft and/or have a complex interface, the contact problem becomes extremely complicated. The sample interface can easily be deformed at virtually any detectable load force. Furthermore, the structure and geometry of the interface can be highly heterogeneous. Obviously, this problem cannot be solved for a general case. Here we overview a class of contact problems, which can be analyzed using a relatively simple analytical model, called the brush model, in which a soft linear elastic material is covered with a molecular brush and/or the surface is rough (Dokukin et al. 2016; Iyer et al. 2009a; Sokolov et al. 2007a). We will demonstrate how this model is applied to the analysis of interfaces of soft materials like cells biological cells. To understand the type of contacts, we start with an overview of the indentation techniques used to study the biointerfaces.

2 Indentation Techniques to Study Biointerfaces

2.1 AFM Is the Technique of Choice

The indentation techniques range from classical macroscopic indenters to rather recent nanoindenters, and atomic force microscopes (AFM). AFM is used mainly for imaging, whereas nanoindenters are utilized mostly to study the elastic properties of materials. Nevertheless, both techniques can be used for the indentation analysis of the interfaces.

When studying soft interfaces at the submicron scale, AFM is the technique of choice. Nanoindenters are not suitable for this purpose because of low force resolution. Nanoindenters can provide nano resolution only on rigid materials, like metals and ceramic. When applied to biological materials and even polymers, nanoindenters provide a typical lateral resolution of microns (Dokukin and Sokolov 2012).

Atomic force microscopy (AFM) is one of the most frequently used scanning probe techniques to study biointerfaces. It is due to a broad range of the working forces the AFM probe can exert on the sample surface. AFM a quite versatile

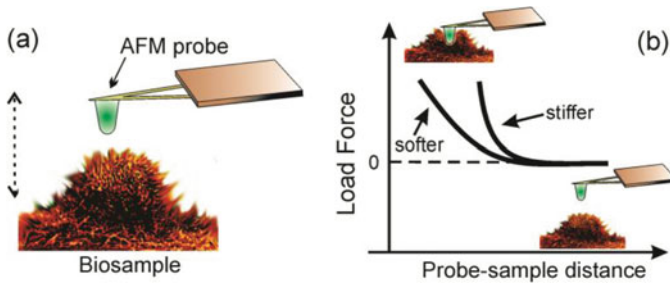


Fig. 2.2 (a) A scheme of the AFM indentation experiment. (b) Schematics of force-distance curves when indenting on a softer and rigid material

tool to detect the physical presence of molecules on the cell surfaces (Sokolov et al. 1996, 2006a, 2015; Burtovyy and Luzinov 2008), in particular, the pericellular coat (Oberleithner 2012; Jungmann et al. 2012; Grimm et al. 2014; Wiesinger et al. 2013), including bacterial services (Camesano and Logan 2000) and polymers (Sokolov et al. 2016).

The indentation measurements can be (quasi)static and dynamic (see, e.g., (Mahaffy et al. 2004; Bippes et al. 2005; Sokolov et al. 2006b; Berdyeva et al. 2005a; Lekka et al. 1999; Park et al. 2005a)). Static measurements are done with an AFM probe that deforms the sample surface relatively slowly. In dynamic measurements, the probe, for example, oscillates with a specific frequency or relaxes after a sharp indentation (typically used two regimes, stress relaxation and creep). Because the dynamic measurements are frequency (or loading rate) dependent, they can provide more information compared to the static one. Nevertheless, to collect a sufficient amount of data to generate statistically robust conclusions, one would need an excessively large amount of time (during such time, the interface could be altered by the measurement). This is the reason why almost all reports on cell mechanics employ quasi-static studies. Furthermore, at the moment, there is no generally accepted model of dynamical mechanical properties of biointerfaces. Hereafter, we focus on quasistatic measurements.

In a typical experiment, an indenting AFM probe of a well-defined geometry approaches a sample surface and starts deforming it under well-controlled load force, load rate, and displacement. It should be noted that it is typical to analyze the retraction force curve in classical indentation experiments to avoid plastic deformation effects. However, it is better to use the approach force curve to analyze the mechanical contact with a biological surface because of two reasons: (1) biological materials are less prone to plastic deformation and (2) bio interface is deformed during the approach, and may need a long time to recover; as a result, the retraction curve may carry the memory of the indenting, or depend on the measurement conditions. The later is not good because any good experiment should minimize the dependence on a specific way of measurements.

Figure 2.2a shows a scheme of such measurements. The distance between a sample and AFM probe is changing in an oscillatory manner to record the entire

ramp of the probe – sample distances. Figure 2.2b presents schematics of two force versus sample – probe distance curves (*aka* force curve) when indenting on stiffer and softer samples. These curves are then processed through one of the existing mechanical models to extract the parameters characterizing the elastic properties of the material.

2.2 Terminology

To describe the mechanical properties of biointerfaces, the concept of Young’s modulus is broadly used. It should also be noted that this concept may be quite confusing when applied to biological materials because it is frequently associated with homogeneous and isotropic material. Biological materials are typically inhomogeneous and can be anisotropic. However, historically the Young’s modulus was introduced as a tensile modulus describing simple stretching experiments of any material. From that point of view, the Young’s modulus can be applied to a complex heterogeneous material, which can be approximated as homogeneous for small deformations (stresses and strains). Nevertheless, many authors prefer to use a more generic “modulus of elasticity” term for this tensile modulus. In the first-order approximation, both these terms can be treated as synonymous.

The other confusion can come from the use of the term stiffness in the biological community, see (Wu et al. 2018) for more detail. It presumably comes from its more intuitively clear meaning (a stiffer material has higher modulus, whereas a higher elastic modulus does not mean higher elasticity in its layman meaning). It should be noted that the term stiffness is already taken in solid mechanics. It means the gradient of the load force with respect to the indentation/deformation depth. Thus, it has even a different dimension compared to the modulus of elasticity. Nevertheless, the term stiffness is broadly used instead of the modulus of elasticity and even the Young’s modulus.

2.3 Heterogeneity of Biointerfaces at the Microscale: The Need in Robust Statistics

It is a short but very important note. In contrast to a typical non-biological material, biointerfaces demonstrate high spatial variability of their properties. It can differ significantly even within the same type of material. Depending on the variability of data, the number of measurements required to obtain robust statistics can be quite different. For example, for biological cells, it ranges from ~10 to 30 cells or more (Sokolov et al. 2006b; Berdyeva et al. 2005a; Lekka et al. 1999; Park et al. 2005a). The exact sample size could be found using the power calculator (Rosner 2010). It depends on a particular question of the study.

Table 2.1 Variations of the Young’s modulus measured over the surface of human cervical epithelial cells. The average modulus value and one standard deviation are shown. The values are shown for a sample of 20 cells and a representative 1 cell. The measurements done with a 5 μm silica sphere and a sharp AFM pyramidal conical probe are presented

	20 cells		1 cell	
Probe	sphere	cone	sphere	cone
Elastic modulus [kPa]	1.59 ± 0.52	6.6 ± 2.1	1.6 ± 0.4	7.1 ± 3.5

Table 2.1 shows an example of variations of the Young’s modulus measured over the surface of human cervical epithelial cells. The results are shown for a sample of 20 cells and for multiple measurements within just one representative cell. One can see that the variations of the modulus values within one cell is comparable with the variation between different cells of the entire cell ensemble. It is also interesting to see that the variation depends on the type of the AFM probe. A larger spherical probe expectedly gives a smaller variation within one cell. However, the relative variation of the modulus between different cells is practically the same for both types of probes (about 30%).

One can also notice from Table 2.1 the presence of a substantial difference between the values of the modulus obtained with spherical and conical probes. Apparently, this is a result of the overstretching of the cell material with sharp conical probes, which leads to a non-linear stress-strain response. Similar behavior was observed for homogeneous polymers (Dokukin and Sokolov 2012). In addition, the Young’s modulus calculated from the force curves collected using a sharp cone probe demonstrates a strong depth-dependence of the modulus of homogeneous polymers. This behavior is virtually identical to the one observed on cells when using a sharp conical AFM probe.

3 Brush Model Is a Way to Reduce the Brushy Contact to a Standard Contact Model

Before we describe the brush contact model, it is instructive to outline generic assumptions typically used when utilizing the contact models of complex, in particular, biological interfaces.

3.1 *Generic Assumptions About Contact Models Used to Describe Biointerfaces*

A common assumption is a flat, or at least, smooth boundary. As we noticed above, the majority of soft and biological interfaces are not flat and covered with various molecules. This brings a common problem of taking into account the non-smooth

boundary possibly coated with molecules, which will be addressed in the next section.

The next assumption relates to the applicability of the standard contact models. To derive the elastic modulus from the indentation experiments, simple mechanical models are typically used, such as the Hertz (for a spherical indenter) and Sneddon (for a conical indenter). All such models assume that the sample comprises a linear elastic homogeneous and isotropic material, or at least the constancy of the elastic modulus. Obviously, virtually all biointerfaces are inhomogeneous and frequently anisotropic. The linearity of biological materials is poorly understood. Technically, the linearity and homogeneity are good approximations when stresses/strains are sufficiently small. This is a simple sequence of the basic physical fact that the potential minimum of the inter-atomic/intermolecular interaction can be approximated with a parabolic potential. Anisotropy typically manifests itself in anisotropic features observable with optical microscopy and can be avoided in many cases.

It is convenient to verify the applicability of a contact model by using the strong linearity principle, the independence of the elastic modulus of the indentation depth (or load force) derived within a particular contact model. It is definitely only a necessary condition of dealing with linear elastic homogeneous and isotropic material. Although no one has proved that this condition is sufficient for dealing with such material, it is highly unlikely that a possible deviation from linearity, homogeneity, and isotropy would compensate each other in a complex material to provide the depth independence of the derived modulus. Despite the ease of verification of this powerful principle, only a few papers utilized it (Dokukin et al. 2017a, b; Guz et al. 2014, 2016a, b; Huth et al. 2019).

The next assumption is in the calculation of just the Young's modulus. It is known that a linear elastic homogeneous and isotropic material should be characterized by two mechanistic parameters. A typical choice is a couple of the Young's modulus and the Poisson ratio. Although the latter is poorly known, it a rather weakly influences the value of the Young's modulus. For example, the entire uncertainty of the Poisson ratio for cells typically lies between 0.3 and 0.5. This leads to a possible error in the Young's modulus of the order of 5% (Guz et al. 2014). This can easily be tolerated and the present level of accuracy of the AFM measurements because the spring constant of the AFM cantilever is rarely known with an error less than 10%.

Another way to avoid comparing different Young's moduli E while keeping the Poisson ratio ν unknown is to introduce the term reduced Young's modulus, E^* . It includes the unknown Poisson ratio as follows:

$$E^* = E / (1 - \nu^2). \quad (2.1)$$

Because this specific combination of the Young's modulus and Poisson ratio is used in the Hertz and Sneddon models, the concept of the reduced Young's modulus is frequently used to completely remove the uncertainty of the unknown Poisson ratio.

3.2 The Need in Well-Defined Large Spherical AFM Probes

The existing models of contact mechanics are built on the assumption of linear local stress-strain response, which is not necessarily true for the large local stresses that appear in the vicinity of the contact with a sharp apex (Dokukin and Sokolov 2012; Shoelson et al. 2004). As was shown (Dokukin and Sokolov 2012; Shoelson et al. 2004; Dimitriadis et al. 2002), these non-linear effects led to a considerable overestimation of the rigidity modulus of the membranes and polymers. Figure 2.3 demonstrates similar results for the analysis of AFM indentation of human cervical epithelial cells when indenting with a cone probe (Fig. 2.3 left; Sneddon model used) and 2.5-micron spherical probe (Fig. 2.3 right; Hertz model used). One can see a substantial difference in the value of the Young's modulus of the same cell type obtained with the different indenters. As we noted above, this difference presumably comes from a non-linear stress-strain response when indenting the cell with a sharp AFM probe.

To avoid the problems of nonlinearity, larger spherical AFM probes have been used to study the mechanics of cells (Sokolov et al. 2006b; Berdyeva et al. 2005a, b; Park et al. 2005a, b). The area of contact with the apex is considerably larger when using such a spherical probe. Typically, the ball probes used were of 1000–5000 nm in diameter compared to the regular 10–100 nm radius of the apex curvature of the AFM probe. This increases the contact area by up to three orders of magnitude. Besides the problems of nonlinearity, these large spherical probes have several additional advantages over the regular sharp probes in the study of biointerfaces:

1. The use of sharp tips to “pock” biological objects, cells for an extended period of time can lead to alteration of the sample properties. For example, cells, being living objects can change their mechanical properties (Mathur et al. 2000). When

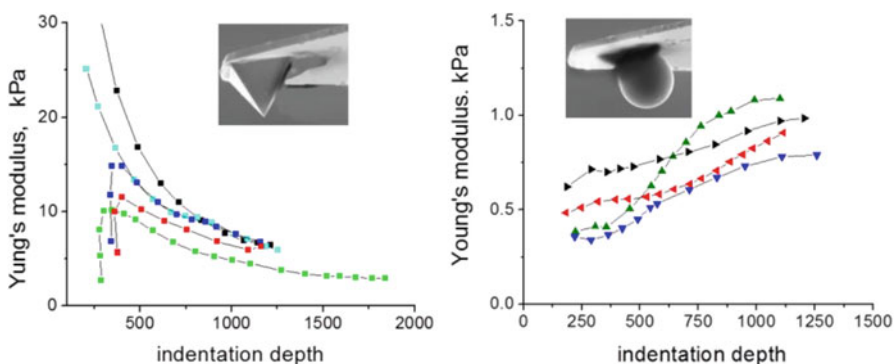


Fig. 2.3 A numerical example of the dependence of the Young's modulus (shown in kPa) on the indentation depth (shown in nanometers) of human cervical epithelial cells when using conical (left) and spherical (right) AFM probes (brush is not taken into account)

using dull probes, the mechanical properties of cells remain constant for several hours of continuous probing (Berdyeva et al. 2005a).

2. Due to the low rigidity at the thin edge of some cells, it is practically impossible, to make measurements with a sharp AFM probe. The sharp probe simply penetrates the thin soft areas of the cell and indicates higher rigidity due to touching the rigid substrate. In contrast, rigidity of this area can easily be measured with the ball probes (Berdyeva et al. 2005a).
3. Biointerfaces can be heterogeneous. A sharp probe can touch the surface right between fibers or directly on the top of the fibers, thus adding substantially to the heterogeneity of the results. As a result, one needs to make substantially more measurements with a sharp probe to obtain robust average data. Therefore, using dull probes is advantageous to decrease the time of measurements, which is crucial because the time of the experiment is limited by the viability of the biological sample.
4. It is of great importance to study mechanics under realistic stresses that occur in biological systems. High local stresses induced by a sharp AFM probe are unlikely to be found *in-vivo*.

To conclude, a large spherical AFM probe is clearly beneficial for studying the mechanical properties of cells. It should be noted that there are nonetheless multiple works in which sharp AFM probes are used to study the interface. Although the results cannot be interpreted in terms of the modulus of elasticity, there are advantages in the use of a sharp AFM probe. First of all, a sharp probe provides a better lateral resolution. Secondly, sharp probes are broadly available and much cheaper compared to expensive colloidal probes. Hopefully, there will be a theory of non-linear contact developed some, which will allow interpreting the obtained high-resolution images in a quantitative manner.

In principle, one could use not necessarily spherical but parabolic probes. For indentations less than the radius of curvature of the probe, the parabolic probes can be considered as spherical. Relatively dull cono-spherical probes could also be considered. Instead of the classical Hertz contact, the Sneddon integrals can be explicitly taken and used (Wu et al. 2018). However, such probes are rather rare. Flat indentors could also be used. However, the user would face the same problem as in the microscopic case, the difficulty of flat contact. Because the topography of the surface is not well known, it is practically impossible to align the flat indenter parallel to the surface.

3.3 Contact Problem in the Brush Model

As was mentioned in the introduction section, a typical biological interface is covered with multiple molecules and typically has a rough geometry, Fig. 2.1. At the macroscale, this problem can be eased using various sample preparation methods, which can substantially decrease the surface roughness. However, at a

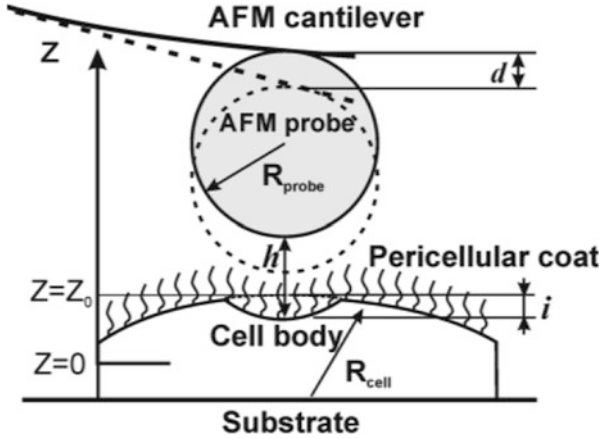


Fig. 2.4 A scheme of AFM-cell geometry used in the brush model. R_{probe} (R_{cell}) are the radius of the AFM probe (cell), Z is vertical position of the AFM scanner, d is the cantilever deflection, Z_0 is the undeformed position of the cell body, i is deformation of the cell body, $Z = 0$ is at the maximum deflection (assigned by the AFM user), and h is the separation between the cell body and AFM probe

small, submicron- and nano- scales it is practically impossible to do. Furthermore, biological objects can be alive. In such a case, the sample preparation is complicated by the requirements of keeping the object alive, and even undisturbed. Thus, it is important to separate in the contact problem the contribution of the material bulk from the contribution of the surface roughness and molecular brush.

Quantitative methods to analyze a typical bio interface, a single biological cell, were proposed in (Sokolov et al. [b, 2013](#); Dokukin et al. [2013](#)). In these so-called brush models, it was possible to separate the elastic deformation of the cell body from the surface roughness (corrugation of the cellular membrane) and the molecular brush. Here we will show how this model allows reducing the complexity of the bio interface to the contact problem of the standard Hertz model. First, we overview the model.

The brush model is described in detail in (Guz et al. [2014](#); Sokolov et al. [2013](#); Dokukin et al. [2013](#); Sokolov and Dokukin [2018](#)). Here we briefly describe its major steps. Figure 2.4 shows a schematic of the indentation of a biointerface covered with a pericellular layer of molecules and membrane protrusions/corrugations. Note that both the molecular layer and the membrane corrugations are shown as a single pericellular coat layer. The reason for such a simplification will be described later.

Geometrical definitions shown in Fig. 2.4 lead to the following simple formula:

$$h = Z - Z_0 + i + d, \quad (2.2)$$

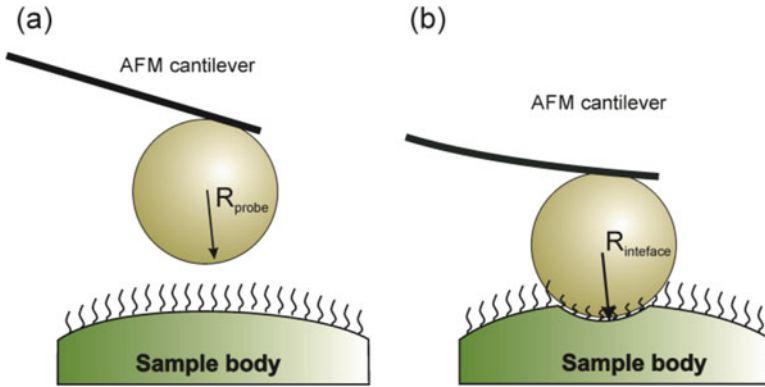


Fig. 2.5 Demonstration of the major assumption of the brush model, the squeezing of the pericellular brush layer, which surrounds a sample body, leads to just a small modification of the probe radius. A scheme of the AFM cantilever with a spherical probe (a) before the contact, and (b) after the full contact with the biointerface

where Z_0 is the position of the undeformed cell body, d is the deflection of the AFM cantilever, h is the distance between the AFM probe and the surface of the cell body, and i is the indentation depth.

The contact problem here should provide the connection between the load force F ($F = kd$, where k is the spring constant of the AFM cantilever) and the indentation depth i . A substantial simplification comes from the fact that the pericellular layer of molecules and membrane corrugations are substantially less stiff than the cell body. As a result, the indenting probe squeezes the pericellular brush layer which complies the shape of the indenter until the stiffness of the squeezed layer becomes equal to the stiffness of the cell body. Assuming that the response of the cell body is linear, the problem is reduced to the classical Hertz model, in which the radius of the probe is modified to the radius of the interface, $R_{interface}$, Fig. 2.5.

The major assumption of the brush model is that the thickness of the squeezed layer is much smaller than the radius of the probe, so that $R_{interface} \approx R_{probe}$. Thus, one can use the classical Hertz model and to write for the connection between the indentation depth i and force F the following relation:

$$i = \left[\frac{9 F}{16 E} \sqrt{\frac{R_{interface} + R_{cell}}{R_{interface} R_{cell}}} \right]^{2/3} \approx \left[\frac{9 F}{16 E} \sqrt{\frac{R_{probe} + R_{cell}}{R_{probe} R_{cell}}} \right]^{2/3}, \quad (2.3)$$

where E is the elastic (Young's) modulus, R_{probe} (R_{cell}) are the radius of the AFM probe (cell). The Poisson ratio of a cell is chosen to be 0.5 (is the most frequently used when describing cells).

3.4 Verification of the Contact Problem in the Brush Model

The validity of the reduction of the contact problem of the complex biointerface to a simple hertz contact problem was verified using homogeneous polymers with the grafted polymer brush (Dokukin and Sokolov 2012). However, the applicability of the model has not been directly verified on such a complex biointerface as the cell surface. Nevertheless, its validity can be indirectly verified by testing the strong linearity principle, independence of the derived modules on the indentation depth.

As we discussed above, it is highly unlikely that all parameters of a biointerface would compensate each other to provide the modules independent of the indentation depth. It is, in particular, unlikely because of the heterogeneity of the biointerface. If one observes the Young's modules independent of the indentation depth across the bio interface surface, it is improbable that all these parameters compensate each other despite the diversity of the parameters over the bio interface. Therefore, it makes sense to use the strong linearity principle to verify the applicability of the brush model, the reduction of the contact problem to the standard Hertz contact problem.

To verify the independence of the Young's modulus of the indentation depth, one should find the modules using experimental data (d versus Z). In principle, it can be done with Eq. (2.2). However, it is a non-linear curve fitting. It turned out that there is a large correlation between the unknown parameters (E , Z_0 , and h). A straightforward simplification is to put the size of the squeezed pericellular brush layer $h = 0$. This solves the problem of cross-correlation between the unknown parameters. Moreover, it is in agreement with the brush model assumption that $R_{\text{interface}} \approx R_{\text{probe}}$ (see also Eq. 2.3). Obviously, it happens when the load force F is sufficiently high.

Figure 2.6a shows an expected example of the Young's modulus dependence on the indentation depth. For small indentations (small load forces), the assumption $h = 0$ is obviously incorrect. The application of Eqs. (2.2) and (2.3) for such a case would result in probing of a partially squeezed but still softer pericellular brush layer, and consequently to a smaller value of the Young's modulus assigned to such force. With the increase of the load force/indentation depth, we should expect to reach a plateau in the modulus dependence. The presence of such a plateau is an indication of the validity of the strong linearity principle. Higher forces may well lead to non-linear response due to or restoration of the material and/or probing of a typically more rigid substrate (if the sample is relatively thin). It should lead to an increase in modulus values. This behavior is presented in Fig. 2.6a. Figure 2.6b shows an example of such an analysis done on a force curve recorded over the surface of a biological cell (human cervical epithelial cancer cell). One can clearly see the confirmation of the expected behavior.

It should be noted that the presence of the plateau in the modulus dependence on the indentation depth is key in the verification of the strong linearity principle. It well may be that the force needed to squeeze the pericellular brush layer is already too large to be associated with the linear stress-strain response of the bio

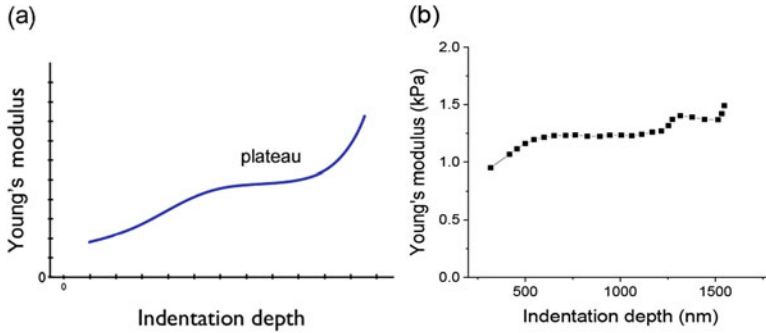


Fig. 2.6 Verification of the contact problem in the brush model. (a) A schematic of expected dependence of the Young's modulus on the indentation depth; (b) an example of experimentally derived dependence. A $5\ \mu\text{m}$ colloidal probe was used

interface material, and/or not causes too large deformation, so the contribution of the rigid substrate becomes substantial. Fortunately, all cell types we have studied demonstrated a sufficient number of force curves ($\sim 50\%$) which provided the modulus plateau, such as human cervical epithelial cells (both normal and cancerous) (Iyer et al. 2009a; Gaikwad et al. 2010), human breast epithelial cancer cells (Dokukin et al. 2017b; Guz et al. 2014), guinea pig fibroblast (Dokukin et al. 2016), mouse neurons (Simon et al. 2016), human leukemia blood cells (Guz et al. 2016b), including rather small blood stem/progenitor cells (Guz et al. 2016a).

3.5 Comparison of the Contact Problem within the Hertz and Brush Models Applied to Biological Cells

Although the brush model is not excessively complicated, it is definitely more laborious to use compared to the classical Hertz model. Therefore, a legitimate question is if the brush model is indeed better than just the Hertz model when applied to such biointerface as the cell surface directly.

Obviously, the Hertz contact problem is based on the assumption of a smooth flat or spherical interface of linear elastic homogeneous and isotropic material. As was mentioned above, the easiest way to verify this assumption is to measure the dependence of the Young's modulus on the indentation depth (or the load force). The relative independence of the modulus, specifically, the presence of a plateau as described in the previous section, will indicate the validity of the assumption, and consequently, the self-consistency of the used contact problem.

Figure 2.7 shows a few examples of the dependence of the Young's modulus derived from the individual force-indentation curves collected over the surface of human breast epithelial cancer cells (MFC-7). One can see better depth independence of the Young's modulus for the case of the brush model compared to

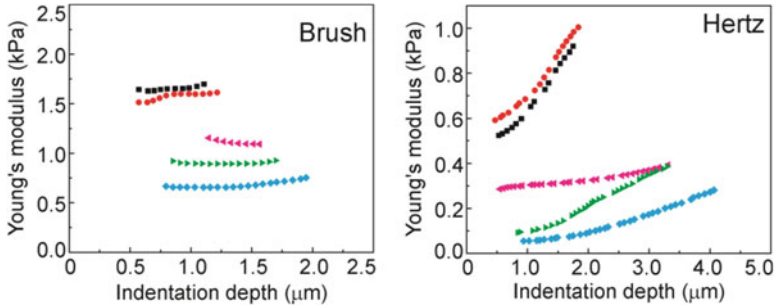


Fig. 2.7 Example of calculation of five force indentation curves measured on MFC-7 human breast epithelial cancer cells, which were processed through the brush contact model (left) and the classical hertz model (right). The same curves processed within each model have the same symbol (and color)

the Hertz one. One can see a curve in Fig. 2.7 which is very close to plateau for the Hertz model. Thus, as was mentioned before, to compare different models or biointerfaces, one needs to provide reliable statistics, which would show more than just a few curves.

Such statistical analysis was performed for the case of human cervical epithelial cells (both normal and cancerous) in (Guz et al. 2014). A gradient of the modulus was introduced to characterize the deviation from the plateau. Mathematically, it was calculated as a standard deviation of the elastic modulus $St.Dev(E)$ calculated for each modulus-indentation curve normalized by the average modulus for that curve $Aver(E)$: $St.Dev(E)/Aver(E) \times 100\%$. Zero value corresponds to the ideal plateau (no depth dependence). This normalized deviation value was calculated for about 300 force curves over the same force range for both Hertz and brush models. The Hertz model showed an average 41% deviation whereas the brush model provides 5.5%. It is generally accepted that the Young's modulus can be measured with an error of less than 10% (mainly due to the uncertainty in the definition of the spring constant of the AFM cantilever). Thus, *the uncertainty of 5.5% can be considered negligible, and the contact problem within the brush model is self-consistent.*

3.6 Pericellular Brush Layer Is Not a Linear Elastic Material

The brush model contains one inexplicit assumption that the deformation of the brush layer does not carry the shearing stress, which would be typical for any elastic material with the nonzero Poisson ratio. Due to this assumption, we can avoid the complexity of a two-layered system when both layers comprise of elastic materials. This assumption is justified by the physical structure of this layer, which consists of a mix of polymer entropic brush and random asperities. In the case of biological

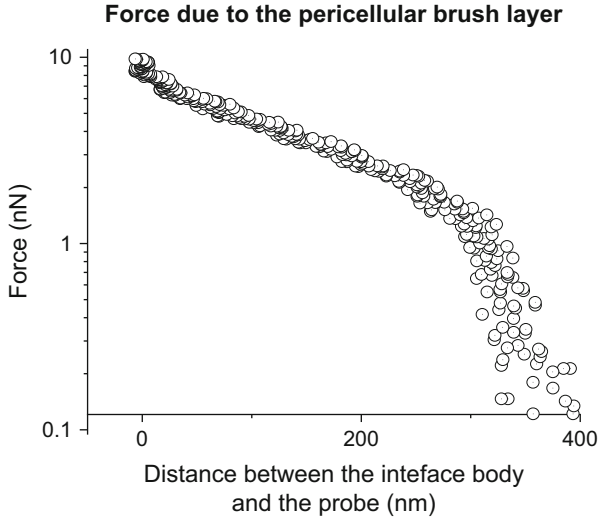


Fig. 2.8 Example of the force due to the presence of the pericellular brush layer derived using Eq. 2.2. A linear dependence in a logarithmic scale of force indicates the presence of exponential force dependence. The force curve was collected on an MFC-7 cell

cells, both contributors seem to be rather rare. As a result, the vertical deformation does not lead to a substantial lateral displacement.

As previously, direct confirmation of the above assumption is very difficult because of the necessity to estimate the density of the pericellular molecules. An indirect way to prove it is to analyze the force due to the pericellular brush layer derived within the brush model. This can be done by using Eq. 2.2, in which the only unknown parameters remaining after finding the modulus as described above, are the deflection of the cantilever (force) and the distance between the probe and the body of the interface.

Figure 2.8 shows an example of such force plotted in a logarithmic scale of force. One can see a clear linear dependence in the logarithmic scale (in the initial part of the curve). It indicates the exponential force dependence on the probe – interface body distance. This is excellent agreement with the assumption of polymer brush behavior, Alexander – de Gennes model (Sokolov et al. 2007b; Hyun et al. 2004; Persson 2007).

Furthermore, as was shown in (Dokukin et al. 2016), the exponential behavior of the pericellular layer survives after enzymatic removal of the brush molecules. Such behavior is explained by the presence of membrane corrugation on the cell surface (well-known microvilli and microridges). This is also in good agreement with the force behavior due to the deformation of randomly distributed asperities. It was predicted theoretically and later (Hyun et al. 2004; Persson 2007) confirmed experimentally using a surface force apparatus (Benz et al. 2006).

Thus, one can conclude that the brush model correctly describes the behavior of the pericellular brush layer, and therefore, indirectly confirms the assumption of the absence of the sharing stress within the pericellular brush layer. This, in turn, justifies the application of a simple Hertz contact problem within the brush model.

4 Conclusion

We described the contact problem between a realistic biointerface and solid indentation probe. The bio interface typically comprises a rough surface as well as substantial molecular coating, which contributes to the deformation of the material of the interface. We suggest using the brush model to reduce the complexity of the contact problem of biointerface to a classical Hertz contact problem. We analyzed the assumptions of the brush model and demonstrated its self-consistency by using the example of biological cells.

Acknowledgments This work was supported by the National Science Foundation, grant CMMI 1937373.

A.1 Appendix

Atomic Force Microscopy Both Bioscope Catalyst (Bruker/Veeco, Inc., CA) AFM placed on Nikon TE2000U confocal Eclipse microscope and Dimension 3100 (Bruker Nano/Veeco, Inc.) AFM with NPoint close-loop scanner ($200\ \mu\text{m} \times 200\ \mu\text{m} \times 30\ \mu\text{m}$, XYZ) were used in this study. A Dimension Icon AFM was equipped with a built-in video microscope that helps to position the AFM probe over the cells of interest (allows observation of areas from 150×110 to $675 \times 510\ \mu\text{m}^2$ with $1.5\ \mu\text{m}$ resolution).

A standard AFM cantilever holder for operation in liquids was used. The force-volume mode was used in this study. In this mode of operation, an AFM probe moves up and down collecting the force-indentation curve at each point of the surface. After recording each force curve, the AFM probe moves up and then is displaced in the lateral direction to the next pixel of the surface to continue force recording. The force-volume images were recorded with the resolution typically of 16×16 pixels within $50 \times 50\ \mu\text{m}^2$ area. The force-indentation curves are analyzed only for a relatively flat or spherical area above the cell nucleus (the incline is smaller than 10–15%).

A standard V-shaped arrow $200\ \mu\text{m}$ AFM cantilevers (Bruker, Santa Barbara, CA) with integrated silicon nitride pyramidal probes (sharp probes) were used. Spherical colloidal probes were prepared as described, for example, in (Berdyeva et al. 2005a; Volkov et al. 2011) in detail. Briefly, standard V-shaped arrow $200\ \mu\text{m}$

AFM tipless cantilevers (Bruker, Santa Barbara, CA) were used to glue 5 μm diameter silica spheres (Bangs Labs, Inc.) to the cantilevers using either the AFM built-in micromanipulator (Dimension 3100 microscope) or a micromanipulator station 6000 (by Micromanipulator, Inc.). The radius of the probe was measured by imaging the inverse grid (TGT1 by NT-MDT, Russia) or by SEM imaging. The cantilever spring constant (0.04–0.3 N/m) was measured using the thermal tuning method (the algorithm built-in in the AFM software) before gluing the spherical probe.

Indenting Speed Measurements of quasistatic elastic modulus imply the use of slow indentation speed. This is rather complicated when dealing with soft materials in general because of the creep, a slow increase of indentation depth under constant load. In the case of biological cells, a slow indentation can also induce a non-trivial biological response of the cell. For instance, cells may start to restructure their cytoskeleton, may develop a nonspecific adhesion to the AFM probe (Gaikwad et al. 2011a; Iyer et al. 2009b; Zhao et al. 2006), and finally, even to move away. As a compromise, the force-indentation curves are typically recorded with a ramp frequency of 1-2 Hz with the vertical ramp size of 3–6 μm . This decreases the viscoelastic effects of the indentation though a difference between the approaching and retracting force-indentation curves is still seen.

Cell Cultures Measurements were done using primary cell cultures derived from the human cervix as described in (Iyer et al. 2009c, 2012; Gaikwad et al. 2011b; Dokukin et al. 2011) and human breast epithelial cancer cells MFC-7 (ATCC HTB-22 cell line). The measurements were done on cells grown sub-confluently directly in the culture dish in either PBS or filtered growth medium. All measurements were done within three-five hours after taking the cells from the incubator.

References

- Benz M et al (2006) The deformation and adhesion of randomly rough and patterned surfaces. *J Phys Chem B* 110(24):11884–11893
- Berdyeva TK, Woodworth CD, Sokolov I (2005a) Human epithelial cells increase their rigidity with ageing in vitro: direct measurements. *Phys Med Biol* 50(1):81–92
- Berdyeva TK, Woodworth CD, Sokolov I (2005b) Human epithelial cells increase their rigidity with ageing in vitro: direct measurements. *Phys Med Biol* 50(1):81–92
- Bippes CA et al (2005) Direct measurement of single-molecule visco-elasticity in atomic force microscope force-extension experiments. *Eur Biophys J* 35:1–6
- Burtovyy R, Luzinov I (2008) Reversibility of pH-induced dewetting of poly(vinyl pyridine) thin films on silicon oxide substrate. *Langmuir* 24(11):5903–5910
- Camesano TA, Logan BE (2000) Probing bacterial electrosteric interactions using atomic force microscopy. *Environ Sci Technol* 34(16):3354–3362
- Cohen M et al (2003) Organization and adhesive properties of the hyaluronan pericellular coat of chondrocytes and epithelial cells. *Biophys J* 85(3):1996–2005
- Colton RJ et al (1991) Probing the surface forces of materials using atomic force microscopy. *Abstr Pap Am Chem Soc* 202:154-Phys

- Dimitriadis EK et al (2002) Determination of elastic moduli of thin layers of soft material using the atomic force microscope. *Biophys J* 82(5):2798–2810
- Dokukin ME, Sokolov I (2012) On the measurements of rigidity modulus of soft materials in nanoindentation experiments at small depth. *Macromolecules* 45(10):4277–4288
- Dokukin ME et al (2011) Cell surface as a fractal: normal and cancerous cervical cells demonstrate different fractal behavior of surface adhesion maps at the nanoscale. *Phys Rev Lett* 107(2):028101
- Dokukin ME, Guz NV, Sokolov I (2013) Quantitative study of the elastic modulus of loosely attached cells in AFM indentation experiments. *Biophys J* 104(10):2123–2131
- Dokukin M et al (2016) Pericellular brush and mechanics of Guinea pig fibroblast cells studied with AFM. *Biophys J* 111(1):236–246
- Dokukin ME et al (2017a) AFM study of polymer brush grafted to deformable surfaces: quantitative properties of the brush and substrate mechanics. *Macromolecules* 50(1):275–282
- Dokukin ME, Guz NV, Sokolov I (2017b) Mechanical properties of cancer cells depend on number of passages: atomic force microscopy indentation study. *Jpn J Appl Phys* 56(8):08LB01
- Fritz M et al (1995) Imaging globular and filamentous proteins in physiological buffer solutions with tapping mode atomic-force microscopy. *Langmuir* 11(9):3529–3535
- Gaikwad R et al (2010) Atomic Force Microscopy helps to develop methods for physical detection of cancerous cells. In: Fourth international conference on quantum, nano and micro technologies: Icqnm 2010, Proceedings, p 18–22
- Gaikwad RM et al (2011a) Detection of cancerous cervical cells using physical adhesion of fluorescent silica particles and centripetal force. *Analyst* 136(7):1502–1506
- Gaikwad RM et al (2011b) Detection of cancerous cervical cells using physical adhesion of fluorescent silica particles and centripetal force. *Analyst* 136(7):1502–1506
- Grimm KB, Oberleithner H, Fels J (2014) Fixed endothelial cells exhibit physiologically relevant nanomechanics of the cortical actin web. *Nanotechnology* 25(21):215101
- Guz N et al (2014) If cell mechanics can be described by elastic modulus: study of different models and probes used in indentation experiments. *Biophys J* 107(3):564–575
- Guz NV et al (2016a) Biophysical differences between chronic myelogenous leukemic quiescent and proliferating stem/progenitor cells. *Nanomed Nanotechnol Biol Med* 12(8):2429–2437
- Guz NV et al (2016b) AFM study shows prominent physical changes in elasticity and pericellular layer in human acute leukemic cells due to inadequate cell-cell communication. *Nanotechnology* 27(49):494005
- Hansma HG, Kasuya K, Oroudjev E (2004) Atomic force microscopy imaging and pulling of nucleic acids. *Curr Opin Struct Biol* 14(3):380–385
- Huth S, Sindt S, Selhuber-Unkel C (2019) Automated analysis of soft hydrogel microindentation: impact of various indentation parameters on the measurement of Young's modulus. *PLoS One* 14(8):e0220281
- Hyun S et al (2004) Finite-element analysis of contact between elastic self-affine surfaces. *Phys Rev E* 70(2):026117
- Iyer S et al (2009a) Atomic force microscopy detects differences in the surface brush of normal and cancerous cells. *Nat Nanotechnol* 4(6):389–393
- Iyer S et al (2009b) Towards nonspecific detection of malignant cervical cells with fluorescent silica beads. *Small* 5(20):2277–2284
- Iyer S et al (2009c) Towards nonspecific detection of malignant cervical cells with fluorescent silica beads. *Small* 5(20):2277–2284
- Iyer KS et al (2012) Physical labeling of papillomavirus-infected, immortal, and cancerous cervical epithelial cells reveal surface changes at immortal stage. *Cell Biochem Biophys* 63(2):109–116
- Jones LM et al (1995) Hyaluronic acid secreted by mesothelial cells: a natural barrier to ovarian cancer cell adhesion. *Clin Exp Metastasis* 13(5):373–380
- Jungmann PM et al (2012) Nanomechanics of human adipose-derived stem cells: small GTPases impact chondrogenic differentiation. *Tissue Eng A* 18(9–10):1035–1044
- Lekka M et al (1999) Elasticity of normal and cancerous human bladder cells studied by scanning force microscopy. *Eur Biophys J* 28(4):312–316

- Mahaffy RE et al (2004) Quantitative analysis of the viscoelastic properties of thin regions of fibroblasts using atomic force microscopy. *Biophys J* 86(3):1777–1793
- Mathur AB, Truskey GA, Reichert WM (2000) Atomic force and total internal reflection fluorescence microscopy for the study of force transmission in endothelial cells. *Biophys J* 78(4):1725–1735
- Oberleithner H (2012) A physiological concept unmasking vascular salt sensitivity in man. *Pflügers Archiv Eur J Physiol* 464(3):287–293
- Park S et al (2005a) Cell motility and local viscoelasticity of fibroblasts. *Biophys J* 89(6):4330–4342
- Park S et al (2005b) Cell motility and local viscoelasticity of fibroblasts. *Biophys J* 89(6):4330–4342
- Persson BNJ (2007) Relation between interfacial separation and load: a general theory of contact mechanics. *Phys Rev Lett* 99(12):125502
- Rosner B (2010) *Fundamentals of biostatistics*, 7th edn. Cengage Learning, Boston
- Shoelson B et al (2004) Evidence and implications of inhomogeneity in tectorial membrane elasticity. *Biophys J* 87(4):2768–2777
- Simon M et al (2016) Load rate and temperature dependent mechanical properties of the cortical neuron and its Pericellular layer measured by atomic force microscopy. *Langmuir* 32(4):1111–1119
- Sokolov I, Dokukin ME (2018) AFM indentation analysis of cells to study cell mechanics and pericellular coat. *Nanoscale Imaging Methods Protocols* 1814:449–468
- Sokolov I, Firtel M, Henderson GS (1996) In situ high-resolution AFM imaging of biological surfaces. *J Vac Sci Tech B* 14:674–678
- Sokolov I, Subba-Rao V, Luck LA (2006a) Change in rigidity in the activated form of the glucose/galactose receptor from E-coli: a phenomenon that will be key to the development of biosensors. *Biophys J* 90:1055–1063
- Sokolov I, Iyer S, Woodworth CD (2006b) Recovery of elasticity of aged human epithelial cells in-vitro. *Nanomed Nanotechnol Biol Med (Nanomedicine)* 2:31–36
- Sokolov I et al (2007a) Detection of surface brush on biological cells in vitro with atomic force microscopy. *Appl Phys Lett* 91(2):023902
- Sokolov I et al (2007b) Detection of surface brush on biological cells in vitro with atomic force microscopy. *Appl Phys Lett* 91:023902-1-3
- Sokolov I, Dokukin ME, Guz NV (2013) Method for quantitative measurements of the elastic modulus of biological cells in AFM indentation experiments. *Methods* 60(2):202–213
- Sokolov I, Zorn G, Nichols JM (2015) Study of molecular adsorption of cationic surfactant on complex surfaces with atomic force microscopy. *Analyst* 141:1017–1026
- Sokolov I, Zorn G, Nichols JM (2016) A study of molecular adsorption of a cationic surfactant on complex surfaces with atomic force microscopy. *Analyst* 141(3):1017–1026
- Toole B (1982) Glycosaminoglycans in morphogenesis. In: Hay E (ed) *Cell biology of the extracellular matrix*. Plenum Press, New York, pp 259–294
- Volkov DO et al (2011) Influence of adhesion of silica and ceria abrasive nanoparticles on chemical-mechanical planarization of silica surfaces. *Appl Surf Sci* 257(20):8518–8524
- Wiesinger A et al (2013) Nanomechanics of the endothelial Glycocalyx in experimental sepsis. *PLoS One* 8(11):e80905
- Wu PH et al (2018) A comparison of methods to assess cell mechanical properties. *Nat Methods* 15(7):491
- Zhang L, Underhill CB, Chen L (1995) Hyaluronan on the surface of tumor cells is correlated with metastatic behavior. *Cancer Res* 55(2):428–433
- Zhao MH et al (2006) Rate- and depth-dependent nanomechanical behavior of individual living Chinese hamster ovary cells probed by atomic force microscopy. *J Mater Res* 21(8):1906–1912
- Zimmerman E, Geiger B, Addadi L (2002) Initial stages of cell-matrix adhesion can be mediated and modulated by cell-surface hyaluronan. *Biophys J* 82(4):1848–1857

Chapter 3

Mechanical Properties of the Cell Surface Layer Measured by Contact Atomic Force Microscopy



Maria N. Starodubtseva

Abstract The rapid progress in the development of the devices and methods of AFM over the past two decades gives confidence that this tool for analyzing the nanomechanical properties of the cell surface can be used soon in clinical practice. For the use of AFM in medicine, it is necessary to clearly understand the relationship between the nanomechanical parameters measured by AFM and the state of the cell or its components. In the chapter, the physical quantities measured by AFM in a contact mode and parameters of the map of nanomechanical properties of the cell surface layer are discussed. The effectiveness of using the AFM parameter to characterize the type and state of cells is illustrated by the example of erythrocytes in hereditary spherocytosis, epithelial cells, and fibroblasts.

Keywords AFM · Nanomechanical properties · Cell surface layer

1 Introduction

Atomic force microscopy (AFM) is a method for characterizing the structural, mechanical and physical properties of a surface, including the cell surface, at the nano- and microscales. It can operate under different conditions (in air or liquids, over a wide range of temperatures) and requires relatively simple procedures to prepare cell samples without the necessary dehydration, labeling with fluorescent dyes, and others. Cell nanomechanics has recently become the center of interest of biologists and biophysicists. Nanomechanical properties of cell surface play an important role in the mechanisms of cell vital activity and functioning. These properties are considered to be markers of cell state and promising markers of different human diseases in medicine. To analyze the nanomechanical cell properties, very small areas (microscale size) of the cell surface can be analyzed using AFM

M. N. Starodubtseva (✉)

Gomel State Medical University, Radiobiology Institute of NAS of Belarus, Gomel, Belarus

© Springer Nature Switzerland AG 2022

F. M. Borodich, X. Jin (eds.), *Contact Problems for Soft, Biological and Bioinspired Materials*, Biologically-Inspired Systems 15,

https://doi.org/10.1007/978-3-030-85175-0_3

techniques. Given rapid progress in the development of the devices and methods of AFM over the past two decades, we can assume that this tool for analyzing the nanomechanical properties of the cell surface will be used in clinical practice soon. To use AFM for diagnostic purposes in medicine it is necessary to clearly understand the relationship between the nanomechanical parameters measured by AFM and the state of the cell or its components.

In the chapter, the parameters of nanomechanical properties of cell surface measured by AFM in a contact mode and their effectiveness for characterizing cell type and cell state are discussed.

2 Cell Surface Layer

Cells are the structural and functional units of living multicellular organisms. Cells also are multiunit constructions (composite material) that mechanical properties are determined by the properties of their basic components functioning in cells as a comprehensive whole. AFM allows probing the mechanical properties of the submicron surface layer of cells consisting of the glycocalyx, membrane, and cytoplasmic layer with the cortical cytoskeleton. The main contribution to the mechanical parameters of this composite material is made by the cortical cytoskeleton. Many works in current scientific literature demonstrate a relationship between the cytoskeleton state and mechanical properties of cells using cytoskeleton modifying drugs (Blanchoin et al. 2014). The thickness of the cell surface layer, for example, for erythrocytes, is about 60–120 nm, taking into account the thicknesses of the glycocalyx (6–15 nm), membrane (4–10 nm), and membrane skeleton (50–100 nm) (Deuticke 2003; Nans et al. 2011) (Fig. 3.1).

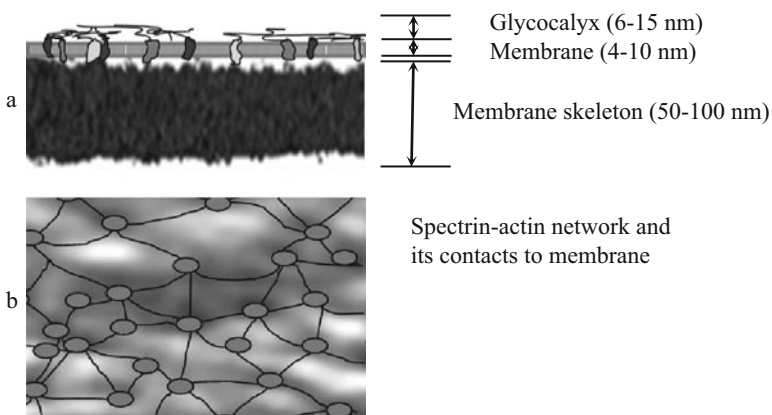


Fig. 3.1 Schematic presentation of the erythrocyte surface layer in normal to the surface (a) and parallel to the surface (b) planes

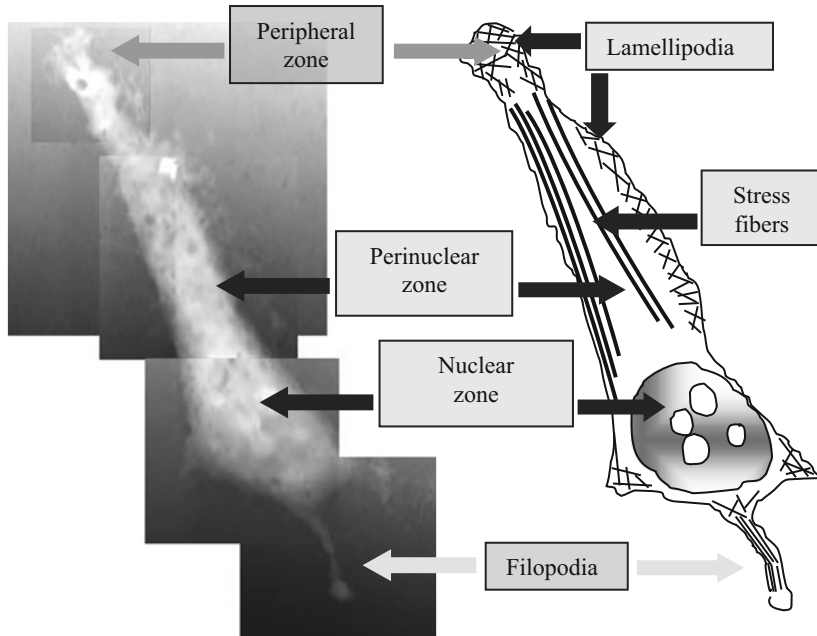


Fig. 3.2 AFM topographic image of the whole epithelial cell of MCF-7 line and the scheme showing the different structures of the different cell zones

The cytoskeleton of erythrocytes, named the membrane skeleton, is a “two-dimensional” triangular mesh-like spectrin-actin network attached to the lipid bilayer. Spectrin forms long flexible heterodimers associated into heterotetramers. The “tails” of heterotetramers bind a junctional complex composed of F-actin, protein 4.1, and actin-binding proteins (dematin, adducin, tropomyosin, and tropomodulin) (Pan et al. 2018). The cytoskeleton is connected to the lipid bilayer via “immobile” band-3 proteins at the spectrin-ankyrin binding sites and via glycophorin proteins at the actin junctional complexes (Lux 4th 2016). The erythrocyte membrane skeleton is not, actually, a two-dimensional one. It is a layer with variable thickness (50–110 nm) depending on cell region (Deuticke 2003) (Fig. 3.1).

The cytoskeleton of other cells is characterized by hierarchical structure and difference in molecular composition at each level of the hierarchical organization. There are three main types of cytoskeletal elements: actin microfilaments, intermediate filaments, and microtubules. The principal components of the cytoskeleton are composite structures themselves. Through interactions with the associated proteins, actin can form a range of structures suited to different functions. These include isotropic networks, branched networks, bundled networks, and stress fibers (Fig. 3.2).

The branched actin filaments are found in lamellipodia, the parallel actin filaments are present in the filopodia and stress fibers (Xu et al. 2004;

Renault et al. 2013). The prevalence of the different basic actin structures varies in different cell types (for example, lamellipodia predominate over filopodia in keratocytes and neutrophils, whereas filopodia predominate over lamellipodia in dendritic cells or neuronal growth cones) (Letort et al. 2015). For a given cell type, the predominance and/or existence of the different actin structures change with the change in the cell state. Moreover, different regions of cells may have different structures of the actin cytoskeleton (Fig. 3.2).

3 Physical Quantities Measured by AFM in Contact Mode

AFM records and controls forces between molecules of a sharp probe (the AFM tip) at the free end of a long cantilever fixed at the other end and molecules of the surface of the object under the study. These forces can be attractive or repulsive depending on the distance between the AFM tip and surface. Topographical features of the surface cause the AFM tip to deflect in a vertical direction while the sample is scanned. This deflection is detected by the laser beam that reflects from the cantilever surface and is sensed by the four-quadrant photodetector converting it into an electrical signal. At small distances, in the range of repulsive forces, the tip and surface are in contact, and the imaging mode is called contact mode. The contact mode can provide imaging surfaces with high quality and resolution. Due to relatively “tight” contact between molecules of interactive bodies, relatively high speed of scanning process and inertia of the piezoscanner and others, the scanned surface of a cell can be mechanically destroyed. Therefore, the contact mode is usually used in air for chemically fixed and dried cells to obtain information about the highly-resolved spatial features of cell surface architectonics and relative nanomechanical properties of the cell surface. While scanning the surface in a contact mode the AFM tip is deflected not only in the vertical direction due to the relief features but also twists in the lateral direction. Twisting the AFM tip relative to the long axis of the cantilever by a certain angle (this mode is also called torsion mode or lateral force mode) results in the movement of the reflected laser beam in the horizontal direction on the photodetector. In this case, in addition to the map of geometrical features of the studied surface (height), a map of lateral forces is recorded (Fig. 3.3). The lateral force map contains information about both the relief of the surface and its mechanical properties. If the scanning process is performed in two opposite directions, it is possible to extract the part related to mechanical properties (F_f , sliding friction force) by subtracting the forward scanning lateral force value ($L1$) from the backward scanning lateral force value ($L2$) (Starodubtseva et al. 2012):

$$F_f = \frac{1}{2} |L1 - L2|. \quad (3.1)$$

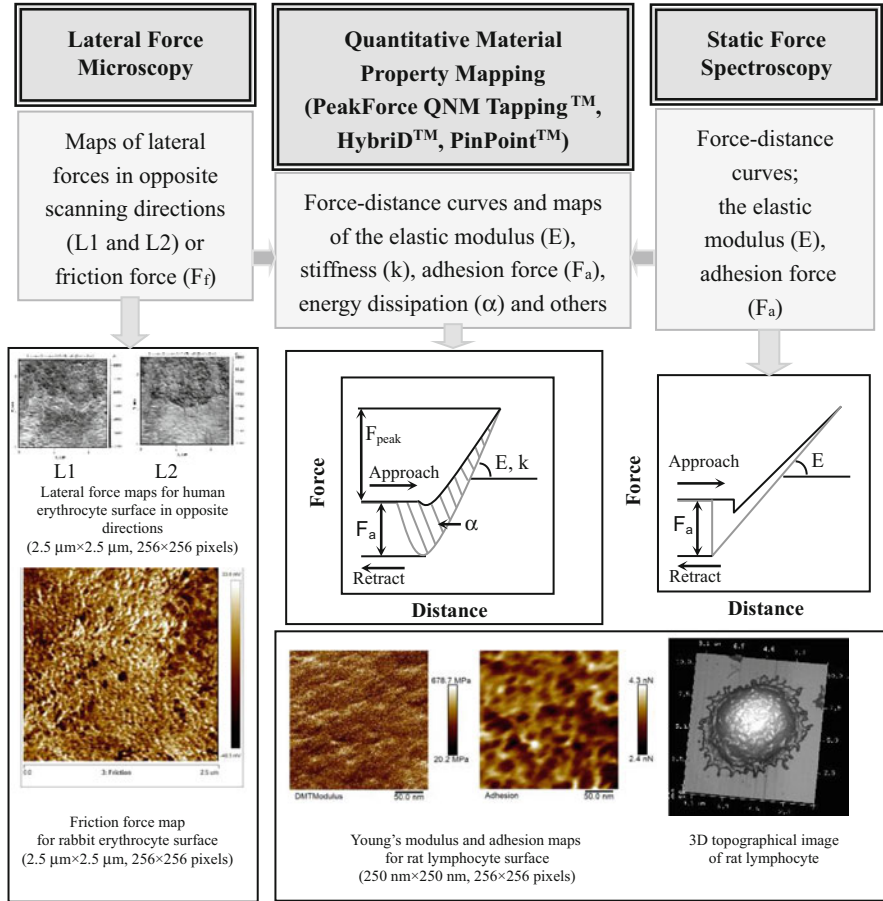


Fig. 3.3 Some AFM modes and measured parameters of mechanical properties

Cell surface frictional coefficients (μ) can be then calculated based on the equation:

$$F_f = \mu F_N, \tag{3.2}$$

where F_f is the friction force, F_N is the normal force.

The parameters of sliding friction force for the selected section of the surface or for the whole scan can be computed and even the map of friction forces can be created as well (Fig. 3.3). Each sublayer of the surface layer of the cells can contribute to the frictional properties of the surface. All of these cellular constituents are physically linked with one another and represent a single whole that makes it difficult to separate the effects of each on frictional properties of the cell surface layer. Friction properties of many cell types were studied by AFM in air and in

liquids including vascular smooth muscle cells (Dean et al. 2010), pancreatic cells (Girasole et al. 2007), erythrocytes, thymocytes, epithelial cells (Starodubtseva et al. 2012; Nikitina et al. 2012; Starodubtseva et al. 2010), and others.

A more frequently used mode for AFM-based imaging of the living cells is an intermittent contact mode (tapping mode) during which the resultant forces can be either attractive or repulsive since the AFM tip moves alternatively toward to or away from the cell surface (oscillates with a resonant frequency). During a very short interval of time, the AFM tip touches the cell surface, which is less destructive for cells compared with scanning in a contact mode and can be used for living cells in liquids. Unfortunately, due to the resonance character of oscillations and absence of direct force control, the intermittent mode is not widely used to measure the parameters of the mechanical properties of the sample surface. Phase shift images of tapping mode characterizing also the spatial distribution of the mechanical properties of the studied surface are used frequently only for obtaining information about the surface geometrical features (Coelho-Dos-Reis et al. 2011; Nagao and Dvorak 1999).

The opportunity to study the mechanical parameters of cells in other modes than scanning modes is the process of indentation of the surface layer with the AFM tip. In the process of indentation of a surface with the AFM tip (force spectroscopy mode) at a single point of the studied surface, the tip approaches to the surface, presses against the material, withdraws from the surface, experiencing the adhesion force at the initial stage of its departure from the surface (Fig. 3.3). Some important mechanical parameters can be estimated by analyzing the force-distance curve recorded during the indentation process. More frequently used parameters measured in force spectroscopy mode are the elastic modulus and adhesion force (Fig. 3.3). For the biological cells, both the non-specific adhesion and ligand-receptor interaction forces can be measured (Whited and Park 2014; Arnal et al. 2015; Zemła et al. 2018). In single-molecule force spectroscopy, the binding strength of ligand receptor pairs is detected. In single-cell force spectroscopy, the adhesion forces of a single cell to a biointerface, which can be tissue, another cell, or a surface functionalized with ligands are measured (Ungai-Salánki et al. 2019). Analysis of non-specific cell adhesion inherent to cancer and normal cells showed that adhesion forces between the AFM tip and cancer cell surface were less in value compared to that of normal cells (Sicard et al. 2017).

The elastic modulus (Young's modulus, E) for cells under the various experimental conditions can be calculated by fitting the force-distance curve to several mathematical models, theoretical bases of which were developed by Hertz (the Hertzian model), Johnson-Kendall-Roberts (the JKR model) and Derjaguin-Muller-Toporov (the DMT model) (Barthel 2008). Elastic modulus is obtained from the slope of the linear part of either approach or retract force-indentation curve. The different mathematical models take into account the different conditions (only elastic contact, adhesion between the interacting bodies and others) of the interaction of the AFM tip and studied body. The parameters of mechanical properties of the cell surface layer depend on many factors such as the load rate, indentation depth, geometry of the AFM probe and studied surface, mathematical model, repeatability

of loading, the precision of the contact point determination, cell region, cell type, and others. In current literature, all the factors are widely discussed (Efremov et al. 2019a; Wu et al. 2018; Lekka and Pabijan 2019; Lekka 2016).

Discussing here the cell surface layer mechanical properties determined by the properties of the cortical cytoskeleton, it is worth emphasizing the importance of the indentation depth for estimating the value of Young's modulus (Sicard et al. 2017; Thomas et al. 2013). On the one side, the AFM tip geometry determines the mathematical model that will be applied for the adjustment and interpretation of the indentation curve. Tips with spherical geometries obey the Hertz mathematical model (the model is appropriate when the indentation depth is less than the radius of curvature of the probe). The tips with a conical geometry obey the Sneddon model (in this case the indentation depth can be close to or exceed the radius of curvature of the probe). On the other side, the geometry of the cell surface layer determines the possible values of indentation depth to obtain the elastic modulus of the structures of indeed interest. If the study focuses on the mechanical properties of the cortical cytoskeleton, it is important to take into account its relative thickness with respect to the thickness of other cell structures involved in the response against mechanical stress. The cytoskeleton layer contacts the plasma membrane on one side and very soft cytosol material on the other side. To exclude the effect of the deformation (bending) of the cytoskeleton layer as a whole the indentation depth should be small compared with the thickness of the cytoskeleton layer. The mathematical models used for estimating Young's modulus assume the indentation depth to be negligible in comparison with the sample thickness as well. The Herz and Sneddon contact mechanics models, for example, are valid for a small indentation depth when the substrate does not affect the calculation (about 5–10% of the sample height). Maximal indentation depth used often in models for the exclusion of the effect of the stiff substrate varies from 0.05 to 0.3 of the layer thickness (Sicard et al. 2017; Ding Yu and Wang 2017). If we assume the same limitation, the indentation depth for probing the elastic properties of erythrocytes should be from 2.5–5 to 15–30 nm because the thickness of lipid bilayer is 4 nm, average thickness of erythrocyte membrane skeletons is 110 ± 13 nm (range 88–128 nm) for the central region and 54 ± 9 nm (range 36–72 nm) at the edge (Deuticke 2003). A sharp spherical tip of 10–50 nm radius (R) requires an indentation depth of about 3–15 nm and less ($0.3R$ in theory). Probing the erythrocyte surface layer of a total thickness of about 120 nm with an AFM probe of 10–50 nm tip radius, we are able to estimate Young's modulus (tensile elastic modulus) of the membrane skeleton mainly without significant interference of other structural parts of erythrocyte at an indentation depth about 7–15 nm. In practice, however, the indentation depth is often chosen more than one was allowed in theory (Lekka 2016; Tian et al. 2015; Efremov et al. 2019b; Grady et al. 2016). Accounting for the 40–80 nm mesh structure of the erythrocyte membrane skeleton, the use of a very sharp (10 nm) AFM tip can lead to an apparent uncertainty in the measurement of the value of the elastic modulus for the whole cell on average. Conical small-radius tips are usually used to map cellular elastic modulus with high spatial resolution, while large-radius spherical tips are used to obtain the average elastic modulus of the whole cell (Sunnerberg

et al. 2019). The sharp tip probes the mechanical response from the cell layer with cortical cytoskeleton network located in the very vicinity to the membrane, while the mechanical stress from the large spherical probe acts more evenly over a large cell surface area and involves the deeper cell layers.

Nowadays, the combination of the advantages of AFM imaging and force spectroscopy has created a new possibility for multiparametric characterizing and nanomechanical mapping of the cell surface layer. The specific mode combinations with the unique brand name were developed by several companies (PeakForce QNM Tapping™ mode (Bruker), HybriD™ mode (NT-MDT), PinPoint™ (ParkSystem), and others) (Fig. 3.3). In PeakForce Tapping mode, the AFM probe oscillates at frequencies well below the cantilever resonance that allows to control and measure the forces between probe and sample, avoid the damaging lateral forces and unwanted resonance effects. The AFM tip moves along the sample surface following the sinusoidal law. As the tip approaches the sample surface, it experiences long-range attractive forces causing the tip to jump into contact with the surface. After contact (in the range of the action of short-range repulsive forces), the loading force reaches the peak point and the tip begins the backward movement, goes through an adhesive minimum (Fig. 3.3). As the result, the maps of the distribution of such mechanical parameters as the elastic modulus, stiffness, adhesive force, energy dissipation, and others are created (Fig. 3.3).

Over the past two decades, some AFM-based approaches have been developed to measure the parameters of viscoelastic properties of the cell surface layer (Rother et al. 2014; Darling et al. 2007; Cartagena-Rivera et al. 2015; Dokukin and Sokolov 2015; Alcaraz et al. 2003; Takahashi and Okajima 2015; Hecht et al. 2015; Caporizzo et al. 2015). The characteristics of the time-depending response of the cell surface layer to mechanical stress (viscoelastic parameters) include parameters describing elastic properties (the storage modulus, instantaneous and long time elastic modulus, and others), viscous properties (the loss modulus, viscosity, and others), and integral relaxation properties (the relaxation time, power-law exponent and others). With the development of the nanomechanical property mapping modes, the assessment of viscoelastic properties directly from the force-distance curves becomes very promising. According to the results obtained in the work (Efremov et al. 2019b), in cells, the viscoelastic behavior prevails over the proelastic relaxation.

4 Parameters of the Maps of Nanomechanical Properties

Measurement of complex surfaces and characterization of the measured surfaces is one of the important problems not only in science but also in technology, for example, in advanced manufacturing technologies of the objects with freeform geometries. There is currently an international standard taking into account the specification and measurement of 3D surface texture. Statistical parameters of 3D surface roughness are assessed using ISO 25178-2:2012 “Geometrical product specifications (GPS)—Surface texture: Areal—Part 2: Terms, definitions and

surface texture parameter” that includes the following set of parameters: (a) height parameters (the statistical parameters of the magnitude of the Z-axis perpendicular to the surface: mean, RMS and others); (b) functional parameters (parameters calculated from the Abbott–Firestone curve obtained by the integration of height distribution on the whole surface: areal material ratio, extreme peak height, inverse areal material ratio); (c) spatial parameters (topographic characteristics based upon spectral analysis: texture direction, auto-correlation length, texture-aspect ratio); (d) hybrid parameters (parameters depend both on the amplitude and the spacing, such as slopes, curvatures etc.: root mean square gradient, developed interfacial area ratio); (e) functional volume parameters (calculated using the Abbott–Firestone curve (areal material ratio curve)); (f) feature parameters (derived from the segmentation of a surface into motifs (hills and dales): density of peaks, arithmetic mean peak curvature and others) (Țălu et al. 2015). The mentioned parameters had been recently used for the analysis of the membrane architectonics of cells based on AFM data (Țălu et al. 2015). Due to the principal difference in the structure and composition of living cells and industrial materials, not all of these parameters are equally useful for characterizing the cell surface geometry and especially the maps of the cell surface properties. Moreover, the map of properties is a three-dimensional physical surface with different units of measure for different axes. The magnitude of the mechanical parameter (the lateral, friction, adhesive forces, Young’s modulus, stiffness, and other) is represented in Z-axis, X- and Y-axes characterize the spatial heterogeneity (pattern) of the parameter. The unit of measure of the magnitude along axes X and Y is the meter (nanometer), the units of measure used for axis Z depend on the physical quantity measured using the certain AFM mode. They can be the newtons (nano- or piconewtons), volts, or arbitrary units.

The basic parameters of the maps of cell surface properties are presented in Table 3.1.

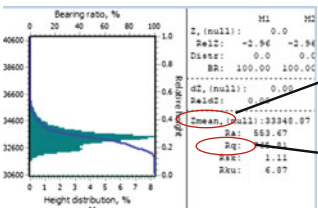
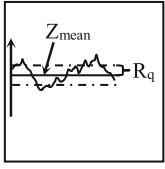
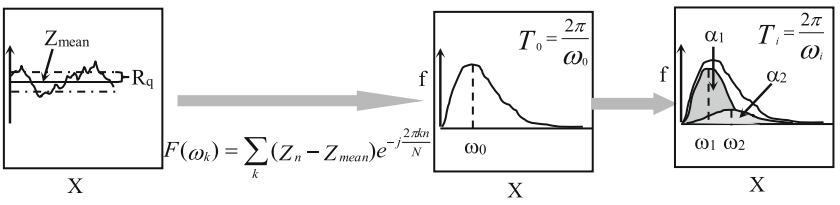
For a map of the microscale cell surface area, the vertical distribution (Z-axis) of the mechanical parameter value can be estimated as the average (the mean or median) over a given area and deviation from the average (the roughness) (Table 3.1). In the case of the apparent complexity (heterogeneity) of the property map, the distribution of mechanical properties can be approximated by several Gaussian peaks. The nanomechanical mapping of human liver tissues performed in work (Tian et al. 2015) revealed some distinguishable peaks for cancerous and paretumoral tissues, which were associated with the presence of differences in properties of the cancer cells and extracellular matrix in the studied tissues.

The roughness measurements themselves cannot fully describe the morphology of the surface structures and their spatial pattern, nor identify the presence of hierarchical structures. The distribution of the mechanical parameter in a lateral plane can be characterized by the parameters of fractal and spatial-spectral analysis.

Hierarchical surface features (in both vertical direction and lateral plane) can be characterized by fractal analysis using two statistical measures known as the fractal dimension (D_F) and lacunarity (λ) (Ling et al. 2016).

There are many fractal dimensions in mathematical and physical literature. The fractal dimensions are classified according to the methods used into three

Table 3.1 Parameters of the mechanical properties of the cell surface layer

Z-parameters	
Average (the mean (Z_{mean}), median)	Roughness (R_q , R_a)
	$Z_{mean} = \frac{1}{N_x N_y} \sum_j \sum_i Z_{j,i}$ $R_q = \left(\frac{1}{N_x N_y} \sum_j \sum_i Z_{j,i} - Z_{mean} ^2 \right)^{1/2}$ 
Spatial-spectral parameters (using the Fourier transform)	
Size of typical structural elements (frequency peaks (ω_i) or spatial periods (T_i))	Proportion of typical element subpopulation (α_i)
 $F(\omega_k) = \sum_k (Z_n - Z_{mean}) e^{-j \frac{2\pi k n}{N}}$	$T_0 = \frac{2\pi}{\omega_0}$ $T_i = \frac{2\pi}{\omega_i}$
Fractal parameters	
Fractal dimension (D_F)	Lacunarity (λ)
$D_F = \lim_{\varepsilon \rightarrow 0} \frac{\lg N(\varepsilon)}{\lg(1/\varepsilon)}$	$\lambda(\varepsilon) = \left[\frac{R_{q_k}(\varepsilon)}{Z_{mean_k}(\varepsilon)} \right]^2 + 1$

major categories: the box-counting methods, the variance methods, and the spectral methods (Balghonaim and Keller 1998; Li et al. 2009). The fractal dimension assessed in different ways was often used to characterize the cell type and cell state on the base of AFM topographical images of the cell surface (Bitler et al. 2018; Bitler et al. 2012). The box-counting dimension is the most frequently used for measurements in various application fields. The reason for its dominance lies in its simplicity and automatic computability (Li et al. 2009). The box-counting dimension of the AFM images is calculated using an algorithm based on the formula written in Table 3.1 (Falconer 1997; Sztojánov et al. 2009; Spodarev et al. 2015), where $N(\varepsilon)$ was the minimal number of cubes with edge length ε that together included the surface under the study.

The AFM image is a digital surface that is a 3D array of numbers. Distance between two adjacent points along axes X and Y is the scanning step (the X/Y step) and defined by the resolution and size of the scanning area. For example, for an image of $2.5 \mu\text{m} \times 2.5 \mu\text{m}$ size and resolution of 256×256 pixels, the X/Y step is about 9.8 nm. The distance between two adjacent points along Z-axis varies depending on the calibration coefficient for AFM cantilever deviations and

chosen units for the magnitude recorded along Z-axis. The difference in the units and calibration coefficients leads to different interpoint distances for Z-axis (Z-scale factor denoted as t). When characterizing the spatial structure of the AFM image by fractal dimension we, firstly, face the problem of the difference of the units of measure for different axes. To solve the problem of uncertainty of the interpoint distances for the Z-axis the dependence of fractal dimension on Z-scale factor ($D_F = f(t)$) can be used. The dependence has two maxima in general. The maximum taken place in the range of small Z-scale coefficient is the best characteristic of the AFM images at a small spatial scale (Starodubtseva et al. 2017a).

D_F is not a unique and sufficient measure of surface complexity, i.e. two images that appear largely different may yield the same D_F due to similarities in roughness. Lacunarity (λ) is another mean of measuring spatial heterogeneity (Ling et al. 2016). Lacunarity increases when the image becomes more spatially heterogeneous (greater variance) and the spatial pattern has more or larger gaps (Ling et al. 2016). The most common algorithm used to calculate the lacunarity of images is the gliding box-counting method developed by Allain and Cloitre (Allain and Cloitre 1991). The lacunarity, $\lambda(\varepsilon)$, is then determined by the formula written in Table 3.1, where $Z_{\text{mean } k}(\varepsilon)$ and $R_{q k}(\varepsilon)$ are the mean and standard deviation of the number of surface points for box size ε (Ling et al. 2016).

The structure of the AFM images can be assessed by spatial-spectral analysis. The AFM image with the size of $N \times N$ points is considered as a collection of N two-dimensional arrays (x, z) with N points in each. The discrete Fourier transform can be applied for each two-dimensional array (x, z) considered as a realization of a random process (Table 3.1), where Z_{mean} is the sample mean, ω_k is the k -th frequency.

A map of the mechanical properties of a surface can be considered as a hierarchical structure including some different-sized periodical structures. To extract periodical structures in the selected frequency range from the Fourier spectrum two ways can be chosen: frequency filtering or splitting into different groups (subpopulations). In the first way, the sample spectrum is filtered as written:

$$F'(\omega_{jk}) = F(\omega_{jk}) \cdot H_{jk} \quad (3.3)$$

where $F'(\omega_{jk})$ and $F(\omega_{jk})$ are the Fourier spectra after and before filtering, H_{jk} is a spectral function of the used filter (Kozlova et al. 2013). For example, the Fourier filtration was used in work (Kozlova et al. 2013) to analyze the hierarchy of the erythrocyte membrane with three spectral windows corresponding to the spatial periods of 600–1000 nm, 70–300 nm, 20–60 nm. The 1st spectral window corresponds to the typical parameters of membrane flickering. The 2nd spectral window was similar in size to the spectrin matrix elements. The 3rd spectral window was close to the typical sizes of protein structures and their clusters. Heights of corrugations h_i ($i = 1, 2, 3$) (the mean spatial period within a given spatial window) were used as parameters.

The second method was used in work (Starodubtseva et al. 2019) to analyze the structure of mechanical property maps for spheroidal erythrocytes in hereditary spherocytosis. The sample median $R_m(\omega_k)$ of spectral densities was approximated by two and three Gaussian functions. Gaussian peaks obtained for periodograms were associated with the main types (subpopulations) of periodical structures on the maps of mechanical properties of the erythrocyte surface layer. The following parameters were used: the mean value of the spatial period (T_i) of the selected Gaussian subpopulation and percentage (α_{T_i}) of the Gaussian subpopulation in the total Fourier spectrum (Table 3.1).

5 AFM Parameters of Cell Surface

5.1 AFM Parameters of Epithelial Cells and Fibroblasts (Effects of the Cell Zone and Cell Type)

The cell is a heterogeneous hierarchical structure. The mechanical properties of its surface layer depend on the cell region. Table 3.2 presents the parameters of mechanical properties obtained using the AFM contact mode for the different regions of breast cancer epithelial cells (MCF-7 cells) adhered to glass slides.

The cell edge region (peripheral zone) is characterized by a higher friction force (F_f) and fractal dimension (D_F) of lateral force maps compared to the other two regions (nuclear and perinuclear zones). High values of F_f and D_F are related to a denser and more developed cytoskeleton structure of the cell leading edge than in other regions.

To compare the cytoskeleton state of the different cell types, it is necessary to analyze the same type of cell regions for them. Table 3.3 presents the parameters of mechanical properties for three types of cells (human primary skin fibroblasts (FB), human lung carcinoma cells (A549), and MCF-7 cells) obtained for the perinuclear zone of cells.

Figure 3.4 shows the topographic images and lateral force maps of microscale size for the cells under study. The surface layer of fibroblasts in the perinuclear zone has significantly high average values of the parameters of elastic, frictional, and

Table 3.2 Parameters of mechanical properties of different cell regions for breast cancer MCF-7 cells

Cell's surface region	F_f , arb. units	R_{qf} , arb. units	D_F
Peripheral	493 ± 13	278 ± 84	2.463 ± 0.007
Perinuclear	$329 \pm 96^*$	219 ± 46	$2.328 \pm 0.135^*$
Nuclear	$326 \pm 62^*$	299 ± 96	$2.419 \pm 0.022^*$

The data are represented as 95% CI. * $p < 0.05$ in comparison with the perinuclear zone parameters, Student t test

Table 3.3 Parameters of mechanical properties of different cell types measured in the perinuclear zone

Cell type	D_{\max}/h	F_T/F_{F-FB}	R_{qt}/R_{qt-FB}	E/E_{F-FB}	F_a/F_{a-FB}	D_F
Fibroblast	40.7 ± 12.8	1.00 ± 0.18	1.00 ± 0.11	1.00 ± 0.13	1.00 ± 0.15	2.449 ± 0.024
MCF-7	$22.6 \pm 6.5^*$	$0.63 \pm 0.36^*$	1.39 ± 0.12	$0.41 \pm 0.02^*$	$0.24 \pm 0.02^*$	$2.351 \pm 0.049^*$
A549	$9.4 \pm 1.3^*$	$0.55 \pm 0.16^*$	$0.69 \pm 0.05^*$	$0.37 \pm 0.03^*$	$0.35 \pm 0.09^*$	$2.327 \pm 0.024^*$

$E_{F-FB} = 239.8$ MPa, $F_{a-FB} = 31.9$ nN, $D_{F-FB} = 2.449$, $F_{F-FB} = 735$ arb. units, $R_{qt-FB} = 320$ arb. units. The indentation depth is 10 nm. The data are represented as 95% CI

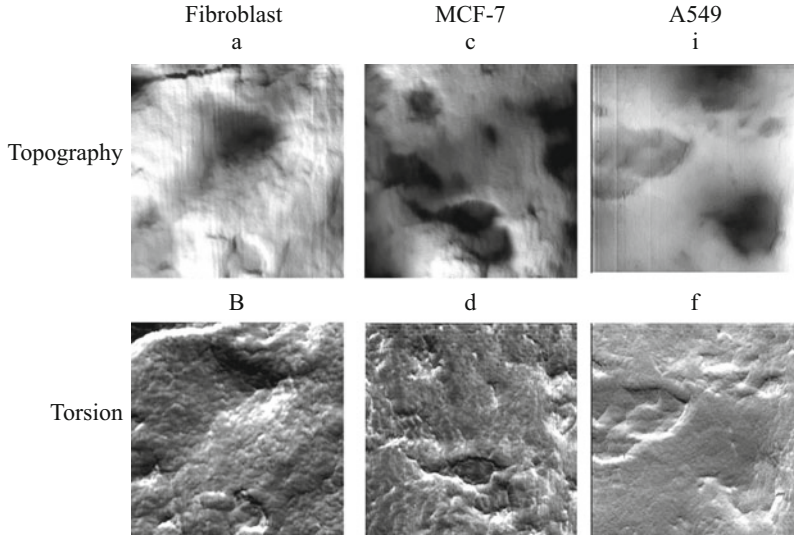


Fig. 3.4 Typical topographic images and lateral force maps for the perinuclear zone of fibroblasts, MCF-7 and A549 cells. Scanning area is $2.5 \mu\text{m} \times 2.5 \mu\text{m}$, resolution is 256×256 pixels

adhesive properties compared to the corresponding parameters of cancer epithelial cells of both cell lines. The decreased fractal dimension is evidence that the cytoskeleton structure of cancer epithelial cells in the perinuclear zones is less developed compared to the more developed cytoskeleton structure of fibroblasts. The weakened cytoskeleton structure of cancer cells determines the lesser spreading ability (D/h parameter) of these cells. There is also a difference between the parameters for two types of the studied cancer cells (F_f , R_{qf}), indicating a difference in the structure and state of their cytoskeleton.

In work (Schillers et al. 2017) it was noted that the variation in Young's modulus (only one parameter of the mechanical properties of cells was discussed) of the same cell type by different research groups can be related to two main sources: biological variability and technical inaccuracy. "The single cells show intrinsic biophysical inhomogeneity due to natural biological distributions of cell physiological activity and morphology". The authors of the mentioned work suggested the standardized nanomechanical atomic force procedure (Schillers et al. 2017) to reduce significantly the technical inaccuracy in measuring elastic properties of cells. Comparative analysis of the mechanical properties of different cells should be carried out probing the cell regions of similar morphology and taking into account the cell state to reduce the impact of the structural differences of the different cell regions on mechanical parameters.

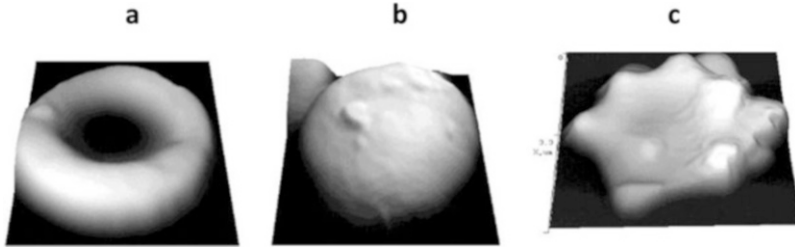


Fig. 3.5 3D Topographic AFM images of the different morphological types of erythrocytes in hereditary spherocytosis. (a) discocyte (D), $7.8 \mu\text{m} \times 9.1 \mu\text{m}$; (b) spherocyte (Sp), $7.2 \mu\text{m} \times 7.8 \mu\text{m}$; (c) echinocyte (E), $6.7 \mu\text{m} \times 8.2 \mu\text{m}$

5.2 AFM Parameters of the Different Types of Erythrocyte in Hereditary Spherocytosis (Effect of the Change in the Cell Surface Layer Structure)

Hereditary spherocytosis is a group of inherited anemias that are characterized by the presence of a significant amount of spherocytes in the peripheral blood (Perrotta et al. 2008). Light microscopy of the blood smears of the patients with hereditary spherocytosis has revealed about 60% of abnormal erythrocytes. The main types of erythrocytes were discocytes (about 40%), spherocytes (about 35%), and echinocytes (about 14%) (Fig. 3.5).

Hereditary spherocytosis is caused by a local weakening of the contacts between the cytoskeleton and the lipid bilayer due to the mutations in genes coding proteins such as spectrin, ankyrin, protein 4.2, anion exchanger 1 (Perrotta et al. 2008). These mutations lead to anomalies in the spatial structure of the cell surface layer. Transformation of discocytes into spherocytes in hereditary spherocytosis goes via vesiculation and loss of the parts of the cell membrane and cytoskeleton (Alaarg et al. 2013), which also changes the spatial structure of the cell surface layer.

The parameters of mechanical properties of the erythrocyte surface layer in hereditary spherocytosis are significantly dependent on the type of erythrocytes (discocyte, spherocyte, or echinocyte) (Table 3.4). Firstly, the parameters of the spatial distribution of mechanical properties showed that, in hereditary spherocytosis, the structural network of membrane-cytoskeleton junctions in discocytes compared with that for spherocytes is less regular, with many large gaps.

If the average distances between local contacts between the cytoskeleton and membrane in the surface layer of discocytes vary in the range $\Delta A_{1/2} = 640 \text{ nm}$ and can be grouped into three classes ($\alpha_1 = 53 \text{ nm}$, $\alpha_2 = 92 \text{ nm}$, $\alpha_3 = 201 \text{ nm}$), the variation range of the corresponding distances for spherocytes is only $\Delta A_{1/2} = 560 \text{ nm}$ with possible grouping into two classes ($\alpha_1 = 76 \text{ nm}$, $\alpha_2 = 143 \text{ nm}$). Fractal dimension increases and lacunarity decreases when discocyte transforms into a spherocyte. These results prove the mechanism of discocyte-spherocyte transformation via vesiculation: the membrane area without the linkage to the

Table 3.4 Parameters of the mechanical properties of discocytes (D), spherocytes (Sp) and echinocytes (E) in hereditary spherocytosis

Cell type	Z-parameter		Integrated parameter		XY-parameter			$a_i(w_i); R^2$
	F_T/F_{T-D} , rel. Units	R_q/R_{q-D} , rel. Units	E_T/E_{T-D} , rel. Units	Df	λ	A, nm	$\Delta A_{1/2}$, nm	
D	1.00 (0.80; 1.33)	1.00 (0.70; 1.35)	1.00 (0.84; 1.13)	2.224 ± 0.017	2.13 ± 0.43	88	640	53 nm (37%), 92 nm (53%), 201 nm (10%) $R^2 = 99.3$
Sp	1.19 (0.96; 1.51)*	0.80 (0.66; 1.00)*	1.19 (1.01; 1.36)*	2.247 ± 0.015	1.03 ± 0.07	98	560	76 nm (66%), 143 nm (34%) $R^2 = 99.2$
E	2.14 (1.16; 2.47)	1.05 (0.83; 1.55)	1.55 (1.53; 1.72)	2.192 ± 0.025	0.85 ± 0.20	102	350	60 nm (37%), 98 nm (43%), 191 nm (20%) $R^2 = 9_{,3}$

F_T/F_{T-D} and R_q/R_{q-D} are relative friction force and relative RMS roughness for friction force map correspondingly obtained with respect to median friction force and median RMS roughness of discocyte sample ($F_{T-D} = 621$ (494; 825) arb. Units, $R_{q-D} = 856$ (595; 1154) arb. units). Data are represented as Me (L-Q; UQ). * $p < 0.05$ in comparison with discocyte sample, Mann-Whitney U test E_T/E_{T-D} is relative elastic modulus obtained with respect to median elastic modulus of discocyte sample. Median Young's modulus of discocyte sample is $E_{T-D} = 108.3$ (87.1; 128.5) MPa (Indentation depth is 10 nm). Data are represented as Me (L-Q; UQ). * $p < 0.001$ in comparison with discocyte sample, Mann-Whitney U test

cytoskeleton under mechanical stress is removed with the consequent fusion of the membrane and condensation of the actin-spectrin network. A relatively high percentage of fine-mesh structure and homogeneity in the spherocyte cytoskeleton in hereditary spherocytosis leads to an increase in the parameters of both elastic properties and friction forces.

Secondary, in the discocyte-echinocyte transformation, the structure of the membrane skeleton does not change so dramatically as in the case of discocyte-spherocyte transformation. The average distances between the local contacts of the cytoskeleton and membrane in echinocytes in hereditary spherocytosis can be grouped into three classes ($\alpha_1 = 60$ nm, $\alpha_2 = 98$ nm, $\alpha_3 = 191$ nm) as in discocyte case but vary in the narrower range $\Delta A_{1/2} = 350$ nm. Moreover, lacunarity is reduced compared to the value for discocytes without a significant change in the value of the fractal dimension. These facts correspond to the structural transformation of the cell surface layer with the membrane skeleton in 3D space (the formation of protrusions on the cell surface). The projection of the membrane skeleton of the changed surface onto the plane is characterized by a denser network than in the case of abnormal discocytes, which leads to an increase in the parameters of both elastic properties and friction forces (Table 3.4). Therefore, the different changes of the cell surface layer, reorganization of the cytoskeleton structure, or the cell surface shape can result in a similar change in mechanical parameters such as the elastic modulus and friction force.

6 Conclusion

It is impossible to understand the pathogenesis of human diseases without a deep knowledge of the processes occurring in single cells. Among such important processes, it is worth mentioning the cell adhesion and cell response to the local (involving micro- and nanoscale areas of the cell surface) mechanical disturbance of the cell surface. This size of the mechanical impact on the cell surface can provide the probe of the atomic force microscope. Using the different AFM modes, it is possible to obtain simultaneously a set of information parameters of the mechanical properties of the cell surface layer of about microscale size in a lateral direction.

The AFM parameters characterizing the cell surface layer are numerous and dependent on AFM modes and theoretical models used for AFM data processing. The parameters include characteristics averaged over microscale surface area as well as parameters of the spatial distribution of cell nanomechanical properties. The set of the mentioned parameters determined by the structure and composition of the cell surface layer depends on the cell type, zone, and state. This set of mechanical parameters forms a so-called “physical-mechanical image” of the cell surface within its microscale area. The concept of the physical-mechanical image determines the position of the studied area of the cell surface in multi-dimensional space of mechanical parameters, which allows further classifying the cell type, state, and pathology.

7 Materials and Methods

Human blood samples of patients of the Republican Scientific Center for Radiation Medicine and Human Ecology (Gomel, Belarus) were obtained by venepuncture with patient permission under ethical consent, and anticoagulated with EDTA-K2. A few drops of human blood were injected into phosphate-buffered saline (pH 7.4) containing 1% glutaraldehyde, incubated for 15 minutes at 37 °C, washed once with Henk's solution, and twice with distilled water. Thin slides were cleaned and stored in 70% ethanol before specimen preparation. The drops of prepared erythrocyte suspension were placed on the slides (cell monolayer) and dried at room temperature (Starodubtseva et al. 2019). Samples of human primary skin fibroblasts, larynx carcinoma cells (HEp-2c cell line), and breast adenocarcinoma cells (MCF-7 cell line) were prepared in the Institute of Radiobiology (NAS of Belarus, Gomel, Belarus). The cell suspensions were placed on the specially prepared glass slides in Petri dishes with growth medium and incubated for 24 h at 37 °C and 5% CO₂. Then the cells were fixed with 0.5% glutaraldehyde (30 min) and washed with deionized water. The cells were dried in a tilted position (75–85%) in an air laminar stream (0.42 m/s) at room temperature (Starodubtseva et al. 2017b).

AFM was performed with atomic force microscope NT-206 (Microtestmachines Co., Belarus) and Bioscope Resolve (Bruker) in the air at room temperature. Using NT-206, topographic images and lateral force maps were recorded using NT-206 with CSC38 probes (level B, $k = 0.03$ N/m, MikroMasch, Bulgaria) with a scanning rate of 0.6–0.7 Hz. Lateral forces were assessed by measuring the cantilever's torsion value and represented in arbitrary units (maximal deviation of a laser beam for the AFM probe torsion detected with the 16-bit analog-to-digital converter of the measuring system was 65,535 arb. units). The following parameters were calculated: the median sliding friction force (F_f) and RMS roughness (standard deviation, R_q) of friction force maps. F_f was quantified as half of the difference of mean lateral forces sensed while scanning in two opposite directions over the area of $2.5 \mu\text{m} \times 2.5 \mu\text{m}$ (forward and backward scans) (Starodubtseva et al. 2012). R_q of friction force map was computed according to the algorithm of the statistical parameter estimation for indirect measurements using the values of R_q of two lateral force maps recorded in opposite directions over the area of $2.5 \mu\text{m} \times 2.5 \mu\text{m}$. The friction map of erythrocyte surface was recorded using Bioscope Resolve in contact mode with DPN-10 probe (level D, $k = 0.08$ N/m, Bruker). The elastic modulus (Young's modulus, E) was assessed by force spectroscopy (NT-206) using NSC11 probes (level A, $k = 3.0$ N/m MikroMasch, Bulgaria). The indentation depth for erythrocyte sample was 10 nm. For probing cancer epithelial cells and fibroblasts the blunted NSC11 probe (MikroMasch, $R = 76\text{--}81$ nm, $k = 3.0$ N/m) was used. The maps of Young's modulus and adhesion force for lymphocyte surface were recorded with Bioscope Resolve (PeakForce QNM Tapping mode, ScanAssist-Air probe, $k = 4$ N/m).

The AFM image with the size of $N \times N$ points was considered as a collection of N two-dimensional arrays (x, z) with N points in each. The discrete Fourier

transform was applied for each two-dimensional array (x, z). Using the sample spectra $F(\omega_k)F(\omega_k)$, the periodograms $R(\omega_k)$ represented the squared root from module of sample spectra were plotted. The periodogram $R(\omega_k)$ was smoothed using the Daniel window and the sample median of the spectral densities was calculated for each frequency ω_k (Starodubtseva et al. 2019). The sample median $R_m(\omega_k)$ of spectral densities was approximated by two or three Gaussian functions using OriginPro[®] 8.0 software. The parameters used in the work were the mean value of the spatial period (T_i) of selected Gaussian population and percentage (α_{T_i}) of the Gaussian population in the total Fourier spectrum, the averaged value of the spatial period (A), and the half-power width ($\Delta A_{1/2}$) of the total Fourier spectrum (Starodubtseva et al. 2019). Fractal dimension (D_F) was calculated for lateral force maps of the cell surface ($2.5 \mu\text{m} \times 2.5 \mu\text{m}$) using the box-counting algorithm (Starodubtseva et al. 2017a). In the modified box-counting algorithm, the digital image (256×256 pixels) was initially divided into 4 equal square fragments. After the calculation of D_F for each fragment, the D_F of the whole image was estimated. To analyze dependence D_F on the Z-scale factor, X- and Y-data of the digital image were not changed but Z-data was multiplied by factor t that was varied in a broad range (10^{-4} – 10^6). D_F was calculated using the box-counting algorithm for each t value and the dependence $D_F = f(t)$ was plotted and analyzed (Starodubtseva et al. 2017a). The curves have two maxima D_{F1} and D_{F2} . The first maximum (D_{F1}) (in the range of t -value from 0.002 to 0.400) was assumed as the fractal dimension of the map of the mechanical properties of the cell surface area of microscale size. The parameter of lacunarity (λ) was estimated as the squared ratio of the standard deviation to the mean for the lateral forces over the maps of $2.5 \mu\text{m} \times 2.5 \mu\text{m}$ size (Smith et al. 1996).

The goodness of fit for the experimental data to normal distribution was checked with the Shapiro-Wilk's W test. Results are presented either the mean and limits of 95% CI or the median and interquartile range (Me (LQ; UQ)). The sample parameters were compared using either Student's t -test or Mann-Whitney U -test for normally and non-normally distributed variables correspondingly.

Acknowledgements The author thanks I. Chelnokova, I. Starodubtsev, E. Mitsura, D. Petrenoyov, N. Shkliarava for their help in obtaining experimental materials, and Prof. Yegorenkov for comments and suggestions in discussing the present work.

Financial support from State Research Program "Nature Management and Ecology" (tasks 3.02, 2016–2020; Belarus) and State Research Program "Natural Resources and the Environment" (task 3.1.2, 2021–2025; Belarus) is gratefully acknowledged.

References

- Alaarg A, Schifferers RM, van Solinge WW, van Wijk R (2013) Red blood cell vesiculation in hereditary hemolytic anemia. *Front Physiol* 4:365
- Alcaraz J, Buscemi L, Grabulosa M, Trepas X, Fabry B, Farré R, Navajas D (2003) Microrheology of human lung epithelial cells measured by atomic force microscopy. *Biophys J* 84(3):2071–2079

- Allain C, Cloitre M (1991) Characterizing the lacunarity of random and deterministic fractal sets. *Phys Rev A* 44(6):3552–3558
- Arnal L, Longo G, Stupar P, Castez MF, Cattelan N, Salvarezza RC, Yantorno OM, Kasas S, Vela ME (2015) Localization of adhesins on the surface of a pathogenic bacterial envelope through atomic force microscopy. *Nanoscale* 7(41):17563–17572
- Balghonaim AS, Keller JM (1998) A maximum likelihood estimate for two-variable fractal surface. *IEEE Trans Image Process* 7:1746–1753
- Barthel E (2008) Adhesive elastic contacts – JKR and more. *J Phys D Appl Phys IOP Publ* 41:163001
- Bitler A, Dover R, Shai Y (2012) Fractal properties of macrophage membrane studied by AFM. *Micron* 43(12):1239–1245
- Bitler A, Dover RS, Shai Y (2018) Fractal properties of cell surface structures: a view from AFM. *Semin Cell Dev Biol* 73:64–70
- Blanchoin L, Boujemaa-Paterski R, Sykes C, Plastino J (2014) Actin dynamics, architecture, and mechanics in cell motility. *Physiol Rev* 94(1):235–263
- Caporizzo MA, Roco CM, Ferrer MC, Grady ME, Eckmann DM, Composto RJ (2015) Strain-rate dependence of elastic modulus reveals silver nanoparticle induced cytotoxicity. *Nanobiomedicine (Rij)* 2:9
- Cartagena-Rivera AX, Wang W-H, Geahlen RL, Raman A (2015) Fast, multi-frequency, and quantitative nanomechanical mapping of live cells using the atomic force microscope. *Sci Rep* 5:11692
- Coelho-Dos-Reis JG, Gomes OA, Bortolini DE, Martins ML, Almeida MR, Martins CS, Carvalho LD, Souza JG, Vilela JM, Andrade MS, Barbosa-Stancioli EF (2011) Evaluation of the effects of Quercetin and Kaempferol on the surface of MT-2 cells visualized by atomic force microscopy. *J Virol Methods* 174(1–2):47–52
- Darling EM, Zauscher S, Block JA, Guilak F (2007) A thin-layer model for viscoelastic, stress-relaxation testing of cells using atomic force microscopy: do cell properties reflect metastatic potential? *Biophys J* 92:1784–1791
- Dean D, Hemmer J, Vertegel A, Laberge M (2010) Frictional behavior of individual vascular smooth muscle cells assessed by lateral force microscopy. *Materials (Basel)* 3(9):4668–4680
- Deuticke B (2003) Membrane lipids and proteins as a basis of red cell shape and its alterations. In: Bernhardt I, Ellory JC (eds) *Red cell membrane transport in health and disease*. Springer, Berlin, pp 27–60
- Ding Yu XG-K, Wang G-F (2017) On the determination of elastic moduli of cells by AFM based indentation. *Sci Rep* 7:45575
- Dokukin M, Sokolov I (2015) High-resolution high-speed dynamic mechanical spectroscopy of cells and other soft materials with the help of atomic force microscopy. *Sci Rep* 5:12630
- Efremov YM, Velay-Lizancos M, Weaver CJ, Athamneh AI, Zavattieri PD, Suter DM, Raman A (2019a) Anisotropy vs isotropy in living cell indentation with AFM. *Sci Rep* 9(1):5757
- Efremov YM, Shpichka AI, Kotova SL, Timashev PS (2019b) Viscoelastic mapping of cells based on fast force volume and PeakForce tapping. *Soft Matter* 15(27):5455–5463
- Falconer K (1997) *Techniques in fractal geometry*. Wiley, Chichester. 256 pp
- Girasole M, Cricenti A, Generosi R, Longo G, Pompeo G, Cotesta S, Congiu-Castellano A (2007) Different membrane modifications revealed by atomic force/lateral force microscopy after doping of human pancreatic cells with Cd, Zn, or Pb. *Microsc Res Tech* 70(10):912–917
- Grady ME, Composto RJ, Eckmann DM (2016) Cell elasticity with altered cytoskeletal architectures across multiple cell types. *J Mech Behav Biomed Mater* 61:197–207
- Hecht FM, Rheinlaender J, Schierbaum N, Goldmann WH, Fabry B, Schäffer TE (2015) Imaging viscoelastic properties of live cells by AFM: power-law rheology on the nanoscale. *Soft Matter* 11(23):4584–4591
- Kozlova EK, Chernysh AM, Moroz VV, Kuzovlev AN (2013) Analysis of nanostructure of red blood cells membranes by space Fourier transform of AFM images. *Micron* 44:218–227
- Lekka M (2016) Discrimination between normal and cancerous cells using AFM. *BioNanoScience* 6:65–80

- Lekka M, Pabijan J (2019) Measuring elastic properties of single cancer cells by AFM. *Methods Mol Biol* 1886:315–324
- Letort G, Ennomani H, Gressin L, Théry M, Blanchoin L (2015) Dynamic reorganization of the actin cytoskeleton. *F1000 Res* 4: pii: F1000 Faculty Rev-940
- Li J, Dub Q, Sun C (2009) An improved box-counting method for image fractal dimension estimation. *Pattern Recogn* 42:2460–2469
- Ling EJ, Servio P, Kietzig AM (2016) Fractal and lacunarity analyses: quantitative characterization of hierarchical surface topographies. *Microsc Microanal* 22(1):168–177
- Lux SE 4th (2016) Anatomy of the red cell membrane skeleton: unanswered questions. *Blood* 127(2):187–199
- Nagao E, Dvorak JA (1999) Phase imaging by atomic force microscopy: analysis of living homoiothermic vertebrate cells. *Biophys J* 76(6):3289–3297
- Nans A, Mohandas N, Stokes DL (2011) Native ultrastructure of the red cell cytoskeleton by cryo-electron tomography. *Biophys J* 101(10):2341–2350
- Nikitina IA, Starodubtseva MN, Grishchuk AI (2012) Surface architectonics and the state of the cytoskeleton in thymocytes exposed to peroxynitrite from rats of different ages. *Adv Gerontol* 2(1):45–50
- Pan L, Yan R, Li W, Xu K (2018) Super-resolution microscopy reveals the native ultrastructure of the erythrocyte cytoskeleton. *Cell Rep* 22(5):1151–1158
- Perrotta S, Gallagher PG, Mohandas N (2008) Hereditary spherocytosis. *Lancet* 372(9647):1411–1426
- Renault L, Deville C, van Heijenoort C (2013) Structural features and interfacial properties of WH2, β -thymosin domains and other intrinsically disordered domains in the regulation of actin cytoskeleton dynamics. *Cytoskeleton (Hoboken)* 70(11):686–705
- Rother J, Nöding H, Mey I, Janshoff A (2014) Atomic force microscopy-based microrheology reveals significant differences in the viscoelastic response between malign and benign cell lines. *Open Biol* 4:140046
- Schillers H, Rianna C, Schäpe J, Luque T, Doschke H, Wälte M, Uriarte JJ, Campillo N, Michanetzi GPA, Bobrowska J, Dumitru A, Herruzo ET, Bovio S, Parot P, Galluzzi M, Podestà A, Puricelli L, Scheuring S, Missirlis Y, Garcia R, Odorico M, Teulon JM, Lafont F, Lekka M, Rico F, Rigato A, Pellequer JL, Oberleithner H, Navajas D, Radmacher M (2017) Standardized nanomechanical atomic force microscopy procedure (SNAP) for measuring soft and biological samples. *Sci Rep* 7(1):5117
- Sicard D, Fredenburgh LE, Tschumperlin DJ (2017) Measured pulmonary arterial tissue stiffness is highly sensitive to AFM indenter dimensions. *J Mech Behav Biomed Mater* 74:118–127
- Smith TG, Lange GD, Marks WB (1996) Fractal methods and results in cellular morphology – dimensions, lacunarity and multifractals. *J Neurosci Methods* 69(2):123–136
- Spodarev E, Straka P, Winter S (2015) Estimation of fractal dimension and fractal curvatures from digital images. *Chaos Solitons Fract* 75:134–152
- Starodubtseva M, Chizhik S, Yegorenkov N, Nikitina I, Drozd E (2010) Study of the mechanical properties of single cells as biocomposites by atomic force microscopy. In: *Microscopy: science, technology, applications and education Badajoz*. Formatex Research Center, Badajoz, pp 740–747
- Starodubtseva MN, Yegorenkov NI, Nikitina IA (2012) Thermo-mechanical properties of the cell surface assessed by atomic force microscopy. *Micron* 43(12):1232–1238
- Starodubtseva MN, Starodubtsev IE, Starodubtsev EG (2017a) Novel fractal characteristic of atomic force microscopy images. *Micron* 96:96–102
- Starodubtseva MN, Starodubtsev IE, Yegorenkov NI, Kuzhel NS, Konstantinova EE, Chizhik SA (2017b) Physical-mechanical image of the cell surface on the base of AFM data in contact mode. *IOP Conf Ser Mater Sci Eng* 256:012016
- Starodubtseva MN, Mitsura EF, Starodubtsev IE, Chelnokova IA, Yegorenkov NI, Volkova LI, Kharin YS (2019) Nano- and microscale mechanical properties of erythrocytes in hereditary spherocytosis. *J Biomech* 83:1–8

- Sunnerberg JP, Moore P, Spedden E, Kaplan DL, Staii C (2019) Variations of elastic modulus and cell volume with temperature for cortical neurons. *Langmuir* 35(33):10965–10976
- Sztojánov I, Crisan DA, Mina CP, Voinea V (2009) Image processing in biology based on the fractal analysis. In: Chen YuSh (Ed) *Image Processing InTech*, p 323–344
- Takahashi R, Okajima T (2015) Mapping power-law rheology of living cells using multi-frequency force modulation atomic force microscopy. *Appl Phys Lett* 107:173702
- Țălu Ș, Stach S, Sueiras V, Ziebarth NM (2015) Fractal analysis of AFM images of the surface of Bowman's membrane of the human cornea. *Ann Biomed Eng* 43(4):906–916
- Thomas G, Burnham NA, Camesano TA, Wen Q (2013) Measuring the mechanical properties of living cells using atomic force microscopy. *J Vis Exp* 76:50497
- Tian M, Li Y, Liu W, Jin L, Jiang X, Wang X, Ding Z, Peng Y, Zhou J, Fan J, Cao Y, Wang W, Shi Y (2015) The nanomechanical signature of liver cancer tissues and its molecular origin. *Nanoscale* 7(30):12998–13010
- Ungai-Salánki R, Peter B, Gerecsei T, Orgovan N, Horvath R, Szabó B (2019) A practical review on the measurement tools for cellular adhesion force. *Adv Colloid Interf Sci* 269:309–333
- Whited AM, Park PS (2014) Atomic force microscopy: a multifaceted tool to study membrane proteins and their interactions with ligands. *Biochim Biophys Acta*, 1 Pt A 1838:56–68
- Wu PH, Aroush DR, Asnacios A, Chen WC, Dokukin ME, Doss BL, Durand-Smet P, Ekpenyong A, Guck J, Guz NV, Janmey PA, Lee JSH, Moore NM, Ott A, Poh YC, Ros R, Sander M, Sokolov I, Staunton JR, Wang N, Whyte G, Wirtz D (2018) A comparison of methods to assess cell mechanical properties. *Nat Methods* 15(7):491–498
- Xu Y, Moseley JB, Sagot I, Poy F, Pellman D, Goode BL, Eck MJ (2004) Crystal structures of a formin homology-2 domain reveal a tethered dimer architecture. *Cell* 116(5):711–723
- Zemła J, Danilkiewicz J, Orzechowska B, Pabijan J, Seweryn S, Lekka M (2018) Atomic force microscopy as a tool for assessing the cellular elasticity and adhesiveness to identify cancer cells and tissues. *Semin Cell Dev Biol* 73:115–124

Chapter 4

Capillary Adhesion Effect in Contact Interaction of Soft Materials



I. G. Goryacheva and Yu. Yu. Makhovskaya

Abstract A model of capillary adhesion between an elastic half-space and an axisymmetric asperity or a periodic system of asperities is presented. The model is based on the contact problem solution for an indenter, whose shape is described by the power law function, in contact with an elastic half-space in the presence of an additional load (Laplace capillary pressure) outside the contact region. The volume of fluid in each meniscus is assumed constant during loading and unloading processes. Methods of calculation of the contact characteristics such as contact and capillary pressures, contact area, and load-distance dependencies are developed. The results obtained are used to analyze the effects of fluid volume in a meniscus, surface tension of fluid, elastic properties of the half-space, shape of an asperity, and mutual influence of neighbor asperities on the contact characteristics. The load-distance dependencies for an asperity and a half-space are shown to have hysteresis, and the corresponding energy dissipation in an approach-retraction cycle is calculated and analyzed depending on the fluid volume, its surface tension, elastic properties of contacting bodies, and shape of the asperity.

Keywords Capillary adhesion · Liquid bridges · Multiple contact · Adhesion hysteresis

1 Introduction

The classical contact problem formulation assumes compressive stress in the contact region and zero stresses outside this region. However, the surface energy of interacting bodies and of liquid films covering these bodies can cause tensile stresses both in and outside contact regions, in particular, as a result of capillary adhesion associated with microscopic liquid bridges (Israelachvili 1992). Usually

I. G. Goryacheva (✉) · Y. Y. Makhovskaya
Ishlinsky Institute for Problems in Mechanics of RAS, Moscow, Russia
e-mail: goryache@ipmnet.ru

© Springer Nature Switzerland AG 2022
F. M. Borodich, X. Jin (eds.), *Contact Problems for Soft, Biological and Bioinspired Materials*, Biologically-Inspired Systems 15,
https://doi.org/10.1007/978-3-030-85175-0_4

most surfaces are covered with thin liquid films condensed from the atmosphere, so the capillary adhesion is quite common. Forces of capillary adhesion attain significant values even for relatively hard materials, e.g., at a magnetic head-disk interface (Liu and Mee 1983; Tian and Matsudaira 1992), they also can considerably influence the interaction of an AFM probe with a sample (Thundat et al. 1993; Rozhok et al. 2004). For soft materials interfaces in biological and bio-inspired systems, capillary adhesion plays a particularly significant part (Huber et al. 2005; Creton and Gorb 2007; Barnes 2012).

Most of the models of elastic adhesive contact, which are available in the literature, relate to Van der Waals intermolecular interaction of dry surfaces. The classical JKR model (Johnson et al. 1971) takes into account the influence of adhesion on the contact stress distribution but it assumes zero stress outside the contact region. Other classical model – the DMT (Derjaguin et al. 1975) model – considers adhesion attraction forces outside the contact region but neglects their effect on the contact stress distribution. The JKR model was generalized to the case where the body shape is described by a power law function (Borodich et al. 2014a), to the case of anisotropic bodies (Borodich et al. 2014b), and thin elastic layer (Argatov et al. 2016; Borodich et al. 2019). An approximate model for the elliptic contact is suggested based on the JKR model (Johnson and Greenwood 2005). The indentation of a cone into an elastic half-space is modeled in (Borodich et al. 2012).

To consider the adhesive contact problem in more accurate formulation taking into account adhesion forces acting outside the contact region and their effect on the stress-strain state, models are developed in which the adhesion pressure is approximated by various functions of the gap between surfaces. In particular, models are suggested in which the adhesion pressure is a constant (the Maugis-Dugdale model (Maugis 1991)), as well as linear and exponential functions of the gap (Barthel 1998). A solution to adhesive contact problem for elastic spheres was obtained as a sum of two Hertzian solutions (Greenwood and Johnson 1998). The Maugis-Dugdale model was generalized to the case of a body whose shape is described by a power law function of an even degree (Goryacheva and Makhovskaya 2001). Based on this result, the solution for a piecewise approximation of the adhesion potential of an arbitrary form is constructed (Goryacheva and Makhovskaya 2004, 2008; Makhovskaya 2016). In (Zheng and Yu 2007; Zhou et al. 2011) the Maugis-Dugdale model is extended to include the case of an elastic half-space in contact with an axisymmetric punch whose shape is described by a power law of arbitrary degree. At the same time, methods are being developed to numerically solve the integral equation of the contact problem for a prescribed form of the adhesion potential (Muller et al. 1980; Attard and Parker 1992; Greenwood 1997; Feng 2001; Soldatenkov 2012, 2019).

The capillary adhesion occurs as a result of the action of capillary forces in menisci of liquid which pull two surfaces together. Capillary forces are defined by the shape of the gap between the surfaces, surface tension of the liquid, and wettability of the surfaces. Thus, specific models should be developed to describe a capillary adhesive contact. Most of the available models consider rigid bodies (Israelachvili 1992; Mattewson and Mamin 1988; Rabinovich et al. 2005; Megias-

Alguacil and Gauckler 2009). Analytic solutions for the capillary adhesion in contact between an elastic half-space and an axisymmetric rigid body are proposed in (Maugis and Gauthier-Manuel 1994; Goryacheva and Makhovskaya 1999; Makhovskaya and Goryacheva 1999). Also, numerical solution of problems on the interaction of elastic bodies in the presence of a liquid meniscus are constructed (see, for example, (Butt et al. 2010; Zakerin et al. 2013)).

In the present chapter, the model is presented to describe the effect of capillary adhesion on the contact characteristics when axisymmetric elastic bodies are approached and separated under normal loading. The model is based on the contact problem solution which takes into account adhesion forces by introducing additional negative pressure outside the contact region, the mutual influence of the adhesion pressure, which depends on the gap, and the contact stress and strain being taken into consideration (Goryacheva and Makhovskaya 1999; Makhovskaya and Goryacheva 1999). It allows one to analyze the influence of shapes of the contacting bodies and amount of liquid in the meniscus on the contact characteristics. It also takes into account no-contact regime of interaction where the surfaces are separated by a liquid bridge. Apart from this, the method suggested makes it possible to calculate the energy dissipation in an approach-retraction cycle and to analyze adhesion in discrete contact of elastic bodies with regular surface relief.

2 Capillary Adhesion in Contact of Smooth Elastic Bodies

Consider a rigid axisymmetric punch interacting with an elastic half-space in the presence of a liquid bridge forming a meniscus. The shape of the punch is described by the power law $f(r) = Ar^{2n}$ where n is an integer. The punch is loaded by the external force q (Fig. 4.1). It is assumed friction is absent between the punch and half-space. Since the punch has axial symmetry and the external force is normal to the half-space surface, its normal elastic displacement u and the contact pressure p at $z = 0$ are functions of only the radial coordinate r .

The gap $h(r)$ between the two surfaces is defined by the relation

$$h(r) = f(r) + u(r) + d \quad (4.1)$$

where d is the distance between the punch top and the undisturbed surface of the elastic half-space. If $h(0) > 0$, the surfaces of the punch and half-space are separated by the meniscus and are not in contact (Fig. 4.1a). If $h(0) = 0$, the surfaces are in contact over the region $\Omega_c = \{r \leq a\}$ (Fig. 4.1b) including the point contact at $a = 0$. In this case, the liquid occupies the domain

$$\Omega_m = \begin{cases} 0 \leq r \leq b, h(0) > 0 \\ a < r \leq b, h(0) = 0 \end{cases}$$

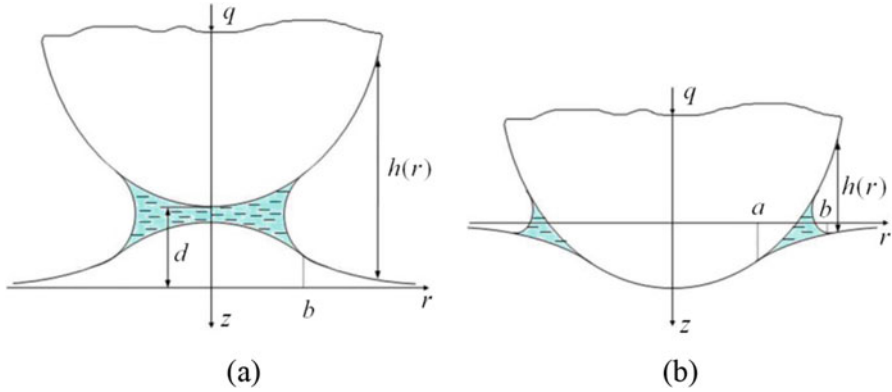


Fig. 4.1 Scheme of interaction between the punch and elastic half-space in the presence of a liquid meniscus

The pressure in the meniscus is lower than the atmospheric pressure by the value p_0 defined by the Laplace formula [4.1]

$$p_0 = \gamma_0 \left(\frac{1}{R_1} + \frac{1}{R_2} \right) \quad (4.2)$$

where γ_0 is the surface tension of the liquid and R_1, R_2 are the curvature radii of the meniscus in two mutually orthogonal directions. These radii are defined by the geometry of the interacting surfaces and wetting angles θ_1, θ_2 of them.

The force of capillary attraction between the punch and half-space has two components (Israelachvili 1992). The first one is the force associated with the surface tension of the liquid film at $r = b$

$$F_s = 2\pi b\gamma_0 (\cos \theta_1 + \cos \theta_2) \quad (4.3)$$

The second force is caused by the pressure (4.2) acting in the ring $a \leq r \leq b$ occupied by the meniscus

$$F_L = \pi (b^2 - a^2) p_0 \quad (4.4)$$

It is assumed that the wetting angles θ_1, θ_2 are zero and the shape of the punch satisfies the condition $f'(b) \ll 1$, then the curvature radii of the meniscus are expressed as

$$R_1 \approx \frac{h(b)}{2}, \quad R_2 \approx b$$

It is also assumed that $h(b) \ll b$. As a result, from the Laplace formula (4.1) it follows that

$$p_0 = \frac{2\gamma_0}{h(b)} \quad (4.5)$$

Since the wetting angles are zero, the force of surface tension of the liquid film (4.3) takes the form $F_s = -4\pi b\gamma_0$. This force is tangential to the boundary of the elastic half-space. The simple estimate shows that this force is much smaller than the Laplace force F_L . Indeed, if the surfaces are separated by the meniscus ($h(0) > 0$), we have $F_L = -\pi b^2 p_0$, from which it follows that

$$\frac{F_s}{F_L} = \frac{h(b)}{b} \ll 1$$

If the surfaces are in contact ($h(0) = 0$), we have $F_L = -\pi(b^2 - a^2)p_0$ and then

$$\frac{F_s}{F_L} = \frac{bh(b)}{b^2 - a^2} \approx f'(b) \ll 1.$$

In what follows, we will neglect the force F_s . By assuming the atmospheric pressure to be zero, we obtain the following condition for the contact pressure $p(r)$ in the region of meniscus

$$p(r) = -p_0, \quad r \in \Omega_f \quad (4.6)$$

and the condition for the contact region

$$h(r) = 0, \quad r \in \Omega_c \quad (4.7)$$

Since we consider the contact of two smooth bodies, and the contact region is much smaller than their curvature, the relationship between the surface displacement and contact pressure can be taken in the form (Johnson 1985).

$$u(r) = \frac{4}{E^*} \int_0^b p(r') \mathbf{K} \left(\frac{2\sqrt{rr'}}{r+r'} \right) \frac{r' dr'}{r+r'} \quad (4.8)$$

where $\mathbf{K}(x)$ is the full elliptic integral of the first kind, $E^* = \pi E/(1 - \nu^2)$, E and ν are the Young modulus and Poisson's ratio of the elastic half-space, respectively. The external force q satisfies the equilibrium condition

$$q = 2\pi \int_0^b r p(r) dr \quad (4.9)$$

To close the system of equations, we need one more condition specifying the capillary pressure p_0 . This condition can differ depending on the specifics of contact.

Constant Capillary Pressure For liquid bridges formed due to capillary condensation and staying in thermodynamic equilibrium with the surrounding wet atmosphere, the capillary pressure is constant and defined by the Kelvin Eq. (4.1)

$$p_0 = -\frac{RT}{V_m} \ln H \quad (4.10)$$

where T is the absolute temperature, R is the gas constant, V_m is the molar volume of the liquid, H is the relative humidity of the surrounding air. For this case, the solution of contact problem with capillary adhesion was obtained in (Israelachvili 1992) for rigid bodies and in (Maugis and Gauthier-Manuel 1994) for a spherical punch and elastic half-space.

Constant Volume of Fluid This is the case when the punch motion is quick enough so that the meniscus is not in equilibrium with the surrounding atmosphere. It is also the case when the liquid bridge is not the result of capillary condensation but is inserted into the gap, e.g., in biological systems. The volume of the liquid v is related to the geometry of the gap as

$$v = \iint_{\Omega_f} rh(r) dr d\varphi \quad (4.11)$$

The solution of contact problem in this case is more complicated since the capillary pressure is a priori unknown. For rigid bodies, the solution with constant volume of fluid in the meniscus was constructed in (Mattewson and Mamin 1988; Rabinovich et al. 2005; Megias-Alguacil and Gauckler 2009). For the elastic half-space, the solution was obtained in (Goryacheva and Makhovskaya 1999; Makhovskaya and Goryacheva 1999). In the present section, the method of solution and the results will be presented for this case.

3 Method of Solution

The method of solution is given in detail in (Goryacheva and Makhovskaya 1999; Makhovskaya and Goryacheva 1999). We introduce the dimensionless quantities

$$\begin{aligned} \rho &= \frac{r}{D}, & P &= \frac{p}{E^*}, & Q &= \frac{q}{E^*D^2}, \\ U &= \frac{u}{D}, & \delta &= \frac{d}{D}, & \beta &= \frac{b}{D}, & V &= \frac{v}{D^3}, & K &= \frac{\gamma_0}{E^*D} \end{aligned} \quad (4.12)$$

where $D = A^{-1/(2n-1)}$ is the characteristic size of the punch.

The Surfaces Separated by the Meniscus ($h(0) > 0$) In this case, the problem solution is given by the relations

$$Q = -\pi\beta^2 P_0 \quad (4.13)$$

$$P_0 = \frac{3}{8\beta} \left(\sqrt{\kappa^2 + \frac{32}{3}\beta K} - \kappa \right) \quad (4.14)$$

$$\delta = \frac{16}{3} P_0 \beta - \beta^{2n} + \kappa \quad (4.15)$$

$$U(\rho) = -4P_0 \begin{cases} \beta \mathbf{E}\left(\frac{\rho}{\beta}\right), & \rho \leq \beta \\ \rho \left[\mathbf{E}\left(\frac{\beta}{\rho}\right) - \left(1 - \left(\frac{\beta}{\rho}\right)^2\right) \mathbf{K}\left(\frac{\beta}{\rho}\right) \right], & \rho > \beta \end{cases} \quad (4.16)$$

where

$$\kappa = \frac{n\beta^{2n}}{n+1} + \frac{V}{\pi\beta^2}.$$

By substituting the expression for P_0 (4.14) into (4.15), we obtain the algebraic equation to be solved numerically to determine the dimensionless radius β of the meniscus. After this, the unknown function of vertical displacement $U(\rho)$ and quantities P_0 and δ are determined from Eqs. (4.16), (4.14) and (4.15), respectively.

Contact of the Surfaces ($h(0) = 0$) By using the dimensionless quantities (4.12) and the parameter

$$c = a/b \quad (4.17)$$

which is the ratio of the radii of contact and meniscus, the solution to the contact problem can be represented as follows. The capillary pressure is defined by the relation

$$P_0 = \frac{B_2 - \sqrt{B_2^2 - 4B_1 K}}{2B_1} \quad (4.18)$$

where

$$\begin{aligned}
 B_1 &= 2\beta \left\{ 1 - c - \sqrt{1 - c^2} \arccos c \right\} \\
 B_2 &= \frac{\beta^{2n}}{\pi} \left\{ \left(1 - \frac{(2n)!!}{(2n-1)!!} c^{2n} \right) \arccos c + \sqrt{1 - c^2} \sum_{k=1}^n \frac{(2k-2)!!}{(2k-1)!!} c^{2k-1} \right\}
 \end{aligned}$$

The volume of meniscus is defined by

$$\begin{aligned}
 V &= 2\beta^{2n+2} \left\{ \sqrt{1 - c^2} \left(\frac{(2n)!!(2n-1)!!}{(2n+1)!!} c^{2n+2} + \sum_{k=0}^n \frac{(2k)!!}{(2k+1)!!} \frac{c^{2k+1}}{n+1} \right) - \right. \\
 &\quad \left. - \left[\frac{(2n)!!}{(2n-1)!!} c^{2n} - \frac{1}{n+1} \right] \arccos c \right\} - \\
 &\quad - \frac{4\pi}{3} P_0 \beta^3 \left[4 - 3c - c^3 - 3\sqrt{1 - c^2} \arccos c \right]
 \end{aligned} \tag{4.19}$$

By substituting (4.18) into (4.19), we obtain the equation with unknowns β and c . This equation was solved numerically for β with prescribed c , then according to (4.18) the dimensionless liquid pressure P_0 was determined. The remaining characteristics of the problem were calculated from the following relations

$$\begin{aligned}
 P(\rho) &= \frac{(\beta c)^{2n-1}}{\pi^2} \left[\frac{(2n)!!}{(2n-1)!!} \right]^2 \sqrt{1 - \rho^2} \sum_{k=1}^n \frac{(2k-3)!!}{(2k-2)!!} \rho^{2(n-k)} - \\
 &\quad - P_0 \left(1 - \frac{2}{\pi} \arctan c \sqrt{\frac{1 - \rho^2}{1 - c^2}} \right), \quad \rho \leq 1
 \end{aligned} \tag{4.20}$$

$$\begin{aligned}
 U(r) &= -\frac{2}{\pi} \left((\rho\beta c)^{2n} + \delta \right) \arcsin \frac{1}{\rho} + \frac{2(\beta\rho)^{2n}}{\pi} \sqrt{\rho^2 - 1} \sum_{k=1}^n \frac{(2k-2)!!}{(2k-1)!!} \rho^{2(n-k)} - \\
 &\quad - \begin{cases} 4 \left(P_0 \beta \left\{ \mathbf{E}(c\rho) - \mathbf{E}\left(\arcsin \frac{1}{\rho}, c\rho\right) \right\} \right), & 1 < \rho \leq \frac{1}{c} \\ 4P_0\beta c \left\{ \mathbf{E}\left(\frac{1}{\rho c}\right) - \mathbf{E}\left(\arcsin c, \frac{1}{\rho c}\right) - \right. \\ \left. - \left[1 - \left(\frac{1}{\rho c}\right)^2 \right] \left[\mathbf{K}\left(\frac{1}{\rho c}\right) - \mathbf{F}\left(\arcsin c, \frac{1}{\rho c}\right) \right] \right\}, & \rho > \frac{1}{c} \end{cases}
 \end{aligned} \tag{4.21}$$

$$\delta = -\frac{(2n)!!}{(2n-1)!!} (\beta c)^{2n} + 2\pi P_0 \beta \sqrt{1 - c^2} \tag{4.22}$$

$$Q = \frac{(2n)!!}{(2n+1)!!} \frac{4n(\beta c)^{2n+1}}{\pi} - 2P_0\beta^2 \left(\arccos c + c\sqrt{1 - c^2} \right) \tag{4.23}$$

The latter relationship serves for the determination of the load Q corresponding to a chosen value of c . If the value of the load Q is prescribed, the unknown values β and c can be determined based on the solution of Eqs. (4.19) and (4.23). Note that

the case $c = 0$ corresponds to the point contact area. By assuming $c = 0$ in Eqs. (4.18) and (4.19), we obtain Eqs. (4.14) and (4.15), respectively.

4 Contact Characteristics as Functions of Normal Load

Figure 4.2 depicts the distributions of contact pressure $P(\rho)$ and elastic displacement $-U(\rho)$ for various normal load $-Q = 4.05 \cdot 10^{-5}$ (curves 1), $Q = -1.35 \cdot 10^{-5}$ (curves 2), $Q = -4.74 \cdot 10^{-5}$ (curves 3), and $Q = -5.23 \cdot 10^{-5}$ (curves 4). These results are calculated for $n = 1$, $K = 10^{-4}$ and $V = 10^{-4}$. Curves 1 and 2 correspond to the contact between the punch and half-space, curves 4 to the surfaces separated by the meniscus. Curves 3 (bold lines) are constructed for the case of the point contact.

The results presented in Fig. 4.2a indicate that as the load Q decreases, the contact pressure, the absolute value of the capillary pressure P_0 , and the contact area Ω_c decrease. Figure 4.2b illustrating the shape of the elastic half-space under various loads shows that the meniscus leads to a considerable distortion of the boundary of the elastic half-space. At the outer boundary $\rho = \beta$ of the meniscus region Ω_f , the derivative of the shape function of the elastic half-space boundary is discontinuous.

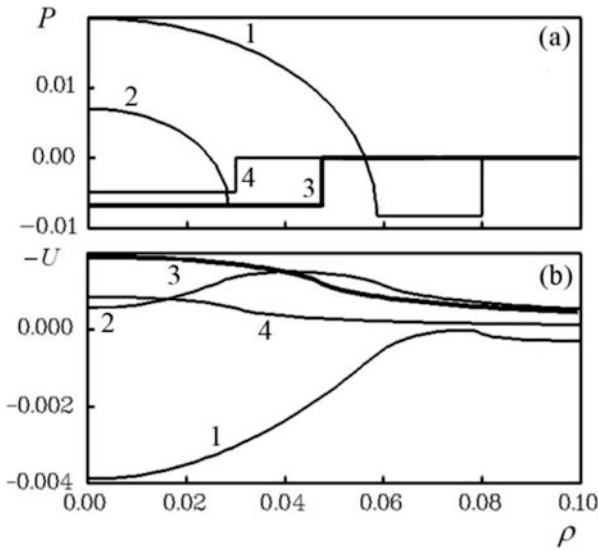


Fig. 4.2 Distributions of contact pressure (a) and displacement (b) for various loads

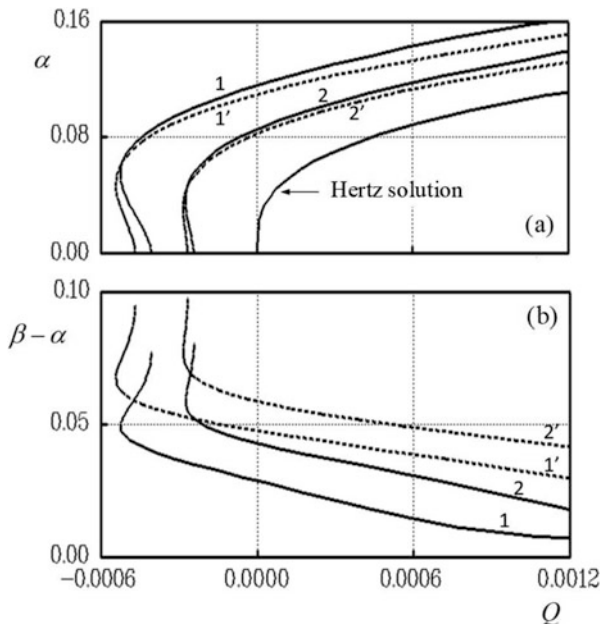


Fig. 4.3 Dependencies of the dimensionless contact radius (a) and meniscus width (b) on the dimensionless load

5 Effect of the Liquid Volume, its Surface Tension, and Elastic Modulus of the Half-Space

In Fig. 4.3, the plots of the contact radius α and meniscus width ($\beta - \alpha$) as a function of the load Q are presented for $n = 1$ and $K = 2 \times 10^{-4}$ (curves 1), $K = 10^{-4}$ (curves 2). The solid curves correspond to $V = 10^{-4}$, while the dashed ones to $V = 2 \times 10^{-4}$. The graphs show that the contact radius is nonzero at negative loads and exceeds the Hertzian contact radius at positive loads. This effect is more significant for larger K . Increasing the liquid volume leads to decrease of the contact area but increase in the area of meniscus.

The Laplace pressure in the meniscus P_0 and dimensionless load Q as functions of the distance δ between the surfaces are presented in Fig. 4.4a and b, respectively. Curves 1, 2 correspond to the dimensionless volume of the fluid $V = 10^{-5}$, curves 1', 2' to $V = 5 \cdot 10^{-5}$. Curves 1, 1' are constructed for $K = 4 \cdot 10^{-5}$, whereas curves 2, 2' for $K = 8 \cdot 10^{-5}$. Here and in what follows, thick parts of the curves correspond to the contact of the surfaces, while thin parts to the surfaces separated by the liquid bridge. An increase in the parameter K , which is associated with the decrease in the elastic modulus of the half-space or increase in the surface tension of the liquid, leads to an increase in the capillary pressure P_0 and the absolute value of the negative load Q at which the contact still exists. As the volume of the liquid V increases, the capillary pressure P_0 decreases sharply, specifically in the case of the contact between the surfaces.

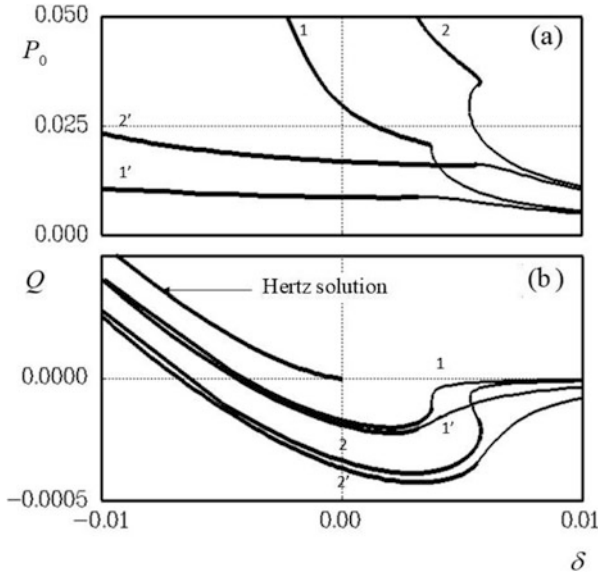


Fig. 4.4 Capillary pressure in the meniscus (a) and load (b) vs. distance between the bodies

The load Q as a function of the distance δ is ambiguous in a certain range of the parameters values (e.g., for small enough dimensionless value V in the meniscus). This implies that the loading and unloading paths do not coincide, which causes the energy dissipation in an approach-retraction cycle. The value of the energy dissipation considerably depends upon the elastic characteristics of the interacting bodies, curvature of their surfaces, as well as on the volume and surface tension of the liquid in the meniscus. The energy dissipation of the surfaces with a liquid bridge in an approach-retraction cycle will be analyzed in Sect. 7.

6 Effect of the Body Shape

Below the results are compared that were obtained for two shapes of the punch $-f(r) = Ar^2$ ($n = 1$, circular paraboloid) и $f(r) = Ar^4$ ($n = 2$). Dimensionless profiles of these punches $F(\rho) = \rho^{2n}$ are shown in Fig. 4.5a by curves 1 ($n = 1$) and 2 ($n = 2$).

Figure 4.5b represents the distributions of the dimensionless contact pressure for two different shapes of the punch $-n = 1$ (curve 1) and $n = 2$ (curve 2) at $Q = 0$, $K = 10^{-4}$, $V = 10^{-4}$. Curves 1', 2' are the pressure distributions at the same values of the parameters for the same contact radius α but for the case of no liquid.

The comparison of the distributions presented shows that for the same contact area, the contact pressure is lower in the presence of the meniscus, than in its absence. The shape of the punch significantly influences the pressure distribution, as well as the width of the meniscus. The results show that as the exponent n increases,

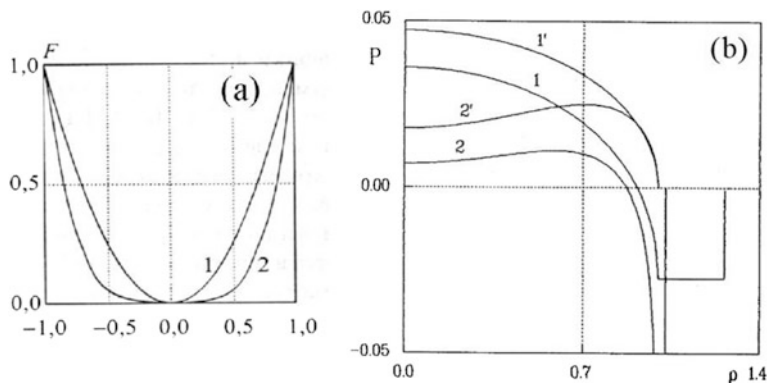


Fig. 4.5 Two different punch shapes (a) and the corresponding contact pressure distributions (b) ($P_0 = -2.05$ for curve 2)

the value of the Laplace pressure P_0 also increases while the width of the meniscus ring decreases. This is accounted for by decreasing in the value of gap $h(r)$ between the surfaces defined by (4.1).

7 Energy Dissipation in an Approach-Retraction Cycle

The analysis of the solution obtained shows nonmonotone and ambiguous dependence of the force on the distance between the bodies. Examples of such dependencies are presented in Fig. 4.6 which depict dimensionless load as a function of dimensionless distance for (b) and dimensionless volume of the meniscus $V = 0.5$. Curve 1 corresponds to the dimensionless surface tension of the liquid $K = 0.025$, curve 2 to $K = 0.05$. The results indicate the function of the load versus distance becomes ambiguous only starting from a certain value of the surface tension parameter K .

Let us consider curve 2 in Fig. 4.6. If the surfaces interact under controlled (monotonically decreasing) load Q then at the minimum load $Q_{pull-off}$ (point E) the surfaces separate with a jump. At a moment of jump they contact over a finite area.

If the surfaces interact under controlled (monotonically increasing) distance δ then they would jump from the point C to the point F. When moving in the opposite direction, i.e. monotonically decreasing the distance δ they would jump from the point A to the point B. Note that the points A and F always correspond to the surfaces separated by the meniscus, whereas the point B and C may correspond to both contact and separated surfaces. So, jump-like coming into contact and breaking of contact occurs. This process is illustrated in Fig. 4.7.

Fig. 4.6 Dimensionless load as a function of distance between the bodies

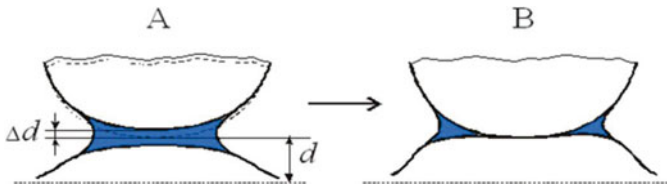
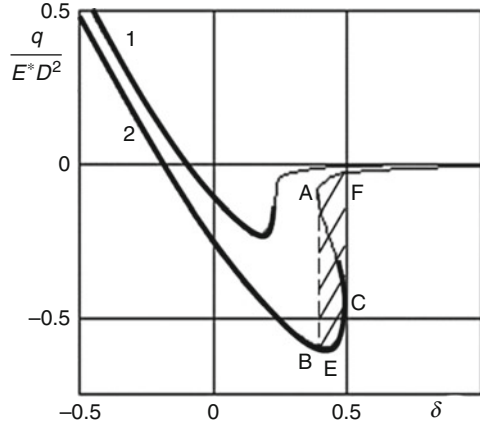


Fig. 4.7 Scheme of jump-like coming into contact

Note that jump-like coming into contact and breaking of the contact occurs without breaking the meniscus. The model assumptions presented in Sect. 2 impose limits on the meniscus geometry – its width must be much larger than its height. Thus, this model cannot be applied for the case of relatively large distances between the bodies and it cannot describe collapse of the meniscus as the bodies are moved apart.

The energy dissipation in an approach-retraction cycle is defined by the area of the dashed region in Fig. 4.6 and given by the relation

$$\Delta w = \int_{ABCF} q(\delta)d\delta \tag{4.24}$$

The value of this energy dissipation was calculated in (Goryacheva and Makhovskaya 2001, 2008) for the cases of both capillary and molecular adhesion. In Fig. 4.8, the dimensionless energy dissipation $\Delta w/(E^*D^3)$ is presented as a function of the dimensionless surface tension for various values of the volume of the meniscus. Solid lines correspond to $n = 1$, dashed line to $n = 2$. The analysis of the solution shows that the energy dissipation differs from zero starting from a certain value of the dimensionless surface tension and increases with increasing surface tension. The value of $\Delta w/(E^*D^3)$ is higher for smaller values of the meniscus volume.

Fig. 4.8 Dimensionless energy dissipation as a function of dimensionless surface tension of the liquid

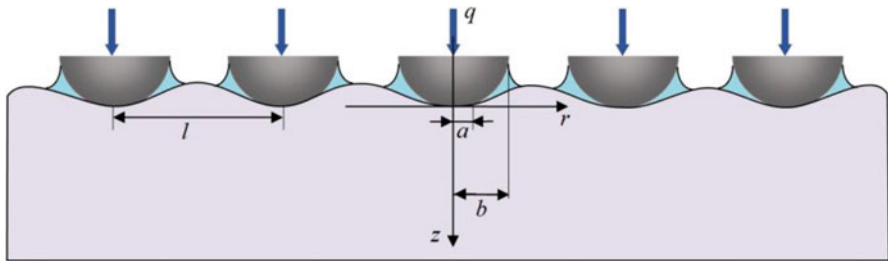
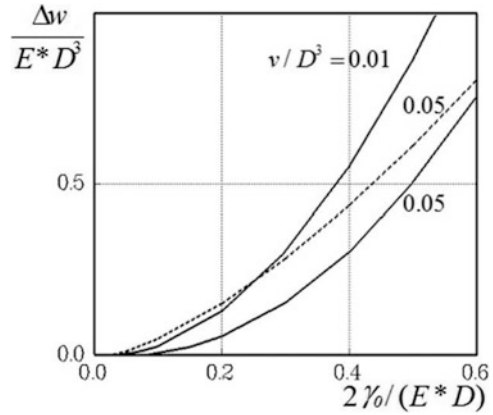


Fig. 4.9 Scheme of discrete contact in the presence of capillary adhesion

8 Capillary Adhesion in Discrete Contact

The approach applied above for the analysis of capillary adhesion in contact of smooth surfaces can be extended to analyze the capillary effect in discrete contact taking into account mutual influence of contact spots. For this purpose, periodic contact problems with capillary or molecular adhesion were considered in (Goryacheva and Makhovskaya 2008; Makhovskaya 2003). In what follows, we present main results for the case of capillary adhesion.

Consider an elastic half-space in contact with a periodic system of punches of the same shape described by the function $f(r) = Ar^{2n}$ located in the nodes of a hexagonal lattice with the step l (Fig. 4.9). Each punch is acted on by the normal force q .

Let the surface of the half space before the interaction is covered with a liquid film of thickness h_1 . It is assumed that under contact, all liquid is gathered into menisci around each contact spot, each meniscus having the same volume

$$v = \sqrt{3}l^2h_1/2 \tag{4.25}$$

The ring-shaped area $a < r \leq b$ around each contact area is occupied by liquid.

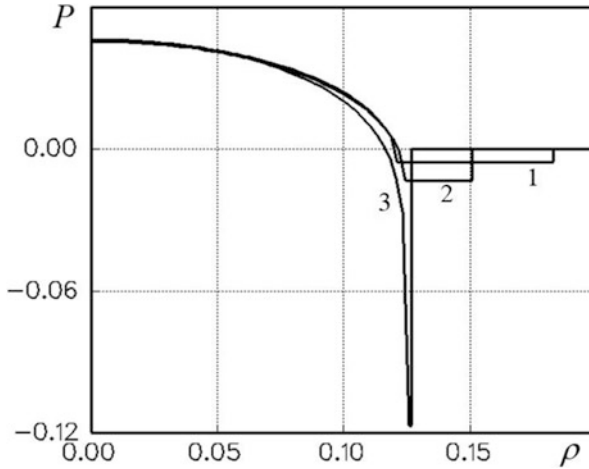


Fig. 4.10 Contact pressure distributions for various distances between the punches

The problem is solved by using the localization method (Goryacheva 1997) according to which to determine the stress-strain state near a contact spot we take into account accurate contact conditions only for the nearest spots, the action of the remaining contacts is approximated by a nominal pressure.

The solution is constructed in dimensionless form by using the dimensionless parameters given by (4.12) except for the dimensionless volume V . Instead of this parameter we use dimensionless thickness of the liquid film before the interaction H_1 and the dimensionless distance between the punches L . These new parameters are defined by

$$H_1 = h_1/D, \quad L = 3^{1/4}l/(\sqrt{2\pi}D) \quad (4.26)$$

In Fig. 4.10, the distributions of dimensionless contact pressure P under a punch are presented for $n = 1$, $K = 5 \times 10^{-5}$, $H_1 = 10^{-4}$, $Q = 10^{-13}$. Curves 1, 2, and 3 correspond to various dimensionless distances between the punches $L = 0.2$, $L = 0.5$, and $L = 1$, respectively. Since the thickness H_1 of the fluid originally covering the half-space is assumed constant, decreasing the distance between the punches leads to decreasing the amount of liquid in each meniscus which in turn leads to a significant increase in the capillary pressure and decrease in the meniscus width $\beta - \alpha$.

From Fig. 4.10, it can be also seen that the contact radius α is a nonmonotone function of the distance between the punches L . This effect is more apparent in Fig. 4.11a that shows α as a function of L . Curves 1 and 2 correspond to the same values of n , K , and Q as were used for the Fig. 4.10 and to various values of the liquid film thickness – $H_1 = 10^{-4}$ (curve 1) and $H_1 = 10^{-3}$ (curve 2). Curve 3 correspond

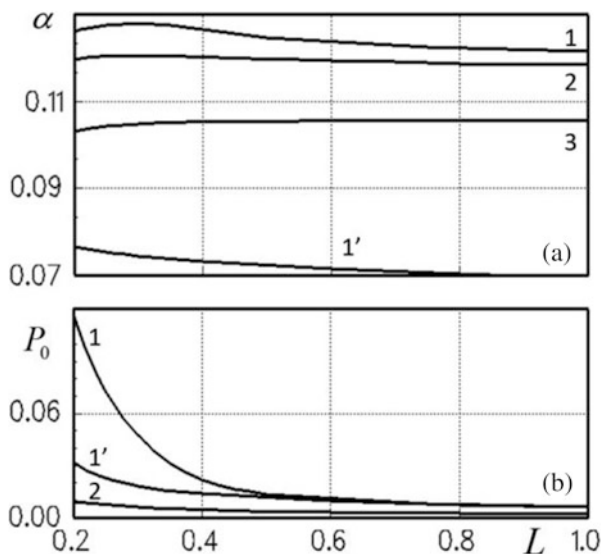


Fig. 4.11 Dimensionless contact radius (a) and absolute value of the Laplace pressure (b) as a function of distance between the punches

to no adhesion contact. Curve 1' is constructed for $H_1 = 10^{-4}$ and a negative load $Q = -10^{-4}$.

The character of the graphs presented in Fig. 4.11a can be explained by the effect of two mechanisms as the distance between the punches changes. The first one is the mutual influence of the punches through the elastic half space which occurs only for relatively small L . For $Q > 0$ this leads to decreasing the contact radius α as the distance L decreases. For $Q < 0$ the mutual influence leads to an increase in α as L decreases. The second mechanism is due to a constant prescribed thickness of the original liquid film H_1 due to which as the punches come closer to each other, the volume of each meniscus decreases. As a result of this, the contact radius α increases as the distance L decreases irrespective of the sign of the load Q . For $Q > 0$, these two mechanisms have opposite effects on the contact radius which accounts for the nonmonotonic character of curves 1 and 2 in Fig. 4.11a. For $Q < 0$ the two mechanisms amplify each other which results in a monotonic graph (curve 1').

Figure 4.11b depicts the dimensionless Laplace pressure P_0 as a function of the dimensionless distance L between the punches. Curves 1, 2, 1' are for the same values of the parameters as the corresponding curves in Fig. 4.11a. The results indicate that the capillary pressure P_0 always increases as the distance L decreases.

In Fig. 4.12, the dimensionless load Q acting per a punch is presented as a function of distance between the punch and the half-space for $n = 1$, $K = 5 \times 10^{-5}$, $H_1 = 10^{-5}$ and various distances between the punches $-L = 0.2, L = 0.4, L = 2$ (curves 1, 2, 3, respectively). Thick lines correspond to the contact, thin ones –

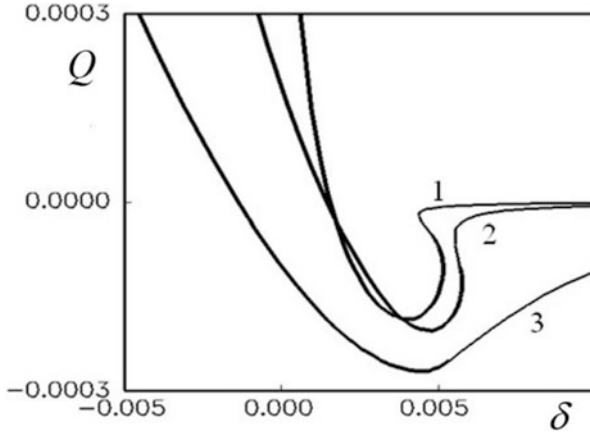


Fig. 4.12 Dimensionless load per one punch vs. distance between a punch and the elastic half space

to the surfaces separated by liquid bridges. The results indicate that as density of contact spots increases, the region of ambiguity of the curves becomes wider.

9 Conclusion

The models for studying the capillary adhesion effect in contact interaction of elastic bodies with contacting shapes described by the power functions are presented in this chapter. The methods of calculation of the contact characteristics such as contact and capillary pressures, contact size, load-approach dependencies and so on are developed.

Analysis of the results obtained allows us to distinguish the following major effects of capillary adhesion in contact interaction of elastic bodies:

- capillary adhesion leads to negative values of the contact pressure, increase in the contact area and existence of contact under a range of negative loads,
- as the volume of liquid decreases and its surface tension increases, the influence of the meniscus on the contact characteristics becomes more significant,
- effect of capillary adhesion is greater for more compliant bodies (with lower elastic modulus E^*) and for shape functions with greater exponent n ,
- a combined effect of elasticity and capillary adhesion is ambiguous character of the load-distance dependencies, i.e., adhesion hysteresis,
- the energy dissipation in an approach-retraction cycle increases as the surface tension of liquid increases and its volume decreases, and also as the elastic modulus decreases.

The approach to study the capillary adhesion effect in discrete contact is also developed. It is based on the solution of the periodic contact problem for the spherical asperities (punches) distributed in the nodes of a hexagonal lattice. The mutual influence of the asperities is taken into account based on the principle of localization. The following conclusions are made based on the calculations under the assumption of the constant volume of the fluid inside the meniscus:

- in the case of discrete contact, as the distance between asperities decreases, the radius of menisci also decreases, while the absolute value of the Laplace pressure increases,
- if each asperity is acted upon by a negative load, the contact area increases as the distance between asperities decreases,
- if each asperity is acted upon by a positive load, the contact area depends nonmonotonically on the distance between asperities.

Based on the models developed in this chapter it is possible to study the approach-retraction cycle of bodies with given contacting shapes under conditions of capillary adhesion and analyze the effects of the contacting shapes at macro- and micro- scales, and the surface properties on the contact characteristics. Based on this knowledge it is possible to control the contact characteristics by choosing the appropriate surface and mechanical properties of contacting bodies.

Acknowledgements The work was carried out under the financial support of the Russian Foundation for Basic Research (grant 20-01-00400-a).

References

- Argatov II, Mishuris GS, Popov VL (2016) Asymptotic modelling of the JKR adhesion contact for a thin elastic layer. *Q J Mech Appl Math* 69(2):161–179
- Attard P, Parker JL (1992) Deformation and adhesion of elastic bodies in contact. *Phys Rev A* 46(12):7959–7971
- Barnes WJP (2012) Adhesion in wet environments—frogs. In: Bhushan B (ed) *Encyclopedia of nanotechnology*, Part 2. Springer, Berlin, pp 70–83
- Barthel E (1998) On the description of the adhesive contact of spheres with arbitrary interaction potentials. *J Colloid Interface Sci* 200:7–18
- Borodich FM, Galanov BA, Prostov YI, Suarez-Alvarez MM (2012) Influence of complete sticking on the indentation of a rigid cone into an elastic half-space in the presence of molecular adhesion. *J Appl Math Mech* 76(5):590–596
- Borodich FM, Galanov BA, Suarez-Alvarez MM (2014a) The JKR-type adhesive contact problems for power-law shaped axisymmetric punches. *J Mech Phys Sol* 68:14–32
- Borodich FM, Galanov BA, Keer LM, Suarez-Alvarez MM (2014b) The JKR-type adhesive contact problems for transversely isotropic elastic solids. *Mech Mater* 75:34–44
- Borodich FM, Galanov BA, Perepelkin NV, Prikazchikov DA (2019) Adhesive contact problems for a thin elastic layer: asymptotic analysis and the JKR theory. *Math Mech Sol* 24(5):1405–1424
- Butt HJ, Barnes WJP, Del Campo A, Kappl M (2010) Capillary forces between soft, elastic spheres. *Soft Matter* 6:5930–5936

- Creton C, Gorb SN (2007) Sticky feet: from animals to materials. *MRS Bull* 32:466–468
- Derjaguin BV, Muller VM, Toporov YP (1975) Effect of contact deformations on the adhesion of particles. *J Colloid Interface Sci* 53(2):314–326
- Feng JQ (2001) Adhesive contact of elastically deformable spheres: a computational study of pull-off force and contact radius. *J Colloids Interface Sci* 238:318–323
- Goryacheva IG (1997) Contact mechanics in tribology. Kluwer Academic Publishers, Dordrecht
- Goryacheva IG, Makhovskaya YY (1999) Capillary adhesion in the contact between elastic solids. *J Appl Math Mech* 63(1):117–125
- Goryacheva IG, Makhovskaya YY (2001) Adhesive interaction of elastic bodies. *J Appl Math Mech* 65(2):273–282
- Goryacheva IG, Makhovskaya YY (2004) Approach to solving the problems on interaction between elastic bodies in the presence of adhesion. *Dokl Phys* 49(9):534–538
- Goryacheva I, Makhovskaya Y (2008) Adhesion effect in contact interaction of solids. *Comptes Rendus Mecanique* 336:118–112
- Greenwood JA (1997) Adhesion of elastic spheres. *Proc R Soc London A* 453(1961):1277–1297
- Greenwood JA, Johnson KL (1998) An alternative to the Maugis model of adhesion between elastic spheres. *J Phys D Appl Phys* 31(22):3279–3290
- Huber G et al (2005) Evidence for capillary contribution to gecko adhesion from single spatula nanomechanical measurements. *Proc Natl Acad Sci U S A* 102:16293–16296
- Israelachvili J (1992) Intermolecular and surface forces. Academic, New York
- Johnson K (1985) Contact mechanics. Cambridge University Press
- Johnson KL, Greenwood JA (2005) An approximate JKR theory for elliptical contacts. *J Phys D Appl Phys* 38:1042
- Johnson K, Kendall K, Roberts A (1971) Surface energy and the contact of elastic solids. *Proc R Soc A* 324:301–313
- Liu CC, Mee PB (1983) Stiction at the Winchester head-disk interface. *IEEE Trans Magn* 19(5):1569–1661
- Makhovskaya YY (2003) Discrete contact of elastic bodies in the presence of adhesion. *Mech Solids* 38(2):39–48
- Makhovskaya YY (2016) Modeling contact of indenter with elastic half-space with adhesive attraction assigned in arbitrary form. *J Frict Wear* 37(4):301–307
- Makhovskaya YY, Goryacheva IG (1999) The combined effect of capillarity and elasticity in contact interaction. *Tribology Int* 32:507–515
- Mattewson MJ, Mamin HJ (1988) Liquid mediated adhesion of ultra-flat solid surfaces. *Mat Res Soc Symp Proc* 119:87–92
- Maugis D (1991) Adhesion of spheres: the JKR-DMT transition using a Dugdale model. *J Colloid Interface Sci* 150:243–269
- Maugis D, Gauthier-Manuel B (1994) JKR-DMT transition in the presence of a liquid meniscus. *J Adhesion Sci Technol* 8(11):1311–1322
- Megias-Alguacil D, Gauckler LJ (2009) Capillary forces between two solid spheres linked by a concave liquid bridge: regions of existence and forces mapping. *AIChE J* 55:1103–1109
- Muller VM, Yushchenko VS, Derjaguin BV (1980) On the influence of molecular forces on the deformation of an elastic sphere and its sticking to a rigid plane. *J Colloid Interface Sci* 77(1):91–101
- Rabinovich YI, Esayanur MS, Moudgil BM (2005) Capillary forces between two spheres with a fixed volume liquid bridge: theory and experiment. *Langmuir* 21:10992–10997
- Rozhok S et al (2004) AFM study of water meniscus formation between an AFM tip and NaCl substrate. *J Phys Chem B* 108. <https://doi.org/10.1021/jp0401269>
- Soldatenkov IA (2012) The use of the method of successive approximations to calculate an elastic contact in the presence of molecular adhesion. *J Appl Math Mech* 76(5):597–603
- Soldatenkov IA (2019) Contact problem with bulk-applied intermolecular interaction forces: a simplified solution method (two-level model). *Mech Solids* 54(2):303–310
- Thundat T et al (1993) Role of relative-humidity in atomic-force microscopy imaging. *Surf Sci* 294:L939–L943

- Tian H, Matsudaira T (1992) Effect of relative humidity on friction behavior of the head/disk interface. *IEEE Trans Magn* 28(5):2530–2532
- Zakerin M et al (2013) Capillary forces between rigid spheres and elastic supports: the role of Young's modulus and equilibrium vapor adsorption. *Soft Matter* 9:4534–4543
- Zheng Z, Yu J (2007) Using the Dugdale approximation to match a specific interaction in the adhesive contact of elastic objects. *J Colloid Interface Sci* 310(1):27–34
- Zhou SS, Gao XL, He QC (2011) A unified treatment of axisymmetric adhesive contact problems using the harmonic potential function method. *J Mech Phys Sol* 59:145–159

Chapter 5

Influence of a Soft Elastic Layer on Adhesion of Rough Surfaces



Q. Li, I. A. Lyashenko, R. Pohrt, and V. L. Popov

Abstract We consider adhesion of (macroscopically) flat-ended rigid indenters which face surface is superimposed with a short wave-length waviness as a simple model for roughness in a contact and an elastic body coated with a soft elastic layer. The soft layer has ambivalent influence on the adhesion strength: (a) due to softness, it facilitates the formation of complete contact, thus essentially increasing the adhesive strength; (b) on the other hand, the theoretical strength in a complete contact decreases because of the small elasticity. We investigate the critical thickness of the surface soft layer for achieving the maximum adhesive strength of the contact. We find that the properties of adhesive contact are changing not continuously with the thickness of the layer and find the corresponding critical values separating different modes of adhesive behavior.

Keywords Adhesion · JKR theory · Roughness · *Nominally* flat-ended cylinder · Soft elastic layer

Q. Li · R. Pohrt
Berlin University of Technology, Berlin, Germany

I. A. Lyashenko
Berlin University of Technology, Berlin, Germany
Sumy State University, Sumy, Ukraine

V. L. Popov (✉)
Berlin University of Technology, Berlin, Germany
National Research Tomsk State University, Tomsk, Russia
Institute of Strength Physics and Materials Science, Tomsk, Russia
e-mail: v.popov@tu-berlin.de

1 Introduction

In 1971 Kendall derived an equation for adhesive strength of a contact between a rigid flat-ended cylindrical indenter (with radius a) and an elastic half space having Young modulus E and Poisson number ν (Kendall 1971)

$$F_A = \sqrt{8\pi E^* \gamma_{12} a^3}, \quad (5.1)$$

where $E^* = E/(1 - \nu^2)$ and γ_{12} is the work of separation per unit area. According to this solution, the strength of an adhesive contact increases with the elastic modulus. This dependency is even further enhanced by the positive correlation between the elastic modulus and the work of adhesion (Rabinowicz 1995). On the other hand, this conclusion seems to contradict to our daily experience that hard bodies do not adhere while very soft bodies show strong adhesion. The solution of the paradox is of course known that it is the roughness preventing an intimate contact of stiff bodies. Very soft bodies, as elastomers, on the contrary, can be easily deformed and fill the roughness without storing too much elastic energy. However, the strength of the resulting complete contact is then lower than of the corresponding ideal contact of stiff bodies (assume it could be achieved).

Note that the derivation of Eq. (5.1) is based on the balance of elastic energy stored in the bodies and the surface energy. The elastic modulus in (5.1) comes from the equation for the stored elastic energy. This means that if we consider an elastic body covered with a *very thin* soft layer (much smaller than the contact size) then the elastic energy will be stored practically completely in the base body. It is then the elastic modulus of the base body which will enter Eq. (5.1) and determine the adhesive strength. The role of the soft layer in the Eq. (5.1) will be limited by changing the work of adhesion. The main aim of proposed work is to determine the optimal thickness h of soft coating of elastic body, at which highest adhesion strength of contact is realized.

For investigation of the adhesive behavior of layered materials, there are many theoretical and experimental studies (Persson 2012; Scaraggi and Comingio 2017; Brito-Santana et al. 2018; Colas et al. 2015). Numerical simulations have been carried out usually by use of Molecular Dynamics (Kang et al. 2012), Finite Element Method (Sridhar and Sivashanker 2003) and Boundary Element Method (BEM) (Wu and Lin 2017). In this work, we use the Fast Fourier Transform-based BEM which is very effective for the numerical simulation of various contact problems including rough contacts (Pohrt and Li 2014). This method has been developed for adhesive contact of homogeneous medium (Pohrt and Popov 2015), and it can reproduce the same results numerically as theoretical solutions given by Johnson, Kendall and Roberts (JKR) (Johnson et al. 1971) because the same idea of energy balance by Griffith was applied. Recently it has been further developed for functionally graded materials (Li and Popov 2018) and layered systems (Li et al. 2020). With the latter one, the adhesive contact between a rigid body and an elastic half space covered with a coating can be numerically simulated, which is also the approach for this study. We investigate the influence of the coating thickness on adhesive properties of the whole system.

2 Adhesive Contact Between a Wavy Surface and a Layered Half-Space

We consider contact between a rigid body and an elastic half space (elastic modulus E_2 , Poisson's ratio ν_2) covered with a soft layer (E_1, ν_1), so $E_1 < E_2$. The rigid body has a square shape with finite size $L \times L$ and its surface has a roughness modeled by a simple one-dimensional sinusoidal function with wavelength λ and amplitude Δ (Fig. 5.1).

We simulate numerically the pull-off process of this wavy indenter beginning with the state of complete contact using the BEM as described above. The simulation area $L \times L$ is discretized with at least 512×512 square elements. The parameters used are the following: elastic half-space with $E_2 = 2 \cdot 10^{11}$ Pa and $\nu_2 = 0.3$ (as a steel plate), surface energy $\gamma_{12} = 0.03$ J/m² (as soft material), size of the indenter $L \times L = 10$ mm \times 10 mm, wavelength of its surface $\lambda = 1$ mm (10 waves on the surface) and amplitude is much smaller than wavelength $\Delta = 10^{-3}$ mm. The layer and the substrate have the same Poisson's ratios $\nu_2 = \nu_1 = 0.3$. We study the influence of elastic modulus and layer thickness on the adhesive behavior.

Related to the adhesive contact of wavy surface, we have to mention the "Johnson parameter" which was introduced by Johnson in the study of an adhesive contact between an *infinite* one-dimensional wavy surface and a homogeneous elastic half space (Johnson 1995):

$$\alpha = \sqrt{\frac{2\lambda\gamma_{12}}{\pi^2\Delta^2E^*}}. \quad (5.2)$$

This parameter governs the adhesive behavior of the wavy surface. It was found that there is a critical value of $\alpha_c \approx 0.57$, exceeding which the full contact is realized even at the moment of the first contact (at zero indentation depth d) (Johnson

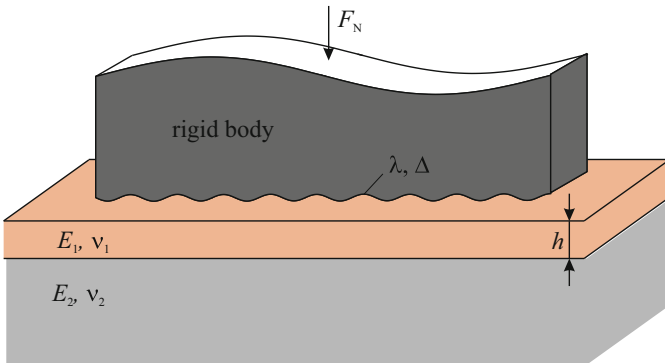


Fig. 5.1 Sketch of contact between a rigid body with wavy surface and an elastic half space covered with a layer

1995). In this work we consider the layered system and finite-size indenter, but this parameter plays still an important role in finding the optimal coating thickness.

For further representation of the simulation results, we will use dimensionless parameters:

$$\tilde{h} = \frac{h}{\lambda_c} = h \frac{2\gamma_{12}}{\alpha_c^2 \pi^2 \Delta^2 E_1^*}, \quad \tilde{F}_N = \frac{F_N}{\sqrt{\pi \gamma_{12} E_2^* (L/2)^3}}, \quad \tilde{d} = d \sqrt{\frac{E_2^*}{\pi (L/2) \gamma_{12}}}, \quad (5.3)$$

where $\alpha_c = 0.57$ and λ_c is critical wavelength represented by other parameters as described in (5.3). The normal force and indentation depth are normalized by the solution for flat-ended-like indenter similar to (5.1). Note that dimensionless parameters for normal force and indentation depth contain the elastic modulus E_2^* of the foundation, not the layer E_1^* , because the elastic energy is stored mainly in the base material if the layer is very thin.

2.1 Influence of Layer Thickness and Elastic Modulus on Complete Area at the First Contact

According to the solution in (Johnson 1995), for the larger Johnson parameter, two surfaces come into the complete contact at the first contact. Observing the Eq. (5.2) in the limiting cases of the layered system, $h \rightarrow 0$ and $h \rightarrow \infty$, it follows

$$\alpha_{h \rightarrow 0} = \sqrt{\frac{2\lambda\gamma_{12}}{\pi^2 \Delta^2 E_2^*}}, \quad \alpha_{h \rightarrow \infty} = \sqrt{\frac{2\lambda\gamma_{12}}{\pi^2 \Delta^2 E_1^*}}. \quad (5.4)$$

Due to $E_2^* > E_1^*$, we have always the situation $\alpha_{h \rightarrow 0} < \alpha_{h \rightarrow \infty}$. This means that by increasing of the layer thickness the area of contact will also increase. Numerically we simulate the adhesive contact and calculate the contact area at zero indentation depth for different values of layer thickness h varying from 0.001 mm to 0.3 mm, and elastic modulus E_1^* from $0.5 \cdot 10^{-5} E_2^*$ to $100 \cdot 10^{-5} E_2^*$ (corresponding to $\alpha_{h \rightarrow \infty}$ varying from 2.47 to 0.17).

The results are shown in Fig. 5.2a, where contact area is normalized by the total area $A_0 = L \times L$. One can see that the contact area at the first contact increases indeed with the layer thickness. But for the smaller values of $\alpha_{h \rightarrow \infty}$ (larger E_1^*), it is not easy to get a complete contact. This can be also explained by the Johnson parameter: in the case of $\alpha_{h \rightarrow \infty} \geq \alpha_c$ (Johnson 1995), the contact configuration with the full contact is possible in principle, otherwise it is impossible for any value of the layer thickness h . The critical thickness h_c for complete contact at zero indentation depth is presented for different elastic moduli of layer (as well as corresponding values of $\alpha_{h \rightarrow \infty}$) in Fig. 5.2b.

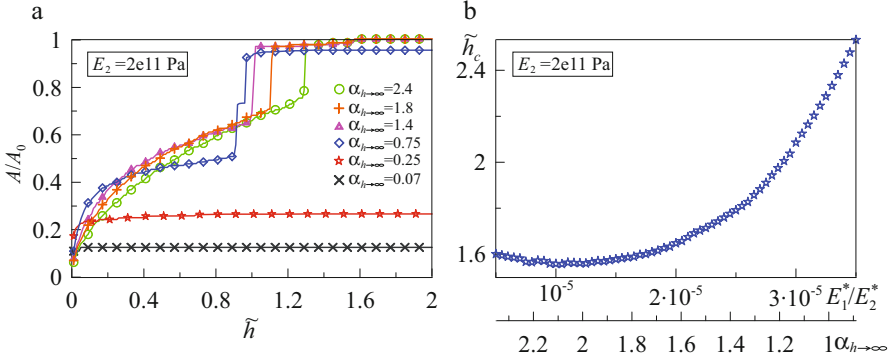


Fig. 5.2 (a) Dependence of the contact area on dimensionless thickness of the coating for different materials of coating. (b) Dependence of critical thickness for complete contact at zero indentation depth on elastic moduli of the layer

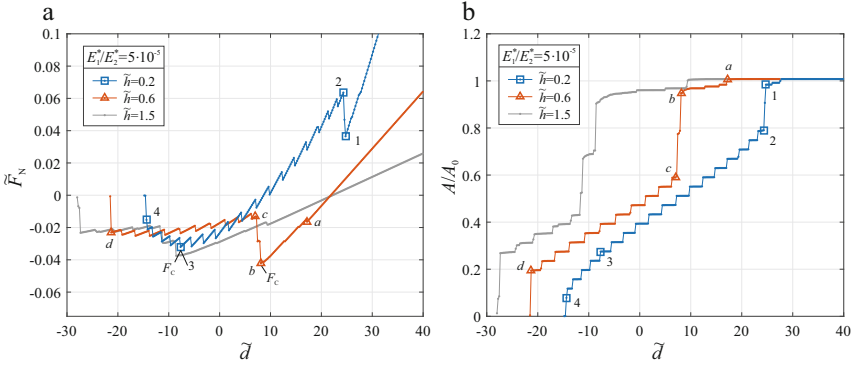


Fig. 5.3 (a) Normal force- and (b) contact area-distance relation in pull-off for the different layer thicknesses. The elastic modulus of layer is $E_1^*/E_2^* = 5 \cdot 10^{-5}$

2.2 Dependence of Strength of Adhesion on Layer Thickness

We focus on the effect of the layer thickness on the adhesive behaviour. The elastic modulus of layer is set as $E_1 = 5 \cdot 10^{-5} E_2 = 10^7$ Pa. 54 cases with layer thicknesses varying from $\tilde{h} = 0.12$ to 2 corresponding to the dimensional values $h = 0.07$ mm to 1.2 mm were simulated. One should note the size of indenter $L = 10$ mm and surface wavelength $\lambda = 1$ mm for the comparison with the coating thickness. The pull-off is simulated from the very large indentation depth where complete contact is achieved to the final detachment. The dependencies of the normal force and normalized contact area A/A_0 on the separation distance for three values of layer thickness $\tilde{h} = 0.2, 0.6$ and 1.5 ($h = 0.12, 0.35$ and 0.88 mm) are shown in Fig. 5.3.

It is seen that the contact stiffness decreases generally with the layer thickness (the slope of curve decreases). Observing the curves for thickness $\tilde{h} = 0.2$ and 0.6 in Fig. 5.3a, one can find that for larger layer thickness $\tilde{h} = 0.6$, the maximal pull-off

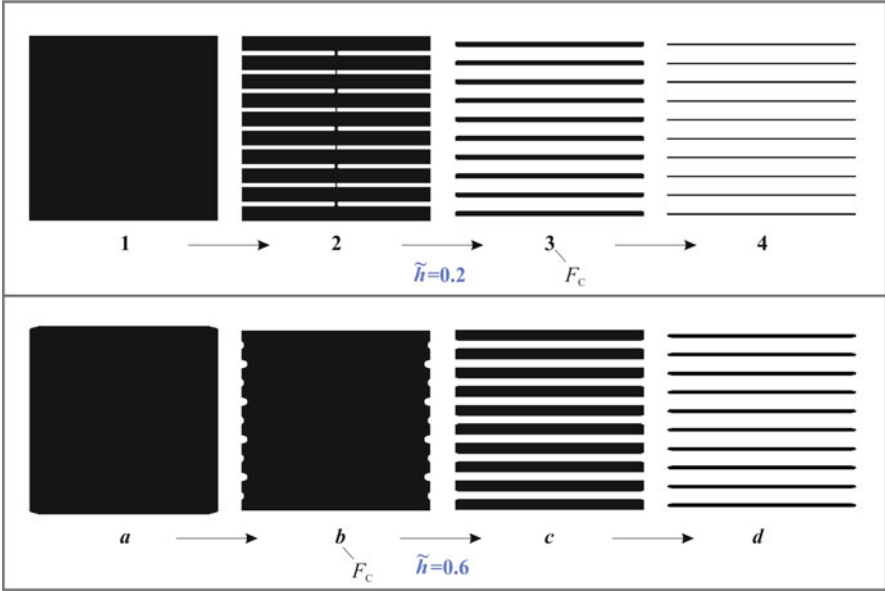


Fig. 5.4 Change in contact area during the pull-off for the case with $\tilde{h} = 0.2$ and 0.6 corresponding to the states 1–4 and **a–d** in Fig. 5.3

force (point *b* marked with triangle) appears at the moment when the contact area jumps from the continuous (almost) full contact to the zebra stripes (see also the contact area changing from *b* to *c* in Fig. 5.4). After that the contact area keeps a stripe shape just becoming thinner gradually (from state *c* to *d*). However, in the case of thin layer with $\tilde{h} = 0.2$, the maximal force is found in the striped pattern state (point 3 marked with square). Here we denote F_C as the maximal pull-off force whose absolute value is usually called *adhesive force*, and d_C as the critical distance for detachment, \tilde{F}_C and \tilde{d}_C are their dimensionless forms. The dependences of contact area on the distance are shown in Fig. 5.3b.

From above we expect that there would be a turning point between these two behaviors: before it, the maximal pull-off force appears at the stripe-shape state, but after this point it happens immediately before the point of *jump*. The adhesive forces \tilde{F}_C for different layer thicknesses are shown in Fig. 5.5a. We can see that the adhesive force decreases first with increasing the layer thickness, but from a critical value of $\tilde{h} = 0.35$ ($h = 0.21$ mm) it increases to a maximum $\tilde{F}_{C,max} = 0.043$ at $\tilde{h} = 0.8$ ($h = 0.47$ mm) and then decreases again. Of course, if the layer becomes even thicker, then the elasticity of the soft layer plays a more important role and the adhesive force will be approaching to the homogeneous case of soft material, therefore adhesive force becomes smaller as predicted in Eq. (5.1). The two examples with $\tilde{h} = 0.2$ and 0.6 described in Figs. 5.3 and 5.4 are located on each side of this critical point $\tilde{h} = 0.35$ (marked with square and triangle also in this curve), and the other example in Fig. 5.3 with thick layer $\tilde{h} = 1.5$ is marked in

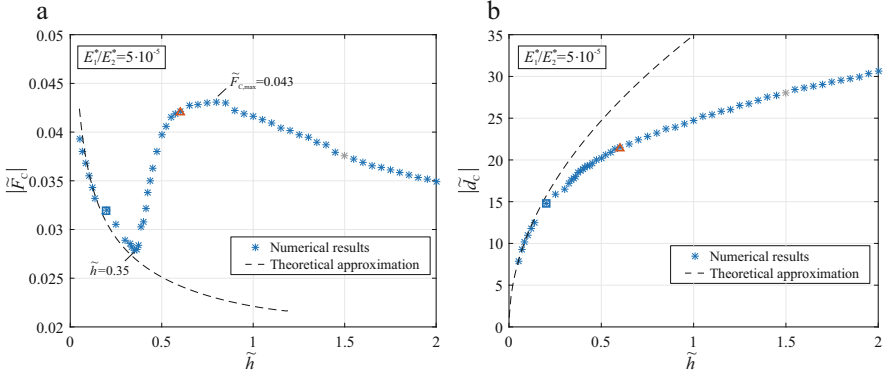


Fig. 5.5 Dependence of adhesive force (a) and critical distance (b) for detachment on the layer thickness. There is a critical thickness $\tilde{h} = 0.35$ under and above which different adhesive behaviors can be observed as shown in Figs. 5.3 and 5.4

gray. From Fig. 5.5b, one can see that the critical separation distance for detachment increases monotonically with the thickness.

3 Discussion on Adhesive Contact with a Very Thin Layer

In recent studies, there have been several theoretical solutions to adhesive contact of thin layers with the assumption of *rigid* foundation with $E_2 = \infty$ (Papangelo 2018; Yang 2006; Barber 1990). In the case of axisymmetric contacts, the elastic force is determined by the linear relation

$$F_N = -kd, \quad (5.5)$$

with effective elastic modulus and stiffness

$$\tilde{E}_1 = \frac{E_1(1 - \nu_1)}{(1 + \nu_1)(1 - 2\nu_1)}, \quad k = \frac{\tilde{E}_1 \pi a^2}{h}, \quad (5.6)$$

where d is the indentation depth. Recently it was further developed for the arbitrary geometry of indenters (Li and Popov 2019). If the contact size is much larger than the layer thickness, then the layer can be represented by a two-dimensional elastic foundation consisting of independent springs which are placed with separation Δx in both directions, and each spring has a stiffness

$$k = \tilde{E}_1 \frac{A_e}{h}, \quad (5.7)$$

where $A_e = (\Delta x)^2$ is the elementary area. The normal force is then sum of all spring forces:

$$F_N = \sum_{cont} k \Delta l, \quad (5.8)$$

where Δl are elongations of the springs. The critical elongation of the springs for detachment is defined as (Li and Popov 2019)

$$\Delta l_c = \sqrt{\frac{2\gamma_{12}h}{\tilde{E}_1}}. \quad (5.9)$$

Following this approach, it is very easy to obtain the elastic force F_N as a function of indentation depth. With the surface profile which we considered in the following

$$h(x) = \Delta \left\{ 1 - \cos\left(\frac{2\pi x}{\lambda}\right) \right\}, \quad (5.10)$$

the normal force is calculated as

$$F_N = \frac{L^2 \tilde{E}_1}{\lambda h} \int_{x_1}^{x_2} \left[d - \Delta \left(1 + \cos \frac{2\pi x}{\lambda} \right) \right] dx = \frac{L^2 \tilde{E}_1}{\lambda h} \left(x(d - \Delta) - \frac{\lambda \Delta}{2\pi} \sin \frac{2\pi x}{\lambda} \right) \Big|_{x_1}^{x_2}, \quad (5.11)$$

$$x_1 = \frac{\lambda}{2\pi} \arccos \left(\frac{1}{\Delta} \sqrt{\frac{2\gamma_{12}h}{\tilde{E}_1}} + \frac{d}{\Delta} - 1 \right), \quad (5.12)$$

$$x_2 = \lambda - x_1. \quad (5.13)$$

The results $\tilde{F}_C(\tilde{d})$ and $A/A_0(\tilde{d})$ for an example with very small value of thickness $\tilde{h} = 0.12$ are shown in Fig. 5.6. For comparison, numerical results from simulation in the study case of Sect. 2 with non-rigid foundation $E_2 \neq \infty$ are added in the figure. They have the very similar adhesive behaviors.

Using the same approach, we consider the different values of layer thickness. The maximal pull-off force \tilde{F}_C and critical distance \tilde{d}_C are shown in Fig. 5.5 with the dashed lines. One can see that they have a good agreement only at the small values of thickness. Because the method (5.7–5.9) is valid only when the layer thickness is much smaller than the contact size. Furthermore, we used the finite elastic modulus of foundation $E_2/E_1 = 2 \cdot 10^4$.

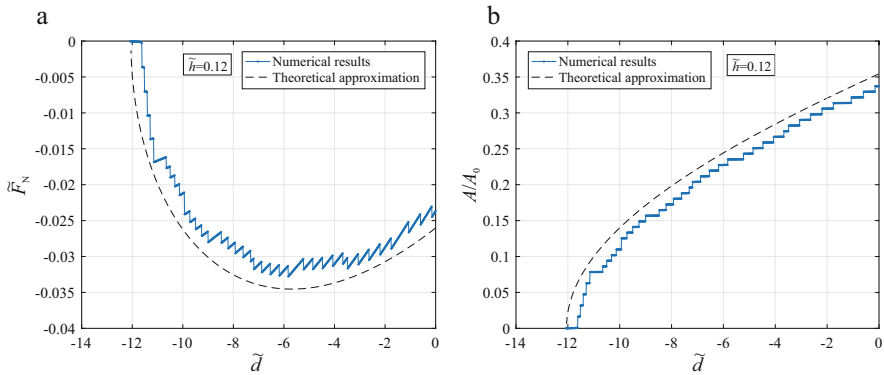


Fig. 5.6 Theoretical solution (dashed line) to thin layer contacts under the assumption of rigid foundation in comparison with numerical results for the smallest value $\tilde{h} = 0.12$: **(a)** force-distance relation and **(b)** contact area-distance relation

4 Conclusions

We investigated numerically adhesion between an elastic half-space with a soft coating and a rigid indenter having a slightly wavy surface. The influence of layer thickness on the strength of adhesion was studied for the case of a rubber-like layer on a steel plate $E_1/E_2 = 5 \cdot 10^{-5}$ and indenter with a small roughness. It was found that the largest adhesive force was achieved for the case of $h/L = 0.047$ ($\tilde{h} = 0.8$) and it appears at the jumping moment from the continuous complete contact to the striped shape. This adhesive behavior of layered system depends on all material parameters, Johnson parameter, geometry of indenters as well as the layer thickness. The further parameter study can be carried out for obtaining a general law in the future work.

Acknowledgements Authors acknowledges financial support by the Deutsche Forschungsgemeinschaft (DFG PO 810-55-1). This research was partially supported by “The Tomsk State University competitiveness improvement programme”.

References

- Barber JR (1990) Contact problems for the thin elastic layer. *Int J Mech Sci* 32(2):129–132. [https://doi.org/10.1016/0020-7403\(90\)90112-V](https://doi.org/10.1016/0020-7403(90)90112-V)
- Brito-Santana H, de Medeiros R, Ferreira AJM, Ramos RR, Tita V (2018) Effective elastic properties of layered composites considering non-uniform imperfect adhesion. *Appl Math Model* 59:183–204. <https://doi.org/10.1016/j.apm.2018.01.009>
- Colas F, Barchiesi D, Kessentini S, Toury T, Lamy de la Chapelle M (2015) Comparison of adhesion layers of gold on silicate glasses for SERS detection. *J Opt* 17(11):114010. <https://doi.org/10.1088/2040-8978/17/11/114010>

- Johnson KL (1995) The adhesion of two elastic bodies with slightly wavy surfaces. *Int J Solids Struct* 32(3–4):423–430. [https://doi.org/10.1016/0020-7683\(94\)00111-9](https://doi.org/10.1016/0020-7683(94)00111-9)
- Johnson KL, Kendall K, Roberts AD (1971) Surface energy and the contact of elastic solids. *Proc R Soc London A* 324:301–313
- Kang J-H, Kim K-S, Kim K-W (2012) Prediction of surface and adhesion energies of nanoimprint lithography materials and anti-sticking layers by molecular dynamics simulation. *Appl Surf Sci* 258(14):5438–5442. <https://doi.org/10.1016/j.apsusc.2012.02.031>
- Kendall K (1971) The adhesion and surface energy of elastic solids. *J Phys D* 4(8):1186–1195
- Li Q, Popov VL (2018) Boundary element method for normal non-adhesive and adhesive contacts of power-law graded elastic materials. *Comput Mech* 61(3):319–329. <https://doi.org/10.1007/s00466-017-1461-9>
- Li Q, Popov VL (2019) Adhesive contact between a rigid body of arbitrary shape and a thin elastic coating. *Acta Mech* 230(7):2447–2453. <https://doi.org/10.1007/s00707-019-02403-0>
- Li Q, Pohrt R, Lyashenko IA, Popov VL (2020) Boundary element method for nonadhesive and adhesive contacts of a coated elastic half-space. *Proc Inst Mech Eng Part J J Eng Tribol* 234(1):73–83. <https://doi.org/10.1177/1350650119854250>
- Papangelo A (2018) Adhesion between a power-law indenter and a thin layer coated on a rigid substrate. *FU Mech Eng* 16(1):19–28. <https://doi.org/10.22190/FUME180102008P>
- Persson BNJ (2012) Contact mechanics for layered materials with randomly rough surfaces. *J Phys Condens Matter* 24:095008. (10pp). <https://doi.org/10.1088/0953-8984/24/9/095008>
- Pohrt R, Li Q (2014) Complete boundary element formulation for normal and tangential contact problems. *Phys Mesomech* 17(4):334–340. <https://doi.org/10.1134/S1029959914040109>
- Pohrt R, Popov VL (2015) Adhesive contact simulation of elastic solids using local mesh-dependent detachment criterion in boundary elements method. *FU Mech Eng* 13(1):3–10
- Rabinowicz E (1995) *Friction and wear of materials*, 2nd edn. Wiley
- Scaraggi M, Comingio D (2017) Rough contact mechanics for viscoelastic graded materials: the role of small-scale wavelengths on rubber friction. *Int J Solids Struct* 125:276–296. <https://doi.org/10.1016/j.ijsolstr.2017.06.008>
- Sridhar I, Sivashanker S (2003) On the adhesion mechanics of multi-layer elastic systems. *Surf Coat Tech* 167(2–3):181–187. [https://doi.org/10.1016/S0257-8972\(02\)00893-9](https://doi.org/10.1016/S0257-8972(02)00893-9)
- Wu JJ, Lin YJ (2017) Boundary element analyses on the adhesive contact between an elastic sphere and a rigid half-space. *Eng Anal Bound Elem* 74:61–69. <https://doi.org/10.1016/j.enganabound.2016.10.011>
- Yang F (2006) Asymptotic solution to axisymmetric indentation of a compressible elastic thin film. *Thin Solid Films* 515(4):2274–2283. <https://doi.org/10.1016/j.tsf.2006.07.151>

Chapter 6

Asymptotic Modeling Scheme for Analysis of Bio-inspired Fibrillar Adhesive Interfaces: A Short Review



Ivan Argatov

Abstract Multi-parameter problems are difficult to analyze numerically, and simple analytical and asymptotic models, which work in different limit situations, could be of great help. While, a phenomenological modeling approach and semi-inverse methods can be used for constructing simple approximate solutions of such problems, it is difficult to be implemented in a systematic way. On the contrary, asymptotic modeling provides a clear scheme for analysis of both multi-parametric and multi-scale problems, and its main ideas are briefly considered in the present review with application to multiple elastic contact at bio-inspired fibrillar adhesive interfaces.

Keywords Asymptotic modeling · Multiple contact · Bio-inspired adhesives · Fibrillar interfaces

1 Introduction

In recent years, biological systems have attracted a great interest with the purpose of borrowing effective solutions from the nature (Arzt et al. 2003; Borodich et al. 2010; Burns et al. 2012; Gorb 2008). One of such examples is given by artificial bio-inspired adhesive materials which mimic the adhesive mechanism of gecko's toes (Boesel et al. 2010; Kwak and Kim 2010; Tian et al. 2006; Zhou et al. 2013).

Along with the development of methods for fabricating new polymeric adhesives with patterned or textured surfaces (Del Campo et al. 2007; Hui et al. 2007), there have been developed approaches for mathematical modeling of multi-scale adhesive contact (Borodich and Savencu 2017; Guidoni et al. 2010; Noderer et al. 2007). The majority of the analytical multi-scale models, as it was observed by O'Rourke et al.

I. Argatov (✉)
Faculty of Technology and Society, Malmö University, Malmö, Sweden
e-mail: ivan.argatov@mau.se

(2016), were developed within the context of phenomenological modeling by using those or other simplifying assumptions (see, e.g., Schargott et al. 2006).

Very recently, Argatov et al. (2019) applied an asymptotic modeling approach to analyze the problem of multiple adhesive contact and, in particular, the effect of microcontacts interaction (Galín 1980; Gladwell and Fabrikant 1982). From one side, this approach allows for a systematic examination of multi-scale contact problems, from the other side, it can be easily generalized to account for the effects of anisotropy, inhomogeneity and time-dependency of material properties. In the present paper, we briefly overview the main ideas of the asymptotic modeling methodology with the application to evaluating the adhesive strength of fibrillar interface (Popov et al. 2017).

2 Asymptotic Modeling of Multiple Contact

Below we discuss the main ideas of asymptotic modeling of multiple elastic contact and provide some technical details of asymptotic analysis. Our considerations are not rigorous, and the reader is referred to the books by Ilyin (1992), Nayfeh (2008), Van Dyke (1964) for more detailed description of the asymptotic methods.

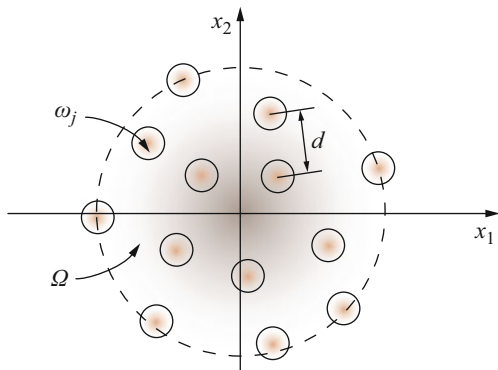
2.1 Small Parameters

Asymptotic methods deal with expansions in the order of a small parameter, which is usually assumed to be dimensionless and positive. When two elastic bodies are brought into contact, the contact area, which is established at the interface, can be characterized by its diameter and a certain shape factor. Due to the surface fibrillar pattern, when it is present, the real contact area is represented by a number of contact spots, which are located inside some apparent contact area of certain size and shape (Pepelyshev et al. 2018). So, additionally, we can introduce the average diameter of contact spots and, e.g., the average distance between two neighboring contact spots. Thus, having at least two geometrical parameters with the dimension of length, we can straightforwardly introduce a dimensionless parameter as their ratio.

To simplify the consideration, we consider a cluster of N circular contact spots ω^j of radii a_1, a_2, \dots, a_N distributed over a domain Ω (see Fig. 6.1). However, instead of the average distance, for asymptotic estimates it is convenient to introduce the *minimum* distance, d , between the centers of contact spots. In this case, we may set

$$\varepsilon_1 = \frac{a}{d}, \quad (6.1)$$

Fig. 6.1 A cluster of circular microcontacts ω^j forming an apparent contact area Ω



where a is the *maximum* of the microcontact radii, thus introducing a small parameter ε_1 , though, which can take values from the interval $(0, 0.5)$, provided the contact spots do not overlap each other.

Further, for the sake of simplicity, let the apparent contact area Ω be a circle of radius R . Then, the contact interface under consideration admits the introduction of the second dimensionless parameter

$$\varepsilon_2 = \frac{d}{R}, \tag{6.2}$$

which, by the definition, is not greater than two.

Finally, for a large number of microcontacts N , its inverse, $1/N$, can be also regarded as a small parameter. However, for regularly distributed microcontacts, the number N is asymptotically related to the small parameter ε_2 .

2.2 Stretched Coordinates

By introducing a Cartesian coordinate system Ox_1x_2 , we will denote the center P_j of the j -th microcontact ω^j by (x_1^j, x_2^j) , so that

$$d = \min_{k \neq j} \sqrt{(x_1^j - x_1^k)^2 + (x_2^j - x_2^k)^2}, \quad j, k = 1, 2, \dots, N.$$

Moreover, let us introduce a local system of Cartesian coordinates $(\hat{x}_1^j, \hat{x}_2^j)$ with the center at point P_j , so that

$$y_1^j = x_1 - x_1^j, \quad y_2^j = x_2 - x_2^j. \tag{6.3}$$

It is clear that, while $(x_1, x_2) \in \omega_j$, we have $\sqrt{(y_1^j)^2 + (y_2^j)^2} < a_j$.

In order to compare different length scales, we introduce the primary length-scale of the multiple contact interface to be coinciding with d and non-dimensionalize the coordinates as follows:

$$\tilde{x}_\alpha = \frac{x_\alpha}{d}, \quad \tilde{y}_\alpha^j = \frac{y_\alpha^j}{d}, \quad \alpha = 1, 2. \quad (6.4)$$

Hence, if $(x_1, x_2) \in \omega_j$, then, in view of (6.1), we will have

$$\sqrt{(\tilde{y}_1^j)^2 + (\tilde{y}_2^j)^2} < \frac{a_j}{d} \leq \varepsilon_1.$$

On the other hand, it is convenient to non-dimensionalize the local coordinates, using the corresponding micro contact radius as

$$\eta_\alpha = \frac{y_\alpha^j}{a_j}, \quad \alpha = 1, 2, \quad (6.5)$$

so that $\sqrt{\eta_1^2 + \eta_2^2} < 1$, when $(x_1, x_2) \in \omega_j$.

From Eqs. (6.4) and (6.5), it follows that

$$\eta_\alpha = \frac{a}{a_j} \frac{y_\alpha^j}{\varepsilon_1}, \quad \alpha = 1, 2. \quad (6.6)$$

The dimensionless local coordinates (6.6) are called *stretched coordinates*. Using the coordinate transformations (6.3) and (6.6), the microcontact spot ω_j can be obtained from a unit circle, ϖ , by translating (via Eqs. (6.3)) and scaling with the factor $(\varepsilon_1 a_j / a)^{-1}$ (via Eqs. (6.6)).

Observe that η_1 and η_2 are in-plane stretched coordinates. If the stress-strain state is considered around the j -th microcontact, additionally the normal stretched coordinate, ζ , is introduced using the same scaling factor. Finally, we note that the choice of the primary length scale d , which according to Eqs. (6.1) and (6.2) is intermediate, is determined by the convenience of analysis, since the macro-scale length scale R can change under the varied contact load (see, e.g., Guidoni et al. 2010; Kern et al. 2017).

It is important to emphasize that due to the chain rule of differentiation, we have

$$\frac{\partial}{\partial x_\alpha} = \varepsilon_1^{-1} \frac{a}{a_j} \frac{\partial}{\partial \eta_\alpha}, \quad \alpha = 1, 2. \quad (6.7)$$

In view of (6.7), it is promising to extend the multi-scale asymptotic analysis for elastic medium models, where the scaling properties are different with respect to different spatial variables, which can be done using the concept of parametric homogeneity (Borodich 1998a,b).

2.3 Asymptotic Matching

Assuming for the sake of simplicity that the adhesive contact is frictionless, the problem of multiple contact, under certain assumptions (see, e.g., Argatov 2003), can be reduced to the governing integral equation

$$\sum_{j=1}^N \iint_{\omega_j} K(\mathbf{x}, \bar{\mathbf{x}}) p_j(\bar{\mathbf{x}}) d\bar{\mathbf{x}} = \delta - \varphi_j(\mathbf{x} - \mathbf{x}^j) \quad (6.8)$$

with respect to the contact pressure densities $p_j(\mathbf{x})$, $\mathbf{x} \in \omega_j$, $j = 1, 2, \dots, N$, where $K(\mathbf{x}, \bar{\mathbf{x}})$ is the surface influence function, δ is the contact approach, and $\varphi_j(\mathbf{y}^j)$ is the local gap function.

Actually, Eq. (6.8) can be regarded as a system of N integral equations

$$\iint_{\omega_j} K(\mathbf{x}, \bar{\mathbf{x}}) p_j(\bar{\mathbf{x}}) d\bar{\mathbf{x}} = \delta - \varphi_j(\mathbf{x} - \mathbf{x}^j) - \sum_{k \neq j} \iint_{\omega_k} K(\mathbf{x}, \bar{\mathbf{x}}) p_k(\bar{\mathbf{x}}) d\bar{\mathbf{x}}, \quad (6.9)$$

where $\mathbf{x} \in \omega_j$, $j = 1, 2, \dots, N$.

The last term on the right-hand side of Eq. (6.9) represents the contribution to the j -th microcontact from the interaction with neighboring microcontacts.

Recall that using the singular solution of the Boussinesq problem, the surface influence function can be represented as

$$K(\mathbf{x}, \bar{\mathbf{x}}) = \frac{1}{\pi E^*} \frac{1}{|\mathbf{x} - \bar{\mathbf{x}}|} + k(\mathbf{x}, \bar{\mathbf{x}}), \quad (6.10)$$

where E^* is the so-called reduced elastic modulus, and $k(\mathbf{x}, \bar{\mathbf{x}})$ is a regular part.

Taking into account formula (6.10), we readily get that after the introduction of the stretched coordinates (6.6) into Eq. (6.9), there will appear terms of different asymptotic order with respect to parameter ε_1 . In the case of an elastic layer and a single circular or elliptical frictionless contact the asymptotic analysis of the contact problem equations was given by Vorovich et al. (1974). Here, we simplify the considerations by omitting many technical details.

Thus, indeed, if $\mathbf{x} \in \omega_j$ and $\bar{\mathbf{x}} \in \omega_j$, then

$$K(\mathbf{x}, \bar{\mathbf{x}}) \simeq \varepsilon_1^{-1} \frac{a}{a_j} \frac{1}{\pi E^*} \frac{1}{|\boldsymbol{\eta} - \bar{\boldsymbol{\eta}}|}, \quad (6.11)$$

where $\boldsymbol{\eta}$ and $\bar{\boldsymbol{\eta}}$ belong to the unit circle ϖ .

On the contrary, if $\mathbf{x} \in \omega_j$ and $\bar{\mathbf{x}} \in \omega_k$ when $k \neq j$, then $K(\mathbf{x}, \bar{\mathbf{x}}) = O(1)$ as $\varepsilon_1 \rightarrow 0$.

Thus, as a zero order approximation, Eq. (6.9) can be simplified as follows:

$$\varepsilon_1^{-1} \frac{a}{a_j} \frac{1}{\pi E^*} \iint_{\omega} \frac{P_j^0(\bar{\eta})}{|\boldsymbol{\eta} - \bar{\eta}|} d\bar{\eta} = \delta - \varphi_j \left(\varepsilon_1 \frac{a_j}{a} \boldsymbol{\eta} \right). \quad (6.12)$$

Here, $P_j^0(\boldsymbol{\eta})$ is the leading asymptotic term of the contact pressure distributed over the j -th microcontact $p_j(\mathbf{x}^j + \varepsilon_1(a_j/a)\boldsymbol{\eta})$.

Though Eq. (6.12) still contains small parameter ε_1 , it can be solved explicitly without further asymptotic simplifications. However, it is clear that by the construction, the leading-order asymptotic approximation $P_j^0(\boldsymbol{\eta})$ does not account for the microcontact interaction.

A straightforward application of perturbation technique (see, e.g., Alexandrov and Shmatkova 1998; Argatov 2003) suggests to reduce Eq. (6.9) to the following one for the first order approximation:

$$\begin{aligned} \varepsilon_1^{-1} \frac{a}{a_j} \frac{1}{\pi E^*} \iint_{\omega} \frac{P_j^1(\bar{\eta})}{|\boldsymbol{\eta} - \bar{\eta}|} d\bar{\eta} = \delta - \varphi_j \left(\varepsilon_1 \frac{a_j}{a} \boldsymbol{\eta} \right) \\ - \varepsilon_1 \sum_{k \neq j} \frac{a_k}{a} K(\mathbf{x}^j, \mathbf{x}^k) \iint_{\omega} P_k^0(\bar{\eta}) d\bar{\eta}. \end{aligned} \quad (6.13)$$

Observe that the double integral in the last term on the right-hand side of Eq. (6.13) can be recognized as the relative zeroth-order approximation for the contact force acting on the k -th microcontact.

Let us now introduce the microcontact forces

$$f_j = \iint_{\omega_j} p_j(\bar{\mathbf{x}}) d\bar{\mathbf{x}}, \quad j = 1, 2, \dots, N. \quad (6.14)$$

By inspection of Eq. (6.13) it becomes apparent that the original integral equation (6.9) can be approximated in the same way as

$$\iint_{\omega_j} K(\mathbf{x}, \bar{\mathbf{x}}) p_j(\bar{\mathbf{x}}) d\bar{\mathbf{x}} \simeq \delta - \varphi_j(\mathbf{x} - \mathbf{x}^j) - \sum_{k \neq j} K(\mathbf{x}^j, \mathbf{x}^k) f_k, \quad (6.15)$$

where the last term on the right-hand side of Eq. (6.15) is a constant, and therefore, it possesses the same complexity as the contact problem for a single contact.

Figure 6.2 shows that the far-field of a circular contact on an elastic half-space is not very sensitive to the spread of the contact pressure distribution—just according to Saint Venant's principle (Sternberg 1954).

Observe that Eq. (6.13) can be considered as the result of asymptotic matching of the stress state near the j -th microcontact with those produced by the other ones.

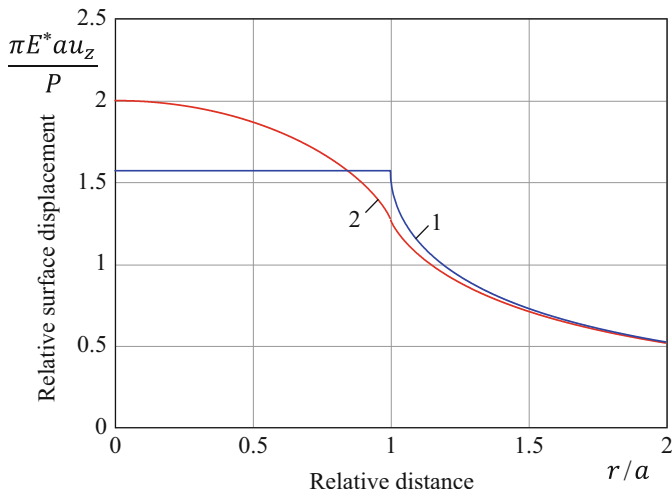


Fig. 6.2 Variation of the surface displacement for an elastic half-space under a flat-ended cylindrical indenter (1) and a uniform normal pressure (2). The relative difference rapidly decreases from 23.37% for $r = a$ to 2.51% for $r = 1.5a$

From another point of view, Eq. (6.15) gives a sort of self-consistent approximation, which in contact problems for a cluster of microcontacts was developed by Greenwood (1966). The analysis of the Greenwood approximation was given by Argatov (2011).

It is also to note here that the function $\varphi_j(\mathbf{y}^j)$ describes the microcontact shape, and its effect has been studied elsewhere (Argatov et al. 2019; Del Campo et al. 2007; Yao and Gao 2007).

2.4 Homogenization of the Contact Pressure

Consider now the situation, where the number of microcontacts N is large. Let the radius R of the apparent contact area Ω be fixed. Also, to fix our ideas, we assume a regular distribution of microcontacts, e.g., at the nodes of a square lattice (see Fig. 6.3). Then, roughly speaking, the number of microcontacts can be estimated as

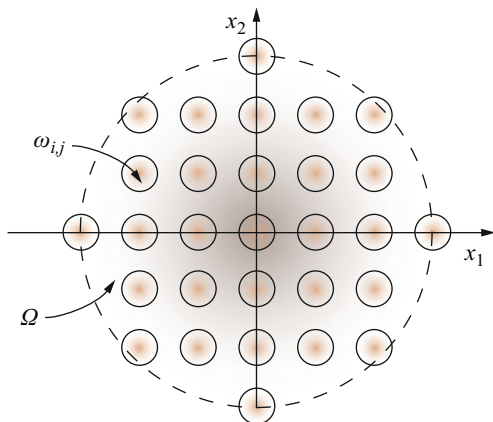
$$N \approx \frac{|\Omega|}{d^2}, \tag{6.16}$$

where $|\Omega| = \pi R^2$ is the area of the circular domain Ω .

Hence, from (6.2) and (6.16) it follows that

$$N \approx \frac{\pi}{\varepsilon_2^2}, \tag{6.17}$$

Fig. 6.3 A cluster of regularly positioned circular microcontacts $\omega_{i,j}$ forming an apparent contact area Ω



and therefore, by increasing N , we inevitably reduce the value of the second dimensionless parameter ε_2 .

In the case of double periodic distribution of microcontacts, it is convenient to denote an individual microcontact as $\omega_{i,j}$, where the indices i and j may take negative integer values, so that the microcontact center is $\mathbf{x}^{i,j} = (id, jd)$. It is assumed that $\sqrt{i^2 + j^2}d \leq R$. In other words, a particular microcontact is regarded to belong to the cluster if it encompasses the microcontact center.

Further, let $p_{i,j}(\mathbf{x})$ be the corresponding microcontact density, $\mathbf{x} \in \omega_{i,j}$. Again, for the sake of simplicity, let us assume that all microcontacts have the same shape and size. For instance, formula $\omega_{i,j} = \left\{ \mathbf{x} : \varepsilon_1^{-1}(\mathbf{x} - \mathbf{x}^{i,j}) \in \varpi \right\}$ determines circular microcontacts of radius a positioned at the point $\mathbf{x}^{i,j}$ (see Eq. (6.1)).

Then, the apparent contact pressure $p_0(\mathbf{x})$, $\mathbf{x} \in \Omega$, can be introduced via the asymptotic formula

$$p_0(\mathbf{x}^{i,j}) \simeq \frac{1}{d^2} \iint_{\omega_{i,j}} p_{i,j}(\bar{\mathbf{x}}) d\bar{\mathbf{x}}, \quad (6.18)$$

which enjoys the force balance at the contact interface.

The homogenized contact problem, whose solution is represented by the function $p_0(\mathbf{x})$, depends on the value of ε_1 . If ε_1 is not supposed to be a small parameter, the homogenization procedure was carried out by Argatov and Mel'nyk (2001), using a combination of the homogenization technique (Bensoussan et al. 1978) and the method of matched asymptotic expansions (Ilyin 1992). If ε_1 is assumed to be small (but not very small) the homogenized contact problem was derived by Argatov (2004) in the form of a Fredholm integral equation of the second kind using the averaging method by Marchenko and Khruslov (1974). Finally, if ε_1 is very small, then the interaction between the microcontacts may be neglected and

the microcontact pressures can be determined independently (Argatov 2011), so that the average contact pressure can be introduced directly through formula (6.18).

Observe (Yao and Gao 2007) that to achieve the maximum adhesion strength of a fibrillar interface, one needs to homogenize the distribution of adhesion forces in order to attain the uniform stress distribution. This can be done with some degree of reliability, when $\varepsilon_1 \ll 1$. Recently, a continuum computational homogenization scheme was applied by Vossen et al. (2014) for developing a multi-scale model for a fibrillar interface.

2.5 Boundary Layer Problem

In Sect. 2.5, we have already encountered with a boundary layer problem. Indeed, Eq. (6.12) was derived by introducing the stretched coordinates (6.6) and by neglecting the effect of all other microcontacts. However, this approach does work only when the number of microcontacts N is fixed. If N is supposed to be a large parameter, then the cumulative effect of interaction with the other microcontacts may not be discarded without estimating its contribution. In particular, this requires evaluating the partial sums of infinite lattice sums $\sum_{i,j} K(\mathbf{0}, \mathbf{x}^{i,j})$. This question was considered with application to the frictionless contact problems for the cases of an elastic layer (Aleksandrov 2002) and an elastic half-space (Argatov 2012; Goryacheva 1998), i.e., when the approximation (6.11) applies on the entire contact interface. Moreover, in the adhesive contact problem, the consideration of the corresponding boundary layer problem is important for formulating the detachment criterion for individual microcontacts (see, e.g., Fleck et al. 2017; Khaderi et al. 2015).

3 Discussion and Conclusions

In the preceding sections, the main focus was put on the asymptotic analysis of the effect of elastic interaction between the individual microcontacts. In the absence of the interaction effect, the problem of detachment of multiple adhesive contact interface could be solved simply based on the solution of the adhesive contact problems for an individual contact. In particular, to determine the single fibre pull-off stress, Tang et al. (2005) applied the Dugdale–Barenblatt cohesive zone model. The generalized Griffith energy criterion in terms of the equivalent stress intensity factor was used by Carbone and Pierro (2012).

In the literature on bio-inspired adhesives, the mentioned above effect is called the effect of backing layer interaction (Bacca et al. 2016; Kim et al. 2007). Usually, the backing layer, which micropillars are attached to, has the form of an elastic layer, and thus, the thickness of the backing layer, h , should be added to the list of geometric parameters of the contact problem.

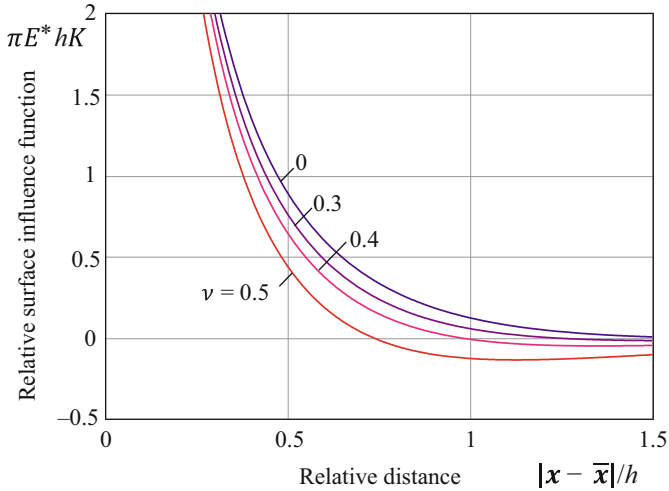


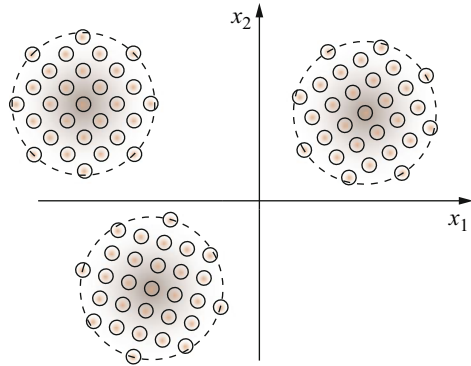
Fig. 6.4 Variation of the surface influence function for a bonded elastic layer for different values of the layer Poisson's ratio

In particular, the backing layer thickness h enters the expression for the surface influence function $K(\mathbf{x}, \bar{\mathbf{x}})$, which in the case of an elastic layer was evaluated in a number of works (Aleksandrov and Pozharskii 1998; Vorovich et al. 1974). It is known that for an elastic layer bonded to a rigid base, the value of $K(\mathbf{x}, \bar{\mathbf{x}})$ decays exponentially if the relative distance $|\mathbf{x} - \bar{\mathbf{x}}|/h$ increases to infinity (see Fig. 6.4). This means that for thin backing layers (to be more precise, when $h \ll R$), the interaction effect significantly weakens for any two microcontacts at a distance greater than a few thicknesses of the backing layer. This explains why the thinner the backing layer is, the higher is the total pull-off force.

It is to emphasize that the purpose of asymptotic modeling is to construct a discrete asymptotic model for multiple contact based on the asymptotic analysis of the corresponding continuous contact problem. The central moment in formulating the discrete adhesive contact problem is the detachment criterion for an individual microcontact (Fleck et al. 2017; Khaderi et al. 2015). This issue was discussed in more detail elsewhere (Argatov et al. 2019). But, it is still to underline here that the more accurate detachment criterion is (e.g., by accounting for non-axisymmetry of the local stress-strain state around a single microcontact), the more complicated would be the asymptotic model.

Observe that though the case of circular microcontacts was considered for the sake of simplicity of presentation, the described above steps of asymptotic analysis can be carried out for a fairly arbitrary contact spots (Argatov 2003). However, in the case of circular microcontacts, the detachment criterion can be formulated in a most simple way. Note also that the criterion of normal detachment for elliptical microcontact was discussed recently by Li et al. (2018).

Fig. 6.5 A system of regular clusters of circular microcontacts



Another simplification tentatively employed in our considerations is the lack of detailed analysis of the elastic deformation of pillars (Bacca et al. 2016; Paretkar et al. 2011). This shortcoming can be overcome by formulating a corresponding boundary layer problem, which accounts for the pillar geometry. Some useful information can be obtained from FEM studies available in the literature (Carbone and Pierro 2013) on the detachment mechanism for individual pillars. It is to note that the shape of individual pillars is an important factor, as it was shown that pull-off force and peel strength of biomimetic mushroom-shaped fibrillar adhesive microstructures can be more than twice as those of the flat-ended pillars (Gorb et al. 2006; Heepe et al. 2014).

Yet another simplification (or even oversimplification) concerns the multi-scale structure of biological adhesive systems (Kwak and Kim 2010) as well as of many artificial adhesives (Boesel et al. 2010). Our analysis involves primarily the asymptotic modeling approach for the multiple contact interface (see Fig. 6.5), and the introduction of two small parameters ε_1 and ε_2 , in principle, allows for application of a two-scale perturbation technique. In an analogous way, we can consider the case of a cluster of microcontacts, which, in addition are hierarchically positioned in the normal direction (Borodich and Savencu 2017; Kim and Bhushan 2007; Schargott 2009; Yang et al. 2017). It is more challenging to account for discrete fractality and self-similarity (Borodich and Onishchenko 1999), which reveals itself in various natural phenomena exhibiting threshold behavior (Borodich 1999). More than that, the analysis of the multi-scale elastic structures, e.g., mimicking gecko's seta/spatula assembly (Kwak and Kim 2010), will also require the use of another asymptotic methods, including those developed to the analysis of fields in multi-structures (Kozlov et al. 1999; Movchan 2006).

To conclude, the asymptotic modeling is a sufficiently flexible approach for the analysis of multi-scale problems, which, in particular, allows to simplify the original problem of multiple contact to a more simple one that is easily accessible for understanding of the governing mechanisms in multiple adhesive contact.

References

- Aleksandrov VM (2002) Doubly periodic contact problems for an elastic layer. *J Appl Math Mech* 66(2):297–305
- Aleksandrov VM, Pozharskii DA (1998) Non-classical mixed problems of the theory of elasticity [in Russian]. *Faktorial*
- Alexandrov VM, Shmatkova AA (1998) Indentation of a paraboloidal punch into an elastic layer and two paraboloidal punches into an elastic half-space. *Mech Solids* 33(4):125–130
- Argatov II (2003) Interaction of several dies on an elastic half-space. *Int Appl Mech* 39(9):1054–1059
- Argatov II (2004) Indentation of a punch with a fine-grained base into an elastic foundation. *J Appl Mech Tech Phys* 45(5):764–773
- Argatov II (2011) Electrical contact resistance, thermal contact conductance and elastic incremental stiffness for a cluster of microcontacts: asymptotic modelling. *Q J Mech Appl Math* 64(1):1–24
- Argatov II (2012) The contact problem for a periodic cluster of microcontacts. *J Appl Math Mech* 76(5):604–610
- Argatov II, Mel'nyk TA (2001) Homogenization of a contact problem for a system of densely situated punches. *Eur J Mech A/Solids* 20(1):91–98
- Argatov I, Li Q, Popov VL (2019) Cluster of the Kendall-type adhesive microcontacts as a simple model for load sharing in bioinspired fibrillar adhesives. *Arch Appl Mech* 89(8):1447–1472
- Arzt E, Gorb S, Spolenak R (2003) From micro to nano contacts in biological attachment devices. *Proc Natl Acad Sci* 100(19):10603–10606
- Bacca M, Booth JA, Turner KL, McMeeking RM (2016) Load sharing in bioinspired fibrillar adhesives with backing layer interactions and interfacial misalignment. *J Mech Phys Solids* 96:428–444
- Bensoussan A, Lions JL, Papanicolaou G (1978) *Asymptotic analysis of periodic structures*. North-Holland, Amsterdam
- Boesel LF, Greiner C, Arzt E, Del Campo A (2010) Gecko-inspired surfaces: a path to strong and reversible dry adhesives. *Adv Mater* 22(19):2125–2137
- Borodich FM (1998a) Parametric homogeneity and non-classical self-similarity. I. Mathematical background. *Acta Mech* 131(1–2):27–45
- Borodich FM (1998b) Parametric homogeneity and non-classical self-similarity. II. Some applications. *Acta Mech* 131(1–2):47–67
- Borodich FM (1999) Mathematical models of discrete self-similarity. *Math Comput Model Dyn Syst* 5(3):245–258
- Borodich FM, Onishchenko DA (1999) Similarity and fractality in the modelling of roughness by a multilevel profile with hierarchical structure. *Int J Solids Struct* 36(17):2585–2612
- Borodich FM, Savencu O (2017) Hierarchical models of engineering rough surfaces and bio-inspired adhesives. In: Heepe L, Xue L, Gorb SN (eds) *Bio-inspired structured adhesives: biological prototypes, fabrication, tribological properties, contact mechanics, and novel concepts*. Springer International Publishing, Cham, pp 179–219
- Borodich FM, Gorb EV, Gorb SN (2010) Fracture behaviour of plant epicuticular wax crystals and its role in preventing insect attachment: a theoretical approach. *Appl Phys A* 100(1):63–71
- Burns LA, Mouritz AP, Pook D, Feih S (2012) Bio-inspired design of aerospace composite joints for improved damage tolerance. *Compos Struct* 94(3):995–1004
- Carbone G, Pierro E (2012) Sticky bio-inspired micropillars: finding the best shape. *Small* 8(9):1449–1454
- Carbone G, Pierro E (2013) A review of adhesion mechanisms of mushroom-shaped microstructured adhesives. *Meccanica* 48(8):1819–1833
- Del Campo A, Greiner C, Arzt E (2007) Contact shape controls adhesion of bioinspired fibrillar surfaces. *Langmuir* 23(20):10235–10243

- Fleck NA, Khaderi SN, McMeeking RM, Arzt E (2017) Cohesive detachment of an elastic pillar from a dissimilar substrate. *J Mech Phys Solids* 101:30–43
- Galin LA (1980) Contact problems of the theory of elasticity and viscoelasticity [in Russian]. Nauka, Moscow
- Gladwell GML, Fabrikant VI (1982) The interaction between a system of circular punches on an elastic half space. *J Appl Mech* 49:341–344
- Gorb SN (2008) Biological attachment devices: exploring nature’s diversity for biomimetics. *Philos Trans R Soc A Math Phys Eng Sci* 366(1870):1557–1574
- Gorb S, Varenberg M, Peressadko A, Tuma J (2006) Biomimetic mushroom-shaped fibrillar adhesive microstructure. *J R Soc Interface* 4(13):271–275
- Goryacheva IG (1998) The periodic contact problem for an elastic half-space. *J Appl Math Mech* 62(6):959–966
- Greenwood JA (1966) Constriction resistance and the real area of contact. *Br J Appl Phys* 17(12):1621–1622
- Guidoni GM, Schillo D, Hangen U, Castellanos G, Arzt E, McMeeking RM, Bennewitz R (2010) Discrete contact mechanics of a fibrillar surface with backing layer interactions. *J Mech Phys Solids* 58(10):1571–1581
- Heepe L, Carbone G, Pierro E, Kovalev AE, Gorb SN (2014) Adhesion tilt-tolerance in bio-inspired mushroom-shaped adhesive microstructure. *Appl Phys Lett* 104(1):011906
- Hui CY, Jagota A, Shen L, Rajan A, Glassmaker N, Tang T (2007) Design of bio-inspired fibrillar interfaces for contact and adhesion—theory and experiments. *J Adhes Sci Technol* 21(12–13):1259–1280
- Ilyin AM (1992) Matching of asymptotic expansions of solutions of boundary value problems. AMS, Providence
- Kern MD, Qi Y, Long R, Rentschler ME (2017) Characterizing adhesion between a micropatterned surface and a soft synthetic tissue. *Langmuir* 33(4):854–864
- Khaderi SN, Fleck NA, Arzt E, McMeeking RM (2015) Detachment of an adhered micropillar from a dissimilar substrate. *J Mech Phys Solids* 75:159–183
- Kim TW, Bhushan B (2007) Adhesion analysis of multi-level hierarchical attachment system contacting with a rough surface. *J Adhes Sci Technol* 21(1):1–20
- Kim S, Sitti M, Hui CY, Long R, Jagota A (2007) Effect of backing layer thickness on adhesion of single-level elastomer fiber arrays. *Appl Phys Lett* 91(16):161905
- Kozlov V, Maz’ya V, Movchan AB (1999) Asymptotic analysis of fields in multi-structures. Oxford University Press, Oxford
- Kwak JS, Kim TW (2010) A review of adhesion and friction models for gecko feet. *Int J Precis Eng Manuf* 11(1):171–186
- Li Q, Argatov I, Popov VL (2018) Onset of detachment in adhesive contact of an elastic half-space and flat-ended punches with non-circular shape: analytic estimates and comparison with numeric analysis. *J Phys D Appl Phys* 51(14):145601
- Marchenko VA, Khruslov EY (1974) Boundary-value problems in domains with fine-grain boundaries [in Russian]. Naukova Dumka, Kiev
- Movchan AB (2006) Multi-structures: asymptotic analysis and singular perturbation problems. *Eur J Mech A/Solids* 25(4):677–694
- Nayfeh AH (2008) Perturbation methods. Wiley, New York
- Noderer WL, Shen L, Vajpayee S, Glassmaker NJ, Jagota A, Hui CY (2007) Enhanced adhesion and compliance of film-terminated fibrillar surfaces. *Proc R Soc A Math Phys Eng Sci* 463(2086):2631–2654
- O’Rourke RD, Steele TWJ, Taylor HK (2016) Bioinspired fibrillar adhesives: a review of analytical models and experimental evidence for adhesion enhancement by surface patterns. *J Adhes Sci Technol* 30(4):362–391
- Paretkar D, Kamperman M, Schneider AS, Martina D, Creton C, Arzt E (2011) Bioinspired pressure actuated adhesive system. *Mater Sci Eng C* 31(6):1152–1159
- Pepelyshev A, Borodich F, Galanov B, Gorb E, Gorb S (2018) Adhesion of soft materials to rough surfaces: experimental studies, statistical analysis and modelling. *Coatings* 8(10):350

- Popov VL, Pohrt R, Li Q (2017) Strength of adhesive contacts: influence of contact geometry and material gradients. *Friction* 5(3):308–325
- Schargott M (2009) A mechanical model of biomimetic adhesive pads with tilted and hierarchical structures. *Bioinspir Biomim* 4(2):026002
- Schargott M, Popov VL, Gorb S (2006) Spring model of biological attachment pads. *J Theor Biol* 243(1):48–53
- Sternberg E (1954) On Saint-Venant's principle. *Q Appl Math* 11(4):393–402
- Tang T, Hui CY, Glassmaker NJ (2005) Can a fibrillar interface be stronger and tougher than a non-fibrillar one? *J R Soc Interface* 2(5):505–516
- Tian Y, Pesika N, Zeng H, Rosenberg K, Zhao B, McGuiggan P, Autumn K, Israelachvili J (2006) Adhesion and friction in gecko toe attachment and detachment. *Proc Natl Acad Sci* 103(51):19320–19325
- Van Dyke M (1964) *Perturbation methods in fluid mechanics*. Academic, New York
- Vorovich II, Alexandrov VM, Babeshko VA (1974) *Non-classical mixed problems of the theory of elasticity [in Russian]*. Nauka, Moscow
- Vossen BG, Schreurs PJG, van der Sluis O, Geers M (2014) Multi-scale modeling of delamination through fibrillation. *J Mech Phys Solids* 66:117–132
- Yang W, Wang X, Li H, Song X (2017) Effects of hierarchical structures and insulating liquid media on adhesion. *Appl Surf Sci* 423:891–899
- Yao H, Gao H (2007) Mechanical principles of robust and releasable adhesion of gecko. *J Adhes Sci Technol* 21(12–13):1185–1212
- Zhou M, Pesika N, Zeng H, Tian Y, Israelachvili J (2013) Recent advances in gecko adhesion and friction mechanisms and development of gecko-inspired dry adhesive surfaces. *Friction* 1(2):114–129

Chapter 7

Spreading of Red Caviar Cells: The Knife-Cell and the Cell-Cell Adhesive Interactions



Feodor M. Borodich and Stanislav N. Gorb

Abstract Caviar is a spread that consists of salt-cured fish roe (fish-eggs). It has been recommended to recovering patients, because it supports healing due to the great variety of useful elements that have been found in high quantities in caviar. Especially popular are salmon and trout roe also known as ‘the red caviar’, e.g. salmon salt-cured roe. However, caviar is usually considered as a delicacy because it is rather expensive. In addition to the benefits of red caviar for health and nutrition, the fish-eggs are a very convenient object for studying adhesive properties of cells. Indeed, the large dimensions of red caviar cells simplify the conditions of tests and increase their precision. Although the structure of a caviar cell (salted fish egg) membrane differs from the phospholipid bilayer structure of many other biological cells, the obtained results may help to understand biological contact phenomena. The present study is dealing with experimental studies and modelling of cell-cell and cell-knife (cell - inorganic hard surface) adhesion. The difficulties in both modelling of the contact interactions by Hertz and JKR theories, and experimental studies of cells having fast drying surfaces along with varying adhesive properties of cells are discussed. It is argued that the results can be used for modelling interactions between collagen based shells and other materials.

Keywords Salt-cured fish roe · Fish-eggs · Collagen based shells · Contact models · Experimental probing of caviar shells

F. M. Borodich (✉)
School of Engineering, Cardiff University, Cardiff, UK
e-mail: [BorodichFM@cardiff.ac.uk](mailto:borodichfm@cardiff.ac.uk)

S. N. Gorb
Department of Functional Morphology and Biomechanics, Zoological Institute, Kiel University,
Kiel, Germany

1 Introduction

In this paper we study contact properties of caviar. We will present results of experimental studies of contact interactions between two caviar cells (salted fish eggs), and between a caviar cell and a knife. The latter we model as a flat rigid surface. It is shown that adhesive properties of caviar have huge influence on these interactions. Therefore, theoretical modelling of contact properties of caviar has to include adhesive interactions.

Let us discuss terminology. In most Slavic languages the term ‘ikra’ means both roe, i.e. the released external egg masses of fish or some other various marine animals, and salt-cured fish roe used as a food. The word caviar has its origin in Persian and Turkic languages, e.g. it sounds as ‘havyar’ in Turkish. Originally, it denoted curried fish eggs of sturgeon from Black Sea, Sea of Azov and Caspian Sea. In this paper, we use the term caviar to denote salt-cured fish roe used in food industry. Hence, we do not bound the use of this term only for sturgeon roe as it is restricted in some places. The salted sturgeon roe is referred further as *black caviar*, while salmon and trout salted fish eggs are called further *red caviar*.

Both red and black caviars have great nutritional value. Indeed, they contain a lot of omega three fatty acids. Caviar has been recommended to recovering patients because it supports healing due to the great variety of useful elements that have been found in high quantities in caviar. Especially popular is salmon and trout red caviar, because it contains 30% protein and many nutrients vitally important for the human health. Caviar can be used as a spread (Fig. 7.1).

Caviar is usually considered as a delicacy, and currently the black caviar of beluga (one of several species of sturgeon) is the most expensive one. However, it was not very expensive in the past. One of the authors (FB) remembers about his visit to the Krasnodar city market in 1967. That year a 80 cl glass jar of Sea of Azov sturgeon black caviar costed less than a 10 kg water melon. However, thirty years later black caviar became extremely expensive. In 1997, a Russian artist Andrey Logvin created an iconic poster, where it is written by black caviar on a background of red caviar “Live has been going successfully” or “Live is a success”. This poster from Tretyakov Gallery collection in Moscow, expressed an irony on self-admiration and optimism of the so-called ‘new Russians’ (Russian

Fig. 7.1 Red caviar as a spread



Fig. 7.2 Andrey Logvin's poster "Live has been going successfully" or "Live is a success" (1997) written by black caviar on a background of red caviar (Tretyakov Gallery collection, Moscow)



and the former Soviet Union 'nouveau riche's), who robbed their own countries (Fig. 7.2).

From the contact mechanics point of view, the fish eggs are a very convenient object for studying adhesive properties of cells. Indeed, the large dimensions of caviar cells simplify the conditions of tests and increase their measurement precision. One needs to realize that caviar cells, in addition to a thin phospholipid bilayer (typical for most of living cells), are surrounded by the fish chorion (Olivar 1987; Rubzov and Chernyaev 1989) that is a relatively thick membrane (envelope) having complex structure. It may have 3–6 layers and contains micropyles (tiny channels that allow sperm to penetrate the membrane). It was reported by Kobayashi (1982) that the envelope of the egg of chum salmon, *Oncorhynchus keta*, consists of three layers: the outer adhesive coat, zona pellucida externa and interna, while the eggs of *Coregonus peled* consist of six layers (Rubzov and Chernyaev 1989).

Surprisingly, there are just a few works dedicated to the detailed studies of mechanical properties of fish-eggs (e.g. Iuchi et al. 1996; Pillarisetti 2008), where rainbow trout (*Oncorhynchus mykiss*), salmon, flying fish and zebrafish (*Danio rerio*) egg cells were studied. Usually, the fish eggs were studied by special devices designed for measuring the strength (the breaking strain) of the egg membrane (see discussion by Zotin (1961)). The egg could be smashed by an inclined surface as in the scheme suggested by Gray (1932) (Fig. 7.3) or the egg could be compressed between two parallel surfaces as in the scheme suggested by Cole (1932) (Fig. 7.4).

The Cole experiment is used more often than the Gray one, because, as it was noted by Harvey (1937), Cole (1932) employed the equation for a thin vessel and by measuring the force (F) necessary to flatten the vessel (a cell) a given amount, he determined not only the tension of the unflattened egg, but also he calculated values for the increase in tension as the surface area increased on flattening.

Although Cole (1932) applied his device for studying sea urchin eggs (see e.g. Davidson et al. 1999), this kind of experiments are still very popular in application to fish-eggs (Zotin 1961; Suga 1963; Rubzov and Chernyaev 1989; Smeshlivaya 2015). The Cole experiments are also very popular in application to sea urchin eggs. Davenport et al. (1986) studied chorion strength of marine teleost eggs using three different experiments: by tearing isolated chorions, by bursting eggs (the Cole experiment), and by penetrating eggs with a fine needle.

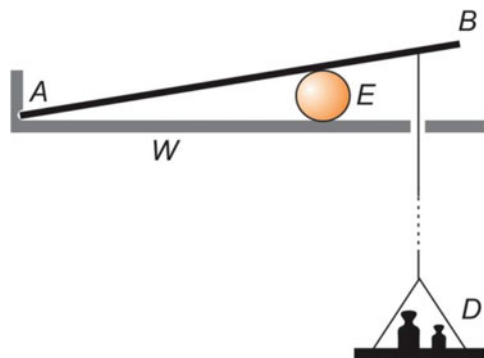
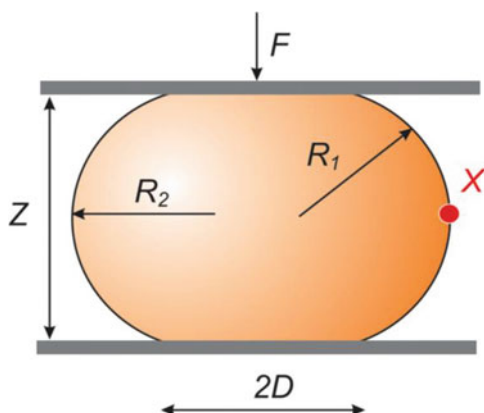


Fig. 7.3 The Gray apparatus for measuring the breaking strain of the chorioon of the fish egg (after Gray, (1932) and Yoneda (1964)). A glass plate AB is hinged firmly but lightly at one end A to a slab of smooth hard wood W . A balance scale (D) is attached to the end B . An egg (E) is placed between the glass plate and the wood, and weights are added to the scale pan until the egg ruptures

Fig. 7.4 The Cole apparatus for measuring the breaking strain of the chorioon of the cell (after Cole, (1932) and Yoneda, (1964)).

Diagrammatic representation of the compressed egg viewed from side. F , force exerted on the egg. X , a point on the cell surface on the equatorial plane. R_1 and R_2 , radii of principal curvatures at the point X . Z , thickness of the egg. D , radius of the area of contact A . $A = \pi D^2$



A description of the Cole experiment may be found elsewhere (see, e.g. Yoneda 1964). The cell (egg) is compressed between two parallel plates. The internal pressure (P), that is calculated as the ratio of the external compressing force (F) and the area of the contact region ($A = \pi a^2$), is in equilibrium with the tension within the membrane (T). The equation of equilibrium at the point X on the equatorial plane, can be written as

$$P = T (1/R_1 + 1/R_2)$$

where R_1 and R_2 are the radii of the principal curvatures of the cell surface at the point X . Cole (1932) found that the tension increases as the surface area increased by flattening and concluded that the membrane is elastic.

Although we follow the established experimental practice and the caviar cells will be compressed between two parallel plates, we do not follow the above described Cole experiment. Instead of this, we present here the results of experiments of depth-sensing indentation (DSI) on the cells. Following the terminology of the Chapter title, we can say that compression of a single caviar cell between two parallel plates is a model of knife-cell or plate-cell interactions, while compression of a caviar cell by another cell is a model of a cell-cell interactions. The fork-cell interactions (penetration of a cell by a fine needle see e.g. Davenport et al. 1986, Pillarisetti 2008) cannot be described using a geometrically linear formulation of the contact problem and, therefore, these problems are out of the scope of this Chapter. The same is related to micropipette aspiration techniques (Mitchison and Swann 1954). Since the Chapter reports the first detailed DSI experiments on caviar cells (the salt-cured fish-eggs), our purpose is to describe qualitatively the specific features of the caviar cell deformations at tests conducted in air and underwater conditions. Hence, we intentionally do not specify the external load values, saying that the force may have arbitrary units, however, we provide our explanations of the observed phenomena.

First, we discuss some theoretical aspects related to the modelling of contact interactions between caviar cells (cell-cell interactions) and between a caviar cell and an inorganic hard surface (the cell-knife interactions). Both non-adhesive Hertz-type contact interactions and adhesive models are considered. Then we present results of experimental studies and describe some difficulties of the experimentation due to continuously altering contact interactions caused by fast drying caviar surfaces and variations of adhesive properties of the cells. It is argued that the herewith presented combination of experimental and theoretical results can be used for modelling interactions between collagen-based shells and other materials.

2 Preliminaries: Theoretical Aspects of Indentation

Contact mechanics provides the theoretical basis for indentation tests and experiments on compression of cells. The formulations of various problems of contact mechanics may be found in many monographs and textbooks (see, e.g. Love 1893; Galin 1961; Johnson 1985; Argatov and Dmitriev 2003; Popov 2010). A detailed discussion of the connection between contact problems and indentation tests was given by Borodich (2014). For the sake of completeness, we will include here some results related to contact problems and clarify several points that may help to avoid misinterpretation of the experimental results. Indeed, Chaudhri and Lim (2007) argued that the current methods of nanoindentation data analysis may lead to incorrect and misleading results. The same is related to contact probing of both non-adhesive and adhesive samples by spherical indenters. One should apply the known solutions of the contact problems taking into account the specific features of the tests.

Usually, the full investigation of a boundary value problem describing contact between two solids includes finding the displacement and stress fields in contacting solids assuming that the material properties of materials of the solids are known as well as the shapes of the solids. However, testing of materials is an inverse problem to the contact mechanics. From an indentation test, one can get the value of the external force applied to the indenter and some parameters measured in the test, e.g. the size of an imprint in a plastic sample. Then one has to use these parameters to estimate the mechanical properties of materials or structures tested. Therefore, it is very important to have theoretical relations connecting the depth of indentation δ and the value of the external load P applied to the indenter. We will see that sometimes it is impossible to get an explicit relation indentation $P(\delta)$ and the connection can be found in a parametric form. For example, in an axisymmetric contact (contact between solids of revolution), both $P(a)$ and $\delta(a)$ may be given as functions of a parameter, in this case the parameter is the radius a of the contact region.

For formulation of contact problems, it is convenient to employ both the Cartesian and cylindrical coordinate frames, namely $x_1 = x$, $x_2 = y$, $x_3 = z$ and r , θ , z , where $r = \sqrt{x^2 + y^2}$, $x = r \cos \theta$, $y = r \sin \theta$.

2.1 Non-adhesive Hertz-Type Contact Problems

Contact mechanics started from pioneering works of Hertz (1882) and Boussinesq (1885). Following Love (1893), we place the origin (O) of two Cartesian systems of coordinates at the point of initial contact between two bodies. Let us assume that axes x and y be the same for both bodies, axes z^+ and z^- be directed along normals to the two bodies drawn towards the inside of each. Then the shapes of contacting bodies can be described as

$$z^+ = f^+(x, y), \quad z^- = f^-(x, y),$$

where the common tangent plane at O is taken as the x, y plane. Here the upper and lower indices $+$ and $-$ mean that the values are attributed to the upper and lower body, respectively.

Hertz showed that the formulation of a contact problem between two linear elastic, isotropic solids is mathematically equivalent to the contact problem between an indenter whose shape function f is equal to the initial distance (the gap) between the surfaces, i.e., $f = f^+ + f^-$, and an elastic half-space, whose contact modulus E^* is constructed from the contact moduli of contacting elastic solids

$$(E^*)^{-1} = (E_+^*)^{-1} + (E_-^*)^{-1}.$$

Here E_+ , ν_+ , E_- , ν_- are the Young moduli and the Poisson ratios of the upper and lower body, respectively, and the contact moduli of the solids are

$$E_+^* = \frac{E_+}{1 - \nu_+^2}; \quad E_-^* = \frac{E_-}{1 - \nu_-^2}.$$

Hertz argued that the shape functions of smooth, convex, three-dimensional (3D) solids may be well described as elliptic paraboloids

$$z^+ = A^+x^2 + B^+y^2, \quad z^- = A^-x^2 + B^-y^2.$$

If we use the equivalent rigid indenter, then its shape in Hertzian approximation is given by

$$z = Ax^2 + By^2.$$

If we consider contact of two elastic spheres, then the equivalent sphere is

$$z = Ar^2 = \frac{1}{2R_{ef}}r^2, \quad \frac{1}{R_{ef}} = \frac{1}{R_+} + \frac{1}{R_-}$$

where R_+ and R_- are the radii of the spheres and R_{ef} is the equivalent radius.

Note that if one of contacting bodies is rigid then its Young and contact moduli are equal to infinity. If one of contacting bodies is flat, then its radius is equal to infinity. It is clear that the problem described by Fig. 7.5a involves the solution of one Hertz contact problem with an effective radius $R_{ef} = R/2$ and $(E^*)^{-1} = 2(E_+^*)^{-1}$ (indeed, $1/R_{ef} = 1/R + 1/\infty = 2/R$), while the problem described by Fig. 7.5b involves formally solutions of three Hertz contact problems: one with an effective radius $R_{ef} = R/2$ and $(E^*)^{-1} = 2(E_+^*)^{-1}$, and two problems with effective radii $R_{ef} = R$ and $E^* = E_+$. Indeed, $1/R_{ef} = 1/R + 1/\infty = 1/R$, i.e. $R_{ef} = R$ and $(E^*)^{-1} = (E_+^*)^{-1} + 1/\infty$, i.e. $(E^*)^{-1} = (E_+^*)^{-1}$.

In the case of compression of a rather soft caviar cell by a hard indenter made of diamond, sapphire or even from polymethylmethacrylate ($E_+ \cong 3 \text{ GPa}$, $\nu_+ \cong 0.39$), one can take the ratio of the contact moduli of the cell and the indenter as $E_-^*/E_+^* \cong 0$ and, therefore, $E^* \cong E_-^*$.

For the sake of simplicity, let us consider the indenter as a rigid body. In contact mechanics, the compressing force P is considered as positive. It follows from the Hertz solution that the depth of indentation (δ) of the nose of the sphere depends on the external force (P) as

$$\delta = \left(\frac{9}{16} \frac{1}{R(E^*)^2} \right)^{1/3} P^{2/3}, \quad a = \left(\frac{3}{4} \frac{R}{E^*} \right)^{1/3} P^{1/3}.$$

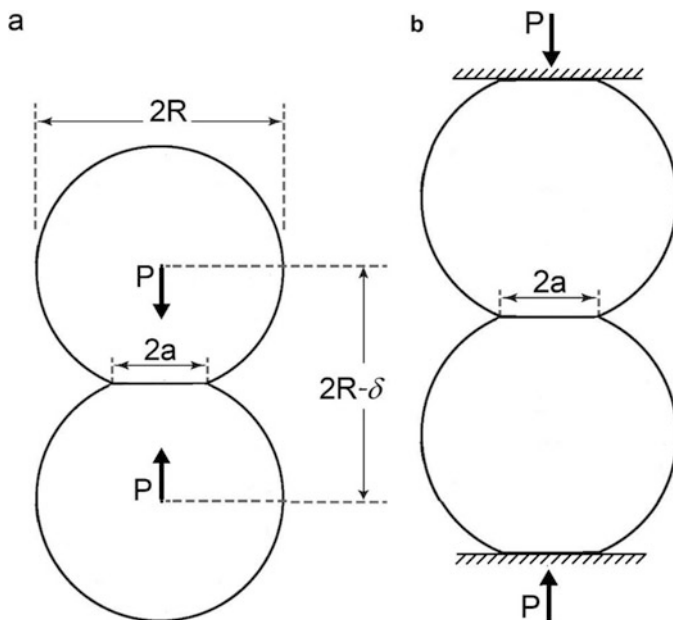


Fig. 7.5 Schematic image of Hertzian contact between two identical elastic spheres of radius $R_+ = R_- = R$ under external load P : (a) contact between spheres loaded at their centers; (b) contact between spheres compressed between two rigid flat surfaces

If the indenter is not rigid, then δ is the approach of solids. This problem is equivalent to the problem of contact between an elastic sphere of an effective radius $R_{ef} = R/2$ and a rigid flat surface (see Fig. 7.5a.)

Boussinesq (1885) solved the contact problem for a circular flat-ended indenter of radius a . He found

$$\delta = \frac{P}{2aE^*}.$$

Love (1939) solved the contact problem for a circular rigid conical indenter

$$z = f(r) = B_1 r = r \cot \alpha$$

of an included semi-vertical angle α . He found

$$\delta = \frac{\pi}{2} B_1 a, \quad P = \frac{\pi}{2} E^* B_1 a^2, \quad \delta = \left(\frac{\pi}{2} \frac{B_1}{E^*} \right)^{1/2} P^{1/2}.$$

As it follows from the above discussion, the above Love's solution is valid, if one assumes that the contact modulus of the indenter is sufficiently higher than the modulus of the sample because in this case $E_-^*/E_+^* \cong 0$ and, therefore, $E^* \cong E_-^*$. One cannot apply the Hertz contact theory to the elastic cone due to the violation of the main assumptions of the theory. As it was noted by Chaudhri (2001), many authors calculate the contact modulus using elastic characteristics of both materials: the sample and the sharp indenter (pyramid or cone). It is evident that one cannot model a cone as a half-space. In addition, the use of Love's solution assumes that one neglects the stress field singularity near the tip of the cone.

If a cell is modelled as an elastic solid and one neglects the adhesive interactions, then the Hertz theory is applicable. In the framework of the theory, the following cases are of importance for a spherical cell of radius R_c or two cells of the same radius.

The cell is compressed between two planes. Then the total approach between the planes δ is the sum of δ_1 and δ_2 that are the approaches between the elastic semi-sphere of effective radius $R = R_c$ and the upper and the lower planes, respectively. We assume that either the planes are much harder than the cell or they are made of the same material, then $\delta_1 = \delta_2$ and $\delta = 2\delta_1$ (see Fig. 7.5).

The cell is placed on a flat base and it is in contact with a spherical probe of radius R_s . Then the total approach between the upper and lower poles of the cell $= \delta_1 + \delta_2$ where δ_1 is the approach between the elastic semi-sphere of effective radius $R = R_c$ and the base, and δ_2 is the approach between the elastic semi-sphere of effective radius R , $(R)^{-1} = (R_c)^{-1} + (R_s)^{-1}$, and the spherical probe.

The cell is placed on a flat base and it is in contact with a conical probe. Then the total approach between the upper and lower poles of the cell $= \delta_1 + \delta_2$, where δ_1 is the approach between the elastic semi-sphere of effective radius $R = R_c$ and the base, and δ_2 is the approach between a rigid cone and an elastic half-space whose elastic properties are the same as the properties of the cell.

Two cells are attached to the upper and the lower planes, respectively, and the upper cell is in contact with the lower cell. Then the total approach between the cells δ is the sum of $2\delta_1$ and δ_2 where δ_1 is the approach between the elastic semi-sphere of effective radius $R = R_c$ and the base, and δ_2 is the approach between a rigid plane and an elastic semi-sphere of effective radius $R = 0.5R_c$.

As it will be seen from photographs, the adhesive effects are very important in problems of contact loading of caviar cells and, therefore, one needs to use the adhesive contact mechanics approach.

2.2 Adhesive Contact Problems in Geometrically Linear Formulation

Mechanics of adhesive contact between elastic spheres was founded by Derjaguin (1934). In his pioneering paper, Derjaguin studied both adhesion between rigid

particles and elastic ones. He argued that elastic deformations should be taken into account. He also introduced the so-called Derjaguin approximation that is used explicitly or implicitly in an overwhelming number of papers on mechanics of adhesive contact. Finally, he introduced the approach based on calculating the total amount of energy involved in contact. The classic JKR (Johnson-Kendall-Roberts) and DMT (Derjaguin-Muller-Toporov) theories are based on the same energy approach (Johnson et al. 1971; Derjaguin et al. 1975), when distances between contacting surfaces are small, while the JKR theory assumes that the adhesive forces act only within the contact region.

For a contact with a resultant radius R , the adjusted JKR deflection is defined by a summation with classical Hertz deflection, in equivalent notation $\left(\frac{a^2}{R}\right)$, and effect induced by adhesion:

$$\delta_{JKR} = \left[\left(\frac{a^2}{R}\right) - \sqrt{\frac{2\pi w a}{E^*}} \right].$$

The radius $a(P)$ (we have denoted it above as $a_{JKR}(P)$) resulting from loading with adhesion is:

$$a^3 = \frac{3R}{4E^*} \left(P + 3w\pi R + \sqrt{6\pi R w P + (3wR)^2} \right);$$

Here w is the work of adhesion, i.e. the energy needed to separate two surfaces from contact to infinity.

It follows from the JKR theory that an elastic adhesive sphere has non-zero initial radius of contact zone $a(0)$ (see Figs. 7.6b and 7.7)

$$a(0) = \frac{9\pi w R^2}{2E^*}.$$

If the force P is equal to zero, then according to the DMT theory, the contact radius is also zero (the same as in the Hertz contact theory), while according to the JKR theory, the solids have non-zero contact at radius $a(0)$ at $P = 0$ due to adhesion, as it has just been shown above. As it will be shown below, experiments show that $a(0) \neq 0$. Thus, we will not discuss further the DMT theory.

3 Experimental Studies

The caviar cells were taken from a can bought in a supermarket in Kiel (wild salmon caviar from gorbusha). The experimental studies consisted of two parts: the initial

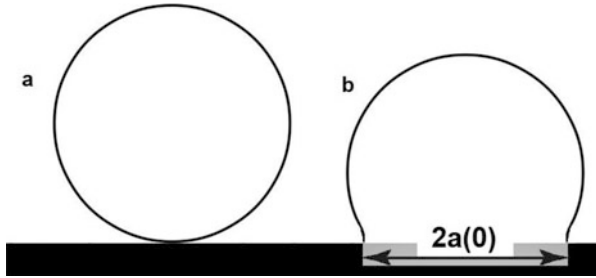
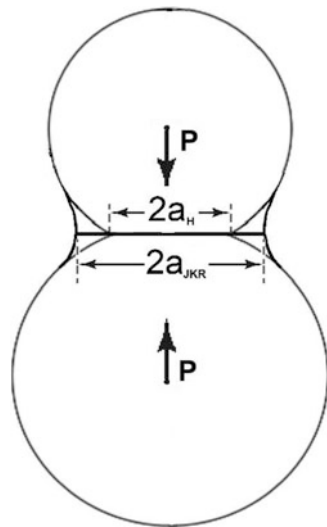


Fig. 7.6 Schematic image of initial contact between an elastic sphere of radius R and a rigid flat surface without external load ($P = 0$): (a) initial point contact according to the Hertz and DMT theories; (b) initial contact with non-zero radius according to the JKR theory

Fig. 7.7 Schematic image of contact between two elastic spheres under external load P without consideration of adhesive interactions (the Hertz theory) and adhesive contact according to the JKR theory. Note that the radius of contact region $a_H(P)$ calculated according to the Hertz theory is smaller than the radius of contact region $a_{JKR}(P)$ calculated according to the JKR theory



tests to get some information on hydration and dehydration of caviar cells, and DSI tests for a single caviar cell and two interacting cells.

3.1 Experimental Device

The Basalt-1 force tester (Tetra GmbH, Germany) was employed for experimental loading of caviar cells. The tester has a flat moving horizontal glass table (“knife”) that is assumed to be infinitely rigid. We would like to remind that the table in this paper is a model of a knife and the horizontal base is a model of a dish. Therefore, we have a caviar fish egg between a dish and a knife, and interactions between two caviar eggs adhered to the dish and the knife, respectively. The interacting force between the moving table and the sample was recorded as a force versus time curve.

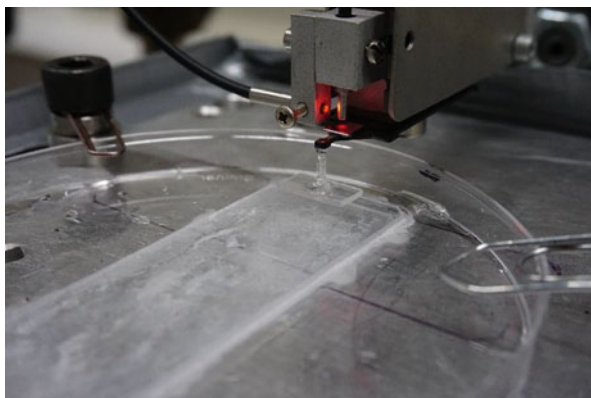


Fig. 7.8 The used Basalt-1 force tester (Tetra GmbH, Germany) for measuring the load-displacement curves of the caviar cells. The tester has a flat moving horizontal glass table (“knife”) that is assumed to be infinitely rigid

One can find a detailed description of the used Basalt-1 force tester (Tetra GmbH, Germany) by Perepelkin et al. (2019a, 2020, 2021). The same tester with a spherical probe was also used previously for adhesion measurements of the attachment pads of insects and for testing the performances of both Borodich-Galanov (BG) and the extended BG (eBG) methods to evaluate elastic and adhesive properties of materials (Borodich et al. 2012a, b, 2013). All experiments were carried out at room temperature (22–24 °C) and at a relative humidity of 47–56%. An accuracy of about 10 μN was achieved for force measurements. The spring constant was determined with an accuracy of approximately ± 2.5 N/m. The load-displacement curves of the caviar cells were measured with the same value of the maximum displacement (Fig. 7.8).

The displacement of the horizontal moving table attached to a glass cantilever beam with known spring constant was detected by the fiber-optic sensor (see Fig. 7.6).

The experimental DSI studies were concentrated mainly on two schemes: (i) a single caviar cell was located on a horizontal base and it was compressed by a horizontal moving table (the cell-knife interactions); (ii) a single caviar cell located on a horizontal base was compressed by another caviar cell attached to the horizontal moving table (the cell-cell interactions) (Fig. 7.9).

3.2 Hydration and Dehydration of Caviar Cells

We would like to note that the experimental measurements were mainly carried out by our colleagues Dr. N. Perepelkin and Dr. A. Kovalev. The experiments were performed for both fresh intact uncured fish roe and for red caviar (the salt-cured fish

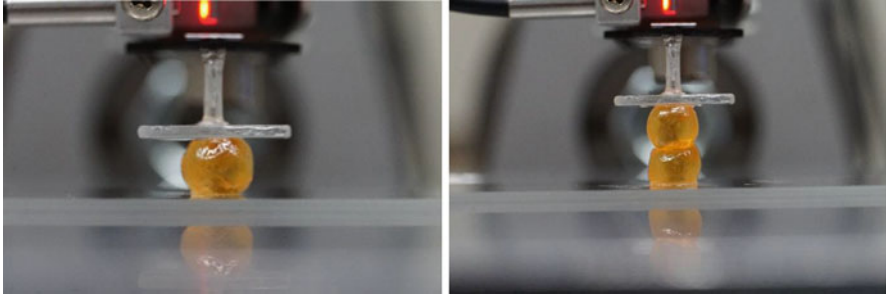


Fig. 7.9 Contact testing the caviar cells by the Basalt-1 force tester: (a) Compression of a single caviar cell; (b) compression of two caviar cells in contact

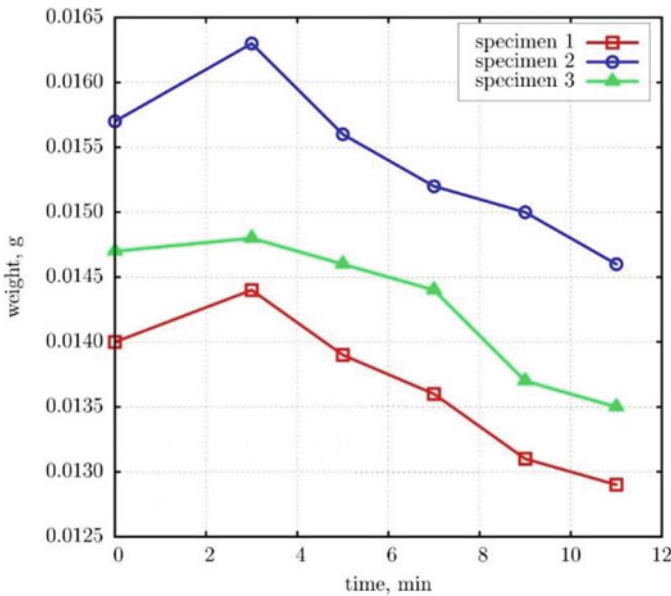
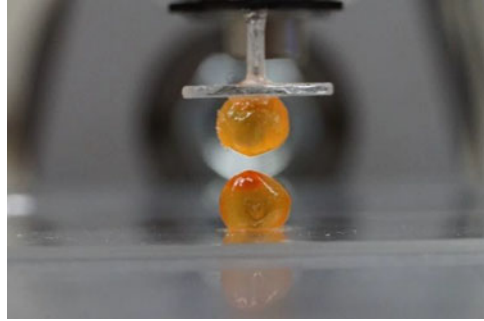


Fig. 7.10 The hydration and dehydration of caviar cells: hydration during the first 3 min. and dehydration of the cells during the next 8 min

roe). The former studies are out of the scope of the current work. Here we worked with salt-cured fish roe. In the first series of tests, several caviar cell eggs were put into distilled water for 3 min and then air-dried for next 8 min. Their weight was monitored (see Fig. 7.10).

Analysing Fig. 7.10 graphs, one can see that being in the water, a cell absorbs some amount of water (about 2–3% of its initial mass), while it loses about 8% of its initial mass during the further dehydration. Even after the hydration, the cell membrane was not in tension, while after the dehydration the cell surfaces became

Fig. 7.11 Separation of cells. The cells stuck to knife (upper cell) and dish (lower cell), respectively. One can observe non-zero contact region between both rigid substrates and cells under zero load



rather hard. In another experiment, an egg was kept in distilled water for 30 min. Significant changes of the egg shape were recorded.

It is clear that the mechanical properties of fish-eggs in natural environment and salt-cured caviar cells are rather different. The difference is caused not only by salty environment but also by dehydration of caviar cells. Indeed, it is known (Lebedeva 1985; Rubzov and Chernyaev 1989) that a mature fish-egg of initial diameter 1.5 mm after 40 h long water treatment solidifies and strongly swells up to diameter 2.25 mm. Thus, the surface area of the cell increases from 7.07 to 15.90 mm², and the volume increases from 1.77 to 5.96 mm³, which results in the three-fold extension of the outer shell.

If a caviar cell interacted with a knife or dish without any preliminary hydration, then the characteristic size of the contact region between the cell and the substrate was very large (see Fig. 7.11). It is clear that the main assumption of the Hertz and DMT theories that the initial contact is at a single point (see Fig. 7.6a) was violated.

3.3 *Depth-Sensing Indentation of Caviar Cells*

It is known (see, e.g. Borodich 2014) that the depth-sensing indentation (DSI) techniques mean that a material sample is probed by an indenter loaded by the force P and the displacement δ (the approach of the distant points of the probe and the sample) is measured. The load and the displacement are recorded as functions of time t and using functions $P(t)$ and $\delta(t)$ the $P - \delta$ relation can be established. The DSI techniques were introduced in the Laboratory of Tribology led by Prof. M.M. Khrishchov by his PhD student Kalei (Kalei 1968). The DSI techniques are widely used for estimations of properties of small or very thin material samples. The above-mentioned solutions to contact problems for a sphere, a cone and a flat-ended circular punch were used by Bulychev et al. (1975) in order to derive the famous BASH relation for the slope S of the $P - \delta$ curve

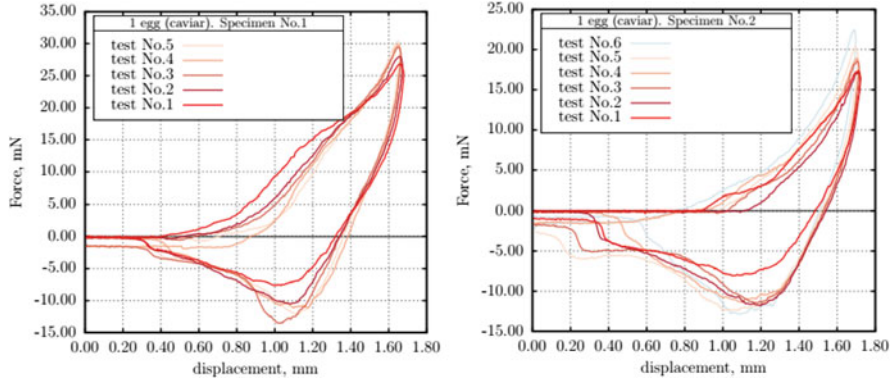


Fig. 7.12 Force-displacement curves observed for the single caviar cell DSI tests for two different caviar cells

$$\frac{dP}{d\delta} = 2aE^* = 2E^* \sqrt{\frac{A}{\pi}},$$

where A is the area of the contact region. Note that if the former of the above equalities flows from the exact solution of Hertz-type contact problems, the latter is an approximation that is exact only for axisymmetric problems. The BASH relation and its modifications are the corner stone of modern depth-sensing indentation techniques that involves nanoindenters with pyramidal tips.

Formally, the BASH relation allows to estimate the contact modulus of tested materials from the unloading branch of the force-displacement curve (see the critique of the BASH approach by Borodich (2014), Galanov and Dub (2017), and Perepelkin et al. (2019a)). However, the usefulness of the sharp pyramidal or conical relations in application to caviar cells is rather doubtful, because sharp indenters may penetrate the cell membrane. Hence, the flat indenters were employed in our study.

The results of several DSI tests are presented in Figs. 7.12 and 7.13. One can see in Fig. 7.12 that the dependance of the curve from the loading-unloading cycle number is small. The hysteresis effect is clearly observable. The tests were performed with a fixed prescribed value of the maximum displacement of the knife (rigid table).

Because we did not plan to use sharp indenters for studying mechanical properties of fish eggs, it was initially planned to employ a modification of the BG method (Borodich and Galanov 2008) for evaluation values of the elastic contact modulus E^* and work of adhesion w of caviar cells. However, there arose some difficulties for realization of the plan.

The BG method can be described in the following way. A tested sample of material is loaded by a spherical indenter (a DSI test). Then the $P - \delta$ curve transformed to dimensionless form using two scaling parameters: one for applied

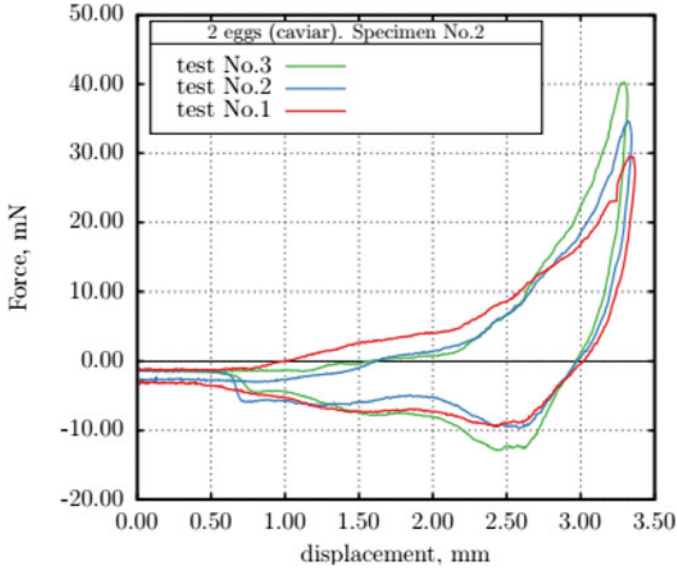


Fig. 7.13 Force-displacement curves observed for DSI tests of compression of two caviar cells (the specimen 2). The hysteresis effect is clearly observable, though the dependence of the curve from the loading-unloading cycle number is small). The tests were performed with a fixed prescribed value of the maximum displacement of the knife (rigid table)

loads and one for recorded displacements. The dimensionless $P - \delta$ curve (this means that the new loads and the displacements made dimensionless using the scaling parameters) is fitted by well-established theories of adhesive contact; these were the JKR and DMT theories. The values of the scaling parameters are estimated after the curve fitting procedure. The seeking estimations for E^* and w may be found from the values of the scaling parameters. It is clear that the seeking values of E^* and w were not measured directly, but rather estimated in a non-direct way. It was found experimentally and by means of numerical simulations that the procedure of the BG method is quite fast and robust (see Borodich et al. 2012a, b, 2013).

Recently the BG method was significantly extended mainly by efforts of Dr. N. Perepelkin (Perepelkin et al. 2019a). The modifications of the extended BG (eBG) method were related not only to the introduction of the orthogonal distance fitting (ODF) approach instead of the least-square approach, and an introduction of a new objective functional of the BG method based on the ODF concept, but they included an extension of the BG method to a general class of mathematical models of adhesive contact, when the external load and the displacement of the indenter are defined as parametric functions of the contact radius along with a new approach to fitting that drastically reduces the computational costs of the fitting procedure. New series of experimental tests confirmed that both the original BG and eBG methods are very robust in application to linear elastic materials (Perepelkin et al. 2019a, 2020).

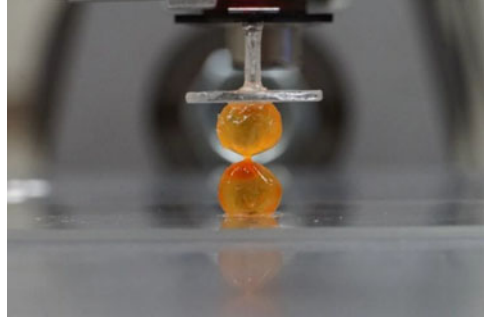
The original JKR model (Johnson et al. 1971) was developed for describing contact between two linearly elastic spheres. However, later the JKR approach was extended to any material with rotational symmetry of the elastic properties, in particular for transversely isotropic solids and homogeneously prestressed solids (Borodich 2014; Borodich et al. 2014, 2021). In the recent paper Perepelkin and Borodich (2021) have developed an explicit form of solution to the general JKR-type problems without specifying any *a priori* conditions except the validity of the superposition principle and axial symmetry. Hence, the eBG method can be applied to study any axisymmetric contact problem for materials having linear or linearized properties. Borodich et al. (2021) argued that to consider contact problems for biological cells, one needs to take into account the initial prestress of the cell membrane.

Taking into account these very far extensions of the JKR formalism, it was planned to apply the eBG method to the caviar cells. However, the problem is more difficult than it was initially estimated. Indeed, one can observe in Figs. 7.9 and 7.11 that cells from a caviar can demonstrate significant deviations from spherical form. In addition, the JKR theory is not directly applicable to non-linear viscoelastic materials, while the effects of viscoelasticity may be significant in the case of caviar cells. Finally, adhesive mechanisms involved in interactions between cell surfaces are not reduced to van der Waals interactions. In fact, these interactions involve rather sticky materials covering the cell surfaces.

One of confirmations of the last statement is the following. It follows from the JKR theory and its extensions that as soon as the external tensile load between an elastic sphere and a rigid plane or between two elastic spheres reaches the critical value ($P = P_c$), there is an abrupt separation between the surfaces (to get the full theoretical graphs of the JKR theory, one needs to reduce the external load; this condition is not usually realized in experimental devices). The critical load P_c corresponds to the lowest point of the $P - \delta$ curve. However, one can observe in Fig. 7.12 that there is no abrupt separation between the surfaces, while the tensile force decreases gradually with an increased distance between the surfaces, i.e. when the distance between the knife and the dish increases (the distance between the support and the flat surface of the experimental table). The experimental $P - \delta$ curve obtained for another experimental scheme of interactions between two caviar eggs adhered to the dish and the knife, respectively (see Figs. 7.9b and 7.11), is presented in Fig. 7.13. One can see in Fig. 7.13 that the values of tensile forces decrease even slower than in experiments on loading of a single caviar cell.

In fact, this is not a new observation. As early as in XVII century, Robert Hooke discussed the adhesion phenomena based on his observations of liquors, syrups, and other “tenacious and glutinous bodies,” he wrote (Hooke 1665) “*it is evident, that the Parts of the tenacious body, as I may so call it, do stick and adhere so closely together, that though drawn out into long and very slender Cylinders, yet they will not easily relinquish one another . . .*”. These ‘*long and very slender cylinders*’ we have observed in contact between self-healing polymer materials (Perepelkin et al. 2019b) and they may be also observed in cell-cell contacts (see Fig. 7.14).

Fig. 7.14 A slender cylinder between two caviar cell surfaces arose during separation of the cells



Adhesive properties of the cell surface of the fish eggs may directly depend on the microhair-like coverage originating from the shell. Indeed, as early as 40th of XX century, it was noted by I.S. Logoiko (Biological Faculty of Moscow State University) that the surfaces of fish-eggs of different ecological groups have rather different hair-like structures or protuberances of the secondary shells of the eggs; he assumed that the adherence of the eggs depends directly on the number of the protuberances and their size (Cherfas 1956). This hypothesis is in agreement with recent experimental studies between soft materials and rough surfaces (Pepelyshev et al. 2018) that confirmed that the adherence between rough surfaces depends on the ability of the surfaces to establish regions of full adhesive contact and the size of the true contact area. The microhair-like coverage of soft materials helps to increase the area of true contact region, while the hard coverage may prevent establishment of the adhesive contact (see a discussion by Borodich et al. 2010 and by Pepelyshev et al. 2018).

4 Conclusion

The present study tries to combine an experimental study and modelling of cell-cell and cell-solid adhesion of salt-cured fish roe (fish eggs). The difficulties in both modelling of the contact interactions by Hertz and JKR theories and experimental studies of cells are due to the varying cell shape, mechanical properties and adhesive properties of the cells. The results show that the fluid content during hydration and dehydration strongly alter stiffness of the cell and its adhesive properties. The latter may also depend on the apparent presence of microhairs on the outer shell surface, as previously described in the literature. However, the results can be used for modelling interactions between collagen based shells filled with fluid and other materials. The mechanism of adhesive interactions between cells and hard substrates and between cells themselves should be a very promising topic for further studies. From the contact mechanics theory point of view, in the future, one could apply the extended JKR formalism and a version of the eBG method to the above experiments

after development of models of adhesive contact between two spherical membranes that are not fully filled by liquid.

Acknowledgments This work was initiated during visit of one of the authors (F.M. Borodich) to the Functional Morphology and Biomechanics Group at Kiel University leading by another author (S.N. Gorb) in October–December, 2017. The visit was supported by a grant of the Alexander von Humboldt Foundation within Renewed Research Stays Programme. The authors are grateful to AvH Foundation for supporting the visit. The authors are very grateful to Dr. N.V. Perepelkin (currently at Leeds Beckett University, UK) and Dr. A.E. Kovalev (Kiel University, Germany) for providing them with results of experimental tests.

References

- Argatov II, Dmitriev NN (2003) Fundamentals of theory of elastic discrete contact. Politekhnik, St. Petersburg. (Russian)
- Borodich FM (2014) The Hertz-type and adhesive contact problems for depth-sensing indentation. *Adv App Mech* 47:225–366. <https://doi.org/10.1016/B978-0-12-800130-1.00003-5>
- Borodich FM, Galanov BA (2008) Non-direct estimations of adhesive and elastic properties of materials by depth-sensing indentation. *Proc R Soc Ser A* 464:2759–2776. <https://doi.org/10.1098/rspa.2008.0044>
- Borodich FM, Gorb EV, Gorb SN (2010) Fracture behaviour of plant epicuticular wax crystals and its role in preventing insect attachment: a theoretical approach. *Appl Phys Mater Sci Process* 100:63–71. <https://doi.org/10.1007/s00339-010-5794-x>
- Borodich FM, Galanov BA, Gorb SN, Prostov MY, Prostov YI, Suarez-Alvarez MM (2012a) Evaluation of adhesive and elastic properties of materials by depth-sensing indentation of spheres. *J Appl Phys A Mater Sci Proc* 108:13–18. <https://doi.org/10.1007/s00339-012-6982-7>
- Borodich FM, Galanov BA, Gorb SN, Prostov MY, Prostov YI, Suarez-Alvarez MM (2012b) An inverse problem for adhesive contact and non-direct evaluation of material properties for nanomechanics applications. *Nanoscale Syst Math Model Theory Appl* 1:80–92. <https://doi.org/10.2478/nsmmt-2012-0006>
- Borodich FM, Galanov BA, Gorb SN, Prostov MY, Prostov YI, Suarez-Alvarez MM (2013) Evaluation of adhesive and elastic properties of polymers by the BG method. *Macromol React Eng* 7:555–563. <https://doi.org/10.1002/mren.201300107>
- Borodich FM, Galanov BA, Keer LM, Suarez-Alvarez MM (2014) The JKR-type adhesive contact problems for transversely isotropic elastic solids. *Mech Materials* 75:34–44. <https://doi.org/10.1016/j.mechmat.2014.03.011>
- Borodich FM, Galanov BA, Keer LM, Suarez-Alvarez MM (2021) Contact probing of prestressed adhesive membranes of living cells. *Phil Trans R Soc A* 379:20200289. <https://doi.org/10.1098/rsta.2020.0289>
- Boussinesq J (1885) Applications des potentiels ‘a l’Étude de l’équilibre et du Mouvement des Solides Élastique. Gauthier-Villars, Paris
- Bulychev SI, Alekhin VP, Shorshorov MK, Ternovskii AP, Shnyrev GD (1975) Determination of Young’s modulus according to indentation diagram. *Ind Lab* 41:1409–1412
- Chaudhri MM (2001) A note on a common mistake in the analysis of nanoindentation data. *J Mater Res* 16:336–339
- Chaudhri MM, Lim YY (2007) Nanoindentation techniques: a critical assessment of the current methods of data analysis. *Key Eng Mater* 345-346:1107–1114. <https://doi.org/10.4028/www.scientific.net/KEM.345-346.1107>
- Cherfas BI (1956) Fish farming in natural reservoirs. *Pishchepromizdat*, Moscow
- Cole KS (1932) Surface forces of the *Arbacia* egg. *J Cell Comp Physiol* 1:1–9

- Davenport J, Lønning S, Kjørsvik E (1986) Some mechanical and morphological properties of the chorions of marine teleost eggs. *J Fish Biol* 29:289–301
- Davidson LA, Oster GF, Keller RE, Koehl MAR (1999) Measurements of mechanical properties of the blastula wall reveal which hypothesized mechanisms of primary invagination are physically plausible in the sea urchin *Strongylocentrotus purpuratus*. *Dev Biol* 209:221–238
- Derjaguin B (1934) Untersuchungen über die Reibung und Adhäsion, IV. Theorie des Anhaftens kleiner Teilchen. *Kolloid Zeitschrift* 69:155–164
- Derjaguin BV, Muller VM, Toporov YP (1975) Effect of contact deformations on adhesion of particles. *J Colloid Interface Sci* 53:314–326. [https://doi.org/10.1016/0021-9797\(75\)90018-1](https://doi.org/10.1016/0021-9797(75)90018-1)
- Galanov BA, Dub SN (2017) Critical comments to the Oliver–Pharr measurement technique of hardness and elastic modulus by instrumented indentations and refinement of its basic relations. *J Superhard Mater* 39:373–389. <https://doi.org/10.3103/S1063457617060016>
- Galín LA (1961) Contact problems in the theory of elasticity. In: Sneddon IN (ed) North Carolina State College, Department of Mathematics and Engineering Research. (NSF Grant No. G16447, 1961)
- Gray J (1932) The osmotic properties of the eggs of the trout (*Salmo farjo*). *J Exp Biol* 9:277–299
- Harvey EN (1937) Methods of measuring surface forces of living cells. *Trans Faraday Soc* 33:943–946
- Hertz H (1882) Ueber die Berührung fester elastischer Körper. *J reine angewandte Mathematik* 92:156–171. (English transl. Hertz, H. (1896) On the contact of elastic solids. In: Miscellaneous Papers by H. Hertz. Eds. D.E. Jones and G.A. Schott, Macmillan, London, 146–162)
- Hooke R (1665) Micrographia: or some physiological descriptions of minute bodies made by magnifying glasses with observations and inquiries thereupon. John Martin and James Allestry, Printers to the Royal Society, London
- Iuchi I, Ha C-R, Sugiyama H, Nomura K (1996) Analysis of chorion hardening of eggs of rainbow trout, *Oncorhynchus mykiss*. *Develop Growth Differ* 38:299–306
- Johnson KL (1985) Contact mechanics. Cambridge University Press, Cambridge
- Johnson KL, Kendall K, Roberts AD (1971) Surface energy and the contact of elastic solids. *Proc R Soc London A* 324:301–313. <https://doi.org/10.1098/rspa.1971.0141>
- Kalei GN (1968) Some results of microhardness test using the depth of impression. *Mashinovedenie* 4(3):105–107. (Russian)
- Kobayashi W (1982) The fine structure and amino acid composition of the envelope of the chum salmon egg. *J Fac Sci Hokkaido Univ Ser VI, Zool* 23(1):1–12
- Lebedeva OA (1985) The development of fish-eggs and larvae of Peled. *Proc GosNIORH* 236:74–85. (Russian)
- Love AEH (1893) A treatise on the mathematical theory of elasticity, vol 2. University Press, Cambridge
- Love AEH (1939) Boussinesq’s problem for a rigid cone. *Q J Math* 10:161–175
- Mitchison JM, Swann MM (1954) The mechanical properties of the cell surface. I. The cell elastimeter. *J Exp Biol* 9:277–299
- Olivar MP (1987) Chorion ultrastructure of some fish eggs from the south-East Atlantic. *S Afr J Mar Sci* 5:659–671. <https://doi.org/10.2989/025776187784522793>
- Pepelyshev A, Borodich FM, Galanov BA, Gorb EV, Gorb SN (2018) Adhesion of soft materials to rough surfaces: experimental studies, statistical analysis and modelling. *Coatings* 8:350. <https://doi.org/10.3390/coatings8100350>
- Perepelkin NV, Borodich FM (2021) Explicit transformation between non-adhesive and adhesive contact problems by means of the classical JKR formalism. *Phil Trans R Soc A* 379:20200374. <https://doi.org/10.1098/rsta.2020.0374>
- Perepelkin NV, Kovalev AE, Gorb SN, Borodich FM (2019a) Estimation of the elastic modulus and the work of adhesion of soft materials using the extended Borodich-Galanov (BG) method and depth sensing indentation. *Mech Mat* 129:198–213. <https://doi.org/10.1016/j.mechmat.2018.11.017>

- Perepelkin NV, Martin-Martinez JM, Kovalev AE, Borodich FM, Gorb SN (2019b) Experimental testing of self-healing ability of soft polymer materials. *Meccanica* 54:1959–1970. <https://doi.org/10.1007/s11012-019-00965-w>
- Perepelkin NV, Borodich FM, Kovalev AE, Gorb SN (2020) Depth-sensing indentation as a micro- and nanomechanical approach to characterisation of mechanical properties of soft, biological, and biomimetic materials. *Nano* 10:15. <https://doi.org/10.3390/nano10010015>
- Perepelkin NV, Argatov II, Borodich FM (2021) Evaluation of elastic and adhesive properties of solids by depth-sensing indentation. *J Adhesion* 97:569–610. <https://doi.org/10.1080/00218464.2019.1686981>
- Pillarisetti A (2008) Mechanical manipulation and characterization of biological cells. PhD thesis, University of Maryland
- Popov VL (2010) Contact mechanics and friction. Springer, Heidelberg
- Rubzov VV, Chernyaev GA (1989) Construction of outer skin of egg. In: Reshetnikov YS, Mukhachev IS (eds) *Coregonus peled* (Gmelin, 1788): systematics, morphology, ecology, production. Nauka, Moscow, pp 205–211
- Smeshlivaya NV (2015) Ecological and physiological aspects of reproductive activity function of whitefish in the Ob'-Irtys' basin. PhD thesis, State Fish Centre (GOSRYBCENTR), Tumen
- Suga N (1963) Change of the toughness of the chorion of fish eggs. *Embryologia* 8:63–74
- Yoneda M (1964) Tension at the surface of sea-urchin egg: a critical examination of Cole's experiment. *J Exp Biol* 41:893–906
- Zotin AI (1961) Physiology of water metabolism in embryos of fish and cyclostomes. USSR Academy of Sciences Publishers, Moscow. (Russian)

Chapter 8

Mechanical Characterisation of Polymeric Materials Using Nanoindentation



Hassan Gonabadi, Arti Yadav, and Steve Bull

Abstract This chapter describes the mechanical behaviour of polymeric and soft materials through combined computational and experimental studies. Many soft materials exhibit time-dependent or a very large non-linear strain behaviour known as viscoelasticity/viscoplasticity and hyper elasticity or viscous-hyper elasticity respectively. A comparative study using nano-indentation of polymeric materials has been performed through combined experimental and Finite Element methods. Several constitutive models are available in the literature to analyse the experimental response of polymeric materials, however, the correct constitutive models are required to accurately model the mechanical behaviour of a given material system. Three widely used hyper elastic models, including the Mooney-Rivlin, Ogden and Arruda-Boyce models are studied for the analysis using the Finite Element software ANSYS. Also, due to the time dependent behaviour of soft materials the viscoelasticity and viscoplasticity behaviour based on the Prony series and Perzyna/modified time hardening models are discussed. Conventional macroscopic mechanical tests have been performed on PMMA, epoxy resin and polyurethane rubber materials using uniaxial tensile testing in conjunction with digital image correlation (DIC) technique to provide input data for Finite Element modelling of the indentation process. FE analysis of the indentation tests was then carried out and the results are compared with experimental data. This study helps to identify the deformation behaviour and mechanical characteristics of soft materials.

Keywords Contact probing · Rubber-like polymers · Viscoelasticity · Viscoplasticity · Finite elements · Numerical simulations · Experiments · ·

H. Gonabadi · A. Yadav · S. Bull (✉)
School of Engineering, Newcastle University, Newcastle upon Tyne, UK
e-mail: steve.bull@newcastle.ac.uk

© Springer Nature Switzerland AG 2022
F. M. Borodich, X. Jin (eds.), *Contact Problems for Soft, Biological and Bioinspired Materials*, Biologically-Inspired Systems 15,
https://doi.org/10.1007/978-3-030-85175-0_8

1 Introduction

Soft biomaterials are produced from a wide range of polymers (Shtil'man 2003). One of the main advantages of using polymers as a biomaterial is that their chemical structure and functionality can be easily modified which allows the tailoring of properties such as mechanical response, bioadherence, etc. (Zadpoor 2015). Many polymers are therefore extensively used in biomedical applications as implants, scaffolds, or wound-dressing foams (Shtil'man 2003; Ifkovits and Burdick 2007; Ulery et al. 2011). However, any chemical and physical changes in the structure of soft polymeric materials significantly influences their mechanical properties (Piskin 1995; Dutcher and Marangoni 2004). For instance, where soft materials mainly reside in aqueous environments, chemical degradation can result in material failure (Piskin 1995; Oyen 2008). Therefore, understanding the mechanical behaviour is essential and this often needs to take place at very high spatial resolution. Unlike metals and ceramics, which show predominantly elastic-plastic behaviour, characterising the mechanical properties of soft polymeric materials is very complex and challenging (Oyen 2008; Sinha and Briscoe 2009). Most of the soft polymeric materials exhibit both elastic/hyper elastic and viscoelastic/viscoplastic properties at different strain rates and temperatures (Alfrey and Doty 1945; Li et al. 2018). Viscoelastic/viscoplastic behaviour such as strain rate dependency and time dependent relaxation requires diverse range of analyses to evaluate mechanical response.

A mathematical framework to determine the stress-strain behaviour of a loaded material is called a constitutive model (Dorfmann and Muhr 1999; Dean et al. 2011). A number of existing constitutive models, such as linear, bilinear, hyper elastic, or viscoelastic/viscoplastic models, can be used to characterise the mechanical behaviour of soft materials (Gurtin 1973; Dean et al. 2011; Fill et al. 2012). However, the structure of soft materials such as polymers and elastomers is complex and the constitutive response can be entirely different compared to the typical engineering materials (Ogden 1973; Blatz et al. 1974; MacManus et al. 2016). Therefore, obtaining an accurate constitutive model is a key issue in the better understanding of the mechanical behaviour of polymers, elastomers or soft biomaterials used in implants, scaffolds, etc. Depending on the structure and composition, soft materials often exhibit elastic, plastic, viscous (time-dependent) and hyper elastic behaviours (Ogden 1973; Dorfmann and Muhr 1999; Dean et al. 2011). For soft materials under small deformation the stress can be considered proportional to strain and can be fitted to linear elastic models, i.e., ($\sigma = E\varepsilon$ (Gurtin 1973)); typically linear elasticity can be described with two material constants (i.e Young's modulus and Poisson's ratio) (Gurtin 1973). In the case of hyper elastic soft materials, these show a large deformation when a load is applied which returns to the original shape after the load is released, and a stress that varies nonlinearly with respect to strain (Mooney 1940). This hyper elasticity is described by a few constitutive models to precisely characterise the nonlinear stress-strain data of such soft materials (which are described in the Sect. 1.4).

The mechanical properties of soft materials can be determined using conventional methods such as, tensile, compression, or bending tests (Moerman et al. 2009; Nie et al. 2009). But soft materials display large deformation behaviour at a given applied load, and their surfaces or sub surfaces are often very different from bulk materials (Mooney 1940). Therefore, in order to locally investigate the mechanical properties and deformation characteristics of soft materials at small (micro/nano) scale such as thin films, composites, or nanobiological applications, the nanoindentation test method is probably the most suitable test method (Li and Bhushan 2002). However, nanoindentation measurements on soft materials can vary considerably with applied loading conditions (Li and Bhushan 2002; Zhang et al. 2010). In particular, the time dependent nature of soft materials must be considered when measuring their properties. Numerous studies have shown the mechanical characterisation and measurement sensitivity using nanoindentation with varying load conditions (Li and Bhushan 2002; Fischer-Cripps and Nicholson 2004; Zhang et al. 2010). Understanding the effect of the test time, and the degree to which mechanical response is dependent on intrinsic materials properties, is necessary to fully explain the mechanical behaviour of soft materials using nanoindentation testing under different loading conditions.

In this chapter an overview of the mechanical properties of soft materials is presented. The mechanical behaviour of most soft materials displays both nonlinearity and viscoelasticity as well as viscoplasticity. Therefore, a detailed understanding of the mechanical properties of soft and elastomeric (rubber-like) materials is an important part of our investigation. Firstly, as a consequence of effect of test time, nanoindentation relaxation of polymeric materials such as PMMA and epoxy resin materials has been studied. In PMMA, Prony series parameters obtained from nanoindentation experiments were determined using an analytical expression from the literature and subsequently the parameters were input into the Finite Element model of nanoindentation in order to validate the experimental results. In case of epoxy resin, the results of creep testing (variation of the strain versus time) and also the results of tensile testing at various strain rates were used to determine the Viscoplastic model parameters (modified time hardening and Perzyna models), subsequently the parameters were used as input data into the Finite Element model to verify the experimental parameters.

Secondly, polyurethane rubber is used as a model hyper elastic material. The Mooney Rivlin, Ogden and Arruda-Boyce models were used for the Finite Element analysis. Numerical solutions were compared with experimental data which were utilised to understand the stress strain behaviour of hyper elastic materials. It is found that different constitutive models are required for the different materials studied.

1.1 Structure and Mechanical Response

The mechanical response of biomaterials based on polymeric systems is much more variable than that of metals or ceramics. A major part of this comes from the different structures that these largely amorphous materials can adopt and the fact that these are not as dense and predictable as those of crystalline materials. This results in different stress-strain behaviour depending on the initial structure and how it changes during loading; therefore an understanding of the engineering and true stress-strain response of different materials and how it relates to the structure is paramount. Figure 8.1a shows the tensile engineering stress-strain curve for a typical ductile metal. The initial linear behaviour is reversible and is due to elastic behaviour (the slope gives the Young's Modulus of the material) and the deviation from linear behaviour is due to plasticity which is related to the propagation of mobile defects (dislocations) in the material. The engineering stress continues to rise after the onset of plastic deformation up to the point when a plastic instability develops and the test sample cross-section is locally reduced (necking). From this point the engineering stress which is based on the original cross-sectional area of the test sample is reduced with increasing strain up to the point of fracture, but the true stress continues to increase as the load carrying area reduces. In ceramic materials fracture may occur prior to plastic deformation and only the elastic behaviour is seen.

In a semi crystalline polymer a similar curve is often observed (Fig. 8.1b). An initial linear elastic section is followed by a non-linear (plastic) behaviour but the curve shows a maximum stress and then a plateau of stress at a lower level with a considerable change in extension and a final increase before failure. In this case the neck that forms does not continue shrinking until the specimen fails. Rather, the material in the neck stretches only to a certain "draw ratio" beyond which the material in the neck stops stretching and new material at the neck shoulders necks down. The neck then propagates until it spans the full gauge length of the specimen, a process called drawing. The increase in strain hardening rate needed to sustain the drawing process in semi crystalline polymers arises from a dramatic transformation in the material's microstructure. These materials are initially "spherulitic," containing flat lamellar crystalline plates, perhaps 10 nm thick, arranged radially outward

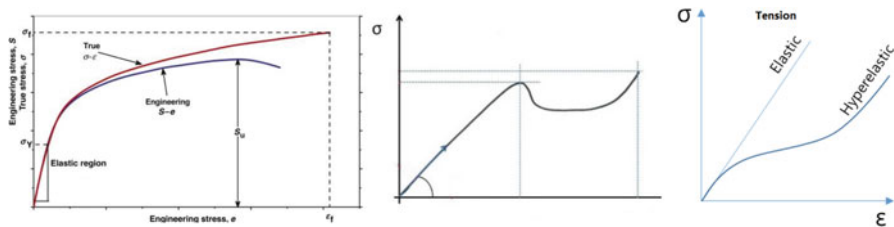


Fig. 8.1 Stress-strain response of (a), ductile metal, (b), semi crystalline polymer and (c), elastomer

in a spherical domain. As the induced strain increases, these spherulites are first deformed in the straining direction. As the strain increases further, the spherulites are broken apart and the lamellar fragments rearranged with a predominantly axial molecular orientation to become what is known as the fibrillar microstructure. With the strong covalent bonds now dominantly lined up in the load-bearing direction, the material exhibits markedly greater strength and stiffness than in the original material.

In elastomeric materials (Fig. 8.1c) a non-linear stress-strain curves is also observed but this is often completely reversible. The behaviour is elastic but the stiffness depends on the applied strain. The effect of tensile load is to stretch and align the polymer chains in the loading direction within the movements that are allowed by their original arrangement, available free space in the structure and degree of entanglement. This hyper elastic behaviour generally results in a reduction of stiffness with increasing strain at low loads followed by an increase at high strain once chain alignment is maximised.

The structure of materials based on polymer chains (and molecular films) is also more likely to be changed by thermal effects even at temperatures around room temperature. Most amorphous polymeric materials show a glass transition temperature where behaviour changes from elastomeric to glassy on cooling. The value of T_g depends on the mobility of polymer chains and for many polymers this lies between 170 and 500 K. Some polymers (like PMMA) are used in their glassy state and are relatively hard and brittle. Other polymers (e.g. polyurethane elastomers, polyisoprene) are used above T_g and are soft and flexible in nature; their T_g values are below room temperature.

In addition, changes in the polymer chain structure by rotation and untying can occur even a modest temperature giving a viscous component to the deformation process. Viscoelastic response is thus key in understanding the behaviour of polymeric materials. Elastic materials deform instantaneously when a load is applied, and “remember” their original configuration, returning there instantaneously when the load is removed. In solids, the relaxation of the structure at the molecular level is extremely small and, therefore, their response is essentially elastic. On the other hand, viscous materials do not show such characteristics, but instead exhibit a time-dependent behaviour. While under a constant stress, a viscous body strains at a constant rate, and when this load is removed, the material has “lost” its original configuration, remaining in the deformed state. In liquids, molecular reorganization generally occurs very rapidly and structural memory at the molecular level is very short. The response is essentially viscous unless the testing experiment is very fast. Viscoelastic materials exhibit certain characteristics of these two behaviours and show time-dependent behaviour, a “fading memory”, partial recovery, energy dissipation, etc. This may be linear (stress and strain are proportional) or nonlinear.

Polymers are the most important viscoelastic systems. Above the glass transition temperature, the response of these materials to a mechanical perturbation involves several types of molecular motions. For instance, the rearrangement of flexible chains may be very fast on the length scale of a repeated unit. These movements imply some type of cooperativity in the conformational transitions that produce

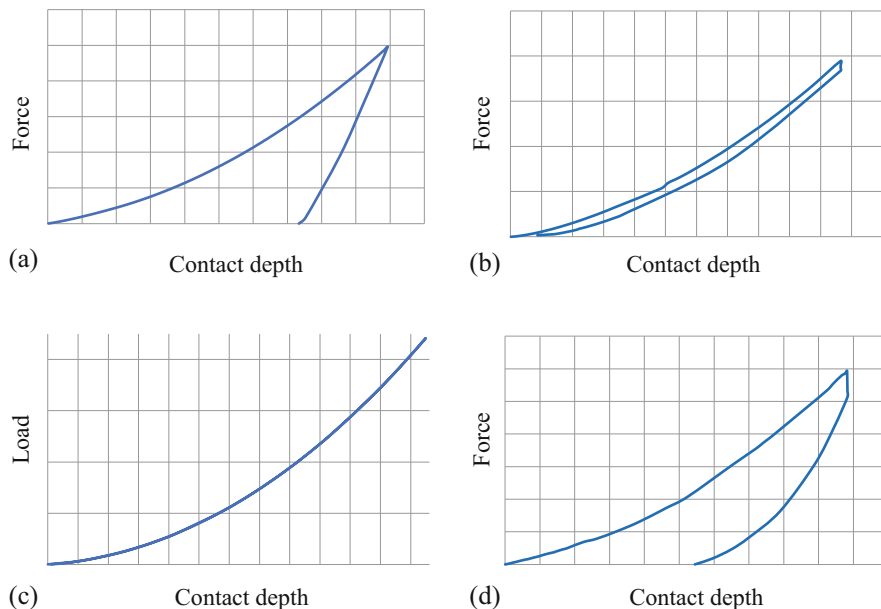


Fig. 8.2 Typical load-displacement fingerprints for (a) a glassy material (elastic-plastic) (b) an elastic/viscoelastic material (c) an elastic/hyper elastic material (d) an elastic-viscoplastic material

them. Cooperativity occurs even as the relaxation propagates along the chains, involving a growing number of segments of the backbone as time passes. At very long times, disentanglements of the chains takes place, and the longest relaxation time associated with this process shows a strong dependence on both the molecular weight and the molecular architecture of the system. The disentanglement process governs the flow in the system. As a consequence of the complexity of the molecular response, polymer chains exhibit a wide distribution of relaxation times that extend over several orders of magnitude in the time or frequency domain. At short time or at high frequency the response is mainly elastic, whereas at long time or low frequency it is mainly viscous. Obviously, the elastic component of the deformation is recoverable but the viscous component is not.

These differences in mechanical behaviour lead to differences in response in any mechanical test including nanoindentation tests which are used when material is only available in small amounts. A range of different load-displacement responses are measured (Fig. 8.2) and it is not possible to use a single analysis method to derive useful comparative data or a mechanistic understanding of the deformation processes occurring. Careful modelling of the measured data is therefore necessary.

Appropriate constitutive models for deformation are needed for all of the above cases. Whereas a single value for elastic modulus may be sufficient for crystalline materials this is not generally the case for polymers. In Sects. 1.3.2, 1.3.3 and 1.4 some of the constitutive models for hyper elastic, viscoelastic and viscoplastic materials which may be required are described.

1.2 *Conventional Mechanical Testing vs Nanoindentation*

For mechanical characterization, traditional mechanical methods such as tensile, compression, shear or bending tests can provide macro-scale information which can differ at the nano-scale level since most soft materials are non-homogeneous materials. Also, these testing methods have some challenges such as complex gripping geometry and the requirement for specific shapes and sizes of test samples (Nie et al. 2009). Therefore, in order to locally investigate the mechanical properties and deformation characteristics of soft materials at micro/nanoscale, the nanoindentation test method is probably the most common test method.

Nanoindentation is a depth sensing technique in which continuously measures load, displacement and time providing the mechanical response to the contact deformation; from this mechanical testing method, parameters such as hardness and modulus can be calculated (Fischer-Cripps and Nicholson 2004). Nanoindentation is easy to use, it does not generally require specialised laboratory infrastructure or a vacuum chamber. Properties such as viscoelasticity, creep, fracture toughness, and strain hardening effects localised to the contact region can be also extracted from the analysis of loading-unloading cycles (Ebenstein and Pruitt 2006). In contrast, the traditional mechanical methods such as tensile, compression, shear and flexural tests can only provide global deformation information which can differ to that from the nanoscale level since most soft materials are non-homogeneous (Bradley et al. 2001). Also, these conventional testing methods have some challenges which were described earlier (Dvir et al. 2011).

In the nanoindentation process, the load is applied through the transducer and the probe displacement is continuously measured to provide a load-displacement curve. The displacement is usually measured by capacitance while the force actuation is provided by force generation due to expansion of a piezoelectric element, magnetic coils, or electrostatically (Fischer-Cripps and Nicholson 2004). A schematic representation of nanoindentation is shown in Fig. 8.3, where the tip mounted directly onto the middle plate of a three-plate capacitor and a normal load is applied to move the tip downwards. The resulting load-displacement curve serves as the mechanical fingerprints of the material, from where the mechanical properties can be determined.

When testing compliant such as biomaterials three typical types of load-displacement fingerprint are often observed depending on the material tested:

1. Totally elastic or hyper-elastic response in which the loading and unloading curves are identical (Fig. 8.2c). This is typical of elastomeric materials with very low elastic moduli where the stresses generated during the indentation cycle are too small to drive plasticity.
2. Elastic-viscoelastic response in which the loading and unloading curves are offset from each other by the viscoelastic behaviour during a hold period (Fig. 8.2b). This is typically observed in non-crosslinked polymers such as PMMA at low test loads. The deformation is reversible and no visible impression is observed

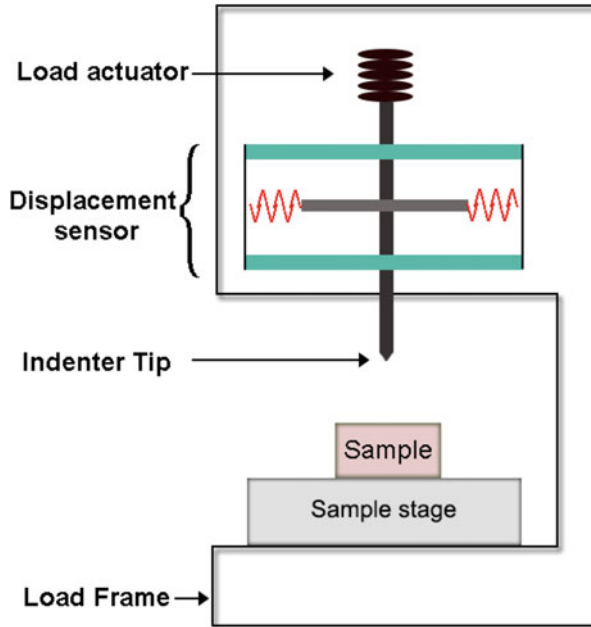


Fig. 8.3 Schematic representation of a nanoindenter machine

but the rate of recovery is slow enough that a visible offset between the loading and unloading curves is observed that disappears when the test is completed.

3. Elastic-viscoplastic response in which a permanent impression is created which does not recover fully after the test. A load-displacement curve that is similar to that seen when testing elastic-plastic materials is produced (Fig. 8.2d). This involves breaking of bonds and is more commonly observed for cross-linked polymers like epoxy resin systems.

This chapter discusses the analysis of all these types of curves and compares the results to the widely used conventional nanoindentation analysis method developed by Oliver and Pharr (Oliver and Pharr 1992) which is introduced in the next section.

1.3 Nanoindentation Theory

Nanoindentation has emerged as a convenient technique to determine the mechanical properties of polymeric materials. Thanks to the recent technological advances to the transducer sensitivity of nanoindentation equipment, continuous checking and monitoring of the load and contact depth is permitted throughout the load-unload cycles. Depth sensing micro-indentation was first conducted by Fröhlich (Fröhlich et al. 1977) and then used as a method to characterize the surface properties of

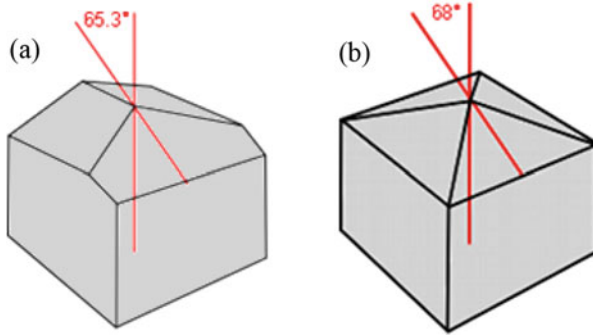


Fig. 8.4 Geometry of indenter tips (a) Berkovich, (b) Vickers

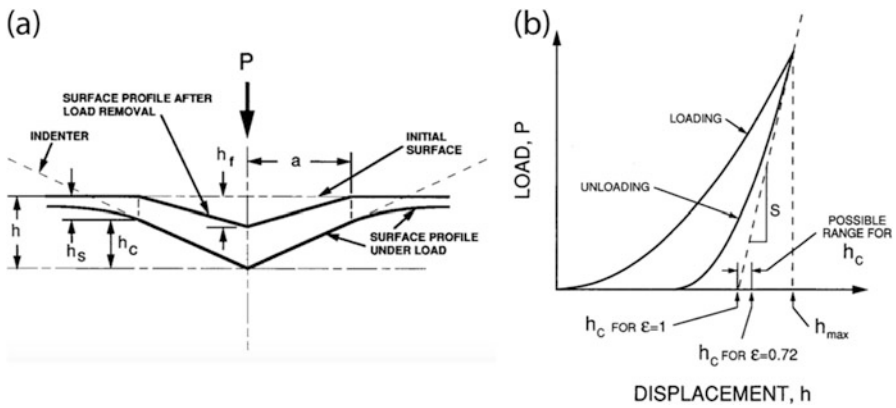


Fig. 8.5 (a) A schematic representation of surface showing the section before and after indenting, (b) A schematic representation of typical nanoindentation load-displacement curve, also showing the graphical interpretation of the contact depth (Oliver and Pharr 1992)

materials. Although for conventional macro and micro-scale hardness testing, an indenter geometry of a four faceted pyramidal Vickers tip (Fig. 8.4b) is mainly used, when it comes to the nanoscale measurement, the three faceted pyramidal Berkovich indenter (Fig. 8.4a) is preferred. The Berkovich tip shape was invented by a Russian scientist (Berkovich 1950) where the area to depth ratio of this indenter geometry is similar to that of the Vickers indenter.

In the Nano-indentation process, either under displacement or load control mode, a diamond indenter tip is pushed into the bulk material. During the indentation cycle, the displacement is monitored with respect to the load. A typical load displacement curve from nanoindentation experiment is shown in Fig. 8.5b. The Oliver and Pharr (2010) method is the main used method to analyse the unloading part of load displacement curves and therefore to determine hardness and elastic modulus. The hardness H is defined as

$$H = \frac{P_{max}}{A} \quad (8.1)$$

Where P_{max} is the maximum applied load, and A is the projected area. The contact area, A which can be evaluated from the contact depth, h_c , at the maximum load of P_{max} , can be expressed as

$$A = c_0 h_c^2 \quad (8.2)$$

where c_0 , is the coefficient and it depends on the indenter tip geometry. For a Berkovich tip, the value of c_0 is about 24.5. As can be seen in Fig. 8.5 the contact depth, h_c , which is the actual contact depth between the indenter and material, is different from the maximum contact depth, h_{max} at the maximum applied load, due to the elastic deformation surrounding the indenter area. The contact depth, h_c is given by

$$h_c = h_{max} - \epsilon \frac{P_{max}}{S} \quad (8.3)$$

where S , is the contact stiffness, and can be extracted from the slope of unloading curve. ϵ is a constant, that depends on geometry of indenter. The projected contact area can be calculated either from the cross-sectional image of the indenter shape or directly measured from the imprint geometry under the scanning electron microscope (Briscoe et al. 1998; Pharr et al. 2010). However, determining actual contact area is highly dependent on contact depth and the cross-sectional shape along the contact depth (Pharr et al. 2010). In order to consider the bluntness of the tip Oliver & Pharr proposed an area function which is mainly applicable for a Berkovich tip and is given as

$$A = 24.5 h_c^2 + c_1 h_c^1 + c_2 h_c^{0.5} + c_3 h_c^{0.25} \dots \quad (8.4)$$

Once the contact area, A and stiffness, S are determined, the reduced modulus, E_r can be calculated following the pioneering work of Bulychev, Alekhin, Shorshorov (BASH) and their co-workers from the analysis of the frictionless contact problem. This gives

$$E_r = \frac{S\sqrt{\pi}}{2\beta\sqrt{A}} \quad (8.5)$$

where β is correction factor ($\beta = 1.034$) for a Berkovich indenter tip. The reduced modulus, E_r represents the elastic modulus occurring both in the indenter and the materials, and the Young's modulus can be extracted from the given equation

$$E_r = \frac{1 - \nu_s^2}{E_s} + \frac{1 - \nu_i^2}{E_i} \quad (8.6)$$

where ν_s and ν_i are the Poisson's ratios of the sample and indenter respectively, and E_s and E_i are the elastic modulus of the sample and indenter respectively.

In summary, it must be noted that the determination of elastic modulus of polymeric materials using nanoindentation data has been shown to be erroneous. The Oliver and Pharr method explained earlier is inaccurate and cannot be applied to the nanoindentation unloading curves obtained for polymeric materials (Tranchida et al. 2007); due to the effects of pile up, viscoelasticity/viscoplasticity and hydrostatic stress, a clear difference exists between the elastic modulus calculated using macroscopic tensile testing of polymers and those calculated using nanoindentation, with indentation modulus normally overestimating the elastic modulus.

1.3.1 Material Pile Up

According to the elastic contact theory (Sneddon 1965), during the indentation, the "sink-in" behaviour occurs in the region around the indentation. Based on this behaviour, the projected contact area is calculated from the indentation load displacement data and therefore Hardness and Modulus of the indented material are calculated. However, depending on the material under indentation (i.e. occurrence of plastic deformation), the material at the maximum indentation depth, may sink in or pile up around the indenter as shown in Fig. 8.6. When pile-up occurs, the contact depth (h_c) is bigger than the maximum indentation depth (h_{max}). As a result, the contact area can be underestimated by the theory of nanoindentation and the mechanical properties extracted by the Oliver and Pharr method are overestimated. It has been shown that the nanoindentation theory has failed to acceptably calculate the exact projected contact area for the elastic-plastic indentation, therefore the contact area can be underestimated significantly depending on the work hardening and the ratio of modulus to the yield stress (Bolshakov and Pharr 1998).

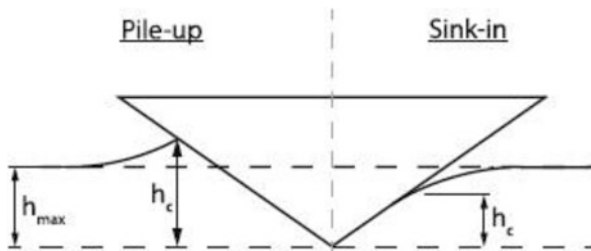


Fig. 8.6 Pile up and sink in behavior of material at max indentation depth. (Hardiman et al. 2016)

1.3.2 Viscoelasticity

The difference between indentation modulus and macroscopic tensile modulus has been related to the viscoelastic (time dependent) behaviour of materials (VanLandingham et al. 2001; Oyen 2007; Tranchida et al. 2007; King et al. 2013). In fact, the initial part of unloading curve of load displacement data is affected by the viscoelastic creep. This results in a 'nose' in the load displacement curves and therefore a negative value for the unloading slope (contact stiffness). For example, during the nanoindentation unloading curve, the occurrence of a 'nose' is seen when the indentation is conducted on PMMA (Briscoe et al. 1998). In an attempt to reduce the influence of viscoelastic effects on the unloading part of a nanoindentation test, adding a constant load hold segment between the loading and unloading segment has been proposed (Hochstetter et al. 1999). Therefore, determination of the optimum holding time for each material to adequately reduce the influence of creep on the initial part of the unloading data is necessary when characterizing the nano-mechanical behaviour of materials.

Polymers and soft materials exhibit time dependent behaviour such as creep, stress relaxation, or frequency dependent of dynamic properties (Brinson and Brinson 2008). These viscoelastic materials show both elastic and time dependent response, that are primarily responsible for energy loss since they store as well as dissipate mechanical energy under the deformation, with the response of stress-relaxation or creep.

Recently, nanoindentation has been considered as a possible way to measure the viscoelastic properties as well. For example, Cheng et al. (2000) demonstrated an analytical solution for linearly viscoelastic deformation using flat-punch indentation. Lu et al. (2003) and Huang et al. (2004) developed methods for viscoelastic functions of polymers in the time domain and frequency domain respectively. Odegard et al. (2005) studied the dynamic viscoelastic behaviour of various polymers. Vanlandingham et al. (2005) determined the relaxation modulus and creep compliance. Thereafter numerous studies have been performed using nanoindentation with conical, spherical and Berkovich indentation on polymers and soft materials (Briscoe et al. 1998; Dean et al. 2011).

As mentioned above, almost all soft biomaterials exhibit time-dependent behaviour. Apart from typical indentation methods to characterize time-dependent behaviour, dynamic testing is also widely used, where instead of a trapezoidal load function, a sinusoidal load is applied for measuring the storage and loss modulus directly as a function of loading frequency. Dynamic indentation tests have been shown to be pivotal for both in identification of mechanical properties of soft materials and assessing their viability. This allows for the continuous evaluation of the hardness and Young's modulus of the given material over the depth of the indentation. Apart from hardness and Young's modulus measurements, this method is useful for the experimental determination of the local creep and strain-rate dependent mechanical properties of materials, as well as the local damping of viscoelastic materials. Mishuris et al. (Argatov et al. 2013) has provided useful insights on mechanical properties of biological tissues (articular cartilage)

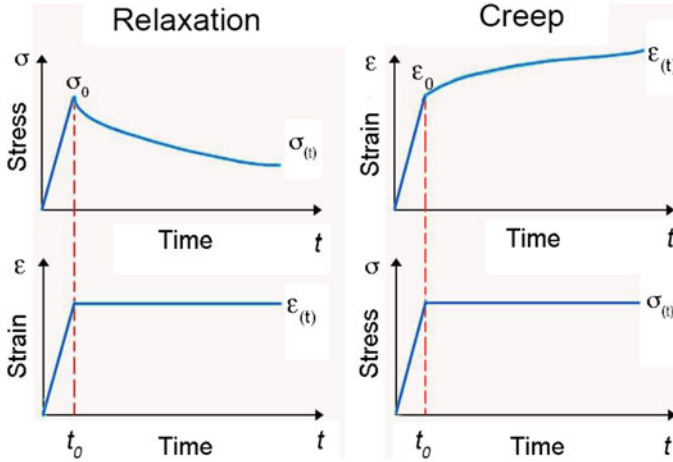


Fig. 8.7 Schematic representation of time-dependent behaviour of stress- relaxation (left) and creep (right)

using dynamic spherical indentation tests at various geometrical parameters of the indenter.

Considering the complexity of the loading conditions and time-dependent behaviour, including complicated constitutive response and some explicit analysis connected with physiological conditions is more likely to be necessary in future studies of soft biomaterials. The dependency of the stress-strain behaviour of soft biomaterials with respect to time is largely responsible for the absorption of energy, where the approach to quantifying the material response is not straightforward since most of the data analysis is complex due to the viscoelastic models used. For instance, in the case of a nonlinear viscoelastic model, there is no direct analytical expression for the indentation behaviour and not always a complete range of the required material property data at the sample scale. This necessitates the use of finite element analysis (FEA) modelling approaches with an appropriate materials response included, such as from a fitted database, or an inverse FEA analysis method for data optimisation. Therefore, in order to evaluate a more realistic analysis and materials behaviour both experimental approaches and modelling need to be used (Fig. 8.7).

Experimental results of indentation tests can be fitted to determine viscoelastic parameters. A generalized Maxwell model is extensively used to consider the correlation between nanoindentation load-displacement data and the relaxation modulus as a function of time (Huang and Lu 2006). Typically, the model is formulated by Prony series expressions, to characterize the continuous viscoelastic contribution of the materials in terms of a number of different relaxation processes with different shear modulus and relaxation time.

$$G(t) = G_{\infty} + \sum_{j=1}^N G_j \cdot e^{-t/\tau_j} \quad (8.7)$$

where G_{∞} is the equilibrium shear modulus, G_j is the magnitude of the shear modulus, and τ_j is its relaxation time. Due to its simplicity, this model is widely used to describe viscoelastic materials such as polymers and many soft biomaterials.

1.3.3 Viscoplasticity

As mentioned in the above section, many soft materials exhibit the time dependent behaviours that include creep, stress relaxation, or frequency dependence of dynamic properties (Lu et al. 2003; Huang et al. 2004). If these are reversible they can be regarded as viscoelastic but this is not always the case. Viscoplasticity also occurs depending on the rate of the applied loading, but the time-dependent material response is irreversible and accompanied by unrecoverable plastic deformation (Perzyna 1966; Batra and Kim 1990). A viscoplastic model is required for large strain deformation. For qualitative analysis, several tests such as hardening, creep, or stress relaxation at constant elongation are performed to describe the viscoplasticity (Batra and Kim 1990). To predict the stress-strain curve the viscoplasticity is generally modelled using Perzyna approach (Simo and Hughes 2006).

Perzyna and Modified Time Hardening Models

In viscoplasticity, the material deformation is rate dependent and undergoes unrecoverable deformation. The rate-dependent behaviour of polymers and soft materials in general is widely modelled using a viscoelastic constitutive law (Odegard et al. 2005). However for viscoplasticity, the Perzyna and Modified time hardening models can be used for rate dependent behaviour of soft materials (Simo and Hughes 2006). The Perzyna model as a function of plastic strain can be expressed as

$$\dot{\varepsilon}_{pl} = \gamma \left(\frac{\sigma}{\sigma_0} - 1 \right)^{1/m} \quad (8.8)$$

where ε_{pl} is the plastic strain, m is the hardening parameter, γ is the viscosity parameter, and σ_0 is the static stress. In the Perzyna model, the results of stress-strain response of polymeric samples under tensile testing at various strain rates are used to determine the Perzyna parameters (Perzyna 1963a, b, 1966). The model assumes that the plastic strain rate ($\dot{\varepsilon}_{pl}$) is a function of a hardening/softening parameter (m), the material viscosity parameter (γ), and the static yield stress (σ_0). The stress strain rate graph is created and fitted with Perzyna material model of viscoplasticity to identify the required parameters.

To identify the modified time hardening parameters, the variation of strain versus time (creep test) is used in curve fitting and, as a result, Modified Time hardening parameters (i.e. constants C_1 to C_4 in Eq. 8.9 are determined.

$$\varepsilon_r = \frac{C_1 \times \sigma^{C_2} \times t^{C_3+1} \left(\exp\left(-\frac{C_4}{T}\right) \right)}{C_3 + 1} \quad (8.9)$$

where ε_r is the strain rate, σ is the stress level where creep test is performed, t is the time and T is the temperature.

1.3.4 Hydrostatic Stress

When applying nanoindentation testing on materials (in particular polymers), the stressed material beneath the indenter tip is constrained by the neighbouring relaxed material (unstressed), this leads to the accumulation of great compressive hydrostatic stress in the indentation region (Atkins and Tabor 1965), which is why many researchers believe that the effect of hydrostatic stress state is the main reason for the difference between modulus of polymers calculated by macroscopic tensile testing and nanoindentation (Doerner and Nix 1986; Briscoe and Sebastian 1996; VanLandingham et al. 1999). In the literature an expression (Eq. 8.10) has been developed in order to calculate the indentation modulus, free from the influence of hydrostatic stress (Hardiman et al. 2016).

$$E_{(0)} = E - 2 \left(H - \frac{H}{C} \right) (5 - 4\nu) (1 - \nu) \quad (8.10)$$

Where $E_{(0)}$ is the elastic modulus, E is the affected indentation modulus by hydrostatic stress state, ν is the Poisson's ratio, H is the indentation Hardness and C is the factor of constraint suggested by (Atkins and Tabor 1965). It has been shown that taking into consideration the effect of hydrostatic stress by the above expression can result in a 15% increase in the match between indentation modulus and macroscopic modulus of polymeric materials.

1.4 General Hyper Elastic Models

Most soft materials such as elastomers exhibit non-linear stress-strain behaviour known as hyper elasticity, in which the stress-strain behaviour is usually derived from a strain energy density function. The strain energy density function depends on properties such as isotropy, incompressibility, initial level of porosity, etc. (Boyce and Arruda 2000; Horgan and Saccomandi 2002). Numerous constitutive

models such as Neo-Hookean, Ogden, Mooney-Rivlin, or Arruda Boyce models based on energy density functions are available in the literature for large strain deformation (Gent 1996). The Ogden model is older and widely used in finite element simulations, whereas Neo-Hookean, Mooney-Rivlin or Arruda-Boyce are mainly used for low, moderate and high strain analyses, respectively (Gent 1996; Dorfmann and Muhr 1999).

1.4.1 Mooney-Rivlin Model

The Mooney-Rivlin model is one of the most widely used models to predict the stress-strain behaviour of hyper elastic materials (Mooney 1940). It is based on two invariants of the left Cauchy-Green deformation tensor, and it works well with the large strain in uniaxial elongation and shear (Mooney 1940; Rivlin and Saunders 1951). Mooney-Rivlin can be derived from the following relationship between the strain density function and the stretch ratio

$$W = C_1 (\bar{I}_1 - 3) + C_2 (\bar{I}_2 - 3) \quad (8.11)$$

Where C_1 and C_2 are empirical parameters, and \bar{I}_1 and \bar{I}_2 are the first and second deviatoric invariants of the left Cauchy-Green deformation tensor. The invariants ($\bar{I}_1 = \lambda_1^2 + \lambda_2^2 + \lambda_3^2$ and $\bar{I}_2 = \lambda_1^2 \lambda_2^2 + \lambda_2^2 \lambda_3^2 + \lambda_3^2 \lambda_1^2$) are described in terms of principal stretch ratios λ_1 , λ_2 and λ_3 .

1.4.2 Neo-Hookean Model

The Neo-Hookean model is a hyper elastic material model, which can be used to predict the stress-strain behaviour of hyper elastic materials at low strains; this model is very similar to Hooke's law (Ogden 1997). At the beginning the Neo-Hookean model's stress-strain behaviour is linear, but after certain point the stress-strain behaviour changes to non-linear (Ogden 1997; Gent 2012). A neo-Hookean model is one of the simplest models that can make good approximation at relatively small strain analysis (Ogden 1997). It is based on one invariant of the right Cauchy-Green deformation tensor. The strain density function of an incompressible Neo-Hookean model material can be expressed as

$$W = C_1 (\bar{I}_1 - 3) \quad (8.12)$$

Where C_1 is empirical parameter, and \bar{I}_1 is the first deviatoric component of the right Cauchy-Green deformation tensor.

1.4.3 Ogden Model

The Ogden model is a hyper elastic material model, which can be used to predict the stress-strain behaviour of complex hyper elastic materials at larger strain levels (Ogden 1973). This model is the most widely used model up to now since it is capable of modelling stress-strain curves for strains up to 700%, whereas Mooney-Rivlin is typically best for strains below 100% (Ogden 1973). The strain density function for the Ogden model can be expressed as

$$W = \sum_{I=1}^N \frac{\mu_i}{\alpha_i} (\lambda_1^{\alpha_i} + \lambda_2^{\alpha_i} + \lambda_3^{\alpha_i} - 3) \quad (8.13)$$

Where λ_1 , λ_2 and λ_3 are the principal stretch ratios, whilst μ_i and α_i are the empirically determined materials parameters.

1.4.4 Arruda-Boyce Model

The Arruda-Boyce model is a hyper elastic material model, which is based on an eight-chain model in which hyper elastic material is represented by eight identical polymer chains. This model requires two material parameters (the rubbery chain modulus and the limiting chain extensibility) and it works well to capture the collective nature of network deformation (Arruda and Boyce 1993). The strain density function for an Arruda-Boyce model, using the first five terms of the inverse Langevin function can be expressed as

$$W = \mu \sum_{I=1}^5 \frac{C_i}{\lambda_m^{2i-2}} (\bar{I}_1^i - 3) \quad (8.14)$$

here, μ is the initial rubbery shear modulus, and λ_m is the initial chain extensibility. \bar{I}_1 is the first deviatoric strain invariant.

2 Experimental and Numerical Methodology

2.1 Nanoindentation Test

In this work, depth sensing nanoindentation testing was conducted on viscoelastic and viscoplastic materials (i.e. PMMA and epoxy resin) using a Hysitron Triboindenter fitted with the Berkovich diamond indenter (500 nm tip end radius). An array of nine indents (3 × 3) was created. The distance between the indent was maintained 15 μm to avoid the interaction between the indents. To make sure

that the nanoindentation results are not influenced by errors due to the shape of indenter, standard fused silica specimen was initially used to calibrate the tip area function. The tests were performed under displacement control mode using a single cycle indentation (load-hold-unload) protocol and during each cycle, a 5 s hold was imposed at the peak displacement. This was done to account for the effect of creep and viscosity. In addition, before the indentation testing, specimens were held for 24 h inside the nanoindentation enclosure in order to minimize the effect of thermal drift and to minimise the offset the specimen temperature with that of the environment. In this study, Atomic force microscopy (AFM) scans contributed to identify the occurrence of epoxy resin pile up and therefore the effect of pile up was corrected using the FEM method. The blunt Berkovich used can be regarded as a conical indenter with a spherical cap. For displacements less than about 60 nm the contact can be regarded as dominated by the spherical cap whereas at greater displacements the contact is dominated by the conical indenter geometry.

Nanomechanical response of hyper elastic material (polyurethane rubber) was conducted numerically, however the input parameters for the FE model were calculated experimentally. The numerical tests were performed under displacement control mode using a single cycle indentation (load-hold-unload) protocol and during each cycle, a 1 s hold was imposed at the peak displacement. More details about the methodology of computational nanoindentation on the hyper elastic material are given in Sect. 3.3.

2.2 Finite Element Modelling of the Nanoindentation

In this study, because of the complexity of the contact problem in soft polymers (large deformation and the stress-strain relationship with strong nonlinear features), the ANSYS Finite Element program was used to simulate the nanoindentation process for the nonlinear elastic materials. For this purpose, a 2D axisymmetric FE model with a conical indenter (half angle of 70.3°) and a tip radius of 50 or 500 nm was used in order to accurately reproduce the nanoindentation experiment through the simulation. To build the nanoindentation model in this study, a 4-node planar element (PLANE182) was used to model the entire areas of the indenter and the bulk material. The element has axisymmetric modelling functionality and can be used for the large deformation problems in nanoindentation. In addition, it can be integrated with CONTA171 and TARGE169 elements to define the surface-to-surface contact model (bottom surface of the indenter and the top surface of the bulk material). Since a large localized strain/deformation occurs in the contact region beneath the indenter, a very fine mesh ($2.5 \text{ nm} \times 2.5 \text{ nm}$) was used close to the contact zone, while a coarser mesh was used outside this region. The appropriate number of elements and element size were obtained by improving mesh density using mesh sensitivity study of the load versus displacement curve; therefore the FE model is mesh independent. Symmetric boundary conditions were applied along the axis of symmetry (the horizontal direction displacement was set to zero). The

bottom side of the bulk material is also constrained by a fixed boundary condition. The height and the width of the model were set to a value of 300 times bigger than maximum indentation depth to minimize the samples edge and free boundary effects. The friction coefficient between the tip indenter and the upper surface of bulk material was set to 0.1 (Johnson and Johnson 1987; Mata and Alcala 2004).

The indenter was modelled as deformable body in the ANSYS program, with its elastic properties the same as diamond (Young's modulus of 1140 *GPa* and Poisson's ratio of 0.08). The mechanical properties (hyper elastic model parameters), determined from macroscopic tension testing were supplied to the Finite Element code to simulate the nanoindentation testing. The indented sample was modelled as a hyper elastic material following Mooney Rivlin, Ogden and Arruda Boyce constitutive laws (Table 8.6), while when it comes to the viscoelastic and viscoplastic polymeric materials such as PMMA and epoxy resin, the Prony shear relaxation model and Perzyna/modified time hardening parameters are used in the FE model of the indented sample respectively. More details about how these parameters are identified are explained in later Sections (3.1 and 3.2).

To optimize the efficiency and avoid the convergence issues, a displacement control mode was used for the movement of the indenter. A downward displacement was applied to the indenter to simulate the indentation process. The corresponding load was obtained by the reaction force for a given indentation depth. In order to consider the effect of hyper elasticity and viscous hyper elasticity, the loading procedures of loading-holding- unloading indentation were applied with the maximum displacement varied from 50 nm to 1000 nm. The indenter reaches the maximum displacement within 1 s and then is held for 1 s and finally gets back to the initial place within a second. The analysis of the FE calculated load-displacement curve provides the contact modulus and hardness of the bulk material following the procedure based on the Oliver and Pharr method (Oliver and Pharr 1992). In this method, the contact stiffness (S) is calculated from the initial slope of unloading curve (Fig. 8.8a). This is related to the contact modulus (E_r) using equation:

$$S = \frac{dP}{dh} = \frac{2E_r\sqrt{A_c}}{\sqrt{\pi}} \quad (8.15)$$

Where, A_c is the contact area at the indentation depth. According to the Oliver and Pharr method, the contact area is calculated via the area function for the indenter tip geometry used.

However, since the load-displacement curve in this study is based on Finite Element simulation, the contact area (A_c) is determined in the FE model from the last point of contact at maximum load (Fig. 8.8b).

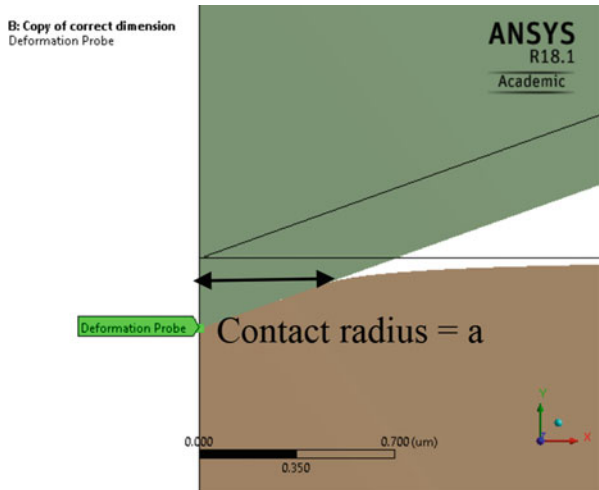
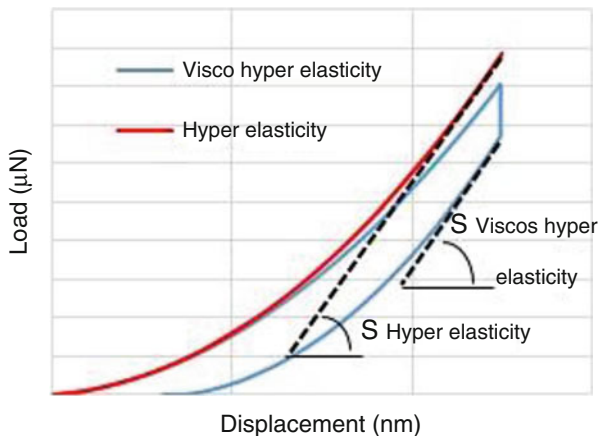


Fig. 8.8 (a) A typical load-displacement curve obtained from the numerical Nano-indentation test on sample with purely hyper elastic properties and a sample with combined viscos hyper elasticity properties showing their contact stiffness which were used to calculate the elastic modulus, (b) Deformed and un deformed shape of bulk material under indentation showing the contact area used in Oliver and Pharr method to calculate the elastic modulus

3 Results

3.1 Viscoelasticity

Viscoelasticity which has elastic and viscous components is usually characterized by relaxation testing. Generally in a relaxation experiment, either a constant tensile, compressive or shear strain is applied on the material, thereafter stress relaxation occurs over time. The variation of stress versus time is fitted with

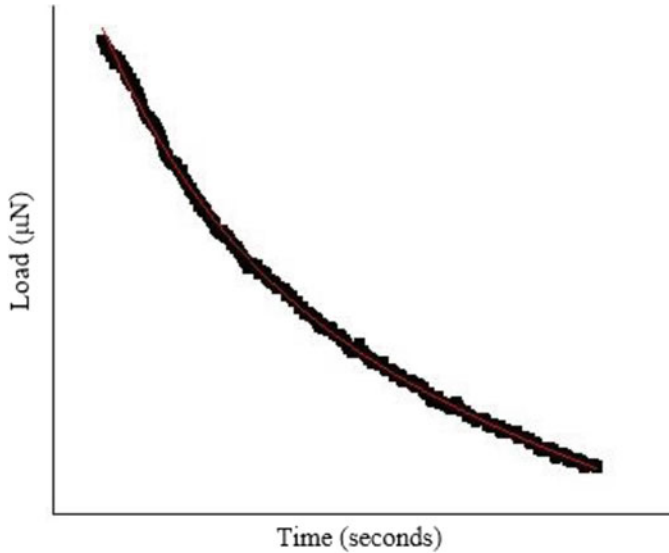


Fig. 8.9 Variation of load during the holding time and curve fitting using exponential function

Table 8.1 Prony series parameters of PMMA used in FE model

Index	Relative moduli(i)	Relaxation time (i) s	G0
1	0.07341	0.8	1.0975
2	0.1475	18.457	
3	0.1478	18.683	

a number of models (e.g. Prony series model). The nanoindentation process in polymeric materials such as PMMA involves nonlinear contact mechanics and time dependent properties (viscoelasticity). A methodology based on combined FEM and nanoindentation experiments was used for developing an analysis procedure to characterize the micromechanical behaviour of PMMA. Initially, an FEM based inverse method is implemented to account for the effect of viscoelasticity (Prony series) parameters of the bulk polymer. These parameters can be calculated using the analytical expression derived based on the conical indentation of a homogeneous linear viscoelastic half space (Baral et al. 2017). The analytical expression used to calculate the Prony series parameters (Eq. 8.16) is used for fitting the load-time curve which was obtained during the holding time in (Fig. 8.9), with results in (Table 8.1). These parameters are then reused in the FE model of nanoindentation of bulk PMMA to predict the experimental load displacement data in Fig. 8.10 (Baral et al. 2017).

$$F(t) = \frac{\pi \tan(\beta)}{1-\nu} \left(\frac{a}{h}\right)^2 \times \left[G_0 \cdot h_1^2 + 2 \sum_{i=1}^n G_i \cdot r_1^2 \tau_i \exp\left(-\frac{t-t_1}{\tau_i}\right) \times \left[\frac{h_1}{r_1} + \tau_i \exp\left(-\frac{h_1}{r_1 \tau_i}\right) - 1 \right] \right] \tag{8.16}$$

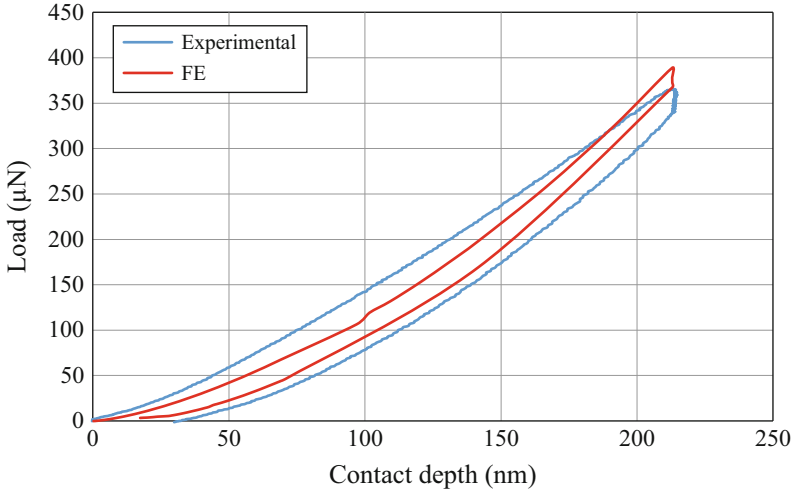


Fig. 8.10 Comparing numerically and experimentally calculated load displacement curves

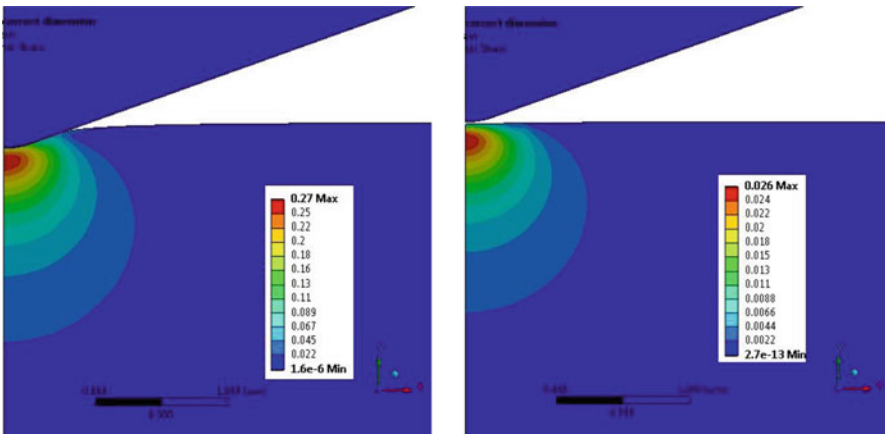


Fig. 8.11 Von Mises strain fields (a) at maximum displacement, (b) after complete unloading

Using the above Prony series parameters and the mechanical properties of PMMA (obtained from macroscopic tensile testing, elastic modulus: 3.00 GPa and Poisson’s ratio: 0.35) in the FE model indicates that there is a good correlation between the experimental data and the FE simulation. The agreement between numerical and experimental result can be used to validate the viscoelasticity parameters introduced into the FE model. The von Mises strain fields developed in the 2D FE model of PMMA is shown in Fig. 8.11 providing an insight into the strain distribution when characterizing the bulk PMMA using the nanoindentation method.

3.2 Viscoplasticity

The nanoindentation process on polymeric materials such as epoxy resin involves nonlinear contact mechanics and strain rate dependent properties (viscoplasticity) as well as the effect of material pile up. To account for these effects, an FE based inverse method (combined FEM and nanoindentation experiment) was used for developing an analysis procedure to characterize the micromechanical behaviour of bulk epoxy resin. Initially, the FEM based inverse method is implemented to account for the effect of viscoplasticity of the bulk polymer. To do this, viscoplasticity parameters are determined using tensile and creep testing (at various strain rates) on epoxy resin and then these parameters are used in FE models of nanoindentation on bulk epoxy resin for verification of load displacement data. To correct for the effect of pile up, rather than estimating the projected contact area using the Oliver and Pharr method, the FE calculated contact area was used by detecting the last contact point at maximum load in the FE mesh, resulting in a more accurate measurement of the indentation modulus of the epoxy resin.

3.2.1 Viscoplasticity Models

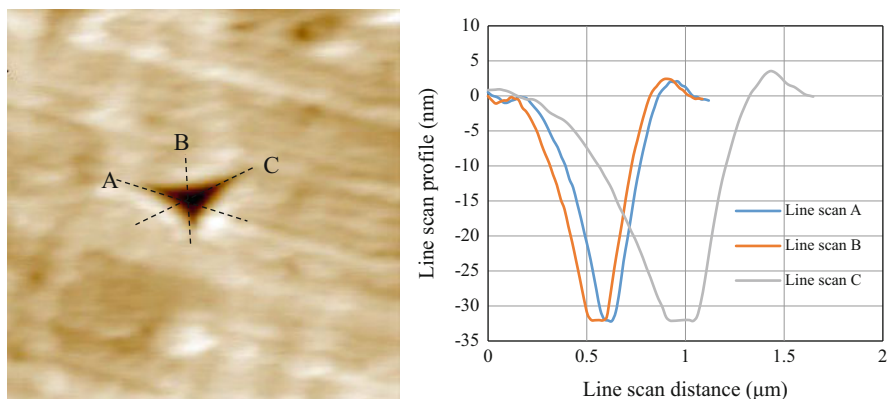
In order to analyse the time dependent response of the epoxy resin under nanoindentation, viscoplasticity models were applied in the numerical simulation for verification using the static properties in Table 8.2. To account for the effect of viscoplasticity, two methods based on Perzyna and Modified time hardening were implemented. On the Perzyna model, the results of stress-strain response of the epoxy resin under the tensile tests at various strain rates were used to determine the Perzyna parameters. This was done based on the ideas presented by Perzyna (1963a, b, 1966). The model assumes that the plastic strain rate ($\dot{\epsilon}_{pl}$) is a function of a hardening/softening parameter (m), the material viscosity parameter (γ), and the static yield stress (σ_0). The stress strain rate graph is created and fitted with Perzyna material model of viscoplasticity (Table 8.3) to identify the required parameters. To identify the modified time hardening parameters (Table 8.3), the variation of strain versus time at the stress level of 10 MPa (obtained from a creep test) was determined and fitted with the Modified Time hardening model.

Table 8.2 Isotropic elastic-perfectly plastic properties of bulk epoxy resin (obtained from macroscopic tension test) used for the FE model of nanoindentation

Properties	Epoxy resin (isotropic)
E (GPa)	3.78
ν	0.35
G (GPa)	1.48
Yield strength (MPa)	85

Table 8.3 Viscoplasticity models and calculated parameters of epoxy resin used in FE model

Model	Parameters			
Perzyna $\dot{\epsilon}_{pl} = \gamma \left(\frac{\sigma}{\sigma_0} - 1 \right)^{1/m}$	σ_0 (MPa)	m	γ	
	70	0.1505	218.62	
Modified time hardening $\epsilon_r = \frac{C_1 \times \sigma^{C_2} \times t^{C_3+1} \left(\exp\left(-\frac{C_4}{T}\right) \right)}{C_3+1}$	C_1	C_2	C_3	C_4
	3.78e-5	1	-0.85	0

**Fig. 8.12** AFM image of a residual impression from an indentation carried out on the bulk epoxy resin, highlighting locations of line scans, (b) Line scans A, B and C

3.2.2 Comparison with Experiment

An AFM images of the residual impression from an indentation on bulk epoxy resin and the amounts of pile up around it are shown in Fig. 8.12. The data from the AFM scans was post-processed using the AFM data analysis software Gwyddion. The tests were performed under displacement control mode using a single cycle indentation (load-hold-unload) protocol and during each cycle, a 5 s hold was imposed at the peak displacement.

When performing indentations on a polymer such an epoxy resin, due to the effect of pile up (Fig. 8.12), the Oliver and Pharr method underestimates the contact area. In this study, because of the viscoelastic recovery which the epoxy resin experiences on reduction of the maximum indentation load; methods of calculating the projected contact area based on the residual impression (Saha and Nix 2001; Beegan et al. 2003; Kese and Li 2006; Zhou et al. 2008; Hardiman et al. 2016) as well as depth-corrected contact area based on the measured pile up profile (Cao et al. 2006; Zhou et al. 2008; Hardiman et al. 2016) fail to correct the effect of material pile up on indentation modulus of epoxy resin as the height of the measured pile-up is a not representative of the state of pile-up under the indenter at maximum indentation load. In addition, the Oliver and Pharr method

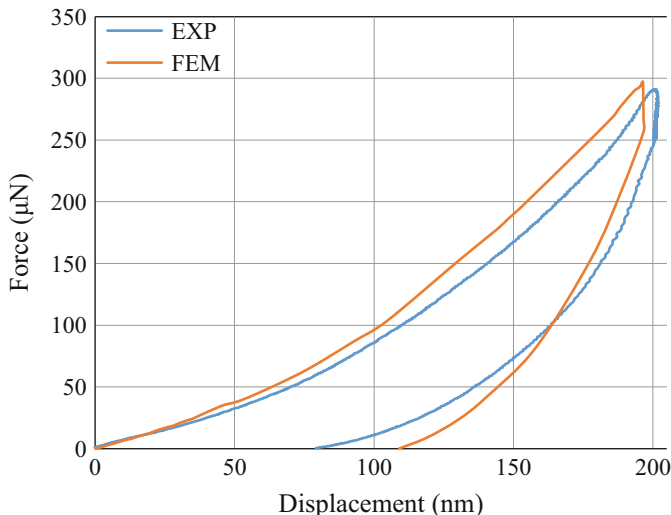


Fig. 8.13 Force-displacement curve on bulk epoxy resin

does not take into account the effect of viscoplasticity, therefore, in order to correct the effect of above phenomena (material pile up and viscoplasticity effects) for the measurement of elastic modulus, FE calculated load displacement curves are generated and compared with experimentally generated load displacement curves (Fig. 8.13). Agreement is good but the small difference between experimental load displacement curves and the computed results from the FE model is probably due to the effect of surface roughness, adhesion force and indentation process-associated factors (e.g. sample mounting and fame compliance) which are not considered in the numerical model. The maximum load reached by all the nanoindentations experiments on bulk epoxy resin only varies between 280–300 μN indicating that the resulting data curves for all indentations are relatively consistent and reproducible due to the careful and uniform process of polishing the sample. The agreement between numerical and experimental results validates the viscoplasticity parameters introduced into the FE model. The von Mises stress fields developed in the 2D FE model of bulk epoxy resin at the maximum indentation depth are shown in Fig. 8.14 providing an insight into the stress distribution when characterizing the bulk epoxy resin using the nanoindentation method.

In order to correct the effect of pile up, the ratio of contact area calculated from the FE model to the contact area calculated from the Oliver and Pharr method (Eq. 8.4) is used and therefore an area correction factor was applied to the experimental indentation test data (Table 8.4). The elastic modulus of bulk epoxy resin calculated from the experimentally generated load displacement curves is corrected by the area correction and reported in Table 8.5. It must be noted that, the elastic modulus of the bulk epoxy resin has been calculated by averaging data from 4×4 (8.16) indentations using the Oliver and Pharr method and the mean value of modulus was

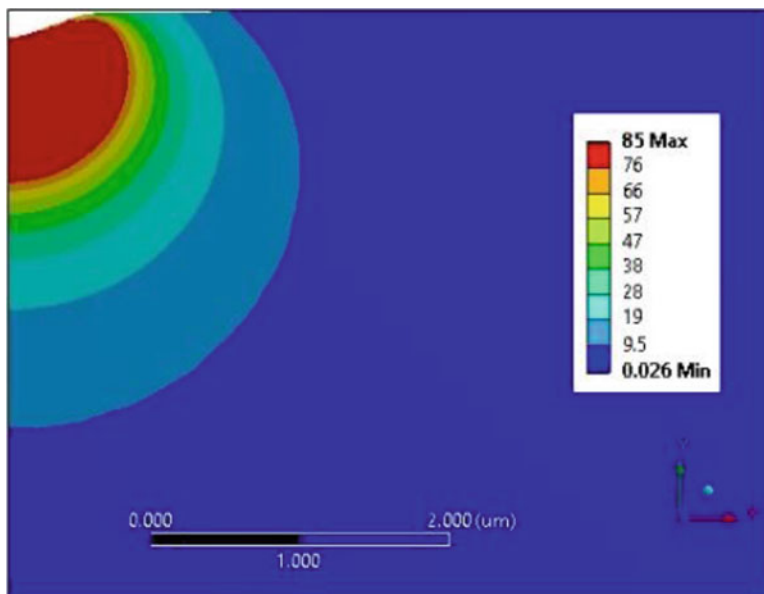


Fig. 8.14 Von Mises stress field on 2D axisymmetric FE model of nanoindentation of bulk epoxy resin

Table 8.4 Ratio of contact area calculated from FEM to the contact area calculated from Oliver and Pharr method

Epoxy resin	Area correction ($\frac{A_{FEM}}{A_{OP}}$)
Bulk material	1.08

calculated as 5.22 GPa with a standard deviation of 0.3 GPa. After accounting for the effect of material pile up (using the area correction in Table 8.4) and the effect of hydrostatic stress using the relation (Eq. 8.10) which is detailed in (Rodríguez et al. 2012; Hardiman et al. 2016), the remaining difference of about 11.5% between the indentation modulus of bulk epoxy resin (i.e. 4.21 GPa) and the macroscopic tensile modulus (i.e. 3.78 GPa) is mainly due to the effect of creep/viscoplasticity. Although the effect of creep has been considered by addition of a constant displacement hold segment between the loading and unloading segments (i.e. 5 s hold segment), the FE analysis of indentation on the bulk epoxy resin at various holding time and/or displacement rate shows that increasing holding time or reducing strain rate result in an indentation modulus of the epoxy resin which compares very well with the bulk tensile modulus. As can be seen in Fig. 8.15, the results can be produced free from the effect of time dependent deformation behaviour of the epoxy resin by either increasing holding time (to 500 s) or reducing the displacement rate to 0.002 $\mu\text{m/s}$. It was found that nullifying the effects of the viscoplastic deformation can lead to reductions of the modulus of the order of 10–12%.

Table 8.5 Experimentally calculated indentation modulus of epoxy resin and the effect of pile up (using FEM) and hydrostatic stress

Elastic modulus (GPa)	Nano-indentation Oliver& Pharr	Pile up effect (-3.8%)	Hydrostatic stress effect (-16%)	Tensile modulus (GPa)	Difference
Bulk epoxy resin	5.22 ± 0.3	5.02	4.21	3.78	+11.5%

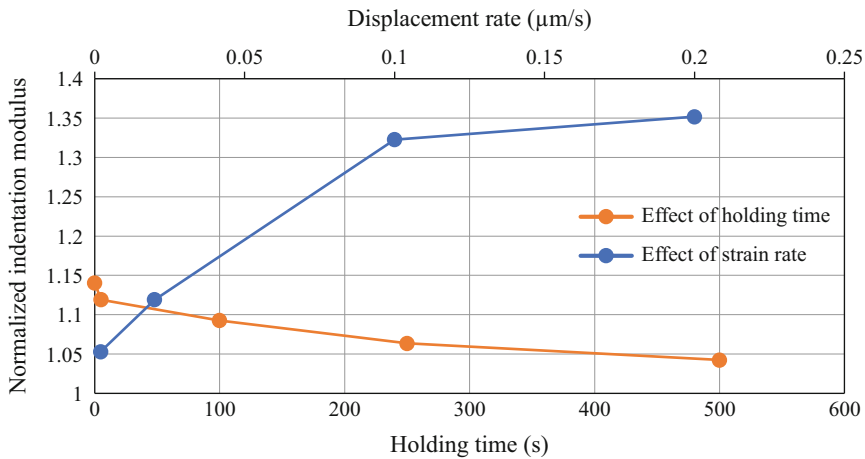


Fig. 8.15 Effect of loading rate (at the constant hold time of zero) and holding time (at the constant loading rate of 0.2 µm/s) on elastic modulus calculated using the FE model of nanoindentation on bulk epoxy resin, Normalized modulus is the ratio of indentation modulus calculated from the FE load displacement curve over the macroscopic tensile modulus

3.3 Viscous-Hyper Elastic Materials

Soft materials such as biological tissues can have both the large strain and time dependent behaviour at once, therefore viscous behaviour needs to be considered for obtaining the mechanical properties of such soft materials. In order to study the viscous response of the soft materials using nanoindentation, a viscoelasticity model and hyper elasticity models were applied simultaneously in the FE model. As described in earlier sections, the three hyper elastic models, namely Mooney-Rivlin, Ogden and Arruda-Boyce models were used to determine the nonlinear behaviour. The viscoelasticity demonstrates the time dependent behaviour that includes creep, stress relaxation, or frequency-dependent dynamic properties. The viscoelasticity can be described using a power law variation of stress with respect to time. One widely used model for this is known as the Prony series model described previously. The constitutive model for viscous-hyper elasticity is a combination of the hyper elastic Mooney-Rivlin, Ogden and Arruda Boyce models, and the time dependent Prony series model.

3.3.1 Methodology of Tension Testing and Determination of Viscoelastic/Hyper Elastic Model Parameters

In this study, the parameters of various hyper elastic material models that characterize the soft polymer (bulk specimen in nanoindentation) were obtained from the uniaxial tension test. The various hyperelastic strain energy functions and their corresponding uniaxial stress-strain relationships were used in this study for the curve fitting to find their parameters following the Nelder-Mead optimization method are listed in Table 8.6.

The tensile test was conducted in conjunction with a video gauge system (DIC measurement set up) to measure the components of strain and Poisson’s ratio. Subsequently this information was used to build the stress-strain curve. In order to use the DIC technique during the tensile testing, a camera was placed perpendicular to the specimen surface to register digital images of it during the deformation. The image acquisition was started as soon as the tension test began. The registered images were processed using an algorithm in the DIC software (VIC 2D) (Solutions 2009) which outputs full field strain measurement with high spatial resolution. The DIC technique is based on the recognition of geometrical changes in the grey intensity distribution of the surface speckle patterns before and after deformation. Therefore in order to make the process work, the specimen surface is marked with a random speckle pattern (Fig. 8.16). In this work, this was done by alternately spraying white and coloured paint. The artificial stochastic spot pattern (random speckle pattern) of the specimen surface is used as the carrier of the surface displacement/strain information.

In order to evaluate the viscous hyper elasticity response of the polymeric specimen under nanoindentation, a viscoelasticity model and hyper elasticity model were combined and applied in the FE model. The hyper elasticity component was described by Mooney Rivlin, Ogden or Arruda Boyce constitutive laws. The viscoelasticity which has elastic and viscous parts is usually characterized by relaxation or creep testing. Generally in relaxation experiments, either a constant tensile, compressive or shear strain is applied on the material, and the stress variation is recorded. Therefore, because of the viscous effects in the material stress relaxation

Table 8.6 Hyper elastic strain energy function with their uniaxial stress strain equations

Hyper elastic material model	Strain energy (Ψ) uniaxial stress-stretch equations
Mooney-Rivlin (Mooney 1940)	$\Psi = C10(I_1 - 3) + C01(I_2 - 3) + C11(I_1 - 3)(I_2 - 3)$ $\sigma = 2C10(\lambda - \lambda^{-1}) + 2C01(1 - \lambda^{-3}) + 6C11(\lambda^2 - \lambda - 1 + \lambda^{-2} + \lambda^{-3} - \lambda^{-4})$
Ogden (1972)	$\Psi = \sum_{i=1}^N \frac{2C_i}{\alpha_i^2} (\lambda_x^{\alpha_i} + \lambda_y^{\alpha_i} + \lambda_z^{\alpha_i} - 3)$ $\sigma = \sum_{i=1}^N \frac{2C_i}{\alpha_i} \left(\lambda^{\alpha_i-1} - \lambda^{-\alpha_i} / 2^{-1} \right)$
Arruda-Boyce (1993)	$\Psi = \mu \sum_{i=1}^5 \frac{C_i}{\lambda_L^{2(i-1)}} (I_1^i - 3^i)$ $\sigma = 2\mu (\lambda - \lambda^{-2}) \sum_{i=1}^5 \frac{iC_i}{\lambda_L^{2(i-1)}} I_1^{i-1}$

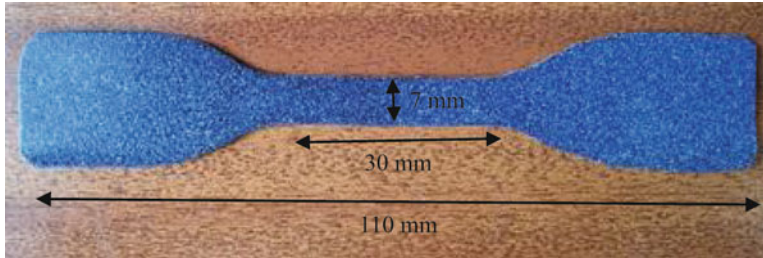


Fig. 8.16 Geometry of tensile test specimen marked with random speckle pattern

occurs over the time. The variation of stress with respect to time is fitted with a number of models (in this study Prony series model was used). In shear relaxation experiment, the Prony series is:

$$G(t) = G_0 - \sum_{i=1}^N G_i \left(1 - \exp\left(\frac{-t}{\tau_i}\right) \right) \quad (8.17)$$

Where G_0 , G_i and τ_i are the elastic shear modulus, relative modulus and relaxation time. In this study it is assumed that $N = 1$, $G_1 = 0.33$ and $\tau_1 = 1$.

3.3.2 Tensile Testing Results

Obtaining complete stress-strain curves during contact loading is complex in soft materials due to the inhomogeneity of the stress state, whereas the stress-strain curves under uniaxial loading can be easily assessed. Therefore, determining the constitutive parameters from the hyper elastic stress-strain behaviour of rubber required uniaxial tensile experiments. Figure 8.17 shows a typical stress-strain response of polyurethane rubber determined at a strain rate of 10 min^{-1} . To build the stress-strain curve, stress was calculated based on the variation of load obtained from the load cell of the testing machine divided by the original cross sectional area of the sample and the strain data was extracted from the DIC. For a representative tension stress-strain curve up to 120% strain (Fig. 8.17), the DIC calculated strain field (i.e. longitudinal component of strain) is shown illustrating the localized strains and the areas on the surface of the sample where damage develops. The polynomial fit to the tensile stress strain data was used to determine the corresponding variation of tangent modulus versus strain (Fig. 8.18). Although it is not possible to define the equivalent Elastic modulus and Poisson's ratio that characterize the mechanical performance of this material, an initial value for elastic modulus can be calculated when the material begins to deform in tension. During the tension test, it was found that initially strain softening occurs (decrease in the elastic modulus) and later strain hardening (increase in the elastic modulus) occurs. As it can be seen from Figs. 8.17

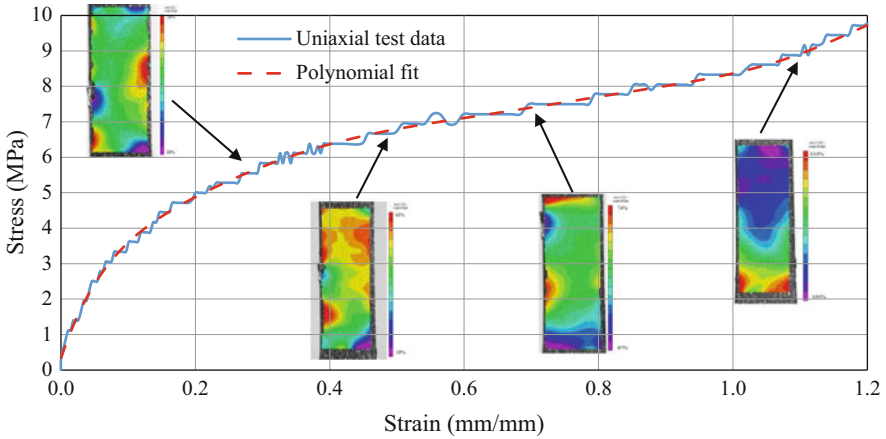


Fig. 8.17 Tensile stress-strain response and DIC calculated strain maps during the deformation

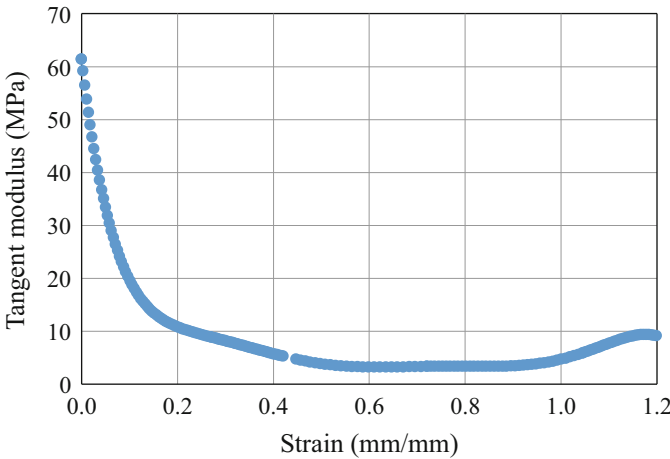


Fig. 8.18 Variation of tangent modulus versus strain using the Polynomial fit

and 8.18, the initial response of the specimen under tensile loading is linear with the average Elastic modulus and Poisson’s ratio of 62 ± 5 MPa and 0.5 respectively. This is followed by a drop-in modulus from 62 MPa to less than 10 MPa until the nominal value of strain is about 0.8, and thereafter hardening behaviour was observed.

In order to describe the nonlinear mechanical behaviour of the studied material, three widely used hyper elastic material models including Mooney Rivlin, Ogden and Arruda-Boyce were used. Figure 8.19 shows the uniaxial stress-strain curve which was used to fit with the above material models. In this study, the FE software ANSYS was used to determine the unknown hyper elastic parameters depending

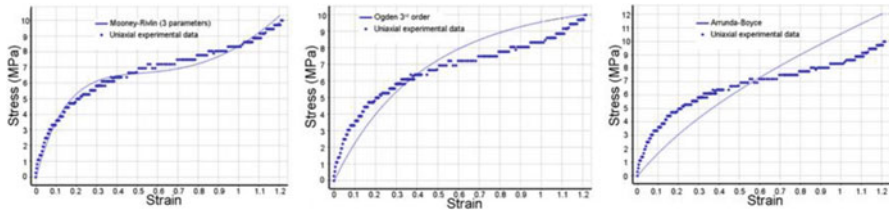


Fig. 8.19 Fitting the uniaxial test data using different hyperplastic models. (Mooney-Rivlin, Ogden and Arruda Boyce)

on the chosen model. This fitting approach avoids any material stability issues that occur when trying to generate optimum fitting parameter for an elastomeric material using the Ogden model as may be encountered in some dedicated fitting packages (e.g. hyperfit). The hyper elastic material parameters obtained from the results after fitting the constitutive models are provided in Table 8.7. As can be seen in Fig. 8.19, the Mooney-Rivlin model appears to be a better fit with a relatively good match to experimental data when compared to the Ogden and Arruda-Boyce models. This indicates that the Mooney-Rivlin method matched to the experimental results of the specific rubber material we have chosen; this mainly depends on the rubber-material used since the Ogden model is the best fit choice for the rubber material used in ‘O’ ring seals. However, in this study the numerical simulation of displacement-controlled nanoindentation using all these above-mentioned hyperelastic models was analysed. Given the varying fit quality it is interesting to note what effect the selection of model will have on modelled indentation behaviour.

3.3.3 Finite Element Modelling

For indenting soft materials, the load-displacement behaviour is different from that of stiff materials, a relatively large displacement is achieved for a given (small) applied load. Thus, the contact area plays an important role in mechanical characterisation of soft materials. In the literature, commonly dull tips such as spherical or flat ended tips are widely used. In order to analyse the mechanical behaviour of hyper elastic and viscous hyper elastic material under nanoindentation testing, 2D axisymmetric FE simulations were carried out. This resulted in the generation of reaction forces (P) versus displacement (h) during the indentation process. To understanding the effect of the tip, the FE simulation was done using two different tip radii, namely 50 nm and 500 nm. Also, the contact depth varied from 50 nm to 1000 nm in each case. The mechanical properties (hyper elastic model parameters), known from macroscopic tension testing was supplied to the Finite Element code (ANSYS) to simulate the nanoindentation testing. The FE modelling of nanoindentation was performed under the displacement control mode using a single cycle indentation (load-hold-unload) protocol and during each cycle, a 1 s hold was imposed at the peak displacement. The indented sample was

Table 8.7 Hyperplastic material parameters of obtained results after fitting the constitutive models

Hyper elastic material model	Mooney-Rivlin	Ogden	Arruda-Boyce
Parameters	$C_{10} = -11.37$ $C_{01} = 19.754$ $C_{11} = 1.7989$	$C_1 = 17.266$ $\alpha_1 = 0.3282;$	$C_2 = 17.267;$ $\alpha_2 = 0.33763;$ $C_3 = 17.269, \alpha_3 = 0.33481$ $\mu = 5.423$ Limiting network stretch = $1.1869e^8$

modelled as a hyper elastic material following Mooney Rivlin, Ogden and Arruda Boyce constitutive laws. The FE projected contact area under nanoindentation was determined from the last contact point at maximum load in the FE mesh.

3.3.4 Model Predictions and Experiment

Figure 8.20, shows the FE calculated load-contact depth ($P-h$) curves obtained from the nanoindentation on the specimen with purely hyper elastic and viscous hyper elastic properties. As can be seen, compared to different purely hyper elastic material models, the maximum load required to achieve the displacement of 500 nm is higher when the Mooney Rivlin model is used in the FE model of the indented sample. Combining viscosity (Prony shear relaxation model) with the hyper elasticity in the FE model of the indented sample results in lower load throughout the indentation cycle. In addition, compared with the Ogden and the Arruda Boyce model, conducting indentation on the sample with Mooney Rivlin behaviour, results in a steeper slope in the initial part of the unloading curve indicating an increase in the contact stiffness. The indentation force generated during nanoindentation with two different tip radii (50 nm and 500 nm) was also investigated and it is shown that, at the same indentation depth, the larger tip radius (blunt tip) induces a higher indentation load irrespective of material model used. This is due this fact that, at a given indentation depth, the larger tip radius deforms a greater amount of material compared to the smaller radius tip (sharp tip) during the indentation processes; as a result, higher indentation load is needed to apply enough pressure on the indenter to penetrate into the specimen to the target contact

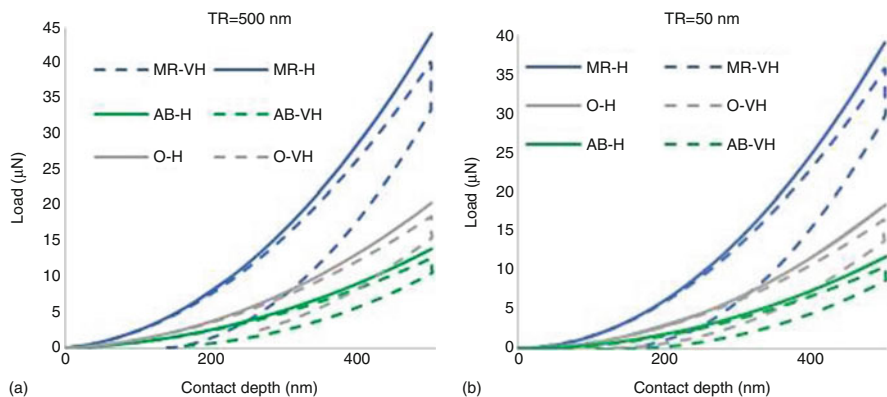


Fig. 8.20 FE calculated load-depth curves of nanoindentation on hyper-elastic and viscous hyper elastic material model (a) tip radius of 500 nm, (b) tip radius of 50 nm. Mooney Rivlin hyper elastic = MR-H, Mooney Rivlin viscous hyper elastic = MR-VH, Ogden hyper elastic = O-H, Ogden viscous hyper elastic = O-VH, Arruda Boyce hyper elastic = AB-H, Arruda Boyce viscous hyper elastic = AB-VH

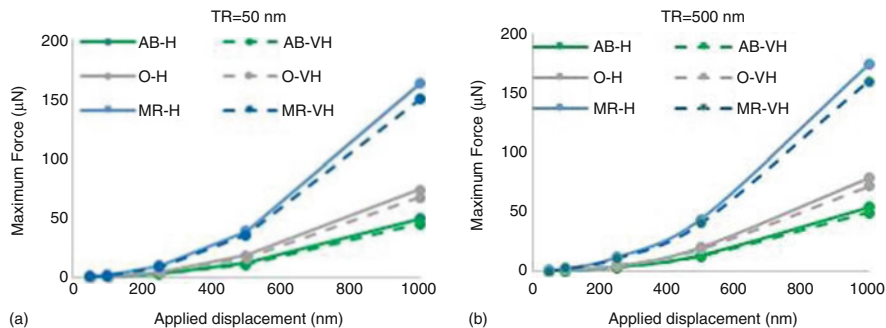


Fig. 8.21 Variation of maximum force versus displacement (a) tip radius of 50 nm, (b) tip radius of 500 nm for hyper-elastic and viscos hyper elastic material model, Mooney Rivlin hyper elastic = MR-H, Mooney Rivlin viscos hyper elastic = MR-VH, Ogden hyper elastic = O-H, Ogden viscos hyper elastic = O-VH, Arruda Boyce hyper elastic = AB-H, Arruda Boyce viscos hyper elastic = AB-VH

depth. Comparing Fig. 8.25 to Fig. 8.26 or Fig. 8.27 to Fig. 8.28, it can be seen that bigger deforming volumes are also created when using the larger tip radius. Although, due to limited space, only the FE calculated load contact depth curves for the maximum applied displacement of 500 nm are shown here (Fig. 8.20), for different displacements similar load displacement behaviour can be seen. Of course the magnitude of maximum load at different displacement is also different (Fig. 8.21).

Following the procedure based on the Oliver and Pharr method (described in Sect. 1.3 and 2.1), the analysis of the FE calculated load-displacement curve provides an elastic modulus of the material using either the purely hyperelastic material model or the viscous hyper elastic material model. The effect of indenter tip geometry and contact depth, on the elastic modulus for the different material models is shown in Figs. 8.22, 8.23 and Fig. 8.24. Using the Arruda Boyce model (Fig. 8.22), hyper-elasticity effects are insensitive to the both varied tip radius and indentation depth. Although viscous effects are sensitive to the variation in indentation depth, they are insensitive to the varied tip radius for indentation depths less than 250 nm and become more sensitive when indentation depth increases.

Using the Mooney Rivlin material model (Fig. 8.23) shows that both hyper-elasticity and viscosity effects are insensitive to the varied tip radius, however, their effects are sensitive to the varied indentation depth. Comparing the variation of elastic modulus obtained from the hyper elastic and viscous hyper elastic models for different indentation depths the elastic modulus obtained from the viscous hyper elastic model can be replaced by a purely hyper elastic model and vice versa to calculate the elastic modulus. In addition comparing Fig. 8.23 with Fig. 8.18, shows that for a small indentation depth (0–250 nm) the elastic modulus obtained from either a hyper elastic model or a viscous hyper elastic model matches well with tangent modulus obtained from the initial linear part of tensile stress strain curve, however, as the indentation depth increases, the FE model of nanoindentation overestimate the elastic modulus.

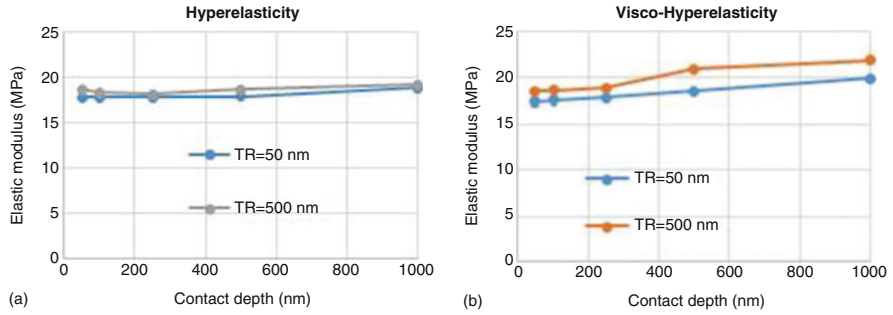


Fig. 8.22 Variation of elastic modulus versus displacement during the nanoindentation testing on specimen with (a) purely hyper elastic model (Arruda Boyce), (b) Viscous hyper elasticity model (Combined Prony shear relaxation and Arruda Boyce model)

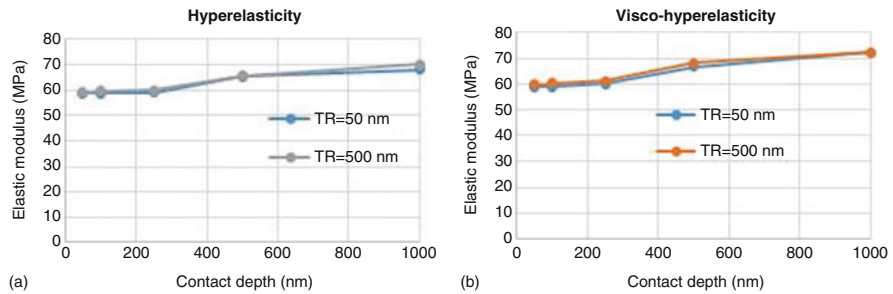


Fig. 8.23 Variation of elastic modulus versus displacement during the nanoindentation testing on specimen with (a) purely hyper elastic model (Mooney Rivlin), (b) Viscous hyper elasticity model (Combined Prony shear relaxation and Mooney Rivlin model)

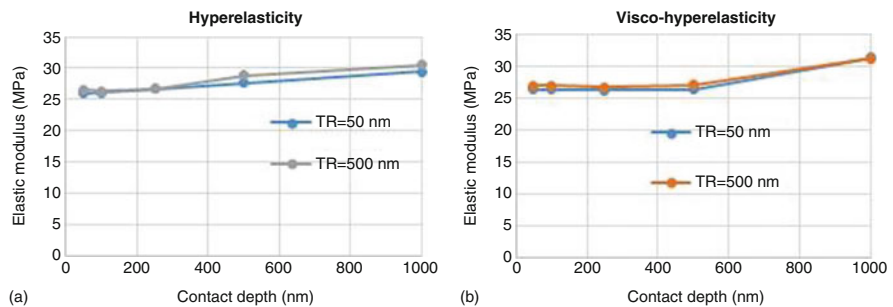


Fig. 8.24 Variation of elastic modulus versus applied displacement during the nanoindentation testing on specimen with (a) purely hyper elastic model (Ogden), (b) Viscous hyper elasticity model (Combined Prony shear relaxation and Ogden model)

Using the Ogden material model (Fig. 8.24) shows that for indentation depth less than 250 nm, hyper-elasticity effects are insensitive to the variation in tip radius but it becomes a bit more sensitive when indentation depth increases. In addition,

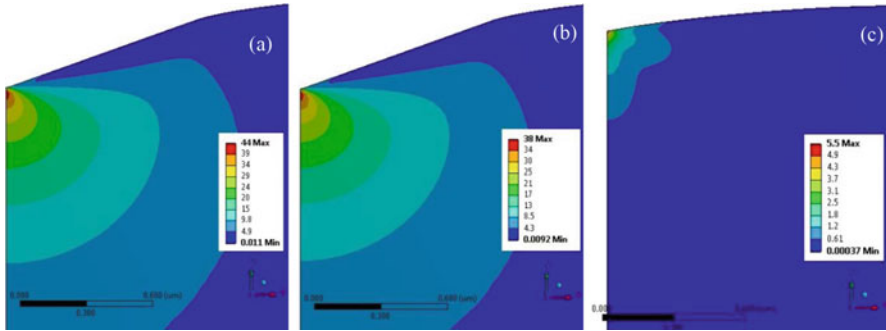


Fig. 8.25 Evolution of von Mises stress distribution during the nanoindentation of visco hyper elastic material using combined Prony shear relaxation and Mooney-Rivlin model) with the indenter tip radius of 50 nm after (a), 1 s, (b) 2 s (c) 3 s

the viscosity effects are insensitive to the variation in tip radius, while they are also insensitive to the contact depth (for indentation depth less than 500 nm)

In order to understand the effect of indenter tip radius on the mechanics of nanoindentation of soft polymeric materials with either purely hyper elastic or viscous hyper elastic properties, FE calculated Von Mises stress distribution are shown in Figs. 8.25, 8.26, 8.27 and 8.28. As it can be seen in these figures, the stress fields in nanoindentation testing of specimen is affected by the size of the indenter. Regardless of the indentation depths and material models, a sharper tip induces higher stress values. For example for testing a sample with purely hyper elastic behaviour (Mooney Rivlin model) at the maximum displacement of 500 nm, a conical indenter tip with 500 nm radius induces maximum stress of 30 MPa as opposed to 52 MPa when the tip radius is 50 nm. In addition, sharper conical tip produces a smaller deforming volume compared to a larger tip. Similar comparison can be made for testing a sample with viscous hyper elastic behaviour (Prony shear relaxation model combined with Mooney Rivlin). Obviously, because of the relaxation model used in the FE model in the material of a nanoindented sample, the maximum stress values are lower compared to the purely hyper elastic model. In addition, compared to the purely hyper elastic model of an indented sample, the residual stress after complete unloading, shows the effect of viscoelasticity (Prony shear relaxation) in the FE model. Regardless of the material models used for the FE analysis of nanoindentation, the highest stress value is located under the contact area between the indenter tip and specimen (not at the surface of tested specimen but deeper under the indenter as might be expected from Hertzian contact theory). The stress fields of other hyper elastic and viscous hyper elastic material models (Ogden and Arruda Boyce) are similar to the stress fields of the Mooney Rivlin model, while the maximum stress values obtained by Ogden and Arruda Boyce are lower.

Figure 8.29 compares the elastic modulus measured experimentally using the uniaxial tensile test and that reconstructed numerically from nanoindentation by giving the tensile data as input to the FE model of nanoindentation to extract

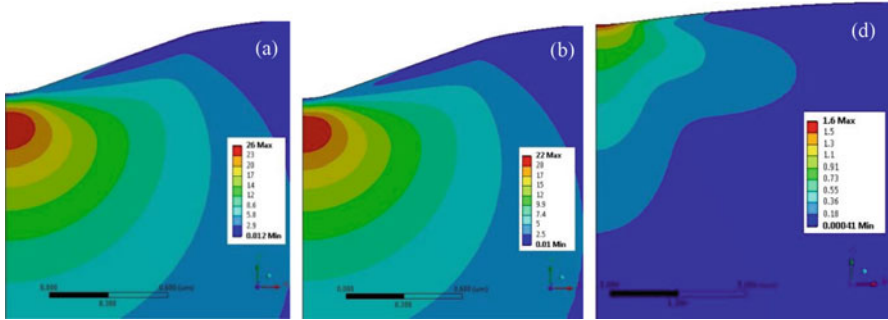


Fig. 8.26 Evolution of von Mises stress distribution during the nanoindentation of viscous hyper elastic material using combined Prony shear relaxation and Mooney-Rivlin model and indenter tip radius of 500 nm after (a), 1 s, (b) 2 s (c) 3 s

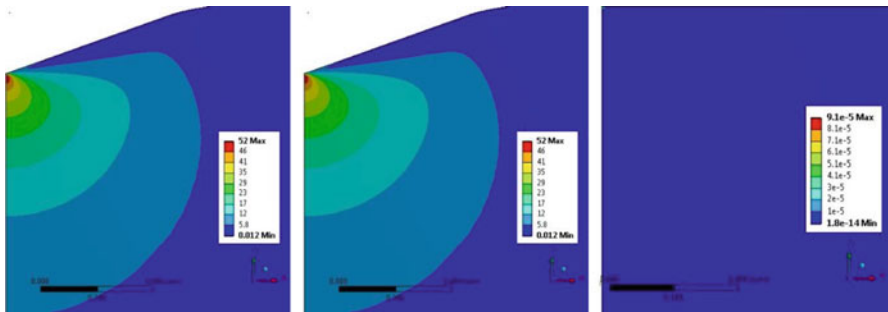


Fig. 8.27 Evolution of von Mises stress distribution during the nanoindentation of pure hyper elastic material using Mooney-Rivlin model and indenter tip radius of 50 nm after (a), 1 s, (b) 2 s (c) 3 s

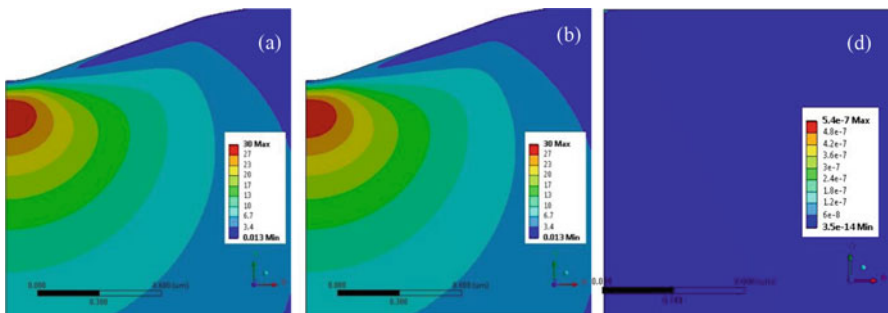


Fig. 8.28 Evolution of von Mises stress distribution during the nanoindentation of pure hyper elastic material using Mooney-Rivlin model and indenter tip radius of 500 nm after (a), 1 s, (b) 2 s (c) 3 s

constitutive parameters using various hyperelastic models. From the Fig. 8.29 it can be observed that the finite element simulations output of averaged modulus

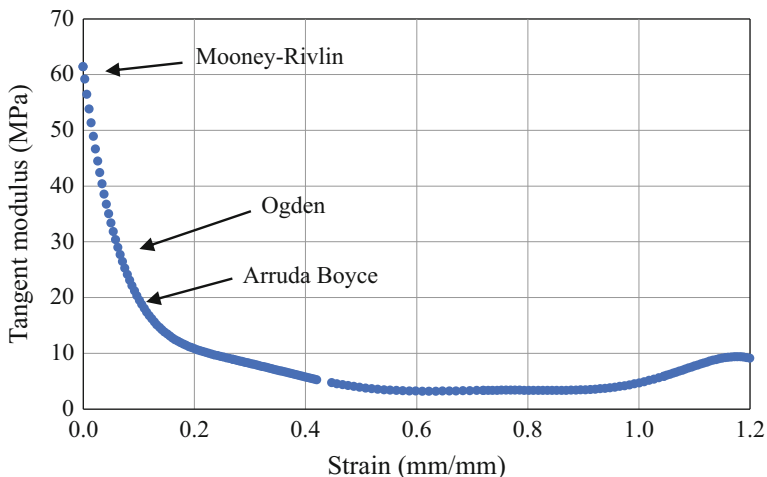


Fig. 8.29 Comparison between the elastic modulus obtained from FE calculated nanoindentation load displacement data and experimentally tensile stress-strain data

of different hyperelastic materials using the Mooney Rivlin, Ogden and Arruda-Boyce model closely matches with the experimental data. The numerical validation of the experimental results of elastic modulus was appropriately fit over the entire range of the strain. The Mooney-Rivlin model was found to be suitable to represent accurately nonlinear mechanical behaviour and shown the excellent agreement with numerical validation of the experimental results over a wide range of strains. The average elastic modulus E was about 62 MPa for Mooney-Rivlin. Both the Arruda-Boyce and Ogden models predicted the lower elastic modulus compared with the Mooney Rivlin model. The average elastic modulus E was about 17.3 MPa for Arruda-Boyce model, and the average elastic modulus E was about 28.5 MPa for Ogden model. Thus the results confirm that the Mooney-Rivlin approach is most suitable for small strain hyperelasticity whilst the other models are more suitable at larger strains.

4 Conclusions

The extraction of mechanical behaviour of soft materials using nanoindentation is performed through combined experimental and numerical simulations. Hyper elastic constitutive models such as the Mooney Rivlin model, the Ogden model and the Arruda-Boyce model as well as viscoelastic/viscoplastic models such as Prony shear relaxation, Perzyna and Modified time hardening models are required for the FEM. The input parameters can be extracted from the uniaxial tensile test and digital image correlation (DIC) technique on PMMA, epoxy resin and polyurethane rubber materials.

In a rubber-like polymer with hyper elastic properties, the Mooney-Rivlin model was found to be suitable to represent accurately nonlinear mechanical behaviour and shows excellent agreement with numerical validation of the experimental results over a wide range of strains. When it comes to the combined viscoelasticity and hyperelasticity properties of rubber like materials, it was found that viscosity effects are sensitive to the varied indentation depth and insensitive to tip radius respectively when this material model is used.

In polymers like epoxy resin, although atomic force microscopy images of residual impressions showed regions of material pile-up, the viscoplastic recovery which occurs following indenter unloading makes the determination of the contact areas problematic. The use of FEM to predict the projected indentation contact area, given the viscoplasticity parameters (e.g. Modified time hardening and/or Perzyna) of epoxy resin, is shown to be useful when extracting the mechanical properties from the nanoindentation technique. It was also shown that the overestimation of the elastic modulus calculated by the nanoindentation test method in relation to the macroscopic conventional test methods (e.g. tensile and/or compressive tests) is mainly related to the effects of material pile up, viscoplasticity and hydrostatic stress. It was found that, the FE calculated indentation modulus will be in a good agreement with macroscopic tensile modulus values provided that the viscoplastic deformation is allowed to finish prior to unloading. FEA suggested that, this can be obtained by altering indentation settings (i.e. holding segment and/or strain rate), therefore the elastic modulus of bulk epoxy resin can be determined, independent of the viscous effects.

In polymeric materials which only show viscoelasticity properties (e.g. PMMA), it was found that analytical expression developed in the literature can be successfully used to determine the Prony series parameters. Using these parameters in an FE model, resulted similar load displacement data obtained from the experimental nanoindentation.

Thus, the combined FE and experimental nanoindentation approach used in this study shows that appropriate constitutive models are needed to characterize mechanical and deformation behaviour of polymers and therefore, careful modelling of experimental data is necessary for understanding deformation mechanisms.

Acknowledgements This work was supported by EPSRC through the NECEM project (EP/R21503/1).

References

- Alfrey T, Doty P (1945) The methods of specifying the properties of viscoelastic materials. *J Appl Phys* 16(11):700–713
- Argatov I et al (2013) Accounting for the thickness effect in dynamic spherical indentation of a viscoelastic layer: application to non-destructive testing of articular cartilage. *Eur J Mech-A/Solids* 37:304–317

- Arruda EM, Boyce MC (1993) A three-dimensional constitutive model for the large stretch behavior of rubber elastic materials. *J Mech Phys Solids* 41(2):389–412
- Atkins A, Tabor D (1965) Plastic indentation in metals with cones. *J Mech Phys Solids* 13(3):149–164
- Baral P et al (2017) Theoretical and experimental analysis of indentation relaxation test. *J Mater Res* 32(12):2286–2296
- Batra R, Kim C (1990) Effect of viscoplastic flow rules on the initiation and growth of shear bands at high strain rates. *J Mech Phys Solids* 38(6):859–874
- Beegan D et al (2003) A nanoindentation study of copper films on oxidised silicon substrates. *Surf Coat Technol* 176(1):124–130
- Berkovich E (1950) Three-faceted diamond pyramid for studying microhardness by indentation. *Zavod Lab* 13(3):345–347
- Blatz P et al (1974) Strain energy function for rubberlike materials based on a generalized measure of strain. *Trans Soc Rheol* 18(1):145–161
- Bolshakov A, Pharr G (1998) Influences of pileup on the measurement of mechanical properties by load and depth sensing indentation techniques. *J Mater Res* 13(4):1049–1058
- Boyce MC, Arruda EM (2000) Constitutive models of rubber elasticity: a review. *Rubber Chem Technol* 73(3):504–523
- Bradley G et al (2001) Rubber modeling using uniaxial test data. *J Appl Polym Sci* 81(4):837–848
- Brinson HF, Brinson LC (2008) *Polymer engineering science and viscoelasticity*. Springer, New York
- Briscoe BJ, Sebastian KS (1996) The elastoplastic response of poly (methyl methacrylate) to indentation. *Proc R Soc Lond Series A Math Phys Eng Sci* 452(1946):439–457
- Briscoe B et al (1998) Nano-indentation of polymeric surfaces. *J Phys D Appl Phys* 31(19):2395
- Cao Y et al (2006) Nanoindentation measurements of the mechanical properties of polycrystalline Au and Ag thin films on silicon substrates: effects of grain size and film thickness. *Mater Sci Eng A* 427(1–2):232–240
- Cheng L et al (2000) Flat-punch indentation of viscoelastic material. *J Polym Sci B Polym Phys* 38(1):10–22
- Dean G et al (2011) Modeling nonlinear viscoelasticity in polymers for design using finite element analysis. *Polym Eng Sci* 51(11):2210–2219
- Doerner MF, Nix WD (1986) A method for interpreting the data from depth-sensing indentation instruments. *J Mater Res* 1(4):601–609
- Dorfmann A, Muhr A (1999) *Constitutive models for rubber*. CRC Press, Boca Raton
- Dutcher JR, Marangoni AG (2004) *Soft materials: structure and dynamics*. CRC Press, Boca Raton
- Dvir T et al (2011) Nanotechnological strategies for engineering complex tissues. *Nat Nanotechnol* 6(1):13
- Ebenstein DM, Pruitt LA (2006) Nanoindentation of biological materials. *Nano Today* 1(3):26–33
- Fill TS et al (2012) Analytically determined mechanical properties of, and models for the periodontal ligament: critical review of literature. *J Biomech* 45(1):9–16
- Fischer-Cripps AC, Nicholson D (2004) Nanoindentation. *Mechanical engineering series. Appl Mech Rev* 57(2):B12–B12
- Fröhlich F et al (1977) Performance and analysis of recording microhardness tests. *Phys Status Solidi A* 42(1):79–89
- Gent A (1996) A new constitutive relation for rubber. *Rubber Chem Technol* 69(1):59–61
- Gent AN (2012) *Engineering with rubber: how to design rubber components*. Carl Hanser Verlag GmbH Co KG, Munich
- Gurtin M (1973) *The linear theory of elasticity. Linear theories of elasticity and Thermoelasticity*. Springer, Berlin
- Hardiman M et al (2016) The effects of pile-up, viscoelasticity and hydrostatic stress on polymer matrix nanoindentation. *Polym Test* 52:157–166
- Hochstetter G et al (1999) Strain-rate effects on hardness of glassy polymers in the nanoscale range. Comparison between quasi-static and continuous stiffness measurements. *J Macromol Sci—Phys* 38(5–6):681–692

- Horgan CO, Saccomandi G (2002) Constitutive modelling of rubber-like and biological materials with limiting chain extensibility. *Math Mech Solids* 7(4):353–371
- Huang G, Lu H (2006) Measurement of Young's relaxation modulus using nanoindentation. *Mech Time-dependent Mater* 10(3):229–243
- Huang G et al (2004) Measurements of viscoelastic functions of polymers in the frequency-domain using nanoindentation. *Mech Time-dependent Mater* 8(4):345–364
- Ifkovits JL, Burdick JA (2007) Photopolymerizable and degradable biomaterials for tissue engineering applications. *Tissue Eng* 13(10):2369–2385
- Johnson KL, Johnson KL (1987) *Contact mechanics*. Cambridge University Press, Cambridge
- Kese K, Li Z-C (2006) Semi-ellipse method for accounting for the pile-up contact area during nanoindentation with the Berkovich indenter. *Scr Mater* 55(8):699–702
- King JA et al (2013) Mechanical properties of graphene nanoplatelet/epoxy composites. *J Appl Polym Sci* 128(6):4217–4223
- Li X, Bhushan B (2002) A review of nanoindentation continuous stiffness measurement technique and its applications. *Mater Charact* 48(1):11–36
- Li Y et al (2018) Non-contact tensile viscoelastic characterization of microscale biological materials. *Acta Mech Sinica* 34(3):589–599
- Lu H et al (2003) Measurement of creep compliance of solid polymers by nanoindentation. *Mech Time-dependent Mater* 7(3–4):189–207
- MacManus DB et al (2016) Mechanical characterization of the P56 mouse brain under large-deformation dynamic indentation. *Sci Rep* 6:21569
- Mata M, Alcalá J (2004) The role of friction on sharp indentation. *J Mech Phys Solids* 52(1):145–165
- Moerman KM et al (2009) Digital image correlation and finite element modelling as a method to determine mechanical properties of human soft tissue in vivo. *J Biomech* 42(8):1150–1153
- Mooney M (1940) A theory of large elastic deformation. *J Appl Phys* 11(9):582–592
- Nie X et al (2009) Dynamic tensile testing of soft materials. *Exp Mech* 49(4):451–458
- Odegard G et al (2005) Characterization of viscoelastic properties of polymeric materials through nanoindentation. *Exp Mech* 45(2):130–136
- Ogden RW (1972) Large deformation isotropic elasticity—on the correlation of theory and experiment for incompressible rubberlike solids. *Proc R Soc Lond A Math Phys Sci* 326(1567):565–584
- Ogden R (1973) Large deformation isotropic elasticity—on the correlation of theory and experiment for incompressible rubberlike solids. *Rubber Chem Technol* 46(2):398–416
- Ogden RW (1997) *Non-linear elastic deformations*. Courier Corporation, North Chelmsford, MA
- Oliver WC, Pharr GM (1992) An improved technique for determining hardness and elastic modulus using load and displacement sensing indentation experiments. *J Mater Res* 7(6):1564–1583
- Oliver WC, Pharr GM (2010) Nanoindentation in materials research: past, present, and future. *MRS Bull* 35(11):897–907
- Oyen ML (2007) Sensitivity of polymer nanoindentation creep measurements to experimental variables. *Acta Mater* 55(11):3633–3639
- Oyen ML (2008) The materials science of bone: lessons from nature for biomimetic materials synthesis. *MRS Bull* 33(1):49–55
- Perzyna P (1963a) The constitutive equation for work-hardening and rate sensitive plastic materials. *Proc. Vibrational Problems* 4:281–290
- Perzyna P (1963b) The constitutive equations for rate sensitive plastic materials. *Q Appl Math* 20(4):321–332
- Perzyna P (1966) Fundamental problems in viscoplasticity. *Adv Appl Mech Elsevier* 9:243–377
- Pharr GM et al (2010) The indentation size effect: a critical examination of experimental observations and mechanistic interpretations. *Annu Rev Mater Res* 40:271–292
- Piskin E (1995) Biodegradable polymers as biomaterials. *J Biomater Sci Polym Ed* 6(9):775–795
- Rivlin RS, Saunders D (1951) Large elastic deformations of isotropic materials VII. Experiments on the deformation of rubber. *Phil Trans R Soc Lond Series A Math Phys Sci* 243(865):251–288

- Rodríguez M et al (2012) Determination of the mechanical properties of amorphous materials through instrumented nanoindentation. *Acta Mater* 60(9):3953–3964
- Saha R, Nix W (2001) Soft films on hard substrates—nanoindentation of tungsten films on sapphire substrates. *Mater Sci Eng A* 319:898–901
- Shtil'man MI (2003) *Polymeric biomaterials*. VSP, New York
- Simo JC, Hughes TJ (2006) *Computational inelasticity*. Springer Science & Business Media, New York
- Sinha SK, Briscoe BJ (2009) *Polymer tribology*. World Scientific Publishing, Singapore
- Sneddon IN (1965) The relation between load and penetration in the axisymmetric Boussinesq problem for a punch of arbitrary profile. *Int J Eng Sci* 3(1):47–57
- Solutions C (2009) *Vic-2D. Reference Manual*
- Tranchida D et al (2007) Mechanical characterization of polymers on a nanometer scale through nanoindentation. A study on pile-up and viscoelasticity. *Macromolecules* 40(4):1259–1267
- Ulery BD et al (2011) Biomedical applications of biodegradable polymers. *J Polym Sci B Polym Phys* 49(12):832–864
- VanLandingham M et al (1999) Characterization of nanoscale property variations in polymer composite systems: 1. Experimental results. *Compos A: Appl Sci Manuf* 30(1):75–83
- VanLandingham MR et al (2001) Nanoindentation of polymers: an overview. *Macromolecular symposia*, Wiley Online Library
- VanLandingham MR et al (2005) Viscoelastic characterization of polymers using instrumented indentation. I. Quasi-static testing. *J Polym Sci B Polym Phys* 43(14):1794–1811
- Zadpoor AA (2015) Mechanics of biological tissues and biomaterials: current trends. *Materials* 8:4505–4511
- Zhang J et al (2010) Characterization of indentation response and stiffness reduction of bone using a continuum damage model. *J Mech Behav Biomed Mater* 3(2):189–202
- Zhou X et al (2008) Investigation on methods for dealing with pile-up errors in evaluating the mechanical properties of thin metal films at sub-micron scale on hard substrates by nanoindentation technique. *Mater Sci Eng A* 488(1–2):318–332

Chapter 9

Indentation Tests of Biological Materials: Theoretical Aspects



Xiaoqing Jin, Pu Li, and Feodor M. Borodich

Abstract The term ‘biological material’ includes many meanings, and here it means materials that constitute living organisms. The variety of material parts of living organisms is huge. They may be hard and soft, elastic and viscoelastic, quite often sizes of constitutive parts are within micro or nano scales and they can be considered as structured biocomposite materials. The traditional methods of materials testing are not applicable to evaluating mechanical properties of materials of very small volumes. It is also very difficult to apply traditional approaches for characterization of very soft materials. Therefore, indentation techniques are widely used to estimate mechanical properties of biological materials. In this review paper, we briefly discuss some results related to mechanics of contact between an indenter and a deformable sample. Then we critically examine the common approaches to interpretation of indentation experimental data. Finally we discuss the results of indentation tests of biomaterials having rather different properties: bones, snake skins, and cartilages, along with resilin and elastin-based materials. We argue that also depth-sensing indentation is a valuable tool for studying mechanical properties of biomaterials, one should be aware that the theoretical models used for justification of modern nanoindentation tests are based on non-adhesive contact, while the influence of adhesive interactions increases as the scale of samples goes down to micro and nanoscales.

Keywords Nanoindentation · Hardness · Estimation of elastic modulus · Bones · Cartilages · Snake skins

X. Jin (✉) · P. Li
College of Aerospace Engineering, Chongqing University, Chongqing, China
e-mail: jinxq@cqu.edu.cn

F. M. Borodich
College of Aerospace Engineering, Chongqing University, Chongqing, China
School of Engineering, Cardiff University, Cardiff, UK
e-mail: BorodichFM@cardiff.ac.uk

1 Introduction

It is known that many biological materials have a complex structure made of materials having rather different mechanical properties (see e.g. Gao 2006; Meyers et al. 2008). Hence, they can be classified as complex composites. Although mechanical properties of these materials at macro and meso scales may be estimated using standard mechanical tests, e.g. using tensile testing engines or by bending of material samples, the traditional methods of materials testing are not applicable to evaluating mechanical properties of materials of very small volumes. Because the biological materials are inhomogeneous at the micro-level, special approaches are needed to assess the mechanical properties of their constitutive components.

Currently depth-sensing indentation (DSI) techniques are widely used to estimate properties of small or very thin material samples. Indeed, indentation techniques can be employed to evaluate mechanical properties of materials of very small volumes or very thin layers. This chapter is devoted to review of theoretical approaches to DSI, the connections between results of contact mechanics and methods to evaluate mechanical properties from DSI experiments along with a review of applications of DSI methods to various biological materials such as bones, cartilages, resilin, elastin and living cells.

The depth-sensing indentation techniques were introduced by Kalei (1967) in his PhD thesis prepared under supervision of M.M. Khrushchov (1890–1972). and the first paper describing these techniques was published in 1968 (Kalei 1968). Kalei's indenter was a modification of a standard four-side pyramid PMT-3 microhardness tester built by Khrushchov and Berkovich (1950, 1951). Kalei presented the load-depth of indentation diagrams for various materials. In particular, he presented an experimental diagram of indentation of a chromium film of 1 μm thickness when the maximum depth of indentation was 150 nm. He has also presented results of DSI for some plastics that clearly showed the creeping effects for the viscoelastic materials. The DSI techniques can be applied to both sharp indenters (pyramids or cones) and blunt indenters, e.g. spherical indenters.

The popularity of the DSI techniques employing sharp pyramidal indenters is mainly due to the introduction of the BASH formula (Bulychev et al. 1975) and its interpretation according to Oliver and Pharr (1992). One needs to realize that the theoretical background of the DSI techniques in application to sharp indenters suffers from the lack of rigorous background, while DSI indentation by spherical indenters may be justified by the use of the well-established theories of adhesive contact (see, e.g. Borodich and Galanov 2008; Borodich 2014; Perepelkin et al. 2020). Nevertheless, the number of papers devoted to material testing by techniques based on the BASH formula (Bulychev et al. 1975) along with the OP interpretation (Oliver and Pharr 1992) is enormous, while the number of papers based on employment of spherical indenters along with the so-called BG method (Borodich and Galanov 2008) is very modest. This is the reason that here the results related to applications of sharp indenters for testing material properties are mainly considered.

2 Hardness Tests and Depth-Sensing Indentation Techniques

In 1722 Réaumur suggested to compare relative hardness of two materials by measuring sizes of plastic indents after compression of the samples. The material samples were prepared as wedges and in the compression tests the axes of the wedges were perpendicular to each other, for details see the review by Williams (1942). The material of a sample having deeper residual indent is softer than the material of another wedge. Then indenters of rather different shapes were used in hardness tests, see the review by Brinell (1900).

2.1 Traditional Hardness Tests

Indentation methods were developed initially for determination of hardness of materials (see, e.g. discussions by Grigorovich 1976; Fischer-Cripps 2011; Borodich and Keer 2004b). The hardness H was defined originally as the ratio of the maximum indentation force to the area of the plastic imprint after unloading

$$\text{Hardness} = \frac{\text{Load}}{\text{Area of imprint}}.$$

Brinell (1900) considered the area of curved surface of a spherical imprint, hence the Brinnell hardness H_B is defined as

$$H_B = \frac{P}{A}, \quad A = \frac{\pi D}{2} \left(D - \sqrt{D^2 - 4a^2} \right).$$

Here a is the radius of the imprint and D is the diameter of the ball. Meyer (1908) suggested to measure the area of the impression projected on the initial contact plane and the Meyer hardness H_M is defined as (see, e.g. Tabor 1951)

$$H_M = \frac{P}{A}, \quad A = \pi a^2.$$

Although the ratio ‘Force / Projected Area’ is called ‘Indentation Hardness’ in ISO Standards and the ratio ‘Force / Contact Area’ is called ‘Martens Hardness’ (see, e.g. Shuman 2005), these definitions go back to Meyer (1908) and Brinell (1900) respectively.

Compared with spherical indenters, conical and pyramidal indenters have the advantage that geometrically similar impressions are obtained at different loads (Mott 1956). Ludwik (1908) suggested to use a diamond cone in a hardness test, while Smith and Sandland (1922, 1925) suggested to use a square-base diamond pyramid (the Vickers indenter).

The three-sided indenters were introduced by Khrushchev and Berkovich for microhardness tests. They were also pioneers in application of transmission electron microscopy for studying the imprints. Berkovich suggested to use such an angle of the three-sided pyramid that the pyramid has the same projected area (A) to depth ratio (h) as a Vickers indenter (Khrushchov and Berkovich 1950, 1951)

$$A \approx 24.5h^2.$$

This so-called Berkovich indenter is widely used in modern indentation tests.

Tabor (1948) and Stilwell and Tabor (1961) studied the shapes of imprints formed in metal samples by spherical and conical indenters. These studies confirmed the observations by Brinell (1900), Ludwik (1908) and Smith and Sandland (1925) that imprints are geometrically similar to the shapes of the indenters. However, the imprints formed by spherical indenters have larger radius than the radius of the indenter, and the included tip angle of a conical indenter is larger than the included tip angle of the indenter. This effect is well known in contact mechanics. It was discussed in detail by Johnson (1985) (see, paragraph 6.4 of his book). However, this effect (the Galanov effect) was first taken into account in indentation models only in 1983 (Galanov et al. 1983, 1984).

2.2 *Fracture Effects in Indentation Tests and Microbrittleness Tests*

Problems of contact between a rigid indenter and a brittle material resulting in cracking were studied by many authors. Hertz (1882b) was the first researcher who mentioned creation of cracks due to punch indentation. Then the problems related to crack formation during indentation into brittle and elastic-plastic materials were intensively studied. Bernhardt (1941) argued that if the external load acting on a sharp indenter in a microindentation test of a brittle material is below some critical load P_{cr} specific for the material, then no cracks are observed. The microbrittleness of minerals and coals is usually calculated using this observation, namely the number of imprints producing cracks in a group of 100 imprints of a sample is calculated and this number is used as the microbrittleness characteristics (see a discussion by Kossovich et al. 2019). One can find literature reviews related to crack formation and fracture during indentation tests in papers by Lawn and Swain (1975), Swain and Lawn (1976), Swain and Hagan (1976) and Kossovich et al. (2020), along with monographs by Lawn and Wilshaw (1975), Kolesnikov and Morozov (1989), Lawn (1993), and Morozov and Zernin (1999). A rather sophisticated behaviour is observed in glass samples under action of a small spherical indenter: median cracks and plastic deformation within a core region along with occasionally Hertzian cone cracks form during the loading cycle, while radial cracks and lateral cracks occur

on the unloading cycle (Swain and Hagan 1976; Lawn 1993; Morozov and Zernin 1999).

2.3 *Depth-Sensing Indentation and Measurements of Hardness*

As it has been mentioned, Kalei (1968) published the first paper on a revolutionary novel technique—depth-sensing nanoindentation. Valentin P. Alekhin was Kalei's room-mate in a PhD student hostel of the USSR Academy of Sciences. Alekhin suggested to use more advanced measurement devices for Kalei's nanoindenter (Alekhin et al. 1972). The DSI technique became popular very rapidly (see, e.g., Ternovskii et al. 1973; Galanov et al. 1983). In 1983 Pethica et al. (1983) monitored indentations to depths as low as 20 nm. The modern sensors have very high precision and they are able to monitor the depth of indentation h and the load P applied to the indenter in scales of few nanometres and micro-Newton, respectively.

Contrary to the above definition of hardness, where the area of residual imprints was measured, in DSI tests hardness is often defined as the load divided by projected area under the indenter at various points on the loading curve or the ratio of current contact force to the current contact area, i.e. the current H_M (see, e.g. Bhattacharya and Nix 1988)

$$\text{Hardness} = \frac{\text{Current Load}}{\text{Current Area of contact}}. \quad (9.1)$$

In essence, interpretations of the hardness tests are rather empirical, however if one employs the Meyer definition then one can apply the Hertz contact theory for theoretical studies of corresponding relations. The Hertz theory includes not only the original problems considered by Hertz (1882a,b) but also it includes problems for punches having more general shapes than the elliptic paraboloid and media that can have more general relation than the constitutive relations of linear elasticity. In particular, it considers the indenters whose shapes may be described as monomial (power-law) functions of degree d and the constitutive relations between stresses σ and strains ϵ may be described as power-law relations of degree κ . Roughly speaking, $\sigma \propto \epsilon^\kappa$. In particular, we have $\kappa = 1$ for the linear elasticity.

We will employ both the Cartesian and cylindrical coordinate frames, namely $x_1 = x, x_2 = y, x_3 = z$ and r, ϕ, z , where $r = \sqrt{x^2 + y^2}$ and $x = r \cos \phi, y = r \sin \phi$. It is assumed that two bodies (the indenter and the sample) contact initially at a point that will be denoted as (O) and is taken as the origin of Cartesian x, y, z and r, ϕ, z -coordinate frames. Then the shape of a power-law shaped indenter $f(r, \phi)$ can be presented as

$$z = f(r, \phi) = B_d(\phi)r^d \quad (9.2)$$

where $B_d(\phi)$ is the height of the indenter at a point $r = 1, \phi$. The shapes described by (9.2) include pyramidal and conical indenters ($d = 1$), spheres ($d = 2$) and flat ended punches ($d = \infty$).

The Hertz-type contact problems are often self-similar (Galanov 1981a,b; Borodich 1983, 1989, 1993). The conditions under which Hertz-type contact problems are self-similarity, may be formulated in the following way (Borodich 1988): *the constitutive relationships are homogeneous with respect to the strains or the stresses and the indenter's shape is described by a homogeneous function whose degree is greater than or equal to unity. It is also assumed that during the process of the contact, the loading at any point is progressive.*

Borodich et al. (2003) and Choi and Korach (2011) argued that the indenters that are very sharp at meso and macro scales, have some tip bluntness (usually at heights less than 100 nm). This is very important for shallow indentation depths. If the above definition (9.1) is used and the indenter bluntness can be described as power-law function (9.2) then Borodich's rescaling formulae (Borodich 1989, 1993) may be employed. For self-similar Hertz type contact problems, these rescaling relations are valid for both linear and non-linear, isotropic and anisotropic materials, and for various boundary conditions within the contact region.

If for some initial load P_1 , one knows the corresponding contact area $A_1 = A(P_1)$, the characteristic size of the contact region $l_1 = l(P_1)$, the displacement $h_1 = h(P_1)$, and the hardness $H_1 = P_1/A_1$ then it follows from the scaling relations that for any external compressing load P ,

$$\frac{l(P)}{l_1} = \left(\frac{P}{P_1}\right)^{\frac{1}{2+\kappa(d-1)}}, \quad \frac{h(P)}{h_1} = \left(\frac{P}{P_1}\right)^{\frac{d}{2+\kappa(d-1)}} \quad (9.3)$$

and

$$\frac{A(P)}{A_1} = \left(\frac{h}{h_1}\right)^{\frac{2}{d}} \quad (9.4)$$

The above rescaling formulae (9.3) and (9.4) were obtained assuming the homogeneity of material properties and that the stress-strain relation remains the same for any depth of indentation. This is not always true.

It follows from (9.4) that $h \sim A^{d/2}$ independently of the work hardening exponent κ and that the hardness is the following function of the depth of indentation

$$\frac{H(P)}{H_1} = \left(\frac{h}{h_1}\right)^{\frac{\kappa(d-1)}{d}}.$$

Therefore, the hardness is a power-law function of the indentation depth, and only for an ideal conical or pyramid-shaped indenters, when $d = 1$, the hardness is constant. Thus, non-ideal shapes of indenters may affect the interpretation of the experimental results.

2.4 Depth-Sensing Indentation and Estimations of Elastic Moduli of Materials

Bulychev and Alekhin along with the former supervisor of their PhD studies Shorshorov published a series of papers (Bulychev et al. 1975, 1976; Shorshorov et al. 1981) where they suggested to estimate the contact modulus of materials using the unloading branch of the indenter force-displacement curve $P - h$ where h is the approach between the indenter and the surface. Note that the approach between an indenter and the sample surface (the depth of indentation) is traditionally denoted by h in materials science community, while in contact mechanics this parameter is often denoted by δ .

Bulychev et al. (1975) noted that for some axisymmetric indenters, the slope of the $P - h$ curve calculated in the framework of the Hertz contact theory satisfies the exact expression

$$\frac{dP}{dh} = 2E^*a, \quad (9.5)$$

where E^* is the contact reduced modulus and a is the contact radius.

It follows from the Hertz contact theory that if an isotropic linear elastic half-space is characterized by the Young's modulus E and the Poisson ratio ν then its contact modulus E^* is defined as

$$E^* = \frac{E}{1 - \nu^2}. \quad (9.6)$$

The problem of contact between two elastic bodies having contact moduli E_1^* and E_2^* respectively is mathematically equivalent to the problem of contact between an isotropic elastic half-space with contact modulus E_I^*

$$\frac{1}{E_I^*} = \frac{1}{E_1^*} + \frac{1}{E_2^*} \quad (9.7)$$

and a curved body whose shape function f is equal to the initial distance between the surfaces, i.e. $f = f_1 + f_2$, where f_1 and f_2 are the shape functions of the solids. To apply (9.7) formula both solids should be approximated as elastic half-spaces. Hence, formally this expression is not applicable to sharp indenters. However, if the indenter is much harder than the biological materials, i.e. $E_2^* \gg E_1^*$ then one can put $E_2 = \infty$ and $E_I^* = E_1^*$.

Bulychev et al. (1975) suggested to use the following approximate expression (the BASH formula)

$$\frac{dP}{dh} = 2E^* \sqrt{\frac{A}{\pi}} \quad (9.8)$$

where A is the contact area. They argued that (9.8) can be applied not only to axisymmetric indenters as (9.5) but also to pyramidal indenters and that the error will be small (Bulychev et al. 1976). This formula is the corner stone of interpretation of results of nanoindentation tests (Hay et al. 1999).

Note that the above expressions follow from the Hertz contact theory assuming that there is no friction between contacting solids. It has been shown by Borodich and Keer (2004a) that in the case of no-slip contact between a rigid indenter and an elastic sample

$$\frac{dP}{dh} = 2C_{NS}E^*a, \quad (9.9)$$

where

$$C_{NS} = \frac{(1 - \nu) \ln(3 - 4\nu)}{1 - 2\nu}. \quad (9.10)$$

For real physical contact, there is some frictional slip at the edge of the contact region and the full adhesion preventing any slip within the contact region is not the case, hence, the values of the correction factor of the BASH relation cannot exceed the upper bound (9.10).

The loading and unloading branches of the $P - h$ relation are normally not the same because the loading branch may involve both elastic and plastic deformations of the material, while it is usually assumed that the unloading process is purely elastic. Hence, one can apply the Hertz-type solutions for the unloading branch (Galanov 1981b). Due to plastic deformation of the sample there is a residual depth h_r after unloading. If we denote by h_{max} the depth at of indentation at the maximum load (P_{max}) then to apply the Hertz-type contact solutions, one needs to shift the origin of the displacement axis by h_r . Then neglecting the distortion of the surface due to plastic deformation, one obtains $P \propto (h - h_r)^{2/3}$ or $P = c(h - h_r)^{2/3}$ for a spherical indenter. Here constant c is defined as $c = P_{max}/(h_{max} - h_r)^{2/3}$. For a pyramidal or conical indenter, one has $P \propto (h - h_r)^{1/2}$. For a general power-law shaped indenter of degree d , one has (Galanov 1981b)

$$P \propto (h - h_r)^{d/(d+1)}. \quad (9.11)$$

The above relations were obtained assuming that the Hertz-type theory is applicable. Taking a derivative of (9.11), one obtains

$$\frac{dP}{dh} \propto \frac{d}{d+1} (h - h_r)^{-1/(d+1)}. \quad (9.12)$$

However, 2 years later Galanov and his co-workers argued that the depth h used in (9.12) should be corrected taking into account the Galanov effect (Galanov et al. 1983, 1984): the real distance between the indenter and the surface of the imprint is not the same as the distance between a flat surface and the indenter. Hence,

analyzing the unloading branch of an experimental $P - h$ curve, one has to take into account both the shift of the displacement axis due to a residual depth of plastic indentation along with the effective distance between the indenter and the imprint surface. In particular, Galanov showed that if the indenter is a cone of semi-angle α , i.e. its shape is described by $f^+(r) = \cot \alpha r$ and it produces a conical indent of semi-angle α' , i.e. the indent shape is $f^-(r) = -\cot \alpha' r$, then instead of the solution obtained by Love (1939), one needs to use the following one

$$P = \frac{2E^*}{\pi} \cdot \frac{1}{\cot \alpha - \cot \alpha'} h^2. \quad (9.13)$$

Nowadays the DSI tests by pyramidal indenters are very popular to estimate mechanical properties (hardness, elastic modulus, fracture toughness) of materials, see e.g. discussions of DSI techniques and their applications by Borodich and Keer (2004b), Bull (2005), Menčík et al. (1997), Menčík (2007), Borodich (2011, 2014), and Argatov et al. (2017). The nanoindentation $P - h$ or $P - \delta$ curves provide a ‘fingerprint of a materials response to contact loading’, see paper by Chen and Bull (2006) who argued that nanoindentation testing is often the only viable approach to assess the damage mechanisms and properties of very thin coatings (less than $1 \mu\text{m}$). This is because it can operate at the required scale and provides fingerprint of the indentation response of the coating/substrate system.

The modern Materials Science community is using the BASH formula with some correction factors (Argatov et al. 2017):

$$\frac{dP}{dh} = \beta \frac{2}{\sqrt{\pi}} E^* \sqrt{A}, \quad \beta = \beta_1 \cdot \beta_2 \cdot \beta_3. \quad (9.14)$$

the factor β_1 due to the concept of the effective indenter shape, which accounts for distortion of the originally flat sample surface by the formation of the hardness impression (this idea is similar to the concept of the Galanov effect, however, it does not replace it, the introduction of the contact area shape factor β_2 , which extends the BASH formula to the non-axisymmetric case, and factor (β_3) for the effects of friction between the indenter and the half-space (Borodich and Keer 2004a,b).

Several practical approaches for evaluation of elastic modulus of material by nanoindentation were developed later (see e.g., Doerner and Nix 1986; Oliver and Pharr 1992; Fischer-Cripps 2011). All these approaches are based on the use of the BASH relation (9.8) or (9.14). It is clear that in order to use these formulae one needs to know the contact area. However, it is very difficult to measure the contact area used in (9.8). Oliver and Pharr (1992) developed a semi empirical approach to estimate the contact area A directly from indentation load and displacement measurements without the need to image the indenter imprint (hardness impression). They suggested to approximate the contact area under a Berkovich indenter of non-ideal shapes by the following indenter relation

$$A(h) = 24.5h^2 + \sum_{i=0}^7 C_i h^{1/2^i} \quad (9.15)$$

where C_i are fitting parameters. As it was noted by Borodich (2014), the approximation (9.15) has already proved its practical usefulness, however it does not have proper theoretical justification.

Recently the Oliver and Pharr approach was critically re-examined, its drawbacks and errors were pointed out by Galanov and Dub (2017). One of the drawbacks is that the Galanov effect was not taken properly into account and, hence the depth of indentation h was not properly calculated.

It is known that the Hertz-type contact problems for transversely isotropic solids and homogeneously prestressed elastic solids are mathematically equivalent to the problems for isotropic elastic solids (see, Willis 1966; Babich and Guz 1984, see also references in Borodich 1990, 2014). These results were used for measuring the elastic properties of anisotropic materials by means of nanoindentation experiments (Vlassak and Nix 1994). In fact they presented a modification of the BASH relation (9.8) where the contact modulus was replaced by an appropriate indentation modulus of material M . A development of the results by Willis (1966), and Vlassak and Nix (1994) was presented by Delafargue and Ulm (2004) who gave explicit formulae for the indentation modulus of a case of orthotropic materials. These formulae are widely used in testing biological materials (see, e.g. Carnelli et al. 2011, 2013; Taffetani et al. 2014).

3 Testing of Biological Materials Using Indentation Techniques

Biological materials consist often of a mixture of soft and hard brittle materials. It is possible to study mechanical response to indentation of a specific components of biocomposites. There is an enormous number of papers devoted to indentation tests of biological materials (see, e.g. reviews by Ebenstein and Pruitt 2006; Lewis and Nyman 2008; Rho et al. 1997, 1999). Here we present just some results of applications of indentation techniques to biological materials demonstrated rather different mechanical properties.

3.1 Testing of Hard Biological Materials

Gao and his co-workers studied the nanostructural mechanical properties of bone-like materials such as bone, tooth and shells. Studying biological materials, Gao (2006) asked and answered many questions including the following ones: (i) why is nanoscale important to biological materials? (ii) how does nature create a stiff composite containing a high volume fraction of a soft material? (iii) how does nature build a tough composite containing a high volume fraction of a brittle material? (iii) how does nature balance the widely different strengths of protein and mineral?

The explanations are based on description of complex hierarchy of structure of biocomposite materials. Evidently, the macroscale tests are not applicable to testing components of the composites whose sizes are within micrometre scale. Therefore, DSI tests were applied by many authors to measure mechanical properties of bone tissue at various structural levels (Ebenstein and Pruitt 2006; Lewis and Nyman 2008; Rettler et al. 2013; Rho et al. 1997, 1999). The determination of the elastic and inelastic properties of bone through micro or nanoindentation experimental tests should be performed by carefully considering at least two main factors; namely: the hierarchical arrangement of constituents and the anisotropy of the material response (Cowin 2001; Currey 2002; Weiner and Wagner 1998). Carnelli et al. (2011) investigated anisotropic elasticity of cortical bone by performing nanoindentation tests along multiple orientations. In particular, they presented results of nanoindentation tests on osteonal bovine bone obtained from a 30 months old cow. The bone along the axial (corresponding to the long bone axis as well as osteonal axis) and transverse (normal to the osteonal axis) directions were studied. Employing the analytical model for anisotropic elastic contact introduced by Delafargue and Ulm (2004), the uniaxial Young's moduli of osteonal bone in the axial and transverse were estimated from the experimental $P - h$ curves applying the Oliver-Pharr approach. Carnelli et al. (2013) described further nanoindentation studies of bone properties when the indentation tests were performed at different points along going radially out from the Haversian canal edge to the external region of the osteon. The four different maximum depths: 50, 100, 200 and 300 nm were controlled in the experiments. The indentation modulus M calculated according to Delafargue-Ulm procedure shows a periodic alternating trend of stiffness with spatial distance radially across the osteon for both the axial and transverse directions.

We would like to underline that the above mentioned procedures for interpretation of the $P - h$ curves assume that materials are elastic-plastic and the unloading branches of the $P - h$ reflect elastic properties of the same material. This approach was accepted by Borodich et al. (2015) when a procedure combined application of DSI to very thin coal samples and the use of transmitted light microscopy was introduced. The nanoindentation studies were caused by the following drawbacks of microhardness tests: (1) results obtained for relatively thick polished samples of coals depend on the presence of voids and microcracks and the inhomogeneity in-depth of a sample; (2) the test results vary for the same sample, hence 10–30 measurements were usually taken to estimate the range of the values obtained; and (3) one cannot estimate the mechanical properties within the border region of two different coal components. The further nanoindentation studies (Epshtein et al. 2015; Kossovich et al. 2016) showed that the values of moduli of thin films of coals glued to rigid support estimated by the Oliver-Pharr approach are in disagreement with values obtained by asymptotic approach. This disagreement was explained by Argatov et al. (2017) and Kossovich et al. (2019): the coal samples during loading have structural transformations and the material of a brittle coal sample within the indentation zone is no longer a continuous elastic medium but rather a fine powder of crushed material. The mechanism of coal dust formation during indentation was described by application of the Galanov-Grigoriev model (see for detail Kossovich

et al. 2020). Thus, applying the procedures for elastic-plastic materials to brittle biological materials, one needs to be careful because the material can be transformed during the indentation test.

3.2 *Testing of Articular Cartilage*

Articular cartilage (AC) is comprised of hyaline cartilage (a type of connective tissue without a nerve network) which has many important functions in an organism. It has excellent tribological properties and it is responsible for transmission of forces between joints. A pioneering paper on contact problems for AC was published by Hayes et al. (1972) who presented solutions to problems of contact between an AC layer and spherical indenter or flat-ended indenter. A monograph dedicated to contact mechanics of articular cartilage layers was presented by Argatov and Mishuris (2015).

Results of indentation testing of human articular cartilage performed using an arthroscopic probe were presented by Bae et al. (2003). The authors reported about the found connections among the effects of aging and degeneration of the tissue, the indentation stiffness, and the traditional indices of cartilage degeneration. These tests were rather different from indentation tests considered in this review. Wang et al. (2012) presented the results of atomic force microscopy studies of sheep cartilage surfaces. They have reported that the mean effective indentation modulus values of worn cartilages were lower than that of healthy cartilage as the control sample. Taffetani et al. (2014) argued that the compressive tests of AC at macroscale have some disadvantages, in particular that the experimental setup can significantly affect the results through misalignments, non-ideal contact conditions between tissue and sample holder and boundary effects which can result in a under- or overestimation of the tissue elastic properties. Hence, they performed nanoindentation tests of AC samples obtained from lateral and medial condyles of a knee of mature bovine. Comparing the results obtained by spherical indenters of radii 25 and 400 μm , they observed size effect similar to the effect reported by Simha et al. (2007) that the drained indentation modulus of bovine patellar cartilage decreased up to three times (from 4.5 to 1.5 MPa) with increasing indenter radius from 0.1 to 1 mm. The effects of AC anisotropy were studied by Taffetani et al. (2014) using the approach by Delafargue and Ulm (2004).

Boi et al. (2019) argued that the nanoindentation based procedure is able to quantitatively evaluate the mechanical gradient between stiff and compliant tissues, such as in the osteochondral region where the interface between hyaline and calcified cartilage plays an integral role in transferring articular loads from the compliant articular surface to the stiffer underlying bone. The interpretation of the experimental nanoindentation results was based on the use of the BASH formula along with the approach by Doerner and Nix (1986).

3.3 *Testing of Snake Skins*

It is known (Klein and Gorb 2012) that snakes use their entire body for sliding locomotion and therefore their skin should be wear-resistant. The nanoindentation experiments performed by Klein et al. (2010) demonstrated that the outer scale layers of the snake skin are harder, and have a higher effective elastic modulus than the inner scale layers. The further experiments by Klein and Gorb (2012) confirmed this conclusion for skins of several other snakes such as *Lampropeltis getula californica*, *Epicrates cenchria cenchria*, *Morelia viridis* and *Gongylophis colubrinus*. The nanoindentation experiments clearly demonstrated a gradient of material properties along the epidermis in the integument of all the species studied. The comparison of the surface microstructure and material architecture demonstrated a gradient in material properties of the integument from a hard and inflexible outside to a soft and elastic inside. This feature is assumed to be a functional mechanism explaining abrasion resistance of the skin material.

3.4 *Testing of Elastin and Resilin-Based Materials*

Resilin and elastin are highly elastic proteins that can be found in insect cuticles and joints of vertebrates, respectively. These proteins provide elasticity to mechanically active organs and tissues. There are relatively small number of papers where DSI or other indentation tests were applied to these materials.

Bioinspired materials that act like living tissues and can repair internal damage by themselves, i.e. self-healing materials, are an active field of research. Here a methodology for experimental testing of self-healing ability of soft polymer materials is described. Using addition of soluble elastin to a collagen hydrogel, Dunphy et al. (2014) prepared collagen-elastin constructs that are mimicking the mechanical properties of a single alveolar wall. The Young modulus of the material produced was about 4 kPa. The materials were tested by loading membranes by spherical indenters.

Rattan et al. (2018) adopted resilin-based hydrogels at various concentrations of resilin-like polypeptides (RLP) as a model material system and employ multiple mechanical characterization techniques including small-strain microindentation to understand structure-property relationships. In particular, they studied the force-displacement curves for puncture experiments with a flat-end indenter of tip inner radius $R = 54 \mu\text{m}$ for various concentrations of RLP hydrogels. The load-displacements curves demonstrated hysteresis effects in both elastic-plastic experiments and fully elastic experiments. Gorb et al. (2000) studied mechanical properties of attachment pads of insects (Orthoptera Tettigoniidae). They argued that the pads do not demonstrate pure elastic properties that characterizes the resilin materials and viscoelastic properties should be present. The indentation of the attachment pads was measured under different loads using a force-tester (Tetra,

Ilmenau, Germany) having spherical indenter. The estimated values of the elastic modulus were 27.2 ± 11.6 kPa). The force tester employed is very useful for studying mechanical properties of soft materials (see, e.g. Perepelkin et al. 2019, 2020).

It was quite clear that the above described theoretical interpretations of the DSI test are not applicable to the elastin-based and resilin-based hydrogels and other self-healing materials and new methods should be developed (see descriptions of some methods by Perepelkin et al. 2019, 2020).

4 Conclusion

We have presented a review of theoretical models used for justification of nanoindentation tests employing sharp (cone or pyramidal) indenters and discussed papers where the indentation test were applied to biological materials. It is shown that the nanoindentation techniques have several advantages, in particular they can be applied to very small volumes or very thin layers. They can also provide very useful information about general structure of tested materials and qualitative information about elastic moduli of materials. On the other hand, these techniques based on the employment of sharp indenters and the use of the BASH relation, or its modifications have several drawbacks. As it has been discussed above, the bluntness of the indenter may affect the estimation of some mechanical characteristics of materials. Evidently, the surface roughness of the specimen or the indenter may also affect the experimental force-displacement curve (see a discussion by Borodich and Galanov 2002). It is generally required for the surface of the tested sample to be very smooth. Further, the derivation of the BASH relation neglects residual stresses in materials; the approaches used for interpretation of experimental data suffer from the lack of rigorous theoretical background, and these approaches neglect adhesive interactions between the indenter and the material sample. Hence, the employment of indenters with pyramidal tips for studying soft materials is rather doubtful.

References

- Alekhin VP, Berlin GS, Isaev AV, Kalei GN, Merkulov VA, Skvortsov VN, Ternovskii AP, Khrushchov MM, Shnyrev, GD and Shorshorov MKh (1972) Micromechanical testing of materials by microimpression. *Ind Lab* 38:619–621
- Argatov I, Mishuris G (2015) Contact mechanics of articular cartilage layers. Asymptotic models. Springer, Heidelberg
- Argatov II, Borodich FM, Epshtein SA and Kossovich EL (2017) Understanding of material properties of thin films attached to substrates: Depth-sensing unloading of elasto-plastic and elasto-brittle materials. *Mech Mater* 114:172–179
- Babich SY, Guz AN (1984) Some spatial contact problems for a prestressed elastic half-space. *Soviet Appl Mech* 20:3–12
- Bae WC, Temple MM, Amiel D, Coutts, RD, Niederauer, GG, Sah RL (2003) Indentation testing of human cartilage: sensitivity to articular surface degeneration. *Arthritis Rheum* 48:3382–3394

- Bernhardt EO (1941) Über die Mikrohärtigkeit der Feststoffe im Grenzbereich des Kick'schen Ähnlichkeitssatzes. *Zeitschrift für Metallkunde* 33:135–139
- Bhattacharya AK, Nix WD (1988) Finite-element simulation of indentation experiments. *Int J Solids Struct* 24:881–891
- Boi M, Marchiori M, Berni M, Gambardella A, Salamanna F, Visani A, Bianchi M, Fini M, Filardo G (2019) Nanoindentation: an advanced procedure to investigate osteochondral engineered tissues. *J. Mech Behavior Biomed Mater* 96:79–87
- Borodich FM (1983) Similarity in the problem of contact between elastic bodies. *PMM J Appl Math Mech* 47:440–442
- Borodich FM (1988) Use of the theory of similarity in the nonlinear problem of contact between an indenter and anisotropic metallic foundations. In: Bogatov AA, et al (eds) Abstracts of reports of all-union conference “Metal”-programme's fulfillers. Krasnoyarskii Polytechnical Institute Press, Abakan, pp 195–196 (Russian)
- Borodich FM (1989) Hertz contact problems for an anisotropic physically nonlinear elastic medium. *Strength Mater* 21:1668–1676
- Borodich FM (1990) Hertz contact problems for an elastic anisotropic half-space with initial stresses. *Soviet Appl Mech* 26:126–132
- Borodich FM (1993) The Hertz frictional contact between nonlinear elastic anisotropic bodies (the similarity approach). *Int J Solids Struct* 30:1513–1526
- Borodich FM (2011) Contact problems at nano/microscale and depth sensing indentation techniques. *Mater Sci Forum* 662:53–76
- Borodich FM (2014) The Hertz-type and adhesive contact problems for depth-sensing indentation. *Adv Appl Mech* 47:225–366
- Borodich FM, Galanov BA (2002) Self-similar problems of elastic contact for non-convex punches. *J Mech Phys Solids* 50:2441–2461.
- Borodich FM, Galanov BA (2008). Non-direct estimations of adhesive and elastic properties of materials by depth-sensing indentation. *Proc R Soc Lond A* 464:2759–2776
- Borodich FM, Keer LM (2004a) Evaluation of elastic modulus of materials by adhesive (no-slip) nanoindentation. *Proc R Soc Ser A* 460:507–514
- Borodich FM, Keer LM (2004b) Contact problems and depth-sensing nanoindentation for frictionless and frictional boundary conditions. *Int J Solids Struct* 41:2479–2499
- Borodich, FM, Keer, LM, Korach CS (2003) Analytical study of fundamental nanoindentation test relations for indenters of non-ideal shapes. *Nanotechnology* 14:803–808
- Borodich FM, Bull SJ, Epshtein SA (2015) Nanoindentation in studying mechanical properties of heterogeneous materials. *J Mining Sci* 51:470–476
- Brinell JA (1900) Mémoire sur les épreuves à bille en acier. in *Communications présentées devant le Congrès international des méthodes d'essai des matériaux de construction, tenu à Paris du 9 au 16 juillet 1900* 2:83–94
- Bull SJ (2005) Nanoindentation of coatings. *J Phys D Appl Phys* 38:393–413
- Bulychev SI, Alekhin VP, Shorshorov MK, Ternovskii AP, Shnyrev GD (1975) Determination of Young's modulus according to indentation diagram. *Ind Lab* 41:1409–1412
- Bulychev SI, Alekhin VP, Shorshorov MK, Ternovskii AP (1976) Mechanical properties of materials studied from kinetic diagrams of load versus depth of impression during microimpression. *Strength Mater* 8:1084–1089
- Carnelli, D, Lucchini, R, Ponzoni M, Contro, R, Vena P (2011) Nanoindentation testing and finite element simulations of cortical bone allowing for anisotropic elastic and inelastic mechanical response. *J Biomech* 44:1852–1858
- Carnelli D, Vena P, Dao, M, Ortiz C, Contro R (2013) Orientation and size-dependent mechanical modulation within individual secondary osteons in cortical bone tissue. *J R Soc Interf* 10:20120953
- Chen J, Bull SJ (2006) A critical examination of the relationship between plastic deformation zone size and Young's modulus to hardness ratio in indentation testing. *J Mater Res* 21:2617–2627

- Choi JH, Korach CS (2011) Tip bluntness transition measured with atomic force microscopy and the effect on hardness variation with depth in silicon dioxide nanoindentation. *Int J Precision Eng Manuf* 12:345–354
- Cowin SC (2001) *Bone mechanics handbook*. CRC Press, Boca Raton
- Currey JD (2002) *Bones: structure and mechanics*. Princeton University Press, New Jersey
- Delafargue A, Ulm FJ (2004) Explicit approximations of the indentation modulus of elastically orthotropic solids for conical indenters. *Int J Solids Struct* 41:7351–7360. <https://doi.org/10.1016/j.ijsolstr.2004.06.019>
- Doerner MF, Nix WD (1986) A method for interpreting the data from depth-sensing indentation instruments. *J Mater Res* 1:601–609
- Dunphy SE, Bratt JAJ, Akram KM, Forsyth NR, El Haj AJ (2014) Hydrogels for lung tissue engineering: biomechanical properties of thin collagen-elastin constructs. *J Mech Behavior Biomed Mater* 38:251–259
- Ebenstein DM, Pruitt LA (2006) Nanoindentation of biological materials. *Nano Today* 1:26–33
- Epshtein SA, Borodich FM, Bull SJ (2015) Evaluation of elastic modulus and hardness of highly inhomogeneous materials by nanoindentation. *Appl Phys A Mater Sci Process* 119:325–335
- Fischer-Cripps AC (2011) *Nanoindentation*. Springer, Berlin
- Galanov BA (1981a) Approximate solution to some problems of elastic contact of two bodies. *Mech Solids* 16:61–67
- Galanov BA (1981b) Approximate solution of some contact problems with an unknown contact area under conditions of power law of material hardening. *Dopovidy Akademii Nauk Ukrain-skoi RSR Ser A* 6:35–40 (Russian and Ukrainian)
- Galanov BA, Dub SN (2017) Critical comments to the Oliver-Pharr measurement technique of hardness and elastic modulus by instrumented indentations and refinement of its basic relations. *J Superhard Mater* 39:373–389. <https://doi.org/10.3103/S1063457617060016>
- Galanov BA, Grigorév ON, Mil'man YuV and Ragozin IP (1983) Determination of the hardness and Young's modulus from the depth of penetration of a pyramidal indenter. *Strength Mater* 15:1624–1628
- Galanov BA, Grigorév ON, Mil'man YuV, Ragozin IP, Trefilov VI (1984) Determination of the hardness and Young's modulus with elastoplastic penetration of indentors into materials. *Sov Phys Dokl* 29:146–147
- Gao H (2006) Application of fracture mechanics concepts to hierarchical biomechanics of bone and bone-like materials. *Int J Fracture* 138:101–137
- Gorb SN, Jiao Y, Scherge M (2000) Ultrastructural architecture and mechanical properties of attachment pads in *Tettigonia viridissima* (Orthoptera Tettigoniidae) *J Comp Physiol A* 186:821–831
- Grigorovich VK (1976) *Hardness and microhardness of metals*. Nauka, Moscow (Russian)
- Hay JC, Bolshakov A, Pharr GM (1999) Critical examination of the fundamental relations used in the analysis of nanoindentation data. *J Mater Res* 14:2296–2305
- Hayes WC, Keer LM, Herrmann G, Mockros LF (1972) A mathematical analysis for indentation tests of articular cartilage. *J Biomech* 5:541–551
- Hertz H (1882a) Ueber die Berührung fester elastischer Körper. *J reine angewandte Mathematik* 92:156–171 (English transl. Hertz H (1896) On the contact of elastic solids. In: Jones DE, Schott GA (eds) *Miscellaneous Papers by H. Hertz*. Macmillan, London, pp 146–162)
- Hertz H (1882b) Ueber die Berührung fester elastischer Körper und über die Härte. *Verhandlungen des Vereins zur Beförderung des Gewerbefleißes*. Berlin, Nov, 1882. (English transl. Hertz H (1896) On the contact of elastic solids and on hardness. In: Jones DE, Schott GA (eds) *Miscellaneous Papers by H. Hertz*. Macmillan, London, pp 163–183)
- Johnson KL (1985) *Contact mechanics*. Cambridge University Press, Cambridge
- Kalei GN (1967) Investigations of methods for determining microhardness (with a measurement of the indentation across a diagonal and along the depth). Candidate's dissertation. Moscow
- Kalei GN (1968) Some results of microhardness test using the depth of impression. *Mashinovedenie* 4(3):105–107 (Russian)

- Khrushchov MM, Berkovich ES (1950) Experience in the application of electronic microscope for measurement of very small imprints obtained at microhardness test. *Izvestiya AN SSSR Otd Tekh Nauk* #11:1645–1649 (Russian)
- Khrushchov MM, Berkovich ES (1951) Methods of determining the hardness of very hard materials: the hardness of diamond. *Ind Diam Rev* 11:42–49
- Klein M.-CG, Gorb SN (2012) Epidermis architecture and material properties of the skin of four snake species. *J R Soc Interf* 9:3140–3155
- Klein M.-CG, Deuschle JK, Gorb SN (2010) Material properties of the skin of the Kenyan sand boa *Gongylophis colubrinus* (Squamata, Boidae). *J Comp Physiol A* 196:659–668
- Kolesnikov YuV, Morozov EM (1989) Mechanics of contact fracture. Nauka, Moscow (Russian)
- Kossovich EL, Borodich FM, Bull SJ, Epshtein SA (2016) Substrate effects and evaluation of elastic moduli of components of inhomogeneous films by nanoindentation. *Thin Solid Films* 619:112–119
- Kossovich EL, Borodich FM, Epshtein SA, Galanov BA, Minin MG and Prosina VA (2019) Mechanical, structural and scaling properties of coals: depth sensing indentation studies. *Appl Phys A Mater Sci Process* 125:195
- Kossovich EL, Borodich FM, Epshtein SA, Galanov BA (2020) Indentation of bituminous coals: Fracture, crushing and dust formation *Mech Mater* 150:103570
- Lawn BR (1993) *Fracture of brittle solids*. Cambridge University Press, Cambridge
- Lawn BR, Swain MV (1975) Microfracture beneath point indentations in brittle solids. *J Mater Sci* 10:113–122
- Lawn BR, Wilshaw TR (1975) Indentation fracture: principles and applications. *J Mat Sci* 10:1049–1081
- Lewis G, Nyman JS (2008) The use of nanoindentation technique for characterizing the properties of mineralized hard tissues: state-of-the art review. *J Biomed Mater Res. B* 87B:286–301
- Ludwik P (1908) *Die Kegeldruckprobe, ein neues Verfahren zur Härtebestimmung von Materialien*. Springer, Berlin
- Menčík J (2007) Determination of mechanical properties by instrumented indentation. *Meccanica* 42:19–29
- Menčík J, Munz D, Quandt E, Weppelmann ER, Swain MV (1997) Determination of elastic modulus of thin layers using nanoindentation. *J Mater Res* 12:2475–2484
- Meyer E (1908) Untersuchungen über Härteprüfung und Härte. *Physikalische Z* 9:66–74
- Meyers MA, Chen P-Y, Lin AY-M, Seki Y (2008) Biological materials: Structure and mechanical properties. *Progress Mater Sci* 53:1–206
- Morozov EM, Zernin MV (1999) Contact problems of mechanics of fracture. *Mashinostroenie, Moscow* (in Russian)
- Mott BA (1956) *Micro-indentation hardness testing*. Butterworths Sc, London
- Oliver WC, Pharr GM (1992) An improved technique for determining hardness and elastic modulus using load and displacement sensing indentation experiments. *J Mater Res* 7:1564–1583
- Perepelkin NV, Martin-Martinez JM, Kovalev AE, Borodich FM, Gorb SN (2019) Experimental testing of self-healing ability of soft polymer materials. *Meccanica* 54:1959–1970
- Perepelkin NV, Borodich FM, Kovalev AE, Gorb SN (2020) Depth-sensing indentation as a micro- and nanomechanical approach to characterisation of mechanical properties of soft, biological, and biomimetic materials. *Nanomaterials* 10:15. <https://doi.org/10.3390/nano10010015>
- Pethica JB, Hutchings R, Oliver WC (1983) Hardness measurement at penetration depths as small as 20-nm. *Philos Mag A* 48:593–606
- Rattan S, Li L, Lau HK, Crosby AJ, Kiick KL (2018) Micromechanical characterization of soft, biopolymeric hydrogels: stiffness, resilience, and failure. *Soft Matter* 14:3478–3489
- Rettler E, Hoepfner, S, Sigusch BW, Schubert US (2013) Mapping the mechanical properties of biomaterials on different length scales: depth-sensing indentation and AFM based nanoindentation. *J Mater Chem B* 1:2789–2806
- Rho J, Tsui TY, Pharr GM (1997) Elastic properties of human cortical and trabecular lamellar bone measured by nanoindentation. *Biomaterials* 18:1325–1330

- Rho J, Roy ME, Tsui TY, Pharr GM (1999) Elastic properties of microstructural components of human bone tissue as measured by nanoindentation. *J Biomed Mater Res* 45:48–54
- Shorshorov, MKh, Bulychev SI, Alekhin VP (1981) Work of plastic and elastic deformation during indenter indentation. *Sov Phys Dokl* 26:769–771
- Shuman D (2005) Atomic force microscope indentation measurement software. In: Wilkening G, Koenders L (eds) *Nanoscale calibration standards and methods: dimensional and related measurements in the micro- and nanometer range*. Wiley, Hoboken, pp 465–480
- Simha N, Jin H, Hall M, Chiravarambath S, Lewis J (2007) Effect of indenter size on elastic modulus of cartilage measured by indentation. *J Biomech Eng* 129:767–775
- Smith RL, Sandland GE (1922) An accurate method of determining the hardness of metals, with particular reference to those of a high degree of hardness. *Proc Inst Mech Eng* 1:623–641
- Smith RL, Sandland GE (1925) Some notes on the use of a diamond pyramid for hardness testing. *J Iron Steel Inst* 111:285–294
- Stilwell NA, Tabor D (1961) Elastic recovery of conical indentation. *Proc Phys Soc* 78:169–179
- Swain MV, Hagan JT (1976) Indentation plasticity and the ensuing fracture of glass. *J Phys D Appl Phys* 9:2201–2214
- Swain MV, Lawn BR (1976) Indentation fracture rocks and glasses. *Int J Rock Mech Min Sci Geomech Abstr* 13:311–319
- Tabor D (1948) A simple theory of static and dynamic hardness. *Proc R Soc London, Ser A* 192:247–274
- Tabor D (1951) *The hardness of metals*. Clarendon Press, Oxford
- Taffetani M, Griebel M, Gastaldi D, Klisch SM, Vena P (2014) Poroviscoelastic finite element model including continuous fiber distribution for the simulation of nanoindentation tests on articular cartilage. *J Mech Behav Biomed Mater* 32:17
- Ternovskii AP, Alekhin VP, Shorshorov MK, Khrushchov MM, Skvortsov, VN (1973) Micromechanical testing of materials by depression. *Ind Lab* 39:1620–1624
- Vlassak JJ, Nix WD (1994) Measuring the elastic properties of anisotropic materials by means of indentation experiment. *J Mech Phys Solids* 42:1223–1245
- Wang M, Peng Z, Watson JA, Watson GS, Yin L (2012) Nanoscale study of cartilage surfaces using atomic force microscopy. *Proc I Mech E Part H J Eng Med* 226:899–910
- Weiner S, Wagner HD (1998) The material bone: Structure mechanical function relations. *Annu Rev Mater Sci* 28:271–298
- Williams SR (1942) *Hardness and hardness measurements*. American Society for Metals, Cleveland
- Willis JR (1966) Hertzian contact of anisotropic bodies. *J Mech Phys Solids* 14:163–176

Chapter 10

Effect of Viscoelasticity in Sliding Contact of Layered Solids



Elena V. Torskaya and Fedor I. Stepanov

Abstract Quasi-static 3-D contact problem for a rigid smooth slider and a two-layered half-space with rheological properties of a layer or a substrate is considered. A method is proposed to study two cases: a viscoelastic layer bonded to a rigid base, and a rigid bending layer on a viscoelastic half-space. The problem is solved using the boundary element method and an iterative procedure. The use of double integral Fourier transforms allows obtaining analytical relations, to which the inverse integral transform is then applied to calculate the influence coefficients used in the boundary element method. For calculations a sphere was used as the slider. The influence of sliding velocity and layer thickness on the distribution of contact pressure is analyzed. The results demonstrate the effect of the rheology of the layer or substrate, resulting in significant asymmetries in contact area and pressure distribution. The dependence of the coefficient of friction arising due to imperfect elasticity on the sliding velocity for different values of the layer thickness is analysed. As in the case of a viscoelastic half-space, these dependences are characterized by non-monotonicity. For the case of a viscoelastic layer, the mutual effect is studied for successive sliding of two indenters, and the results are compared with the case of a viscoelastic half-space.

Keywords Sliding contact · Viscoelastic layer · Deformation component of the friction force · Hysteretic losses · Internal stresses

1 Introduction

Rubbers and other polymers are widely used as coatings for vibration damping, noise reduction and other effects during friction. In many cases, coating materials are much more soft than substrates. Another case is relatively rigid coatings,

E. V. Torskaya (✉) · F. I. Stepanov
Ishlinsky Institute for Problems in Mechanics RAS, Moscow, Russia

© Springer Nature Switzerland AG 2022
F. M. Borodich, X. Jin (eds.), *Contact Problems for Soft, Biological and Bioinspired Materials*, Biologically-Inspired Systems 15,
https://doi.org/10.1007/978-3-030-85175-0_10

199

which are used to improve friction and wear resistance of rubbers (Bai et al. 2018) or to protect the materials from chemical degradation. We can consider friction interaction of such layered solids by means of the model of viscoelastic layer fastened with a rigid half-space or the model of bending rigid layer on the viscoelastic half-space.

One of principal mechanisms of friction force is deformation within interacting solids with imperfect elasticity. The deformation losses occur at different scale levels (Eldredge and Tabor 1955; Tabor 1955; Greenwood and Tabor 1958; Grosch 1963). An experimental study presented in (Eldredge and Tabor 1955; Tabor 1955) was intended to describe friction force occurring in rolling contact. The authors considered a still ball rolling over substrates made of soft metal and rubber. In the first case, the friction force was due to plastic deformations of the substrate. The impact of steel ball leads to gutter formation on the substrate surface. The friction force decreased after each rolling pass. In the case of rubber substrate, the friction force occurs due to viscoelastic properties of substrate material. Lubricated contact of hard sliders and rubber was studied in (Greenwood and Tabor 1958). The sliders were of spherical and conical shape. It was found for the sphere that friction forces occurring due to rolling and sliding were of the same value. The authors concluded that there is the same mechanism causing friction force in both cases, which is hysteretic energy dissipation in material. The combine effect of adhesion and viscoelasticity were studied in (Grosch 1963). This time a rubber indenter was pulled over smooth and rough hard surfaces. The results showed that in the case of smooth substrate friction force increased with increase of sliding velocity until it reached some maximum and started decreasing. While in the case of rough substrate the authors observed two local maximums of friction force. The authors summarized that friction force occurs due to two factors: surface adhesion and hysteretic losses in material. Furthermore, both of these factors depend directly on viscoelastic properties of rubber.

Contact problems for viscoelastic bodies were developed for different applications of materials with rheological properties. A cylinder rolling over a viscoelastic substrate was considered in (Ishlinskii 1938, 1940; May et al. 1959). The substrate was treated by the system of one-dimensional elements able to shrink and bend (Ishlinskii 1938, 1940) under impact of load. In (May et al. 1959) a viscoelastic material was modeled by the Maxwell model and the generalized Maxwell model. Contact problem for a hard spherical roller and viscoelastic half-space was solved analytically (Flom and Bueche 1959). The substrate properties were determined by the Kelvin–Voigt model with one relaxation time. Expressions for contact pressure distribution and friction coefficient were obtained. 2-D contact problem was solved for a cylinder sliding over a viscoelastic substrate described by standard linear solid model with constant Poisson ratio and one relaxation time (Hunter 1961). The author obtained exact analytical solution by means of potential theory deriving harmonic Green's function. Similar approach was applied to solve a more complex problem considering the rolling cylinder to be made of the same materials as the substrate (Morland 1962). The presence of stick and slip zones was taken into

account. In (Galín and Shmatkova 1968) a contact problem for indenter sliding over viscoelastic substrate was studied with considering inertial forces in material.

There are more recent analytical results in modeling of deformation component of the friction force (Persson 2010; Soldatenkov 2015). An approach proposed in (Persson 2010) allows to study contact problem for indenter sliding over a viscoelastic half-space or a viscoelastic layer. The approach allows to calculate the friction force but not the contact pressure distribution. Sliding of a stamp with fractal roughness over a substrate described by Kelvin model was studied in (Soldatenkov 2015).

Nowadays in a great number of papers numerical methods are applied for solution of contact problems. Being universal the finite element method (FEM) is also used for solution of contact problems (Le Tallec and Rahler 1994; Nasdala et al. 1998; Padovan et al. 1992; Padovan and Paramadilok 1985). But when it comes to 3-D problems the computational time becomes significant. More efficient, but less universal is the boundary element method (BEM). In (Aleksandrov and Goryacheva 2005) an analytical solution was obtained for a distributed load moving over a viscoelastic half-space. Mechanical properties of the half-space were defined by Volterra integral operator with exponential creep kernel and a spectrum of relaxation and retardation times. These results were used to solve 3-D contact problems for rigid sliders and a viscoelastic half space with the BEM (Aleksandrov et al. 2010; Goryacheva et al. n.d.; Stepanov and Torskaya 2016; Stepanov 2015). In (Aleksandrov et al. 2010) the case of spherical slider was analyzed for viscoelastic material characterized by three relaxation times. Later the solution was developed to study the effect of tangential force within a contact area (Goryacheva et al. n.d.), stress state of the viscoelastic half-space (Stepanov and Torskaya 2016), and the mutual effect (Stepanov 2015). Contact problem for rigid slider and viscoelastic half-space described by two different models (Maxwell model and the standard linear solid model) was presented in (Carbone and Putignano 2013) with experimental verification. Similar approach was implemented in (Kusche 2016) using fast Fourier transforms FFT for reducing the computational cost. Sliding of a hard indenter over a viscoelastic half-space with elastic ellipsoidal inhomogeneities was studied in (Koumi et al. 2014, 2015). In order to take into account, the inhomogeneities, the Equivalent Inclusion Method was applied at every step of time discretization. FFT were used in order to reduce the computational cost.

For the case of layered viscoelastic solids usually a contact of relatively thin and soft coating is considered; for the case the one-dimensional model can be applied (Soldatenkov 2015; Klüppel and Heinrich 2000; Lyubicheva 2008; Morozov and Makhovskaya 2007; Persson 2001; Goryacheva et al. 2014). This simple model allows to obtain analytical solution even for a 3-D case. Some problems were solved for multiple contact (Soldatenkov 2015; Klüppel and Heinrich 2000; Lyubicheva 2008; Persson 2001) and contact with adhesion (Morozov and Makhovskaya 2007).

In this chapter contact of a rigid slider with a layered substrate is considered for two different structures: a viscoelastic half-space covered with a rigid layer and a rigid half-space covered with a viscoelastic layer. For each case 3D model of viscoelastic material is used in problem formulation. The model for studying

the friction of a viscoelastic body with a hard layer was inspired by the study of polyurethane materials with a rigid carbonized layer. Polyurethanes are used as the top layer of some joint prostheses, and a carbonized surface layer is created to improve the biocompatibility of the material (Chudinov et al. 2018). Results presented in this chapter are mainly provided in (Torskaya and Stepanov 2019; Stepanov and Torskaya 2018). New results of contact problem solution for two sliders and viscoelastic layer illustrate a mutual effect for the case of viscoelastic layer.

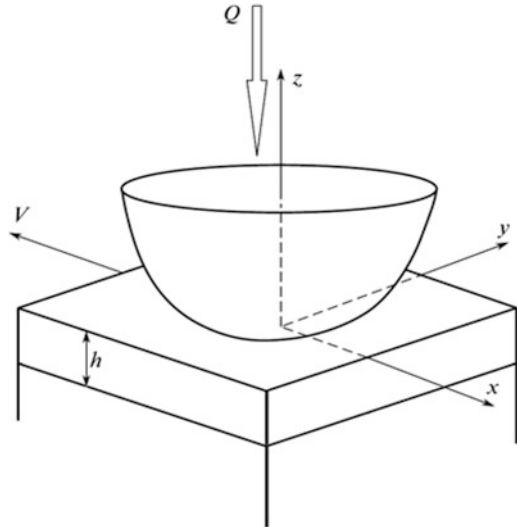
2 Problem Formulation

Let's consider a contact problem for a rigid smooth indenter and a layer with thickness h bonded with a half-space. The slider moves along the Ox axis with constant velocity V . It is loaded with vertical force Q (Fig. 10.1). Origin of coordinate system (x,y,z) is placed at the center of indenter, the Oz axis is directed normally to the unloaded surface of the layered half-space. It is located at the point of initial contact of the layer with indenter.

The following boundary conditions are satisfied ($z = 0$):

$$\begin{aligned} w(x, y) &= f(x, y) + D, \quad (x, y) \in \Omega, \\ \sigma_z &= 0, \quad (x, y) \notin \Omega \\ \tau_{xz} &= 0, \tau_{yz} = 0 \end{aligned} \quad (10.1)$$

Fig. 10.1 Scheme of contact



Here Ω is an unknown contact zone, D – vertical displacement of indenter, $w(x,y)$ – normal displacement of the upper layer boundary, σ_z , τ_{xz} , τ_{yz} are normal and tangential stresses respectively. The shape of the slider is described by a smooth function $f(x,y)$.

Also, a problem for two similar sliders each loaded with equal force Q is considered. Mutual disposition of indenters is so that the line passing through their centers is parallel to axis Ox . The distance L between the sliders is constant. The following boundary conditions take place in this case of problem formulation:

$$\begin{aligned} w_f(x,y) &= f(x,y) - \psi_f(x,y) + D_f, \quad (x,y) \in \Omega_f \\ w_r(x,y) &= f(x,y) - \psi_r(x,y) + D_r, \quad (x,y) \in \Omega_r \\ \sigma_z &= 0, \quad (x,y) \notin \Omega_f, \Omega_r \\ \tau_{xz} &= 0, \quad \tau_{yz} = 0, \end{aligned} \quad (10.2)$$

Functions $\psi_f(x,y)$, $\psi_r(x,y)$ specify vertical displacements occurring within the corresponding contact areas due to impact of the nearby slider. Contact pressures and contact zone should to be found. For single slider the following equilibrium condition is used:

$$Q = \iint_{\Omega} p(x,y) dx dy, \quad (10.3)$$

and in case of two sliders:

$$Q_f = \iint_{\Omega_f} p_f(x,y) dx dy, \quad Q_r = \iint_{\Omega_r} p_r(x,y) dx dy \quad (10.4)$$

We also assume that the pressure becomes zero at the edge of the contact spots.

Interfacial conditions ($z = -h$) were used for the case of perfect adhesion. If we have rigid plate bending on the viscoelastic substrate, normal (w) and tangential (u_x , and u_y) displacements are equal:

$$w^{(1)} = w^{(2)}, \quad u_x^{(1)} = u_x^{(2)}, \quad u_y^{(1)} = u_y^{(2)} \quad (10.5)$$

Indexes correspond to the layer (10.1) and the substrate (10.2). For the rigid substrate conditions (10.5) transform to

$$w = 0, \quad u_x = 0, \quad u_y = 0 \quad (10.6)$$

Viscoelastic materials are used as a coating or as a base together with much more rigid material. So the layer or the base can be considered as a rigid base or as a

plate with flexural stiffness. The following stress-strain relations define mechanical properties of linear viscoelastic material (Goryacheva et al. [n.d.](#)):

$$\begin{aligned}
 \gamma(t) &= \frac{1}{G} \tau(t) + \frac{1}{G} \int_{-\infty}^t \tau(t) K(t - \tau) d\tau; \\
 e_x(t) &= \frac{1}{E} [\sigma_x(t) - \nu (\sigma_y(t) + \sigma_z(t))] + \frac{1}{E} \int_{-\infty}^t [\sigma_x(t) - \nu (\sigma_y(t) + \sigma_z(t))] K(t - \tau) d\tau; \\
 e_y(t) &= \frac{1}{E} [\sigma_y(t) - \nu (\sigma_x(t) + \sigma_z(t))] + \frac{1}{E} \int_{-\infty}^t [\sigma_y(t) - \nu (\sigma_x(t) + \sigma_z(t))] K(t - \tau) d\tau; \\
 e_z(t) &= \frac{1}{E} [\sigma_z(t) - \nu (\sigma_y(t) + \sigma_x(t))] + \frac{1}{E} \int_{-\infty}^t [\sigma_z(t) - \nu (\sigma_y(t) + \sigma_x(t))] K(t - \tau) d\tau; \\
 K(t) &= k \exp\left(-\frac{t}{\omega}\right)
 \end{aligned} \tag{10.7}$$

Here ν is Poisson's ratio, E and G are Young's modulus and shear modulus, respectively. An exponential function depending on retardation time (ω) and relaxation time ($1/k$) is considered as the creep kernel.

3 Method of Solution

First, we consider a uniformly distributed load, which is in motion over the surface of two-layered structure. The load acts within the square with side $a_I = 2a$. Surface boundary conditions are the following:

$$\begin{aligned}
 \sigma_z^{(1)} &= -q, \quad |x| \leq a, |y| \leq a \\
 \sigma_z^{(1)} &= 0, \quad |x| > a, |y| > a \\
 \tau_{xz}^{(1)} &= 0, \quad \tau_{yz}^{(1)} = 0
 \end{aligned} \tag{10.8}$$

For elastic half-space coated by an elastic layer, method to obtain stresses and displacements is developed using double integral Fourier transforms (Nikishin and Shapiro [1970](#)).

The normal displacement of the layer surface is determined by the following (Nikishin and Shapiro [1970](#)):

$$w'(x', y', 0) = -\frac{1}{2G} \int_0^{\pi/2} \int_0^{\infty} \Delta(\gamma, \varphi, \lambda, \chi) \cos(x'\gamma \cos \varphi) \cos(y'\gamma \sin \varphi) d\gamma d\varphi \tag{10.9}$$

Here x', y' are dimensionless coordinates and w' is the vertical displacement of the surface divided to a (the half-side of the square), $\chi = E_1(1 + \nu_2)/E_2(1 + \nu_1)$, $\lambda = h/a$ is dimensionless thickness of the coating, γ, φ are related to double integral Fourier transforms. $\Delta(\gamma, \varphi, \lambda, \chi)$ can be obtained after solution of the system of

six linear functional equations. The system is derived from (10.1, 10.3, 10.5) by representing stresses and displacements as derivatives of two biharmonic functions. In general, expression, which is found for $\Delta(\gamma, \varphi, \lambda, \chi)$, is very complex (Nikishin and Shapiro 1970). But we have the following simple version in the case of elastic layer adhered to undeformable half-space ($\chi = 0$):

$$\Delta(\gamma, \varphi, \lambda) = \bar{q} \left(\frac{-24v^2e^{-4\gamma\lambda} - 8v^2 + 26ve^{-4\gamma\lambda} + 0.4v\gamma\lambda(e^{-4\gamma\lambda} + 1)}{-e^{-2\gamma\lambda}(16v^2 + 4\gamma^2\lambda^2 + 10) + e^{-4\gamma\lambda}(1 + 24v) + 4v - 3} + \right. \\ \left. + \frac{8ve^{-2\gamma\lambda}(\gamma\lambda + 1) + 14v - 6 - 0.3\gamma\lambda e^{-4\gamma\lambda} - 0.2\gamma\lambda e^{-2\gamma\lambda} - 0.3\gamma\lambda - 6e^{-4\gamma\lambda} - 4e^{-2\gamma\lambda}}{-e^{-2\gamma\lambda}(16v^2 + 4\gamma^2\lambda^2 + 10) + e^{-4\gamma\lambda}(1 + 24v) + 4v - 3} \right) \quad (10.10)$$

$$\bar{q} = q \frac{4}{\pi^2} \frac{\sin(\gamma \cos \varphi) \sin(\gamma \sin \varphi)}{\gamma^2 \sin \varphi \cos \varphi},$$

Here \bar{q} is the result of the double integral Fourier transforms applied to constant distributed load given by Eq. (10.8).

For a rigid plate adhered to elastic half-space ($\chi = \infty$), we also have found $\Delta(\gamma, \varphi, \lambda)$, but the expression is more complicated than (10.10).

The case of distributed load moving over a viscoelastic half-space with fixed velocity is considered in (Aleksandrov and Goryacheva 2005) in assumption that the Poisson ratio is a constant and the shear modulus is a time-dependent operator. Following (Aleksandrov and Goryacheva 2005) we have normal displacement of the viscoelastic layer surface from (10.9) in the coordinates related to the center of the loaded square:

$$w'(x', y', 0) = -\frac{1}{2G} \int_0^{\pi/2\infty} \int_0^{\infty} \Delta(\gamma, \varphi, \lambda) \cos(y'\gamma \sin \varphi) \times \\ \times \left(\cos(x'\gamma \cos \varphi) + \int_{-\infty}^0 K(-\tau) \cos((x' + V'\tau)\gamma \cos \varphi) d\tau \right) d\gamma d\varphi, \quad (10.11)$$

where G is the instantaneous shear modulus, $K(t)$ is the creep kernel (10.7), $V' = V/a$.

For the exponential creep kernel from Eq. (10.7), the time integral in Eq. (10.11) can be obtained analytically. Consequently (10.11) is transformed to the following relation:

$$w'(x', y', 0) = -\frac{1}{2G} \int_0^{\pi/2\infty} \int_0^{\infty} \Delta(\gamma, \varphi, \lambda) \cos(y'\gamma \sin \varphi) \times \\ \times \left(\cos(x'\gamma \cos \varphi) + c \frac{\omega V'\gamma \cos \varphi \sin(x'\gamma \cos \varphi) + \cos(x'\gamma \cos \varphi)}{1 + (V'\omega\gamma \cos \varphi)^2} \right) d\gamma d\varphi, \quad (10.12)$$

where $c = k \omega$. The constant pressure q appears linearly in function $\Delta(\gamma, \varphi, \lambda)$, therefore (10.12) may be used for calculation of influence coefficients in boundary elements method, obtaining contact pressure $p(x, y)$ as a piecewise function.

Expressions (10.1) and (10.3) lead to the following system of linear equations:

$$\begin{pmatrix} 4a^2 & \dots & 4a^2 & 0 \\ \kappa_1^1 & \dots & \kappa_N^1 & -1 \\ \vdots & \ddots & \vdots & \vdots \\ \kappa_1^N & \dots & \kappa_N^N & -1 \end{pmatrix} \times \begin{pmatrix} p_1 \\ \vdots \\ p_N \\ D \end{pmatrix} = \begin{pmatrix} Q \\ f_1 \\ \vdots \\ f_N \end{pmatrix}, \tag{10.13}$$

here $p_1 \dots p_N$ are constants, which should be obtained, and $f_1 \dots f_N$ are defined by $f(x,y)$; k_i^j are derived from (10.12):

$$\begin{aligned} \kappa_i^j = & -\frac{1}{2G} \int_0^{\pi/2} \int_0^\infty \Delta'(\gamma, \varphi, \lambda) \cos(y_{ij} \gamma \sin \varphi) \times \\ & \times \left(\cos(x_{ij} \gamma \cos \varphi) + c \frac{\omega V' \gamma \cos \varphi \sin(x_{ij} \gamma \cos \varphi) + \cos(x_{ij} \gamma \cos \varphi)}{1+(V\omega \gamma \cos \varphi)^2} \right) d\gamma d\varphi. \end{aligned} \tag{10.14}$$

Here $(x_{ij}^2 + y_{ij}^2)^{1/2}$ is a distance between elements, $\Delta'(\gamma, \varphi, \lambda) = \Delta(\gamma, \varphi, \lambda)/q$. We start iteration procedure with a contact area, which is knowingly larger than the actual one. The solution of Eq. (10.13) for this zone contains some elements with negative values of pressure. At the next step of iteration, negative values for such elements become zero, and the value of N decreases. In the final of iteration procedure we obtain the contact pressure value $p(x,y)$ and the contact area Ω .

For the case of two sliders we should determine contact characteristics considering the effect of the nearby slider by calculating the values of $\psi_f(x, y)$, $\psi_r(x, y)$ (10.2). Thus, the following systems of equations have to be solved in each step:

$$\begin{aligned} & \begin{pmatrix} 4a^2 & \dots & 4a^2 & 0 \\ \kappa_1^1 & \dots & \kappa_N^1 & -1 \\ \vdots & \ddots & \vdots & \vdots \\ \kappa_1^N & \dots & \kappa_N^N & -1 \end{pmatrix} \times \begin{pmatrix} p_1 \\ \vdots \\ p_N \\ D_f \end{pmatrix} = \begin{pmatrix} Q_f \\ f_1 - \psi_1^f \\ \vdots \\ f_N - \psi_N^f \end{pmatrix}, \\ & \begin{pmatrix} 4a^2 & \dots & 4a^2 & 0 \\ \kappa_1^1 & \dots & \kappa_N^1 & -1 \\ \vdots & \ddots & \vdots & \vdots \\ \kappa_1^N & \dots & \kappa_N^N & -1 \end{pmatrix} \times \begin{pmatrix} p_1 \\ \vdots \\ p_N \\ D_r \end{pmatrix} = \begin{pmatrix} Q_r \\ f_1 - \psi_1^r \\ \vdots \\ f_N - \psi_N^r \end{pmatrix} \end{aligned} \tag{10.15}$$

This two-level iteration procedure continues until contact characteristics of both indenters differ from obtained in the previous step. The resulting contact pressure distributions depend on the mutual position of the sliders.

Since the contact problem solution is obtained it can be used for calculation of stresses in the viscoelastic coating or coated viscoelastic base. The following expressions are obtained for elastic layer and substrate (Nikishin and Shapiro 1970):

$$\begin{aligned}
\sigma_x &= \int_0^{\pi/2} \int_0^{\infty} \left(\Delta_x(v, \gamma, \varphi, \lambda) - \cos^2 \varphi \Delta_u(v, \gamma, \varphi, \lambda) \right) \times \\
&\quad \times \cos(x' \gamma \cos \varphi) \cos(y' \gamma \sin \varphi) \gamma d\gamma d\varphi, \\
\sigma_y &= \int_0^{\pi/2} \int_0^{\infty} \left(\Delta_y(v, \gamma, \varphi, \lambda) - \sin^2 \varphi \Delta_u(v, \gamma, \varphi, \lambda) \right) \times \\
&\quad \times \cos(x' \gamma \cos \varphi) \cos(y' \gamma \sin \varphi) \gamma d\gamma d\varphi, \\
\sigma_z &= \int_0^{\pi/2} \int_0^{\infty} \Delta_z(v, \gamma, \varphi, \lambda) \cos(x' \gamma \cos \varphi) \cos(y' \gamma \sin \varphi) \gamma d\gamma d\varphi, \\
\tau_{xy} &= \int_0^{\pi/2} \int_0^{\infty} \Delta_{xy}(v, \gamma, \varphi, \lambda) \sin(x' \gamma \cos \varphi) \sin(y' \gamma \sin \varphi) \gamma d\gamma \sin \varphi \cos \varphi d\varphi, \\
\tau_{xz} &= \int_0^{\pi/2} \int_0^{\infty} \Delta_{xz}(v, \gamma, \varphi, \lambda) \sin(x' \gamma \cos \varphi) \cos(y' \gamma \sin \varphi) \gamma d\gamma \cos \varphi d\varphi, \\
\tau_{yz} &= \int_0^{\pi/2} \int_0^{\infty} \Delta_{yz}(v, \gamma, \varphi, \lambda) \cos(x' \gamma \cos \varphi) \sin(y' \gamma \sin \varphi) \gamma d\gamma \sin \varphi d\varphi
\end{aligned} \tag{10.16}$$

Functions $\Delta(v, \gamma, \varphi, \lambda)$ are different for the layer and the substrate (Nikishin and Shapiro 1970). Poisson ratio is in expressions (10.16), but they don't depend on Young modulus, so they may be used for calculation of internal stresses in a viscoelastic layer or a viscoelastic base, which have a constant Poisson ratio.

4 Results

Viscoelastic Layer – Rigid Substrate. One Slider First we analyse a contact of a spherical slider of radius R and a viscoelastic layer. We use the following dimensionless parameters: coordinates $(x^*, y^*) = (x, y)/R$, layer thickness $h^* = h/R$, velocity $V^* = V\omega/R = V'\omega a/R$, contact pressure $p^*(x, y) = p(x, y)/G_l$ (where G_l is longitudinal shear modulus), load $Q' = Q/R^2 G_l$.

In Fig. 10.2 contact pressure is shown at two different velocities. For the first case (Fig. 10.2a) noticeable asymmetry due to viscoelasticity of material, is observed. Therefore we have the deformation component of friction force (opposite to the direction of sliding). The friction coefficient is defined as following (Aleksandrov et al. 2010):

$$\mu^* = \frac{M}{QR} = \frac{\iint_{\Omega} xp(x, y) dx dy}{R \iint_{\Omega} p(x, y) dx dy} \tag{10.17}$$

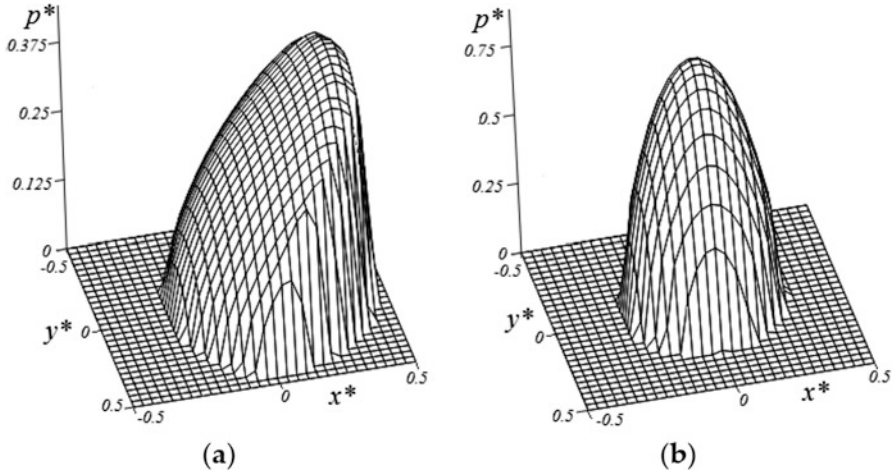


Fig. 10.2 Contact pressure distribution within the contact area for $V^* = 1/3$ (a) and $V^* = 10$ (b), ($h^* = 0.1$, $c = 5$, $\nu = 0.3$, $Q^* = 0.15$)

Following increase of sliding velocity (Fig. 10.2b) the maximum value of pressure increases and the size of contact zone decreases. The pressure distribution becomes nearly symmetrical at the same time. The same phenomenon was obtained in previous studies for 1D models of viscoelastic coating on the hard base (Morozov and Makhovskaya 2007) as well as for homogeneous viscoelastic material (Aleksandrov et al. 2010; Goryacheva et al. n.d.).

Figure 10.3 shows the dependences of friction coefficient μ^* on sliding velocity for a layer (solid line) and for the viscoelastic half-space (dashed line). The dependencies are nonmonotonic. Together with increase of sliding velocity the coefficient first increases and then decreases. Generally we can conclude that at low velocities the hysteretic losses are greater for the coating, but maxima of μ^* are higher for the homogeneous half-space.

The influence of coating thickness on pressure distribution may be analysed through Figs. 10.4 and 10.5. Three different values of coating thickness were used to find the pressure (Fig. 10.4). The velocity value is chosen in such way that viscoelastic properties of material effect significantly on contact pressures. It worth noting that the curve corresponding to the case of viscoelastic half-space have specific bends. Previously resembling results were obtained in (Goryacheva et al. n.d.; Koumi et al. 2014). For thin coatings the curves look similar to results obtained for 1D model of viscoelastic coating (Morozov and Makhovskaya 2007). The influence of layer thickness to pressure maximum is presented in Fig. 10.5. It is obtained for relatively small sliding velocity ($V^* = 1/60$) when the dissipative losses in material are negligible. We can see that the pressure decreases monotonically.

As the viscoelastic materials are often almost incompressible the Poisson ratio becomes an important characteristic for analysis (Fig. 10.6). Three values of sliding velocities were used for the calculations. Figure 10.6 shows that the Poisson ratio

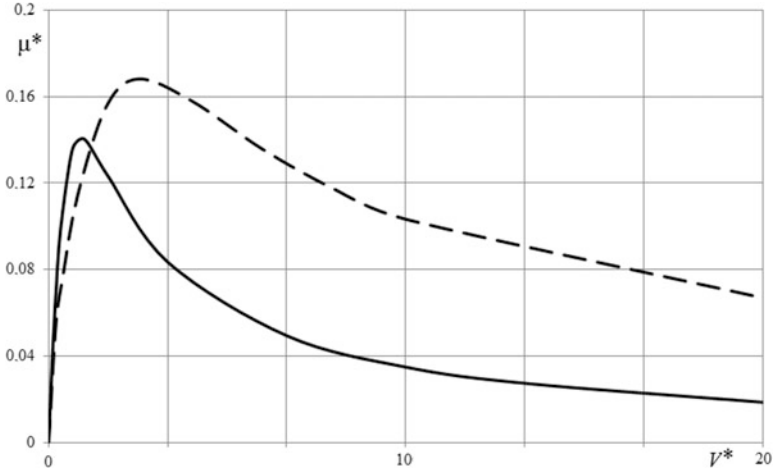


Fig. 10.3 Dependence of deformation component of the friction force on sliding velocity for $h^* = 0.1$ (solid line) and $h^* = \infty$ (dashed line), ($c = 5, \nu = 0.3, Q^* = 0.05$)

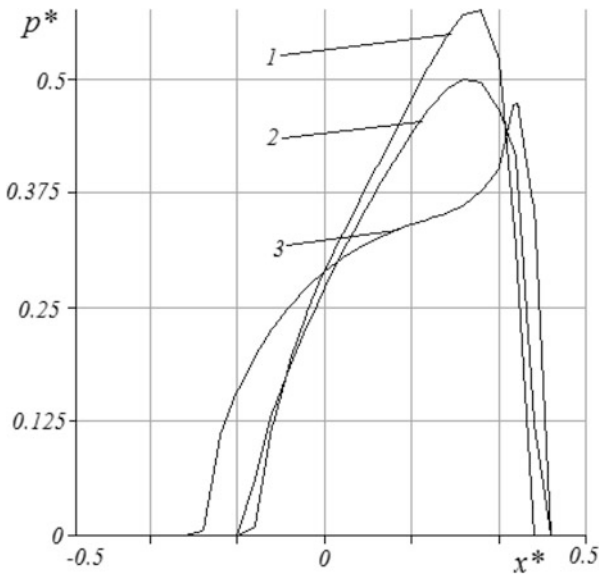


Fig. 10.4 Contact pressure in central section of slider and plane Oy . $h^* = 0.03, 0.1, \infty$ (curves 1–3 respectively), $V^* = 0.05, \nu = 0.3, c = 5, Q^* = 0.1$

sufficiently influence on pressure distribution both at small and at high velocities, when it is close to elastic case (Fig. 10.6a, c). This effect also appears in the case of non-symmetric distribution (Fig. 10.6b). It is especially interesting to analyze the influence of Poisson ratio on friction coefficient in the latter case. Curve 1 in

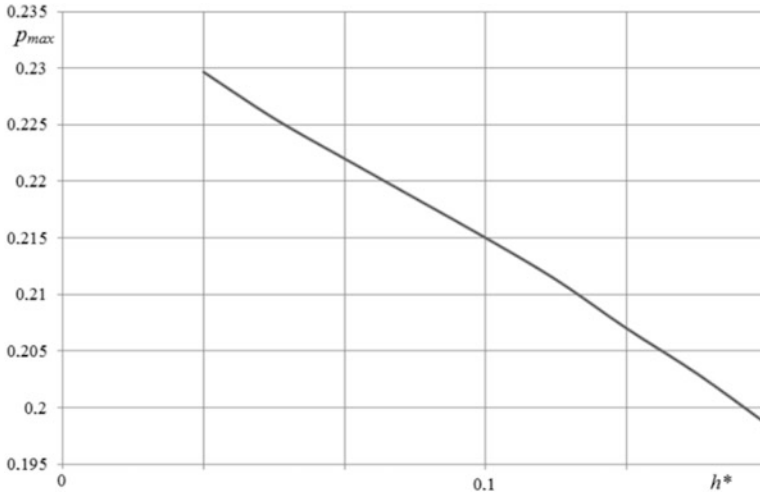


Fig. 10.5 Maximal pressure as a function of coating thickness ($Q^* = 0.1$, $c = 5$, $\nu = 0.3$, $V^* = 1/60$)

Fig. 10.6b corresponds to $\mu^* = 0.1013$, curve 2 – to $\mu^* = 0.1357$, curve 3 – to $\mu^* = 0.1439$.

Internal stresses in viscoelastic layer was analyzed for the case of single indenter. Figure 10.7 represents tensile-compressive stress distribution at the surface. Large tensile stresses often leads to the damage of the material. Maximum of both stresses (tensile and compressive) for all considered input parameters are located at the surface. Negative values refer to compressive stresses, positive – to tensile ones. Maximum of compression is at the same point at which maximal normal stresses occur. At the front of the contact zone there is a sharp jump from positive to negative or zero values; maximum of tension occurs behind the contact area. The analysis shows that tensile stresses depend essentially on layer thickness and on Poisson ratio. Significant decrease of tensile stresses occurs due to decrease of the layer thickness and to increase of Poisson ratio.

Figure 10.8 illustrates the results of calculation for distribution of tangential interfacial stresses τ'_{xz} . The stress concentration may be a reason for layer delamination from the interface. The values are equal to zero at the coating surface; the maximum is reached at the interface for all considered values of thickness. Here negative and positive signs define the direction of stresses action. Stresses reach their absolute maximum under the front side of the contact zone. The influence of Poisson ratio is most significant for shear stresses. We can see that the shear stress maxima are more than 2 times greater for large Poisson ratio (curves 1 is obtained for $\nu = 0.3$ and curve 4 is for $\nu = 0.45$).

Figure 10.9 presents the illustration of how layer thickness effects on principal shear stresses. Almost symmetric picture of stress distribution was obtained for relatively thick layer; it means that the layer thickness influences on manifestation

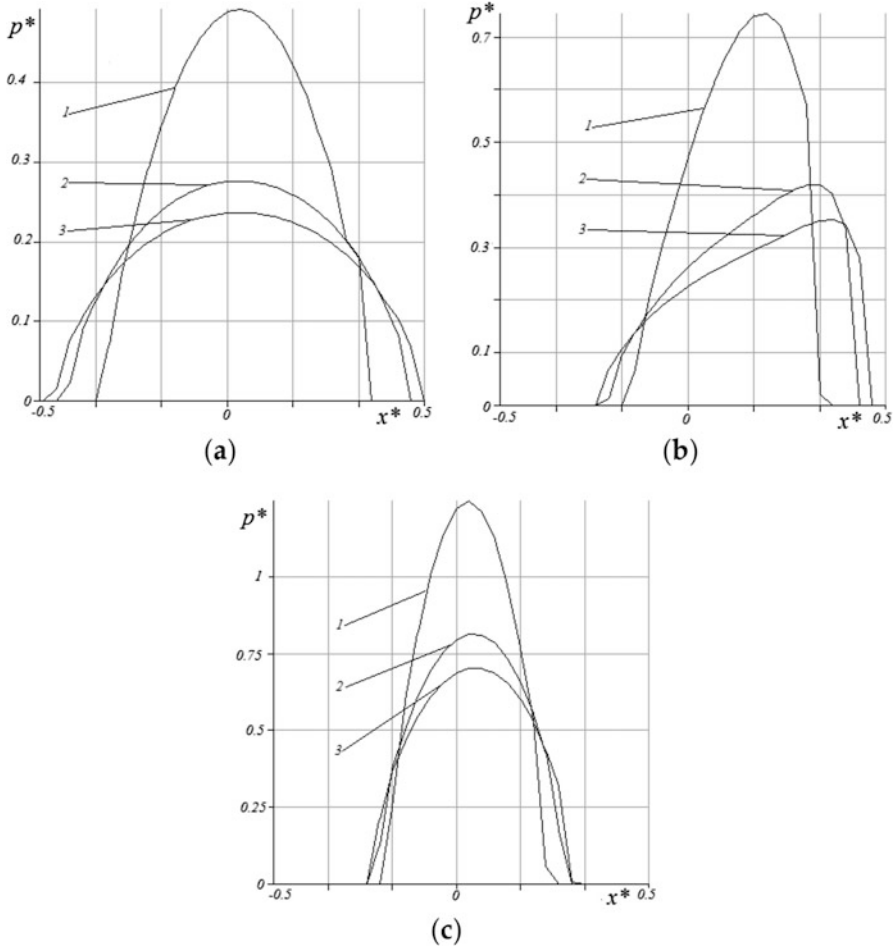


Fig. 10.6 Contact pressure for values of Poisson ratio and velocities and: $V^* = 1/60$ (a), $V^* = 0.3$ (b), $V^* = 10$ (c), $\nu = 0.45; 0.3; 0.2$ (curves 1–3 respectively), $h^* = 0.1$, $c = 5$, $Q^* = 0.1$

of rheological properties of materials in sliding contact. The five times increase of the layer thickness leads to almost three times decrease of maximal value of the principal shear stress inside the layer.

Viscoelastic Layer – Rigid Substrate. Two Sliders Mutual effect of sliders is presented in Fig. 10.10 for two sliders loaded by the same force. Calculations were made for three values of Poisson ratio. Solid lines in Fig. 10.10 represent pressure distribution of the front indenter and dashed lines correspond to the rear one. It is shown that contact area and pressure maximum of the front indenter is displaced in direction of sliding regarding to the rear one. It is also obtained that the mutual effect is stronger for relatively low values of Poisson ratio. The same problem for

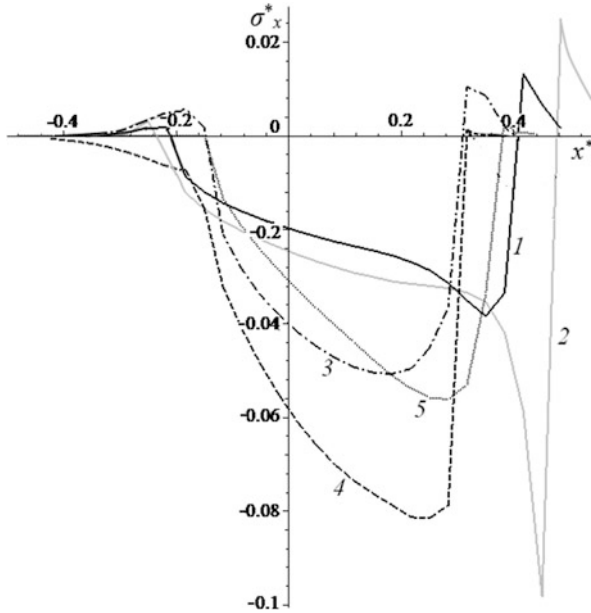


Fig. 10.7 Surface tensile and compressive stress distribution: $V^* = 0.333$ (curves 1,2,4,5), $V^* = 1.666$ (curve 3); $c = 5$, $Q' = 0.1$ (curves 1, 3–5), $c = 20$, $Q' = 0.035$ (curve 2); $h^* = 0.1$ (curves 1–4), $h^* = 0.033$ (curve 5); $\nu = 0.3$ (curves 1–3, 5), $\nu = 0.45$ (curve 4)

the case of viscoelastic half-space was solved earlier (Stepanov 2015); the results showed a significantly stronger effect of mutual influence.

The mutual effect is more essential for stresses at the surface and inside the layer. Figure 10.11 illustrates the effect for tensile-compressive stresses at the surface and shear stresses at the layer-substrate interface. Stresses for the front slider (curves 2) and the rear one (curves 3) are compared with the results for isolated slider (curves 1). Generally stresses under the rear slider are smaller than under the front one. At the surface tensile stresses under the front indenter are greater than under the isolated one, and the layer fracture due to surface tension is more probable. For the chosen input parameters shear stresses at the interface are smaller for both sliders compared with the isolated one.

4.1 Viscoelastic Half-Space Coated by a Rigid Plate

Figure 10.12 represents distribution of contact pressure for two sliding velocities $V^* = 0.05$ (Fig. 10.12a); $V^* = 0.2$ (Fig. 10.12b). Both figures demonstrate the effect of viscoelasticity of the base. It produces sufficient asymmetry of both contact zone

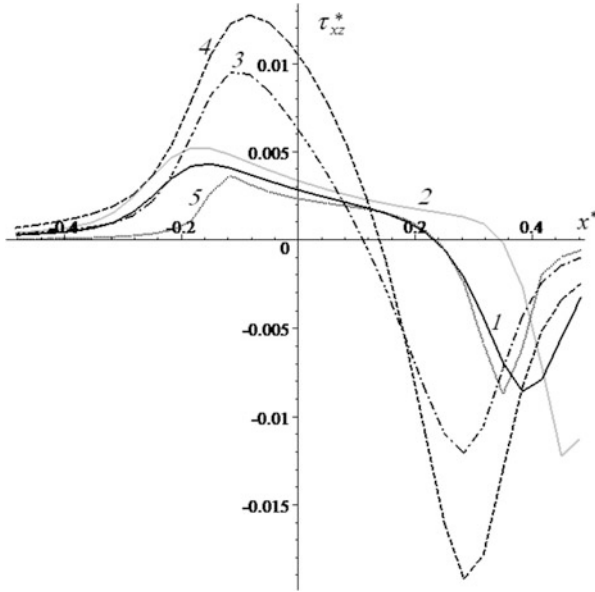


Fig. 10.8 Distribution of stresses τ'_{xz} at the layer-substrate interface: $V^* = 0.333$ (curves 1,2,4,5), $V^* = 1.666$ (curve 3); $c = 5$, $Q' = 0.1$ (curves 1, 3–5), $c = 20$, $Q' = 0.035$ (curve 2); $h^* = 0.1$ (curves 1–4), $h^* = 0.033$ (curve 5); $\nu = 0.3$ (curves 1–3, 5), $\nu = 0.45$ (curve 4)

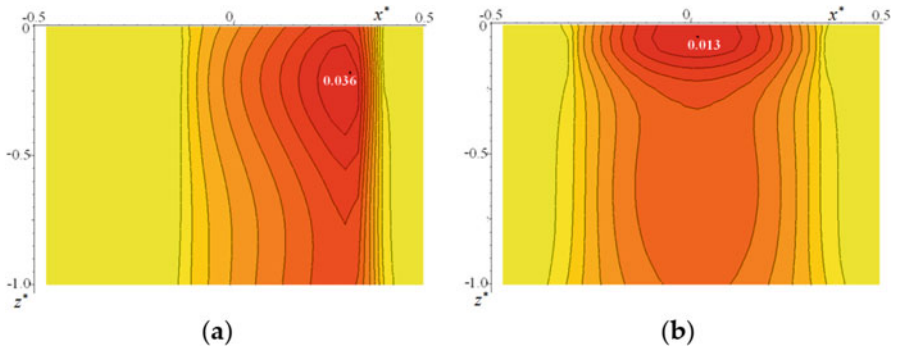


Fig. 10.9 Principal shear stresses for two different layer thicknesses: $V^* = 0.333$; $c = 5$; $\nu = 0.3$; $Q' = 0.1$; $h^* = 0.033$ (a), $h^* = 0.166$ (b)

and pressure distribution. A “chair shape” effect in pressure distribution can be seen in Fig. 10.12a. It occurs due to coating bend and viscoelastic properties of the base.

Contact pressure distributions for four values of layer thickness and for two sliding velocities are presented in Fig. 10.13. The decrease of pressure in a centre of a contact zone can be observed more clearly here. It is interesting to note that the phenomenon takes place for relatively thin layer, while the pressure distribution for thicker layers looks more Hertz-like, which is predictable.

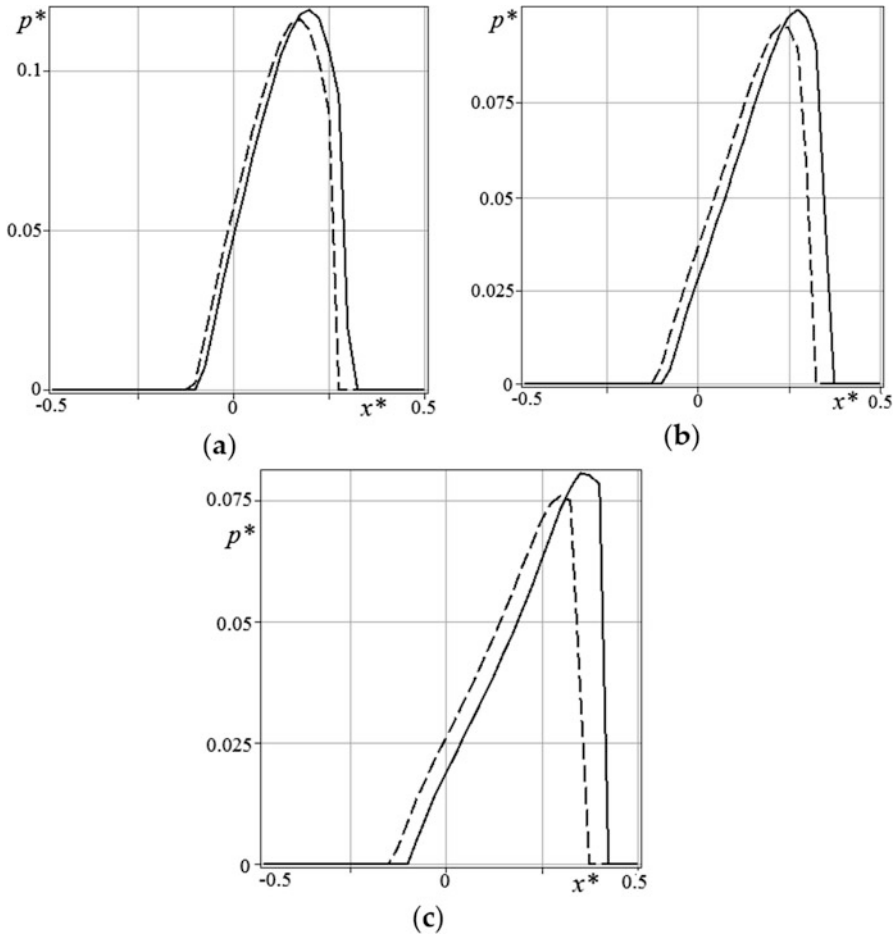


Fig. 10.10 Contact pressure distribution for two sliders: $\nu = 0.45; 0.4; 0.3$ (a, b, c respectively), $L/R = 1.5, c = 5, h^* = 0.1, Q^* = 0.01, V^* = 1$

We also have considered the influence of layer thickness on hysteretic losses. The results in Fig. 10.14 were obtained for two sliding velocities. Almost similar shape of curves 1 and 2 can be seen for relatively thick coatings. For thin coatings the dependence is non-monotonic. Generally, the smaller is sliding velocity the larger is the amplitude of the coefficient as the function of thickness.

Analysis of internal stresses due to contact interaction in an elastic substrate covered by essentially more hard coating (Goryacheva 1998) shows, that stresses at the coating-substrate interface are usually greater than in other points of the substrate. The results presented in Figs. 10.15 and 10.16 illustrate the influence of the rigid layer thickness on normal and tangential stresses at the interface for two different velocities. It can be noted, that for the thickest coating the normal stress

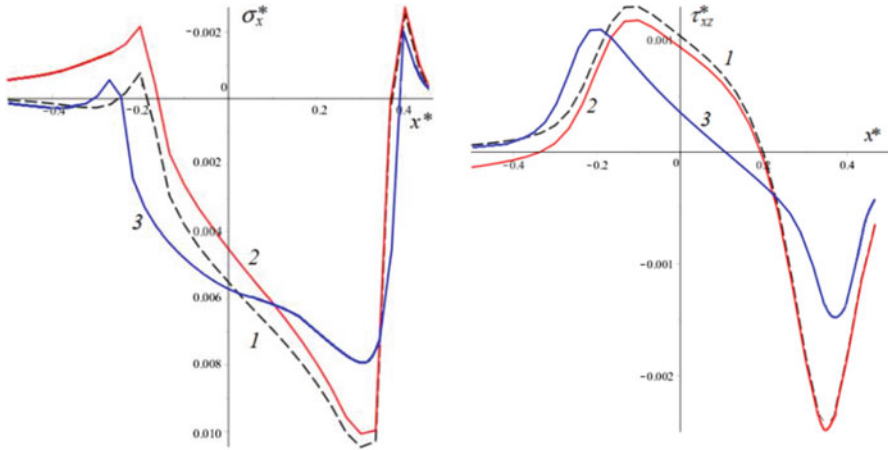


Fig. 10.11 Tensile-compressive (a) and shear (b) stress distribution for two sliders at the surface (a) and layer-substrate interface (b): $\nu = 0.45$, $L/R = 1.5$, $c = 5$, $h^* = 0.1$, $Q^* = 0.01$, $V^* = 0.05$

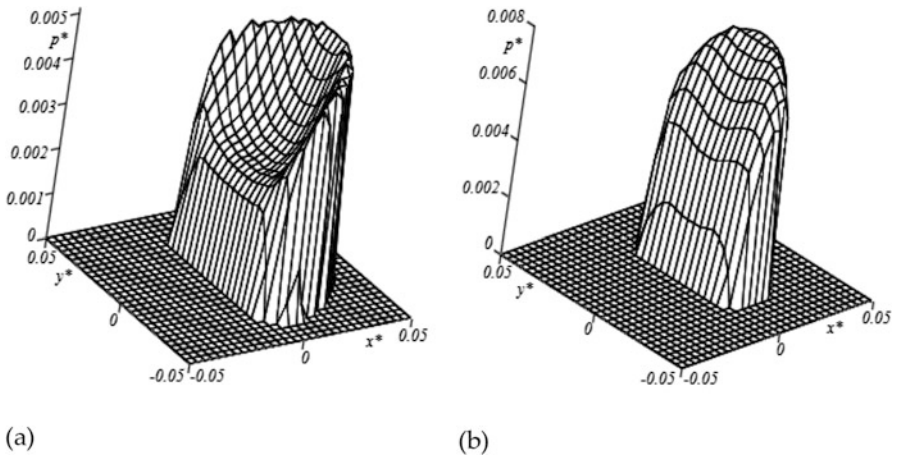


Fig. 10.12 Contact pressure within the contact spot ($c = 6$; $h^* = 0.0133$; $\nu = 0.4$; $Q' = 2.0$; $V^* = 0.05$ (a); $V^* = 0.2$ (b))

distribution is the most uniform, but for the thin layer the distribution is closer to the contact pressure. It can explain the effect of decreasing of hysteretic losses with increasing of the coating thickness. The effect of the layer thickness on interfacial tangential stresses is almost the same as for the case of viscoelastic layer bonded with a rigid substrate, which is described above.

Analysis of stresses in an elastic substrate covered with a much harder coating due to contact interaction (Goryacheva 1998) shows that stresses at the coating – substrate interface are usually higher than at other parts of the substrate. The results in Figs. 10.15 and 10.16 illustrate the effect of hard layer thickness on interfacial

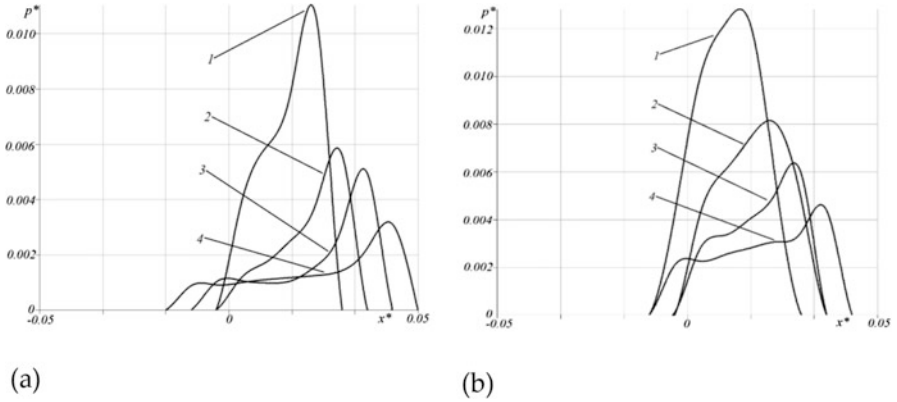


Fig. 10.13 Cross section of contact pressure function for different layer thickness and velocities: $c = 6$; $\nu = 0.4$; $Q' = 2.0$; $V^* = 0.05$ (a); $V^* = 0.2$ (b), $h^* = 0.05$ (curve 1), $h^* = 0.02$ (curve 2), $h^* = 0.0133$ (curve 3), $h^* = 0.0066$ (curve 4)

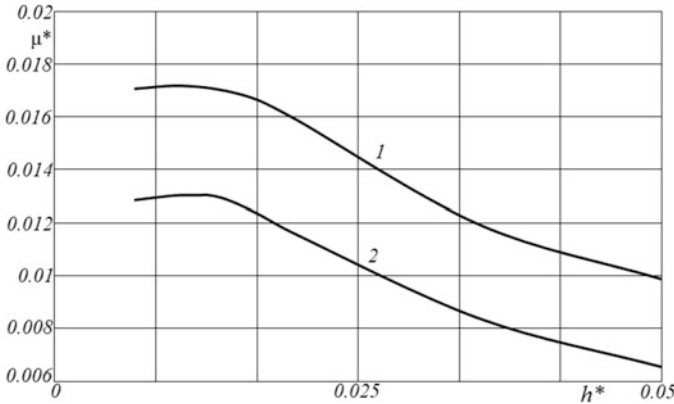


Fig. 10.14 Friction coefficient as a function of layer thickness. ($c = 6$; $\nu = 0.4$; $Q^* = 2.0$; $V^* = 0.05$ (curve 1); $V^* = 0.2$ (curve 2))

stresses (both normal and shear) for two sliding velocities. It should be noted that the normal stress function is the most uniform for the layer with largest thickness. When the layer is thin the function is closer to the contact stresses. This can explain the effect of energy dissipation with an increase in the layer thickness. The effect of the coating thickness on the interfacial shear stresses is practically the same as in the case of a viscoelastic layer adhered to a rigid substrate.

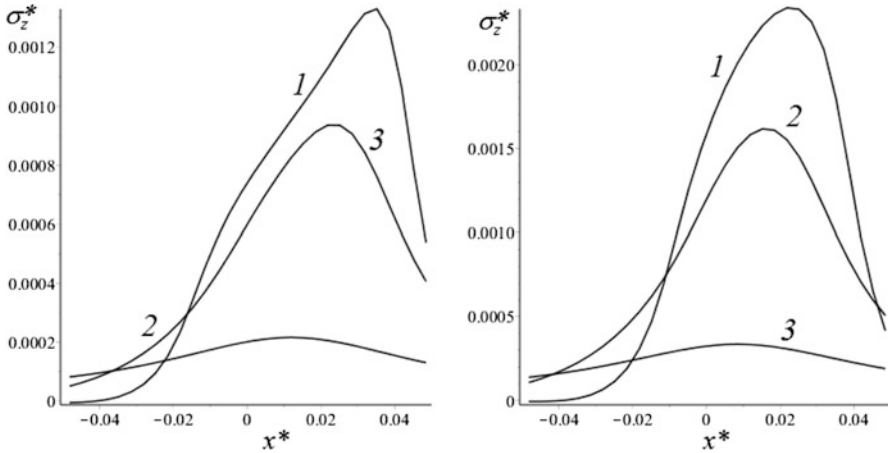


Fig. 10.15 Interfacial normal stresses ($\nu = 0.4$; $c = 6$; $Q^* = 2.0$; $V^* = 0.05$ (a); $V^* = 0.2$ (b); $h^* = 0.0066$ (curve 1), $h^* = 0.0165$ (curve 2), $h^* = 0.05$ (curve 3))

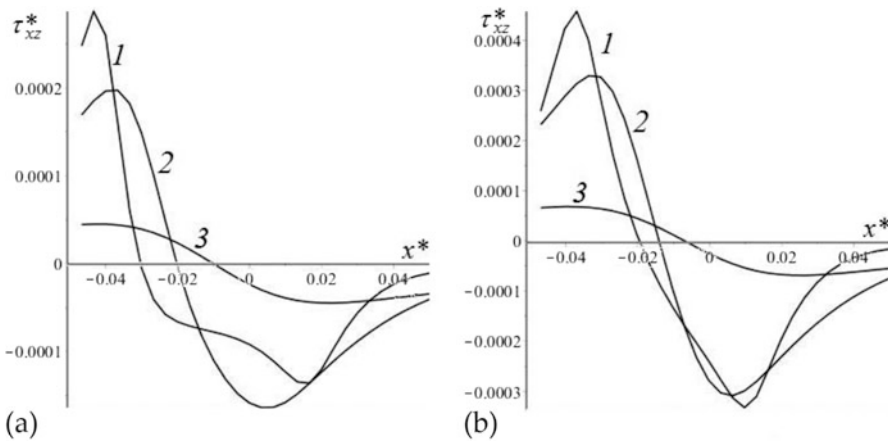


Fig. 10.16 Interfacial shear stresses ($\nu = 0.4$; $c = 6$; $Q^* = 2.0$; $V^* = 0.05$ (a); $V^* = 0.2$ (b); $h^* = 0.0066$ (curve 1), $h^* = 0.0165$ (curve 2), $h^* = 0.05$ (curve 3))

5 Conclusion

A new numerical-analytical method based on double integral Fourier transform is developed and used for solution of two categories of contact problem with sliding:

- a quasistatic motion of smooth slider over a viscoelastic coating adhered to a rigid half-space;
- a quasistatic motion of smooth slider over a rigid plate adhered to viscoelastic base.

Contact pressure, friction coefficient, stresses in the viscoelastic coating or inside the viscoelastic base were obtained. The analysis of the results and their dependence on input parameters was done.

For viscoelastic homogeneous half-space, the velocity, at which the maximum hysteretic losses are realized, depends on the value of normal load and on the combination of the rheological and elastic material properties. For viscoelastic layer (or for layered viscoelastic base) this set of parameters also includes the thickness of the coating. It was found that energy dissipation for low velocities are higher in a layer than in homogeneous half-space (relaxation and retardation times of material are the same). The opposite effect of coating thickness was obtained at higher sliding velocities. In general, the maximum value of friction coefficient due to hysteretic losses is higher for the thicker layer. For the combination of rigid layer and viscoelastic base, the opposite effect is obtained. It should be noted that a similar result was obtained experimentally by friction of polyurethane, on the surface of which a hard carbonized layer of different thicknesses was obtained (Torskaya et al. 2020).

Mutual effect for two indenters sliding one after another is analyzed for the case of viscoelastic layer. It is obtained that the effect is stronger for stresses than for contact characteristics.

The dependence of contact pressure on Poisson ratio is partially apparent: we can see higher values of contact pressure for elastic solids in the case of low-compressive materials. More interesting is to find that large values of interfacial shear stresses take place for low-compressible materials. This effect may lead to coating delamination.

The case of thin coatings with low values of Poisson ratio leads us to the following effect: stresses are weakly depending on coordinate z . In this case a 1-D model of viscoelastic layer can give us rather good approximation for the contact problem solution.

We can use analysis of stresses distribution inside the coating or within viscoelastic base for prediction of the coating fracture.

References

- Aleksandrov VM, Goryacheva IG (2005) Mixed problems of mechanics of deformable solid. In: Proceedings of V Russian conference with international participation, Izd. Sarat. University in Russian, Saratov, pp 23–25. [in Russian]
- Aleksandrov VM, Goryacheva IG, Torskaya EV (2010) Sliding contact of a smooth indenter and a viscoelastic half-space (3D problem). *Dokl Phys* 55(2):77–80
- Bai C, Liang A, Cao Z, Qiang L, Zhang J (2018) Achieving a high adhesion and excellent wear resistance diamond-like carbon film coated on NBR rubber by Ar plasma pretreatment. *Diam Relat Mater* 89:84–93
- Boychenko GA (1955) Resistance to rolling of viscoelastic bodies. *Izd Akad Nauk SSSR* 9:27–31. (in Russian)
- Carbone G, Putignano C (2013) A novel methodology to predict sliding and rolling friction of viscoelastic materials: theory and experiments. *J Mech Phys Sol* 61(8):1822–1834

- Chudinov VS, Kondyurina IV, Shardakov IN et al (2018) Polyurethane modified with plasma-ion implantation for medical applications. *Biophysics* 63:330–339
- Eldredge KR, Tabor D (1955) The mechanism of rolling friction. I. The plastic range. *Proc R Soc (London) Ser A* 229(1177):181–198
- Flom DG, Bueche AM (1959) Theory of rolling friction for spheres. *J Appl Phys* 30(11):1725–1730
- Galin LA, Shmatkova AA (1968) On sliding of a rigid indenter over a viscoelastic half-space boundary. *Prikl Mat Mekh* 3:445–453. (in Russian)
- Goryacheva IG (1973) Contact problem of rolling of a viscoelastic cylinder on a base of the same material. *J Appl Math Mech* 37(5):877–885
- Goryacheva IG (1998) *Contact mechanics in tribology*. Kluwer Academic Publishers, Dordrecht, p 344
- Goryacheva IG, Gubenko MM, Makhovskaya YY (2014) Sliding of a spherical indenter on a viscoelastic foundation with the forces of molecular attraction taken into account. *J Appl Mech Tech Phys* 55:81–88
- Goryacheva IG, Stepanov FI, Torskaya EV Effect of friction in sliding contact of a sphere over a viscoelastic half-space. In: Neittaanmäki P, Repin S, Tuovinen T (eds) *Mathematical modeling and optimization of complex structures. Computational methods in applied sciences*, vol 40. Springer, Cham
- Greenwood JA, Tabor D (1958) The friction of hard sliders on lubricated rubber: the importance of deformation losses. *Proc Phys Soc* 71(6):989–1001
- Grosch KA (1963) The relation between the friction and viscoelastic properties of rubber. *Proc R Soc (London) Ser A* 274(1356):21–39
- Hunter SC (1961) The rolling contact of a rigid cylinder with a viscoelastic half space. *J Appl Mech* 28(4):611–617
- Ishlinskii AY (1938) Rolling friction. *Prikl Mat Mekh* 2(2):245–260. (in Russian)
- Ishlinskii AY (1940) Theory of resistance to rolling (rolling friction) and related phenomena, In *Friction and Wear in Machines*. Izd Akad Nauk SSSR 2:255–264. (in Russian)
- Klüppel M, Heinrich G (2000) Rubber friction on self-affine road tracks. *Rubber Chem Technol* 73:578–606
- Koumi KE, Zhao L, Leroux J et al (2014) Contact analysis in the presence of an ellipsoidal inhomogeneity within a half space. *Int J Solids Struct* 51(6):1390–1402
- Koumi KE, Chaise T, Nelias D (2015) Rolling contact of a rigid sphere/sliding of a spherical indenter upon a viscoelastic half-space containing an ellipsoidal inhomogeneity. *J Mech Phys Sol* 80:1–25
- Kusche S (2016) Frictional force between a rotationally symmetric indenter and a viscoelastic half-space. *ZAMM J Appl Math Mech* 97(2):226–239
- Le Tallec P, Rahler C (1994) Numerical models of steady rolling for non-linear viscoelastic structures in finite deformations. *Int J Numer Methods Eng* 37(7):1159–1186
- Lyubicheva AN (2008) Analysis of mutual influence of contact spots in sliding of periodical system of asperities over Winkler viscoelastic foundation. *J Frict Wear* 29:125–133
- May WD, Morris EL, Atack D (1959) Rolling friction of a hard cylinder over a viscoelastic material. *J Appl Phys* 30(11):1713–1724
- Morland LW (1962) A plane problem of rolling contact in linear viscoelasticity theory. *J Appl Mech* 29(2):345–352
- Morozov AV, Makhovskaya YY (2007) Theoretical-experimental assessment of deformational component of friction coefficient. *J Frict Wear* 28:335–344
- Nasdala L, Kaliske M, Becker A, Rothert H (1998) An efficient viscoelastic formulation for steady-state rolling structures. *Comput Mech* 22(5):395–403
- Nikishin VS, Shapiro GS (1970) *Space problems of the elasticity theory for multilayered media*. VTs AN SSSR, Moscow. [in Russian]
- Padovan J, Paramadilok O (1985) Transient and steady state viscoelastic rolling contact. *Comput Struct* 20(1–3):545–553

- Padovan J, Kazempour A, Tabaddor F, Brockman B (1992) Alternative formulations of rolling contact problems. *Finite Elem Anal Des* 11(4):275–284
- Persson BNJ (2001) Theory of rubber friction and contact mechanics. *J Chem Phys* 115:3840–3861
- Persson BNJ (2010) Rolling friction for hard cylinder and sphere on viscoelastic solid. *Eur Phys J E* 33(4):327–333
- Soldatenkov IA (2015) Calculation of friction for indenter with fractal roughness that slides against a viscoelastic foundation. *J Frict Wear* 36(3):193–196
- Stepanov FI (2015) Sliding of two smooth indenters on a viscoelastic foundation in the presence of friction. *J Appl Mech Tech Phys* 56(6):1071–1077
- Stepanov FI, Torskaya EV (2016) Study of stress state of viscoelastic half-space in sliding contact with smooth indenter. *J Frict Wear* 37(2):101–106
- Stepanov FI, Torskaya EV (2018) Modeling of sliding of a smooth indenter over a viscoelastic layer coupled with a rigid base. *Mech Solids* 53(1):60–67
- Tabor D (1955) The mechanism of rolling friction. II. The elastic range. *Proc R Soc (London) Ser A* 229(1177):198–220
- Torskaya EV, Stepanov FI (2019) Effect of surface layers in sliding contact of viscoelastic solids (3-d model of material). *Front Mech Eng* 5(26)
- Torskaya EV et al (2020) Sliding contact of coated viscoelastic solids: model and experiment. *IOP Conf Ser* 1474:012033
- Ya R, Ivanova N (1964) The rolling viscoelastic cylinder on the base of the same material. *J Appl Mech Tech Phys* 3:179–184

Chapter 11

Characterisation of an AFM Tip Bluntness Using Indentation of Soft Materials



Soft Materials Indentation and Tip Characterisation

Sameeh Baqain, Feodor M. Borodich, and Emmanuel Brousseau

Abstract Bluntness of tips of atomic force microscopy (AFM) probes may affect the precision of AFM measurements of surface topography and accuracy of AFM nanomachining of solid surfaces. Here, various methods for characterisation of AFM tip bluntness are discussed. The results of experimental studies of AFM probe tips are presented. Both tips are considered; (i) the intact tips as received from factory and (ii) worn tips. The tip bluntness is studied in both vertical position of the probes and in working position when the AFM cantilever is inclined by 12° to the horizontal plane. It is suggested to describe the tips as power-law functions, whose exponent d is used as a characteristic of tip bluntness. It is argued that the load displacement curve of an experimental depth-sensing indentation (DSI) test may be used to extract the quantitative measure of the AFM tip bluntness. The experimental results showed that one has to be careful in selecting proper soft material (polymer) for bluntness estimations because it was observed rather often practically linear load displacement curves. This was explained by existence of a stagnation zone of polymer macromolecules in front of the AFM tip that moves downward together with the indenter.

Keywords Bluntness of AFM tip probes · Intact tips · Worn tips · Load-displacement curve · Inclined AFM cantilever

S. Baqain (✉)

School of Engineering, Cardiff University, Cardiff, UK

Mechanical Engineering Department, American University of Madaba, Madaba, Jordan

e-mail: baqainss@cardiff.ac.uk

F. M. Borodich · E. Brousseau

School of Engineering, Cardiff University, Cardiff, UK

© Springer Nature Switzerland AG 2022

F. M. Borodich, X. Jin (eds.), *Contact Problems for Soft, Biological and Bioinspired Materials*, Biologically-Inspired Systems 15,

https://doi.org/10.1007/978-3-030-85175-0_11

1 Introduction

Atomic force microscopy (AFM) was originally introduced by Binnig et al. (1986) as a tool for topographical measurements of surfaces with unprecedented resolution. Current success in characterisation of surface topography of nanoscale objects and biological systems such as insect pulvilli and plant surfaces, various cells and bacteria, human joints, tissues, lizard attachment devices and so on, down to the nanometre scale is a result of the rapid development of scanning probe microscopy (SPM), especially AFM. It is known that AFMs can work in different modes: contact, dynamic and non-contact ones (see, e.g., Tseng et al. 2005). The contact mode provides not only the best resolution of the surface topography (see, e.g., Yao and Wang 2005), but also it enables the researchers to manipulate objects and structures at the micro/nano scale. Therefore, AFM has revolutionised the way in which researchers explore nanoscale objects and biological structures (see, e.g., Hoh et al. 1991).

The precision of AFM applications is highly dependent on the conditions of the AFM probe tip. Due to forces of contact interactions between the tip and the scanned material, the initial shape of the tip may change. In turn, the bluntness of the tip may cause significant errors in the resulting output and interpretation of the output data, see, e.g. Borodich et al. (2003), Yan et al. (2016), and Ramirez-Aguilar and Rowlen (1998).

Thus, there arises a natural question: How can one characterise quantitatively the tip bluntness? Kindrachuk et al. (2006) suggested to use the difference in depth between the ideal and simulated tips as main parameter of the tip bluntness. Alraziqi (2017) presented two possible quantitative characteristics (metrics) of the tip bluntness: (i) the ratio of the tip volume for a given height to the volume of the imaginary cylinder of the same height in which contains the tip; (ii) the degree d of the power-law approximation of the indenter tip.

The latter metric suggested by Alraziqi (2017) arose from the following theoretical arguments. It is known that the shape of non-ideal indenter near the tip can be well approximated by power-law functions of radius of degree d (see, e.g., Borodich et al. 2003). For many materials, contact problems for such indenters are self-similar (see, e.g. Galanov 1981a, b; Borodich 1983, 1989, 2014). In turn, for the self-similar contact problems, the load-displacement curves satisfy the scaling relations and may be presented as special power-law functions (Borodich 1989, 1993, 2014). It was suggested to extract degree d of a blunt tip power-law approximation from the experimental load-displacement curves of elastic indentation of a soft material samples by the AFM tip under consideration (see, e.g., Alraziqi et al. 2016).

In this Chapter, we discuss the various methods for description of the AFM tip bluntness and present results of experimental studies of AFM probe tips. Both tips are considered; (i) the intact tips as received from factory and (ii) worn AFM tips. The blunt tip shapes are studied in both vertical position of the probes and in working position of an AFM, when the AFM cantilever is inclined by 12° to the

horizontal plane. The above-mentioned analytical scaling approaches are compared with results of experimental studies of DSI using the AFM.

2 Preliminaries

The importance of having an accurate tip shape description was discussed in many papers. For example, the direct impact of the tip's geometry on results of piezoresponse force microscopy was discussed by Kalinin and Bonnell (2002). They used piezoresponse imaging in the electrostatic regime in which the capacitive and Coulombic interactions of the surfaces caused an attractive force that occur during indentation. These interactions were in some instances approximated to a plane-plane capacitor which is incorrect due to the capacitive force in a plane-plane geometry cannot cause a tip deflection. The authors concluded that an accurate tip shape is necessary for a correct interaction description. Borodich et al. (2003, 2014a, 2014b) also emphasised the importance of tip bluntness for evaluation of mechanical and adhesive properties of materials from nanoindentation experiments. Further on, this concern also rises when one intends to describe the bluntness of new AFM probes because the information based on data provided by manufacturers can be misleading. Indeed, as it was proven in a number of studies, see, e.g., Sedín and Rowlen (2001) and Jacobs et al. (2016), the actual tip radius values can deviate significantly from their nominal values stated by manufacturers. In addition, the shape of the tip may be not spherical.

As it was mentioned by Alraziqi (2017), various techniques were developed for assessing the geometry of the apex of an AFM tip. These techniques may be subdivided to (i) in-situ and (ii) ex-situ approaches. The former techniques mean that characterization can be conducted on the AFM instrument itself, while the latter technique requires the probe to be physically removed from the AFM and observed using an appropriate microscopy technique. In turn, the in-situ techniques may be subdivided into several groups: (i) the employment of a special tip characteriser, which consists of an array of sharp pins or asperities (see, e.g. Bykov et al. 1998; Bloo et al. 1999); (ii) the use of an alternative material sample, whose geometry could be used to extract the useful information about the tip geometry (see, e.g. Khurshudov et al. 1997); (iii) the use of scanned data for an AFM tip and corresponding mathematical processing of the data and these techniques are usually referred to as the "blind tip reconstruction" methods (see, e.g. Villarrubia 1994); (iv) the utilising an ultra-sharp tip to characterise the probe tip under investigation (see, e.g. Khurshudov et al. 1997); and (v) the assessment of wear volumes of the tip material (see, e.g. Gotsmann and Lantz 2008).

One of the first works dedicated to analysis of the of AFM tip geometry using electron microscopy was in Lantz et al. (1998), where the authors investigated also wear and contamination of the tip. In addition, Bloo et al. (1999) studied the deformation of silicon nitride tips. These studies were followed by an in-depth analysis by Chung and Kim (2003). On the other hand, Bhaskaran et al. (2010) used

both SEM and TEM images to characterise the tip's apex made of diamond-like carbon containing silicon before and after AFM imaging in contact mode tests with forces below 20 nN.

Khurshudov and Kato (1997) investigated the wear mechanisms of AFM tips on both hard (silicon) and soft (polycarbonate) materials. In one test, silicon nitride tips were used in light-loaded scanning of smooth silicon surface. They discovered that the formation of a rough surface with asperities did not significantly affect the quality of the AFM images taken due to the asperities acting as a probing tip. The mechanisms causing the wear on the other hand was probably low cycle fatigue in addition to adhesion as the less likely culprit. The reasoning behind that conclusion is based on the continuous contamination of the surface during testing and was likely to reduce the adhesion effect leaving the low cycle fatigue as the best guess which is supported by the formation of rough surfaces on the tip. In addition, Bloo et al. (1999) supported the idea that low cycle fatigue is in fact the cause of the tip wear in a study that also utilised silicon nitride tips. As for polycarbonate, Khurshudov and Kato (1995, 1997) studied the wear mechanism occurring during scratching in which no plastic deformation was observed even with repeated scratching on the same surface.

Ex-situ methods use electron microscopy including Scanning Electron Microscope (SEM), Transmission Electron Microscope (TEM), Scanning Transmission Electron Microscope (STEM), or High-Resolution Transmission Electron Microscope (HRTEM) techniques. Here, some results of SEM studies will be utilised in order to get some experimental data enable us to characterise the AFM tip.

Due to the contact between the tips and samples, certain changes in the shape of the tips are to be expected. To address this issue, a method used to analyse the tip's condition called the blind tip reconstruction (BTS) was established which produces a 3D image of the tip shape even without the prior knowledge of the geometry of the surface to be scanned. This method was first suggested by Villarrubia (1994) where it utilises the convolution effect inherent in AFM scans due to the bluntness of the tip. Villarrubia joined another experimental study in Dongmo et al. (2000) (Fig. 11.1) where the BTS method was also employed to characterise two diamond profiler tips where they scanned a commercial roughness calibration sample. The resulting tip shape produced using BTS was quite comparable to the profile of the SEM image of the same tip with up to 600 nm distance from the apex.

It will be assumed further that the current shape of the tip apex can be approximated in polar coordinates (r, θ, z) as a power-law function of radius having the exponent of the power-law function d .

This exponent will be used as a numerical parameter for characterisation of the tip bluntness. The power-law approximation gives the ability to extract the tip bluntness value by studying the SEM image of an AFM tip.

In addition, this approximation will enable us to employ the analytical techniques developed mainly by (Borodich 1989, 1993). These techniques are based on self-similarity of Hertz-type contact problems for linear and non-linear materials, whose constitutive laws may be expressed as power-law (see, e.g., Galanov 1981a, b; Borodich 1983, 1989, 1990, 1993; Borodich et al. 2003). For the power-law shaped

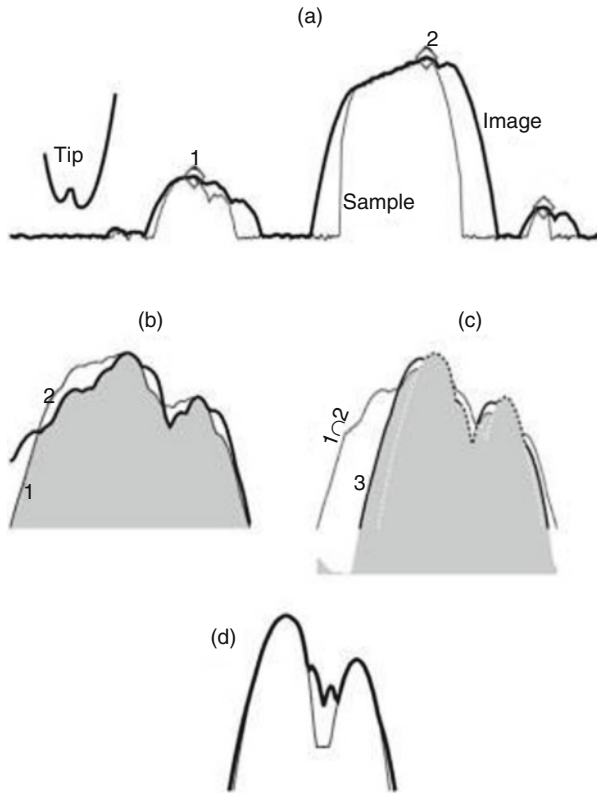


Fig. 11.1 The blind tip reconstruction method by Dongmo et al. (2000)

indenters one can also extend the classic JKR (Johnson-Kendall-Roberts) theory of adhesive contact (Galanov 1993; Galanov and Grigoriev 1994; Carpick et al. 1996; Borodich and Galanov 2004).

In addition, we will analyse the tip in its vertical position as well as its working position, i.e. rotated 12° clockwise about the tip's longitudinal axis as discussed in Heim et al. (2004), Hutter (2005) and Al-Musawi et al. (2016). Given that in practice most tips are not perfect spheres, the inclination of the probe causes a rotation of the tip creating a new apex with a new bluntness value resulting in some practical implications such as a change in the pull-off force (see, e.g., Borodich and Galanov 2004; Carpick et al. 1996; Zheng and Yu 2007).

3 Images of AFM Tips in Working Position

In this section, we will approximate the AFM probe's tip shape extracted from SEM images to a non-axisymmetric power-law function of degree d .

The adhesive contact problems solved in the framework of JKR theory are not self-similar. However, if the shape of the indenter is described by axisymmetric power-law function, one can extend the JKR theory to such indenters, see, e.g. Galanov (1993), Carpick et al. (1996), Borodich and Galanov (2004). The difference between Galanov's solution and Carpick's is that the values of d for former solutions are arbitrary real positive numbers $d \geq 1$, while for latter are integer numbers only.

The values of d will have real positive numbers and only not integers as used in Grierson et al. (2013). Then, the exponent d will be used to quantitatively describe the degree of bluntness of the tip. Because $d = 1$ corresponds to a cone, $d = 2$ to a sphere then the higher the value d the flatter (blunter) the tip is.

For the sake of simplicity, we will assume that the results obtained from vertically indenting materials by a probe are applicable to AFM probe indentation as lateral displacements during the nanoindentation are considered negligible as it will be proven in the following section. Indenters following power-law shapes have self-similar contact problems. Hence, we can apply the Borodich scaling approach and the 3D contact applicable formulae within Borodich (1989, 1993, 2011, 2014), the monomial function in polar coordinates can be expressed as follows:

$$z = B_d(\theta) r^d \quad (11.1)$$

Where $x_1 = r \cos \theta$, $x_2 = r \sin \theta$ and $B_d()$ is a function of the indenter heights at $r = l$. We apply this approximation to the heights up to 30 nm (this is the depth of tip penetration). The relationship between the power-law functions and homogeneous functions can be understood from the definition of homogeneous functions that:

$$h_d(x_1, x_2) = \lambda^{-d} h_d(\lambda x_1, \lambda x_2) = \lambda^{-d} h_d(\lambda r \cos \theta, \lambda r \sin \theta) \quad (11.2)$$

Assuming $\lambda = r^{-1}$, we obtain

$$h_d(x_1, x_2) = \lambda^{-d} h_d(\lambda r \cos \theta, \lambda r \sin \theta) = r^d B_d(\theta) \quad (11.3)$$

$$B_d(\theta) = h_d(\cos \theta, \sin \theta) \quad (11.4)$$

Therefore, it is valid to assume that the indenter shape is presented as a power-law function of degree d or the bluntness of the indenter is expressed by a degree d of the power-law approximation.

Graph in Fig. 11.2 shows the shape of the parabola $z = f(r) = r^d$ where d increases 1, 1.5, 2, 2.5 up to 3 with 1 being the straight line and 3 being the rightmost and most curved one. The previous equation contains a $B_d(\theta)$ part that is not constant function

Fig. 11.2 The power-law function $z = r^d$ with d values 1, 1.5, 2, 2.5, and 3

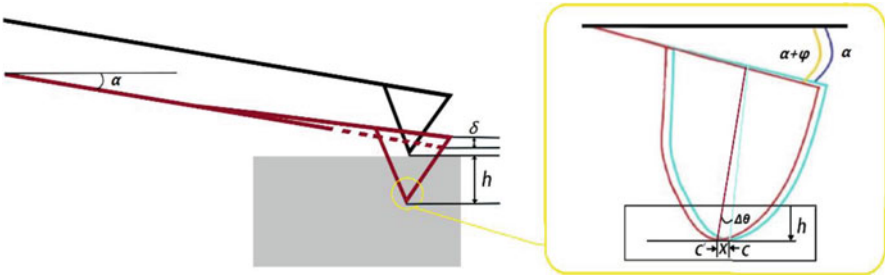
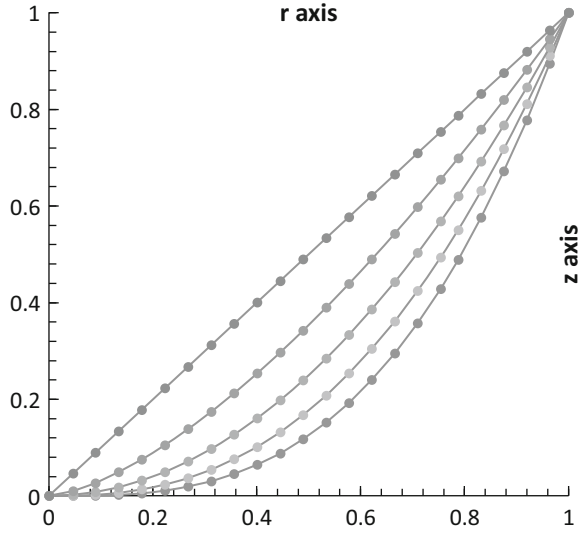


Fig. 11.3 AFM probe in its working orientation

of the angle θ . In fact, $B_d(\theta)$ describes the height of the indenter at some point (θ, r) on a circle of a unity radius $r = 1$.

One has to take into account that the AFM cantilever in its working position is not horizontal (see, e.g., Heim et al. 2004; Hutter 2005; Al-Musawi et al. 2016). In fact, it is inclined by a $\alpha = 12^\circ$, as it is shown in Fig. 11.3. Initially the inclination angle of the cantilever in its mounted position is α , while under the maximum load the angle increases by φ . The total inclined angle of the AFM cantilever is $\varphi + \alpha$.

If the indentation is considered shallow, then we can safely assume that the cantilever inclination angle $\varphi + \alpha \cong \alpha$ during the nanoindentation test. This means that the first point of the probe that may touch the material sample is not at the geometrical tip apex of the probe in its vertical position C' but rather the point C (see the exaggerated version of the AFM probe in Fig. 11.3). During nanoindentation, the tip's point C will have not only vertical displacements but also some shift in the horizontal direction.

If we assume shallow nanoindentation then the maximum nanoindentation depth h_{\max} inside the indented material's surface $h_{\max} \approx 50 \text{ nm}$. From Alraziqi (2017) we can assume:

$$\Delta\theta = \frac{3 h_{\max}}{2 L} \quad (11.5)$$

Assuming $L \approx 100 \mu\text{m}$ (manufacturer provided) then we can find the value of $\Delta\theta = 0.00075^\circ$ (i.e., $\text{rad} = 0.043$) which can be considered as infinitesimal. Then, in this case to find the needed shifting distance X between C and C' we will use the following equation:

$$X = h_t \sin \quad (11.6)$$

Assuming $h_t \approx 10 \mu\text{m}$ then the estimated value of the shifting distance $X = 7.5 \text{ nm}$. Thus, this shift is considerably small, and we can apply the rescaling formulae developed for the case of regular indenter to the AFM probe tips indenting soft elastic materials.

The tip shape can be described by a monomial function of radius $z = B_d(\theta)r^d$ when it is in its vertical position (i.e., $\alpha = 0^\circ$). Here, we argue here that the probe tip apex at the working position (i.e., $\alpha = 12^\circ$) could also be describe as this equation $z_1 = B_d(\theta)r^{d_1}$. For non-axisymmetric shaped tip, it is obvious that d_1 (approximation of the tip bluntness at the maximum depth) is not equal to d of the same tip at the vertical position and will be proven experimentally later.

It is important to remember that representing the AFM's tip shape is not a trivial task that can be solved by simply presentation it as a sphere (see highlights in Fig. 11.4). As the Fig. 11.4 demonstrates, three possible spheres with three different radii can be applied to the same tip of non-ideal shape and all having a certain degree of accuracies. Hence, to get more reliable tip shape representation, the non-ideal nature of the tip shape must be taken into consideration as discussed in Borodich et al. (2003) in addition to Borodich and Galanov (2004).

The axisymmetric assumption used when profiling AFM tips is also erroneous as Fig. 11.5 demonstrates.

As the 3D tip reconstruction Fig. 11.5a, b above clearly shows, the tip is not axisymmetric and follows more of an arbitrarily changing profile due to manufacturing limitations at such small sizes. In addition, if we look at the 3D profile from a top view in Fig. 11.5c, we can dissect it into 8 sections at $0^\circ, 45^\circ, 90^\circ, 135^\circ, 180^\circ, 225^\circ, 270^\circ$ and 315° angles. Such consideration will allow for in depth analysis of the tips non-axisymmetric nature. In Fig. 11.5, the horizontal red line is always along the (0° – 180°) axis and the green lines represent the other 3 profiles.

Fig. 11.4 Non-ideal tip shape with 3 plausible spherical approximations to the real shape in the dark red colour

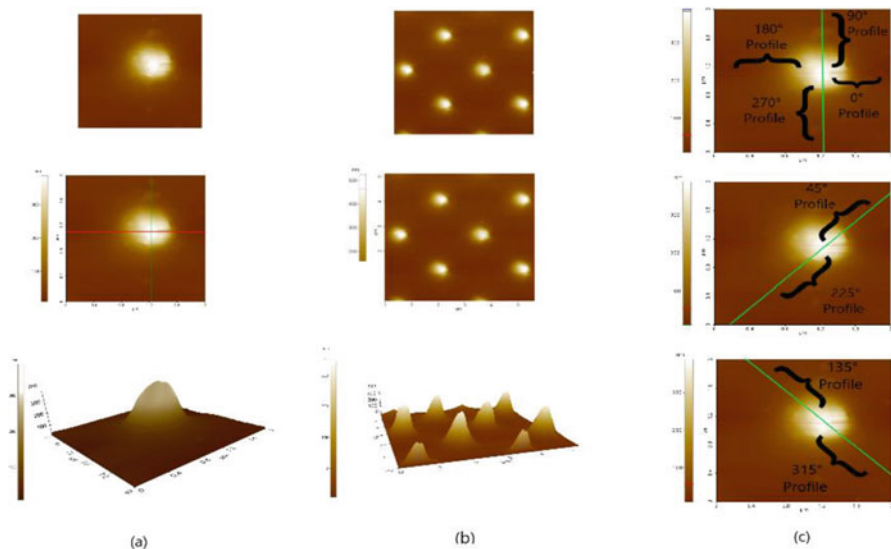
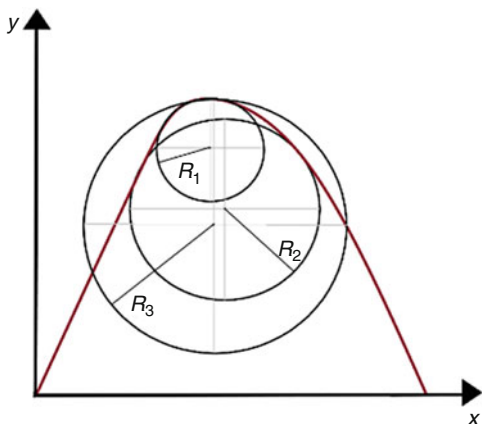


Fig. 11.5 AFM images of the TGT01 tip characteriser scanned by one of the tested tips. Points (a) a single asperity, (b) are of multiple asperities and (c) Illustration of the selection of the (0°–180°), (90°–270°), (45°–225°), (135°–315°) profile cross sections for the tip

4 The AFM Tip in Its Working Position

4.1 SEM Image Analysis

In this section, we will demonstrate the steps taken from extracting the image to fitting the tip shape to the power-law function. Using a scanning electron microscope, 2D images of the tips of Bruker’s RTESPA probes were obtained.

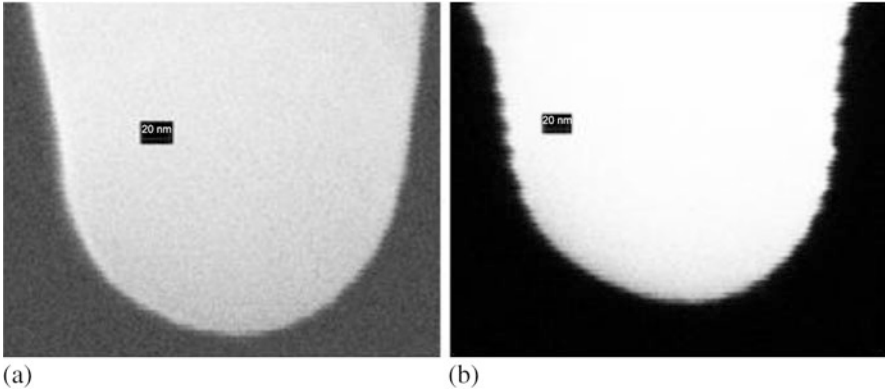


Fig. 11.6 The SEM images of the two probes analysed with 5×10^5 magnification (a) RTESPA-300-125 probe tip (b) RTESPA-150-125 probe tip

Those images were taken with a magnitude of magnification of 5×10^5 . Figure 11.6 shows the raw 2D image extracted from the SEM. As this figure shows, the tip shape is differentiable from the background.

Also, two sets of probes (each set consisting of 5 probes) of model RTESPA-300-125 and RTESPA-150-125 with 125 nm tip radii were analysed. RTESPA-300-125 probes are pre-calibrated with certified stiffness of $k = 40 \text{ N/m}$ where as RTESPA-150-125 are similar but with $k = 6 \text{ N/m}$. Hereafter, probes used will be referred to according to their number in the set and their stiffness (e.g., the fifth probe of the RTESPA-300-125 set will be probe no.5 with $k = 6 \text{ N/m}$). An SEM system by Carl Zeiss of model 1540xB and a dual focused ion beam was used to capture the images were Fig. 11.6a shows the stiffer RTESPA-300-125 probe and in Fig. 11.6b shows the softer RTESPA-150-125. Given that our analysis is based on comparing the tip's geometry to a monomial function, we will convert the image and specifically the tip's surface edge into a curve on a plane so it can be superimposed on the graph mentioned earlier and extract d values by comparison. The RTESPA-300-125 probe will be used to explain the procedure used to extract the bluntness d value.

Firstly, we increase the contrast of the image to the point where a clearly defined line separates the tip and background without any grayscale gradient, as in Fig. 11.7a. A photo processing software was used to edit the raw SEM image Fig. 11.7a resulting in the image obtained in Fig. 11.7b.

An important point to consider when contrasting the image is to make sure that the overall size and shape of the tip does not change, as simply increasing the contrast using any photo editing software can and will increase the size of the tip making it more blunt yielding in inaccurate d values. The point of contrasting the image is to create a well-defined edge that can be detected using a software tool. The software views images as a matrix with each pixel having a different value corresponding to its colour. So, having a defined edge where on one side there are

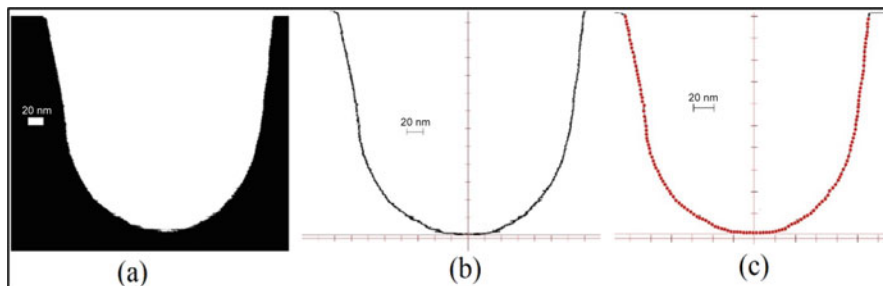


Fig. 11.7 (a) Highly contrasted version of the SEM image (b) Adding the two major axes then the scale onto the added axes (c) Detection of data points

pixels corresponding to white and the other to black with no grey areas makes edge detecting more accurate.

After obtaining a continuous line, the lowest point is now located and is to be assigned a (0,0) value for two axes: horizontal representing the radius and vertical representing the tip's height. From this origin point, two curves will branch out: left-hand side and right-hand side curves. The two mentioned curves will be later for further analysis and to be compared to the power-law function. When the origin point is determined (Fig. 11.7b), horizontal and vertical axes are added to the image where they intersect at the origin point. After that, we clone the dimensions of the image scale (60 pixels \equiv 20 nm or 3 pixels \equiv 1 nm) located on the bottom-left corner to the two axes added as Fig. 11.7b shows. Following that, the two curves are transformed into coordinate points with the right-hand side one having both positive horizontal and vertical values while the left-hand side having positive vertical values but negative horizontal ones. Figure 11.7c shows the detected points. Using this method, the software scans the selected area of interest that is the tip profile and if any noise data ends up being detected those points can be removed manually. The software is programmed in a way that detects black pixels inside the designated area of scanning (excludes the scale). It scans every pixel, detecting black ones and then calculates the distance from the reference origin. Two points on the vertical axis and two on the horizontal are determined manually and from those four points the software automatically interpolates and extrapolates the remaining points. To avoid detecting an excessive amount points, a spacing of 7 pixels between each detected point is imposed on the horizontal axis while 6.5 on the vertical one. After locating the data points on the curve, the software generates a data sheet containing the coordinates of each point detected in a (X, Y) format. As mentioned before, the focus of this study is regarding nanoindentation and nanomachining. So, only the first 30 nm of the tip will be analysed as it is the part is in contact with the machined material.

The method used here consists primarily of the following steps for the right-hand side:

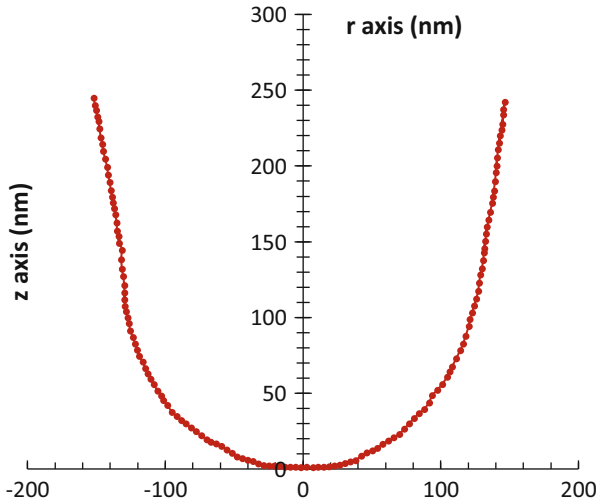


Fig. 11.8 The extracted data points are re-graphed

1. Converting the first 30 nm values into dimensionless values and creating a graph of the resulting values.
2. Creating r vs r^d graphs were $d = 1, 1.5, 2, 2.5$ and 3
3. Superimposing each graph obtained in point 2 on the graph in point.

Meanwhile for the left-hand side:

1. Mirroring the graph to the right-hand side to get positive values on the horizontal axis in addition to the already positive vertical axis.
2. After that, the same three steps are done as in the right-hand side.

Figure 11.8 represents plotting the extracted points as a verification to the work done earlier.

Now we convert the first 30 nm of the tip into dimensionless values (ratios) ranging between 0 and 1 and superimpose them on d values shown in Fig. 11.9a for the left-hand side and Fig. 11.9b for the right-hand side. It should be noted that all tip curve figures from now on will be presented in their respective dimensionless forms.

4.2 Rotating the Tip 12° Clockwise

It is important to remember that the tips operate at 12° clockwise rotated orientation and not vertical as the image shows. So, we apply the rotation matrix to the values obtained earlier.

The rotation matrix for a Clockwise rotation is as in the equation below:

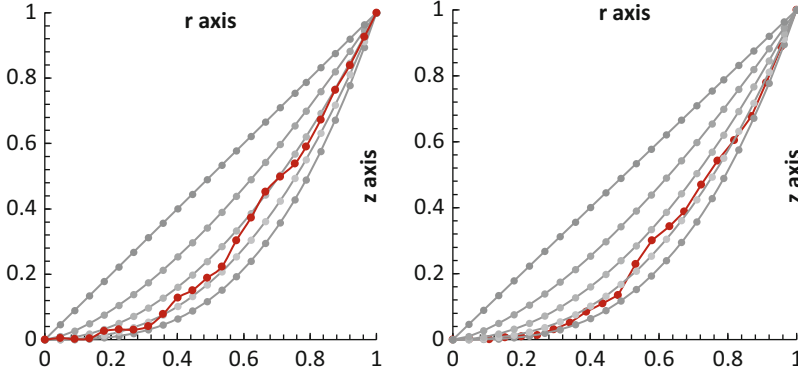


Fig. 11.9 LHS (a) and RHS (b) of actual vertical tip shape (red) over d values 1 to 3 with 0.5 intervals

$$R(-\theta) = \begin{bmatrix} \cos \theta & \sin \theta \\ -\sin \theta & \cos \theta \end{bmatrix}$$

where $\theta = 12^\circ$.

As Fig. 11.10a shows, rotating about the lowest point created a new lowest point. To apply the method, the graph must always be in the positive vertical axis. Hence, we locate the new lowest point and shifting the graph in a way that allows this point to be the new origin or (0, 0), as Fig. 11.10b demonstrates. In addition, the rotation of the tip will expose a different portion of the surface to contact the machined material hence a different value of d are to be expected as Fig. 11.10b highlights.

Figure 11.11 shows the tip in its new orientation both left-hand (a) and right-hand (b) sides compared to different d values.

5 AFM Nanoindentation: Load-Displacement Data

Here, analysis of the load-displacement curves, extracting d values from them and comparing to the results obtained from the SEM images are done. As it has been shown by Galanov (1981b) and Borodich (1989, 1993), if the shape of the tip is described by a power-law function of degree d and the stress-strain relations for a tested sample are described by a power-law functional of degree μ , the non-adhesive problem of indentation is self-similar. This means that if a solution to the contact problem for an indenter of shape f is known for a given load P_1 , then the solution for an indenter of shape cf under the load the load P , may be obtained by re-scaling. Here c is an arbitrary positive constant. Hence, according to Borodich

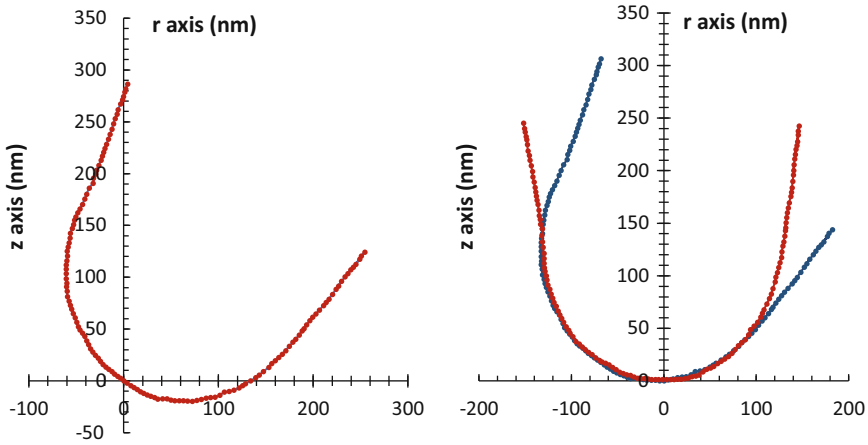


Fig. 11.10 (a) Tip data points after applying the 12° clockwise rotation matrix; (b) Repositioning of the rotated tip shape with a new origin point and no values below zero

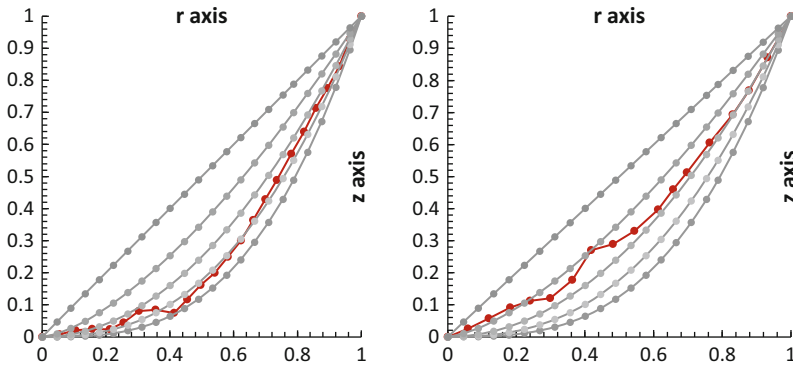


Fig. 11.11 LHS (a) and RHS (b) actual rotated tip shape (red) over d values 1 to 3 with 0.5 intervals

(1993), the indentation depth $h(c, P)$ under loadings P and P_1 may be calculated using the following scaling relation:

$$h(c, P) = c^{(2-\mu)/[2+\mu(d-1)]} (P/P_1)^{d/[2+\mu(d-1)]} h(1, P_1) \quad (11.7)$$

For a pyramid or a cone $d = 1$. In this case, c means the ratio of slopes and for the same indenter $c = 1$. Whereas μ , is also equal to one due to linearity of the material properties. Hence, the load-displacement curve can be used to approximate the tip shape directly using the following relation Borodich et al. (2003):

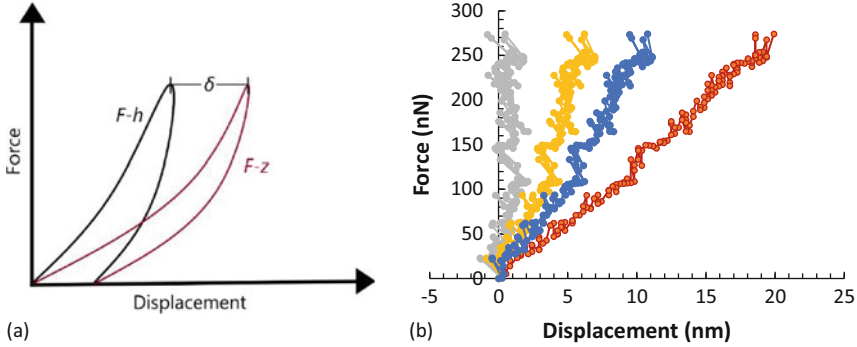


Fig. 11.12 (a) Ideal Force-Displacement curve before and after considering the initial tilt of the AFM probe. (b) Practical unloading curve cases were the calibrated k value of 14.1 N/m produces incorrect curve (Grey) compared to 20 N/m (Yellow) and 30 N/m (Blue) in addition to the original data (Red)

$$d = 1 / (m - 1) \tag{11.8}$$

where d is the tip shape characteristic and m come from the following equation:

$$\text{Log } P \sim \log (h - h_f)^m = m \log (h - h_f) \tag{11.9}$$

where, P is the load, h is the displacement, h_f is the residual displacement, and m is the slope of the unloading part of the load-displacement curve.

The Eq. (11.8) is obtained by comparing a modified version of Eq. (11.1) and Eq. (11.9):

$$\log P = m \log (h - h_f) \tag{11.10}$$

$$\log z = \log B_d (\theta) + d \log r \tag{11.11}$$

Further on, the term $(h - h_f)$ will be referred to as δ in force-displacement curves as in the Fig. 11.12. Where in Fig. 11.12a, the dark red curve is the raw data obtained with an AFM instrument. The black curve shows the required data after removing the cantilever deflection. However, as Fig. 11.12b demonstrates, the process of shifting the data (i.e., using δ) is not a trivial task as any issues with the calibration (sensitivity analysis) will result in an incorrect shift in the data. In the same figure, the red data set is the original curve, and the grey is the one we got after calibrating the probe and finding that k was 14.1 N/m. However, clearly such value is incorrect and a 20 N/m (yellow) or 30 N/m (blue) are more likely to be the correct value for the spring constant of the probe.

5.1 AFM Nanoindentation: Force-Displacement Analysis

The Atomic Force Microscope used in this experiment is the XE-100 model from Park Systems positioned over a TS 150 anti-vibration table from Table Stable dampening vibrations using three individual piezoelectric actuators. Bruker's RTESPA probes were used in this experiment as they are pre-calibrated and have certified spring constant values allowing for more robust experimental outcomes. Multiple trials of the same test and probe were conducted due to the nature of polycarbonate where different indentation locations can produce different indentation behaviour hence the need to deal with average values rather than exact instances as discussed Bouchonville and Nicolas (2019). High bluntness values were not considered because physically they indicate that the contact was completely flat due unattended reasons such as contamination. The fifth and sixth sets of testing, for example, resulted in around 200 load-displacement graphs each (consequently the same number for m and d values) to have better confidence in the results.

The first set of nanoindentations consisted of using probe no.5 with $k = 40 \text{ N/m}$ to indent a polycarbonate (PC) sample. After the first set, probe no.5 with $k = 40 \text{ N/m}$ underwent a series of scratching processes to increase its bluntness and investigate whether it is reflected with a new nanoindentation test which is represented in the second set. Again, tested on a polycarbonate sample. The third and fourth sets of testing involved the use of the softer probe no.5 with $k = 6 \text{ N/m}$ on polycarbonate and copper, respectively. As for the fifth and sixth sets, probe no.4 with $k = 40 \text{ N/m}$ was used on copper and polycarbonate, also respectively. All sets had pre-set values of depth starting from 10 nm up to 100 nm with 10 nm intervals all at different locations within the PC and copper samples. Starting from set four, instead of doing one indentation for each depth, six were done all averaged into one value. Test number 8 (depth of 80 nm) of the second set will be used to present how the data imported from the AFM software is analysed and d value is extracted from it.

Figure 11.13a does not consider the inherent deflection of the probe when mounted in the AFM hence we need to consider $(h - h_f)$ also known as δ all discussed earlier which in turn is considered in Fig. 11.13b. Finally, the log values of both force and displacement are taken and the slope of the new curve is taken which is value m that is used to find bluntness value d .

6 Results and Discussion

6.1 SEM Vertical Orientation

Examining Fig. 11.14, it is clear that the left-hand side (LHS) curves upwards at a further distance from the centre than the right-hand side (RHS) i.e., LHS is blunter. Hence, d values must be higher in the LHS and indeed the LHS as Fig. 11.14 shows

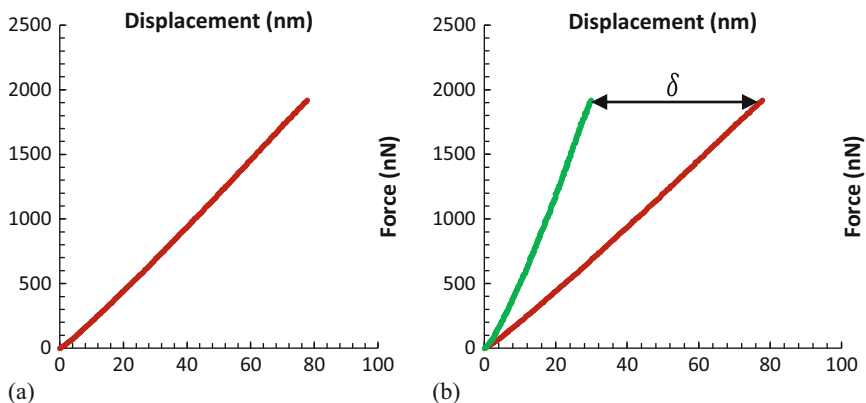


Fig. 11.13 (a) Raw unloading data extracted from AFM software Mirroring and removal of extra unnecessary points Raw unloading data extracted from AFM software (b) taking δ into account (Red line old, Green line new)

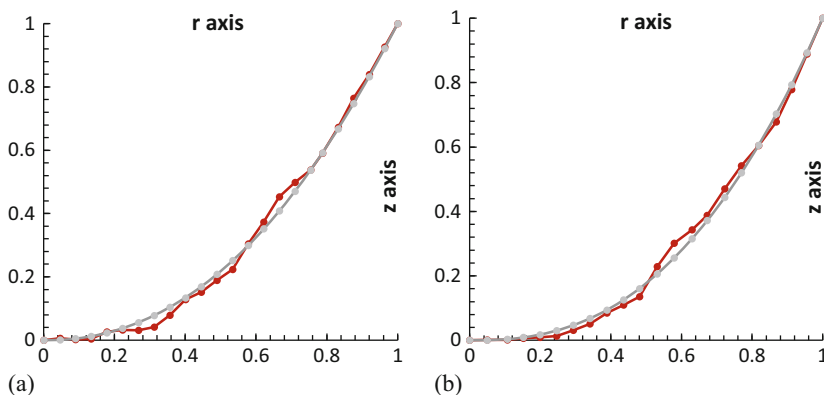


Fig. 11.14 Actual tip shape (Red) and curve fit of power law function (grey) (Dimensionless) for (a) LHS (Vertical) and (b) RHS (Vertical)

almost perfectly follows the $d = 3$ line with a small deviation towards $d = 2.5$ where the RHS varies between $1.5 < d < 2$.

If we want to discuss the changes of d value quantitatively rather than qualitatively and taking the LHS portion for analysis we should expect a value near but less than 3 as discussed earlier. Fig. 11.14a has a best-fit curve over the tip's actual shape. The grey continuous line represents a monomial power law function $z(r) = r^{2.2}$ where $B_d(\theta) = 1$.

As for Fig. 11.14b, it also has a best-fit curve over the tip's actual shape. The grey continuous line represents a monomial power law function $z(r) = r^{2.5}$ where $B_d(\theta) = 1$. Regarding the RTESPA-150-125 probe, the left-hand side had a d value of 1.8 whereas the right-hand side had a 2.1 d value.

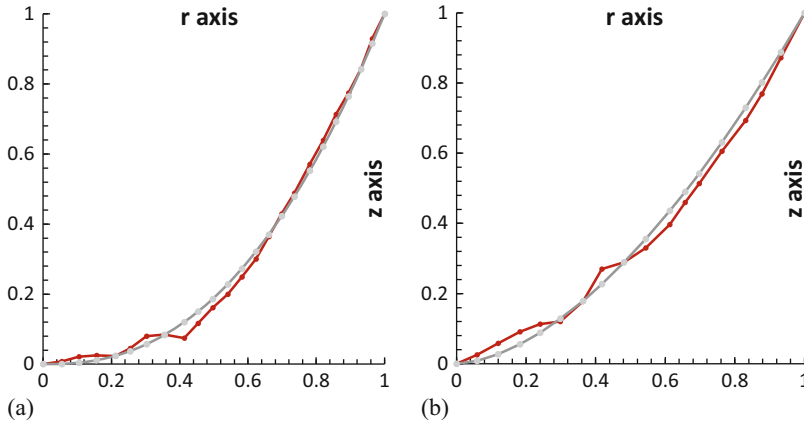


Fig. 11.15 Actual tip shape (Red) and curve fit of power law function (grey) (Dimensionless) for (a) LHS (Tilted) (b) RHS (Tilted)

6.2 SEM 12° Clockwise Rotation

Meanwhile, rotating the tip creates a new lowest point with different d values which contradicts any assumption that suggests that the probe's tip is a circle although some parts have d values close to 2.

Figure 11.15 show the new LHS and RHS tip shapes respectively compared to their best fit curve with monomial power law functions $z(r) = r^{2.4}$ and $z(r) = r^{1.7}$ where $B_d(\theta) = 1$ for both.

Concerning the RTESPA-150-125 probe, the left-hand side had a d value of 2.2 while the right-hand side had a 2.4 d value.

6.3 AFM Nanoindentation

As mentioned earlier, there were six sets of tests. Both m values (slope of log curves) and d values (bluntness values) as well as their averages and standard deviations were recorded. Points of the first half of the unloading curve were considered only due the distortions in the other 50%. The m values were considered due to the inverse relationship between it and d causing m values near unity to be unproportionally high.

Set 1 RTESPA-300-150 probe no. 5 was used in this test with pre-calibrated $k = 40N/m$ and 125 nm tip radius (spherical as stated by the manufacturer). The test sample was polycarbonate. For this set the average m value was 1.41 with 0.14 standard deviation as for the bluntness d value it was 2.73 with 1.07 standard deviation.

Set 2 Same probe as in the first set but blunted by scratching it over a harder material. Here, the average m value was 1.27 with 0.07 standard deviation. As for the d value, the average was 3.79 having 0.74 standard deviation.

Set 3 In this set a $k = 6 \text{ N/m}$ probe was used with all other specifications like the previous stiffer one. Due to its softness, this probe bended heavily and kept twisting due to the electrostatic field of the polycarbonate causing huge distortions in the force-displacement graphs yielding them unusable.

Set 4 The same $k = 6 \text{ N/m}$ probe was utilised but the sample in this case was copper to negate the impact of the electrostatic field. And indeed, it did, the probe behaved as to be expected. However, due to its softness and hardness of the copper sample the results were also unreliable as the slopes extracted were way off which in turn can be explained by the fact that the probe itself was bending and it was not actually penetrating the material. Due to the AFM design, it cannot differentiate between indentation and upward bending as it only detects changes on the reflected laser off the probe and onto the position sensitive photodiode detector (PSPD). The standard deviation in this set was 0.02 which is logical given the crystalline nature of polished copper sample and how it is unlikely for the probe to behave differently at different indentation sites.

Set 5 This set utilised probe number 4 with specifications similar to the one in the first set. The sample was also the crystalline copper one. This set had better average d values than the previous one but given the fact that a large standard deviation in d values indicated that the same issue as above is faced where it is more likely that the probe itself bends instead of real indentation within the copper sample.

Set 6 The same probe used in the fifth set was utilized but this time on a polycarbonate sample making this set a validation one to the first set with a 10 s holding time in this case instead of non as in the first. Here, the average m value was 1.36 with 0.14 standard deviation.

Table below shows average m and d values for all sets mentioned.

Regarding the d values, the average was 2.42 having 3.50 standard deviation.

7 Conclusion

With the increasing need for more accurate AFM probes as measuring tools while not being able to rely on the specification provided by manufacturers, our work presents results of an accurate tip characterisation.

The analysis has been fulfilled for the tip in both vertical and working (12° clockwise orientation) positions. It is highlighted how erroneous it can be to assume that those two orientations are equivalent and interchangeable.

Table 11.1 Average m and d values for test sets

Set no.	m value	d value
1	1.41	2.73
2	1.27	3.79
3	Flat	Flat
4	Flat	Flat
5	Flat	Flat
6	1.36	2.42

Moreover, considering each side of the tip individually plays a bigger role in nanomachining applications where the direction of the machining process does in fact impact the process's outcome (Al-Musawi and Brousseau 2016).

It is suggested to describe the tips as power-law functions, whose exponent d is used as a characteristic of tip bluntness. The novelty of this approach is that it enables representing the tip bluntness with real positive numerical values instead of integers only. For example, if a tip has an d value of around 2.5 whether to approximate it to 2 or 3 will be a difficult task and in either case the error or difference will be quite considerable.

Noting that the data extracted from load-displacement data is 3D representation of the tip shape its value can be considered as a benchmark for the other results.

A plausible explanation of the linear $P - h$ relations (referred to as 'Flat' in Table 11.1) observed in many tests during the experiment may be explained due to the nature of the soft polymer used containing weakly connected macromolecules that may stick to the nose of the indenter creating some sort of a stagnant zone that moves together with the indenter. In fact, the existence of stagnation zone was observed for many materials as in Shaw and Cookson (2005). In the case under consideration, the stagnation zone forms a pseudo-nose of the indenter that penetrates together with the indenter without widening the size of the deformed zone, i.e., it acts similarly to a flat ended cylindrical indenter in the Boussinesq problem. As a result, we observe not a Hertz-type contact problem with continuously increasing contact zone, but a contact region of a constant size, i.e., a Boussinesq-type contact problem for flat-ended cylinder.

References

- Al-Musawi RSJ, Brousseau E (2016) Assessing the applied normal load during contact mode AFM: an issue with the conventional approach. In: International Conference for Students on Applied Engineering (ICSAE), pp 119–122
- Al-Musawi RSJ, Brousseau EB, Geng Y, Borodich FM (2016) Insight into mechanics of AFM tip-based nanomachining: bending of cantilevers and machined grooves. *Nanotechnology* 27:385302
- Alraziqi ZNR (2017) Express analysis of actual bluntness of AFM probe tips. PhD thesis, Cardiff University, Cardiff

- Alraziqi ZNR, Brousseau E, Borodich FM (2016) A new metric to assess the tip condition of AFM probes based on three-dimensional data. In: International Conference for Students on Applied Engineering, ICSAE, pp 24–29
- Bhaskaran H, Gotsmann B, Sebastian A, Drechsler U, Lantz MA, Despont M, Jaroenapibal P, Carpick RW, Chen Y, Sridharan K (2010) Ultralow nanoscale wear through atom-by-atom attrition in silicon-containing diamond-like carbon. *Nat Nanotechnol* 5:181–185
- Binnig G, Quate CF, Gerber C (1986) Atomic force microscope. *Phys Rev Lett* 56:930–933
- Bloo M, Haitjema H, Pril W (1999) Deformation and wear of pyramidal, silicon-nitride AFM tips scanning micrometre-size features in contact mode. *Measurement* 25:203–211
- Borodich FM (1983) Similarity in the problem of contact between elastic bodies. *J Appl Math Mech* 47:440–442
- Borodich FM (1989) Hertz contact problems for an anisotropic physically nonlinear elastic medium. *Strength Mater* 21:1668–1676
- Borodich FM (1990) Hertz contact problems for an elastic anisotropic half-space with initial stresses. *Soviet Appl Mech* 26:126–132
- Borodich FM (1993) The Hertz frictional contact between nonlinear elastic anisotropic bodies (the similarity approach). *Int J Solids Struct* 30:1513–1526
- Borodich FM, Keer LM, Korach CS (2003) Analytical study of fundamental nanoindentation test relations for indenters for non-ideal shapes. *Nanotechnology* 14:803–808
- Borodich FM, Galanov BA (2004) Molecular adhesive contact for indenters of non-ideal shapes. In: ICTAM04, abstracts book and CD-ROM proceedings. IPPT, PAN, Warsaw
- Borodich FM (2011) Contact problems at nano/microscale and depth sensing indentation techniques. *Mater Sci Forum* 662:53–76
- Borodich FM (2014) The Hertz-type and adhesive contact problems for depth-sensing indentation. *Adv Appl Mech* 47:225–366
- Borodich FM, Galanov BA, Suarez-Alvarez MM (2014a) The JKR-type adhesive contact problems for power-law shaped axisymmetric punches. *J Mech Phys Solids* 68:14–32
- Borodich FM, Galanov BA, Keer LM, Suarez-Alvarez MM (2014b) The JKR-type adhesive contact problems for transversely isotropic elastic solids. *Mech Mater* 75:34–44
- Bouchonville N, Nicolas A (2019) Quantification of the elastic properties of soft and sticky materials using AFM. In: Atomic force microscopy. Springer, pp 281–290
- Bykov V, Gologanov A, Shevyakov V (1998) Test structure for SPM tip shape deconvolution. *Appl Phys A Mater Sci Process* 66:499–502
- Carpick RW, Agrait N, Ogletree D, Salmeron M (1996) Measurement of interfacial shear (friction) with an ultrahigh vacuum atomic force microscope. *J Vac Sci Technol B: Microelectron Nanometer Struct Process Meas Phenom* 14:1289–1295
- Chung K-H, Kim D-E (2003) Fundamental investigation of micro wear rate using an atomic force microscope. *Tribol Lett* 15:135–144
- Dongmo L, Villarrubia JS, Jones SN, Renegar TB, Postek MT, Song J-F (2000) Experimental test of blind tip reconstruction for scanning probe microscopy. *Ultramicroscopy* 85:141–153
- Galanov BA (1981a) The approximate solution of certain problems of the elastic contact of two bodies. In: Akademiia Nauk SSSR, *Izvestiia, Mekhanika Tverdogo. Tela*, pp 61–67
- Galanov BA (1981b) Approximate solution of some contact problems with unknown contact area under conditions of power-law hardening of the material. In: Akademiia Nauk Ukrain's' koi RSR, *Dopovidi, Seria A-Fiziko-Matematichni ta Tekhnichni Nauki*, pp 35–40
- Galanov BA (1993). Development of analytical and numerical methods for study of models of materials. Report for the project 7.06.00/001-92, 7.06.00/015-92. Institute for Problems in Materials Science, Kiev. (Ukrainian)
- Galanov BA, Grigoriev ON (1994) Adhesion and wear of diamond. Part I, Modelling. Preprint. Institute Prob. Mat. Sci., Nat. Ac. Sci. Ukraine, Kiev, pp 1–14
- Gotsmann B, Lantz MA (2008) Atomistic wear in a single asperity sliding contact. *Phys Rev Lett* 101:125501
- Grierson DS, Liu J, Carpick RW, Turner KT (2013) Adhesion of nanoscale asperities with power-law profiles. *J Mech Phys Solids* 61:597–610

- Heim L-O, Kappl M, Butt H-J (2004) Tilt of atomic force microscope cantilevers: effect on spring constant and adhesion measurements. *Langmuir* 20:2760–2764
- Hoh JH, Lal R, John SA, Revel J-P, Arnsdorf MF (1991) Atomic force microscopy and dissection of gap junctions. *Science* 253:1405–1408
- Hutter JL (2005) Comment on tilt of atomic force microscope cantilevers: effect on spring constant and adhesion measurements. *Langmuir* 21:2630–2632
- Jacobs TD, Wabiszewski GE, Goodman AJ, Carpick RW (2016) Characterizing nanoscale scanning probes using electron microscopy: a novel fixture and a practical guide. *Rev Sci Instrum* 87:013703
- Kalinin SV, Bonnell DA (2002) Imaging mechanism of piezoresponse force microscopy of ferroelectric surfaces. *Phys Rev B* 65:125408
- Khurshudov A, Kato K (1995) Wear of the atomic force microscope tip under light load, studied by atomic force microscopy. *Ultramicroscopy* 60:11–16
- Khurshudov A, Kato K (1997) Wear mechanisms in reciprocal scratching of polycarbonate, studied by atomic force microscopy. *Wear* 205:1–10
- Khurshudov AG, Kato K, Koide H (1997) Wear of the AFM diamond tip sliding against silicon. *Wear* 203:22–27
- Kindrachuk VM, Galanov BA, Kartuzov VV, Dub SN (2006) On elastic nanoindentation of coated half-spaces by point indenters of non-ideal shapes. *Nanotechnology* 17:1104
- Lantz M, O’Shea S, Welland M (1998) Characterization of tips for conducting atomic force microscopy in ultrahigh vacuum. *Rev Sci Instrum* 69:1757–1764
- Ramirez-Aguilar KA, Rowlen KL (1998) Tip characterization from AFM images of nanometric spherical particles. *Langmuir* 14:2562–2566
- Sedin DL, Rowlen KL (2001) Influence of tip size on AFM roughness measurements. *Appl Surf Sci* 182:40–48
- Shaw MC, Cookson J (2005) *Metal cutting principles*. Oxford University Press, New York
- Tseng AA, Notargiacomo A, Chen T (2005) Nanofabrication by scanning probe microscope lithography: a review. *J Vac Sci Technol B: Microelectron Nanometer Struct Process Meas Phenom* 23:877–894
- Villarrubia JS (1994) Morphological estimation of tip geometry for scanned probe microscopy. *Surf Sci* 321:287–300
- Yan Y, Xue B, Hu Z, Zhao X (2016) AFM tip characterization by using FFT filtered images of step structures. *Ultramicroscopy* 160:155–162
- Yao N, Wang ZL (2005) *Handbook of microscopy for nanotechnology*. Springer
- Zheng Z, Yu J (2007) Using the Dugdale approximation to match a specific interaction in the adhesive contact of elastic objects. *J Colloid Interface Sci* 310:27–34

Chapter 12

The JKR Formalism in Applications to Problems of Adhesive Contact



Feodor M. Borodich

Abstract The JKR (Johnson-Kendall-Roberts) problem of adhesive contact between elastic spheres is an example of a mathematically beautiful theory that has many practical applications. However, it would be erroneous to reduce the JKR theory to just the problem of adhesive contact between spheres. Indeed, simultaneously with the presentation of the JKR theory, Kendall (J Phys D Appl Phys 4:1186–1195, 1971) applied the equilibrium theory of adhesion to bodies of other geometries and coatings. It gives a review of applications of the JKR formalism to axisymmetric indenters of various shapes, various elastic materials, different conditions of contact, and elastic structures. These structures include thin and thick elastic layers and atomically thin stretched membranes. The JKR formalism means that an adhesive contact problem may be solved by combining two ideas: (1) the Derjaguin balance energy approach (Derjaguin, Kolloid Z 69:155–164, 1934) and (2) superposition of solutions to two non-adhesive contact problems (the Hertz-type and the Boussinesq-type problems). The JKR formalism may be used if the distance between the free surface of the material and the indenter surface increases rapidly at the periphery of the contact region and the solutions of two contact problems having the same contact area may be superimposed on each other. It is shown that the JKR formalism may be reinforced if one employs the properties of slopes of the force-displacement diagrams of non-adhesive indentation. For the first time, such reinforcements were demonstrated explicitly by the author (Borodich, Adv Appl Mech 47:225–366, 2014). It is argued that the JKR formalism may be applied to an enormous number of adhesive contact problems for various elastic structures.

Keywords Adhesion · JKR theory · Elastic structures · Graphene membrane · Adhesive layers

F. M. Borodich (✉)
School of Engineering, Cardiff University, Cardiff, UK
e-mail: [BorodichFM@cardiff.ac.uk](mailto:borodichfm@cardiff.ac.uk)

© Springer Nature Switzerland AG 2022
F. M. Borodich, X. Jin (eds.), *Contact Problems for Soft, Biological and Bioinspired Materials*, Biologically-Inspired Systems 15,
https://doi.org/10.1007/978-3-030-85175-0_12

243

1 Introduction

Mechanics of adhesive contact is an important part of nanomechanics. It is known that surface effects become increasingly significant as the size of solids decreases. Indeed, surface forces are normally proportional to the surface area, while the surface area of a particle or an asperity of rough surface is proportional to L^2 , where L is a characteristic size of the object. On the other hand, volumetric forces of an object such as weight and the forces of inertia are proportional to the mass of the object, that in turn is proportional to its volume. The same is related to the amount of elastic energy stored in a deformed solid or in an asperity, these quantities are proportional to the volume of an object, i.e. to L^3 . Hence, the ratio of surface forces to volumetric forces of an object is proportional to $1/L$ and it goes to infinity as L goes to zero. One of the main adhesive effects is caused by van der Waals forces that have a considerable influence only when distances between solids are within the nanometere scale (see a discussion by Borodich et al. 2022). Thus, molecular adhesion becomes increasingly significant as the size of contacting objects or the distances between their surfaces decrease to nano-scales.

Adhesion of surfaces plays a key role in the development of modern micro and nanotechnology and its importance increases if objects are soft. Indeed, soft probes are more prone to sticking than the hard ones because (1) the amount of elastic energy stored in a deformed solid decreases if the material is soft, and (2) the former materials may create a large true contact area with a counter-surface due to their compliance. Moreover, soft materials can even have full adhesive contact with slightly rough surfaces and in this case, the true contact area is greater than the area with a smooth surface. However, if the surface roughness is high, then even soft probes do not have full contact because they contact just with the tops of the asperities of the counter-surface and this causes a decrease of the adhesive forces (Purtov et al. 2013; Pepelyshev et al. 2018). The JKR (Johnson, Kendall, and Roberts) theory of adhesive contact (Johnson et al. 1971) and the JKR formalism are very important for studying contact problems between soft materials, including biological and bioinspired ones.

Although the JKR formalism was used by Johnson et al. (1971), the concept was not formulated explicitly. However, this concept was almost explicitly formulated by Kendall (2001) in his historical comment on the development of the JKR theory. The JKR formalism means that an adhesive contact problem may be solved by combining two ideas: (1) superposition of a Hertz-type non-adhesive contact problem and a Boussinesq-type problem for a flat-ended cylindrical punch (the idea may be traced back to Johnson 1958), and (2) the Derjaguin balance energy approach (Derjaguin 1934). Initially, the formalism was used for solving the problem of adhesive contact between two elastic spheres (Johnson et al. 1971). The JKR theory has been widely used as a basis for modelling of various phenomena, including biological phenomena such as adhesion of cells, viruses, attachment devices of insects and so on (Scherge and Gorb 2001; Kendall et al. 2011; Borodich et al. 2021).

Contact mechanics is a very popular research field. There are many very good books that discuss only mechanics of non-adhesive contact, e.g. books by Shtaerman (1949), Galin (1953) and Argatov and Dmitriev (2003); mechanics of adhesive contact is discussed very briefly in the classic book by Johnson (1985); and there are also excellent books where various aspects of adhesive contact problems are discussed in detail (Derjaguin et al. 1985; Sviridenok et al. 1990; Maugis 2000; Kendall 2001; Popov 2010; Argatov and Mishuris 2018). Starting with the classic review by Derjaguin et al. (1958), there are many reviews dedicated to problems related to contact problems and adhesive interactions between solids (see, e.g. Krupp 1967; Adams and Nosonovsky 2000; Shull 2002). I have also discussed these questions in several reviews (Borodich 2008, 2011, 2014). However these reviews do not include results obtained during the last few years. For the sake of completeness, I review here not only the recent results, but also the history of development of the JKR contact theory. In addition, the main assumptions of the problem formulations and the restrictions caused by the formulations are discussed. It is shown that using the JKR formalism, one can solve problems of adhesive contact for other materials, e.g. transversely isotropic materials, and objects, e.g. elastic thin films or thick coatings rested on a support, or monomolecular thick stretched membranes. It is argued that the JKR formalism may be reinforced if we employ the properties of slopes of the force-displacement diagrams of non-adhesive indentation of elastic materials.

2 The Hertz-Type and Boussinesq Non-adhesive Contact Problems

To explain the specific details of contact problems under consideration, I will need to present the formulations of the Hertz-type and Boussinesq contact problems. I will use both the Cartesian coordinate frame $x_1 = x$, $x_2 = y$, $x_3 = z$ and the cylindrical one ρ , ϕ , z , where $\rho = \sqrt{x^2 + y^2}$ and $x = \rho \cos \phi$, $y = \rho \sin \phi$.

2.1 Formulation of an Axisymmetric Hertz-Type Contact Problem for Linear or Linearized Elastic Solids

Hertz (1882) described the general shape of a smooth convex three-dimensional (3D) body as an elliptic paraboloid. This approximation follows from the truncated decomposition of $f(x_1, x_2)$ into Taylor series, when $f(0, 0) = 0$ due to the assumption that the indenter is convex (hence, initially it has only one point of contact), $\partial f/\partial x = \partial f/\partial y = 0$ due to the assumption that the function has an extremum at $(0, 0)$, and the derivatives of order higher than two are neglected.

For an axisymmetric smooth and convex indenter, the Hertz approximation is

$$f(r) = B_2 r^2, \quad B_2 = 1/(2R) \quad (12.1)$$

where R is the radius of curvature of f at the coordinate origin. The Hertz shape approximation for a sphere of radius R , is also (12.1). In the case of contact between two elastic spheres of radii R_1 and R_2 respectively, one takes R as the effective radius of the spheres ($1/R = 1/R_1 + 1/R_2$).

It is assumed in Hertz 3D problem that the characteristic size l of the contact region is small in comparison with the radii of curvature of the contacting solids and, therefore, the contacting solids may be considered as elastic half-spaces and one can formulate the boundary value problem on the border of the half-spaces. It is known from contact mechanics that the Hertz and Boussinesq problems of contact between a rigid indenter (a punch) and an isotropic linear elastic half-space having the Young's modulus E and the Poisson ratio ν depend on a contact modulus (reduced modulus) of the half-space E^*

$$E^* = \frac{E}{1 - \nu^2}. \quad (12.2)$$

In turn, the problem of contact between two elastic bodies having contact moduli E_1^* and E_2^* respectively, is mathematically equivalent to the problem of contact between an isotropic elastic half-space with contact modulus E_l^*

$$\frac{1}{E_l^*} = \frac{1}{E_1^*} + \frac{1}{E_2^*} \quad (12.3)$$

and a curved body whose shape function f is equal to the initial distance between the surfaces, i.e. $f = f_1 + f_2$, where f_1 and f_2 are the shape functions of the solids.

For the sake of simplicity, I will consider the formulation of the problem of contact between a rigid indenter and an elastic sample because this problem is mathematically equivalent to the Hertz-type problem of contact between two elastic solids (see, e.g. Borodich 2014).

It is assumed in the Hertz-type contact problem that there is no adhesion between solids and an indenter (probe) is vertically pressed into a flat surface by a force P . The compressive forces are considered as positive. The shape of the indenter (probe) $f(x_1, x_2)$ is given. Because the problem is quasi-static, one needs to know the current value of the external parameter \mathcal{P} that characterizes the problem. If the pressing force P is taken as the external parameter, then one has to find the depth of indentation δ (the relative approach of the bodies $\delta > 0$) and the bounded contact region G having unknown characteristic size l . If δ is taken as \mathcal{P} then one has to find P and l . In the case of a circular contact region, e.g. an axisymmetric indenter contacts an isotropic elastic material, one can take the radius of the region a as the characteristic size l .

The contact region G is defined as a region consisting of points where the indenter and the medium are in mutual contact. The region G is located on the boundary plane $x_3 = 0$ that is denoted as \mathbb{R}^2 . The indentation of a material sample causes the displacements u_i and stresses σ_{ij} within the sample.

Initially, the sample is modelled as the positive half-space $x_3 \geq 0$ (later other models will be considered). Then the sought quantities must satisfy the following equations, where and henceforth, a comma before the subscript denotes the derivative with respect to the corresponding coordinate; and summation is assumed over repeated Latin subscripts that take values from 1 to 3:

1. equations of equilibrium

$$\sigma_{ij,j} = 0, \quad i, j = 1, 2, 3; \quad (12.4)$$

2. constitutive relations defined by a linear or linearized functional \mathcal{L} that connects stresses σ_{ij} and strains ϵ_{ij} in the material

$$\sigma_{ij} = \mathcal{L}(\epsilon_{ij}), \quad \epsilon_{ij} = (u_{i,j} + u_{j,i})/2; \quad (12.5)$$

3. conditions at infinity

$$\mathbf{u}(\mathbf{x}, \mathcal{P}) \rightarrow 0, \quad |\mathbf{x}| \rightarrow \infty; \quad (12.6)$$

4. integral condition

$$\int_{\mathbb{R}^2} \sigma_{33}(x_1, x_2, 0, \mathcal{P}) dx_1 dx_2 = -P; \quad (12.7)$$

5. three boundary conditions at the boundary points within and out of the contact region $G(\mathcal{P})$.

In the general case, the contact region G is defined as an open region such that if $(x_1, x_2, 0) \in G$ then the gap $(u_3 - g)$ between the punch and the half-space is equal to zero and surface stresses are non-positive, while outside the contact region, i.e. for $(x_1, x_2, 0) \in \mathbb{R}^2 \setminus G$, the gap is positive and the stresses are equal to zero. These boundary conditions can be written as

$$u_3(x_1, x_2, 0; \mathcal{P}) = g(x_1, x_2; \mathcal{P}), \quad \sigma_{33}(x_1, x_2, 0; \mathcal{P}) \leq 0, \quad (12.8)$$

for $(x_1, x_2, 0) \in G(\mathcal{P})$, where for the general case of the problem of vertical pressing, we have

$$g(x_1, x_2; \mathcal{P}) = \delta(\mathcal{P}) - f(x_1, x_2). \quad (12.9)$$

For $(x_1, x_2, 0) \in \mathbb{R}^2 \setminus G(\mathcal{P})$, the conditions are

$$u_3(x_1, x_2, 0; \mathcal{P}) > g(x_1, x_2; \mathcal{P}), \quad \sigma_{3i}(x_1, x_2, 0; \mathcal{P}) = 0. \quad (12.10)$$

So far, we have formulated only one condition (12.8) within the contact region. The choice of two other conditions depends on the friction within the contact region. If one considers the frictionless problem, then the following two conditions hold

$$\sigma_{31}(x_1, x_2, 0; \mathcal{P}) = \sigma_{32}(x_1, x_2, 0; \mathcal{P}) = 0, \quad (x_1, x_2, 0) \in G(\mathcal{P}) \subset \mathbb{R}^2. \quad (12.11)$$

The frictional conditions within the contact region may be formulated following the idea presented by Galin (1945) who considered the formulation of contact problems when there is friction between the surfaces of bodies. In the frictional contact problem, it is usually assumed (see Bryant and Keer 1982) that the contact region consists of the inner part G_1 , where the interfacial friction must be sufficient to prevent any slip taking place between bodies, and the outer part $G \setminus G_1$, where the friction must satisfy the Amontons-Kotelnikov law of friction. The limiting case of contact with friction is the problem where $G_1 = G$. For the axisymmetric problem of contact, it can be written as the radial displacements u_r are equal to zero at any point of the contact region after it comes into contact with the indenter (the no-slip condition)

$$\frac{\partial u_r}{\partial \mathcal{P}}(r, 0, \mathcal{P}) = 0. \quad (12.12)$$

Thus, the above formulation of the boundary value problem is geometrically linear, this means that all boundary conditions are formulated at the plane $x_3 = 0$. Another specific feature of the Hertz-type contact problem is that the tangential displacements in the formulation of the boundary value problem are neglected and only the vertical displacements are taken into account.

In the case of a spherical indenter (12.1), it follows from the original results by Hertz (1882), the following relations among P , δ and a

$$a = \left(\frac{3R}{4E^*} \right)^{1/3} P^{1/3}, \quad \delta = \frac{a^2}{R} = \left(\frac{9}{16R(E^*)^2} \right)^{1/3} P^{2/3}. \quad (12.13)$$

2.2 The Boussinesq Problems

I would like to explain the terminology related to Boussinesq problems. Let a concentrated force P be applied normally to the surface of the half-space at the point 0, i.e. it is directed along the z -axis. If the material is linear elastic then this is the Boussinesq problem for a concentrated load acting on an elastic half-space. The

classic Boussinesq problem for a flat-ended circular punch has a similar formulation of the contact problem as the Hertz-type contact problem. It can be considered in both frictionless and no-slip formulations of the contact problem. The Boussinesq problem in the latter formulation is referred to as the Boussinesq-Mossakovskii problem. The Boussinesq-Kendall model describes adhesive frictionless contact between a flat-ended axisymmetric punch and an elastic half-space (Kendall 1971). Because the shapes of contacting axisymmetric solids may be more general than spherical or flat ones, the Hertz-type contact problems for convex indenters having arbitrary shapes are sometimes referred to as the Boussinesq problems. In the case of a flat-ended axisymmetric punch of radius a and an elastic half-space, it follows from the results by Boussinesq (1885) the following relations among P and δ

$$P = 2E^*a\delta. \quad (12.14)$$

2.3 Incompatibility of the Hertz-Type and Boussinesq Contact Problem Formulations

It is known (see, e.g. Rvachev and Protsenko 1977 or Borodich 2014) that the above formulation of the contact problems leads to incompatibility of displacement fields. There are two types of incompatibility of the Hertzian contact problems: (1) penetration of the upper material layer into the lower one due to geometrically linear formulation of the problem; (2) penetration of the material into the punch due to neglecting of the tangential displacements in the formulation of the Hertz-type contact problems.

3 The Derjaguin, Sperling, and JKR Models

Effects of molecular adhesion are ignored in the Hertz-type contact problems. Therefore, it is assumed that the fields of displacements and stresses appear in the solids only after the external load is applied. However, molecular adhesion is a very important phenomenon at nanometere scale and the solids can interact with each other even if the external load is not applied (see a discussion by Borodich 2014).

3.1 *Initial Derjaguin's Model of Adhesion*

Derjaguin suggested the following approximation (the Derjaguin approximation) for calculation of adhesive interactions between solids, see page 156 by Derjaguin (1934):

1. the volume molecular attractions are reduced to surface interactions;
2. the surface interactions are taken into account only between closest elements of the surfaces laying on vertical straight lines connecting the solids; and
3. the interaction energy per unit area between small elements of curved surfaces is the same as this energy between two parallel infinite planar surfaces.

The Derjaguin approximation is explicitly or implicitly involved in many modern models of adhesive contact. In addition, he argues that the virtual work done by the external load is equal to the sum of the virtual change of the potential elastic energy and the virtual work that will be consumed by the increase of the surface attractions, see formula (21) by Derjaguin (1934).

Derjaguin tried also to calculate the force of attraction between elastic spheres and between two 3D solids in Hertzian approximation of their shapes. Unfortunately, some of Derjaguin's assumptions and calculations were not correct. For example, Derjaguin's assumption about the shape of deformed solids. Nevertheless, his basic energy *argument was correct because it equated the work done by the surface attractions against the work of deformation in the elastic spheres* (see Kendall 2001, p. 183).

3.2 *The Sperling Model*

In 1964 G. Sperling presented his PhD thesis devoted mainly to the development of a model of adhesion between rough particles. In an appendix of this thesis, using Derjaguin's energy arguments, Sperling (1964) presented a model of contact between a rigid sphere and an elastic half-space. He wrote that the total energy U is represented as a sum of three parts: $U = U_1 + U_2 + U_3$, where U_1 is the energy stored in the half-space due to elastic deformations, U_2 is the surface energy of the contact region $U_2 = -\pi a^2 w$, and $U_3 = C - P_{ext} \cdot \delta$ is the potential energy due to approach of a body under action of an external force and the body can have small displacement in the direction of the force.

Employing a quite sophisticated solution obtained by Jung (1950) for contact between elastic spheres, Sperling (1964) wrote the following expression for the total potential energy U of the contact system

$$U = \frac{2\mu}{15R^2} \frac{m}{m-1} \left[3a^5 + 10R\delta a^3 + 15R^2\delta^2 a \right] - \pi a^2 w - P_{ext}\delta + C \quad (12.15)$$

where $m = 1/\nu$, μ is shear modulus of the material, w is the work of adhesion and C is an arbitrary constant. The work of adhesion is equal to the energy per unit area needed to separate two dissimilar surfaces from contact to infinity. In other words, w is equal to the tensile force integrated through the distance necessary to pull the two surfaces completely apart (Harkins 1919).

Then Sperling argued that the system is at equilibrium where the energy has its minimum. Hence, the derivative of the energy at its minimum has to be equated to zero. By differentiating (12.15), he derived the following two expressions (see equations (88) and (89) in Sperling 1964)

$$\delta = \alpha\sqrt{a} - \frac{a^2}{R}, \quad \alpha = \sqrt{\frac{\pi w}{\mu} \frac{m-1}{m}}, \quad (12.16)$$

and

$$\delta = \beta \frac{1}{a} - \frac{a^2}{3R}, \quad \beta = \frac{P}{4\mu} \frac{m-1}{m}. \quad (12.17)$$

Then the expressions (12.16), (12.17) and the corresponding dimensionless load-displacement curve were analysed. In particular, it was found that the separation force F_{sep} (see (93) in Sperling 1964) is

$$F_{sep} = \frac{3}{2}\pi R w \quad (12.18)$$

and at $P = 0$ the corresponding contact radius a_0 and displacement δ_0 are

$$a_0 = (2R^2 M)^{1/3}, \quad \delta_0 = -(4RM^2/27)^{1/3}, \quad M = \frac{9\pi w}{8\mu} \frac{m-1}{m}. \quad (12.19)$$

Using proper sign convention and $1/\nu$ instead of m (see Borodich 2014), one could present (12.17) and (12.16) as the following relation between the external load P acting on the spheres, the approach of the indenter δ and the adhesive contact radius a

$$P = (4E^*/3R)a^3 - \sqrt{8\pi w E^*} a^3 \quad (12.20)$$

and

$$\delta = a^2/R - \sqrt{2\pi w (E^*)^{-1}} a. \quad (12.21)$$

It is interesting to note that neither the papers by Krupp and Sperling (1965, 1966) where some Derjaguin ideas were developed and some parts of Sperling's PhD thesis were discussed, nor the review paper by Krupp (1967) mentioned the

above theory given as an appendix to the thesis. In addition, as it was noted by Kendall (2001), Sperling had found no experimental evidence to support his theory.

3.3 *The JKRS Model*

Johnson (1958) made an attempt to solve the adhesive contact problem for spheres by adding two simple stress distributions, namely the Hertz stress field to a rigid flat-ended punch tensile stress distribution. Johnson argued that the infinite tension at the periphery of the contact would ensure that the spheres would peel apart when the compressive load was removed. Although Johnson's conclusion about impossibility of adhesive contact was not correct, his suggestion to superpose the stress fields is very fruitful.

According to Kendall (2001, pp. 185–186), the JKR theory historically was developed in the following steps. In 1970 Kendall and Roberts discussed the experimental observations of the contact spots that were larger than expected from the Hertz equation. They found *that the answer lay in applying Derjaguin's method . . . to Johnson's stress distribution*. Johnson presented a mathematical realization of this idea *an evening later*. As Johnson (2003) wrote "It is ironic to note that the stress distribution which was used in 1958 to prove that elastic spheres could not adhere was used in 1971 . . . to show that they could!". Thus, Johnson et al. (1971) applied Derjaguin's idea to equate *the work done by the surface attractions against the work of deformation in the elastic spheres*, to Johnson's stress superposition, and created the famous JKR theory of adhesive contact.

In fact, the above words by Kendall (2001) may be used as a formulation of the JKR formalism.

It is important to repeat that the JKR formalism is based on the use of a geometrically linear formulation of the contact problem, and a combination of both the Hertz contact problem for two elastic spheres and the Boussinesq relation for a flat ended cylindrical indenter.

If there were no surface forces of attraction, the radius of the contact area under a punch subjected to a given external load P_0 would be a_0 and it could be found by solving the Hertz-type contact problem. However, in the presence of forces of molecular adhesion, the equilibrium contact radius a_1 would be greater than a_0 under the same force P_0 .

Independently from Sperling, Johnson et al. (1971) suggested to consider the total energy of the contact system U_T as made up of the following terms

$$U_T = (U_E)_1 - (U_E)_2 + U_M + U_S \quad (12.22)$$

the stored elastic energy U_E , the mechanical energy in the applied load U_M and the surface energy U_S . Here $U_E = (U_E)_1 - (U_E)_2$ is the difference between the stored elastic energies $(U_E)_1$ and $(U_E)_2$ on loading and unloading branches respectively.

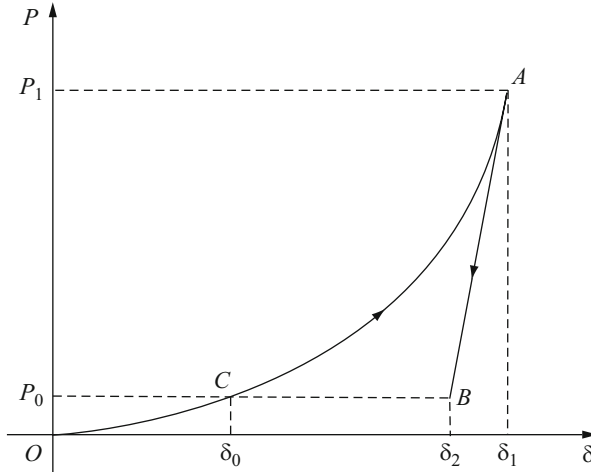


Fig. 12.1 Loading diagram explaining the JKR model of adhesive contact. At branch OA the loading curve $P - \delta$ follows the Hertz $P \sim \delta^{3/2}$ contact relation for a sphere or $P \sim \delta^{(m+1)/m}$ for a monomial punch of degree m , while the relation at the branch AB is linear according to Boussinesq solution

The crucial step of the JKR theory is the JKR formalism, i.e. the interpretation of how the contact system has come to its real state, namely it states that there are two steps: (1) first it has got the real contact radius a_1 and an apparent depth of indentation δ_1 under some load P_1 according to (12.13), then (2) it is unloaded from P_1 to a real value of the external load P_0 according to (12.14), i.e. keeping the contact radius a_1 constant (Fig. 12.1).

The equations derived by Johnson et al. (1971) were exactly the same as (12.20) and (12.21) derived by Sperling (1964). This is the reason that both the JKR and JKRS notations are used to describe the theory of adhesive contact between elastic spheres (see, e.g., Johnson and Pollock 1994).

Comment The original paper by Johnson et al. (1971) used the notations as shown in Fig. 12.1. In 2014 I used the same notations (see, e.g. Borodich 2014). However, critics said that these notations are confusing. Hence, I use for the real values of adhesive contact the following notations $P \equiv P_0$, $a \equiv a_1$ and $\delta \equiv \delta_2$. In addition, the load P_1 and the displacement δ_1 obtained by the use of non-adhesive Hertz-type contact problem will be denoted by P_H and δ_H , respectively.

4 The JKR Formalism

Now I will describe the JKR formalism in various applications. First, I discuss calculations of the original JKRS problem for a spherical indenter and an elastic half-space from the point of view of the JKR formalism. Then, I discuss the

adhesive contact for monomial (power-law) shaped bodies with frictionless and no-slip boundary conditions. Further, I consider the arbitrary shaped blunt axisymmetric solids. Next, the above results are extended to transversely isotropic linear elastic solids and homogeneously prestressed non-linear elastic solids whose stress field is disturbed by indentation. All problems that I have just mentioned used approximation of contacting solids as elastic half-spaces. Therefore, I consider next the adhesive contact problems for elastic layers (thin and thick) covering rigid foundation. I consider also adhesive contact problems for stretched membranes having monomolecular thickness, e.g. a graphene drum. Finally, I discuss the recent results related to general extensions of the JKR formalism.

4.1 *The JKR Formalism in Application to Frictionless Contact for Spherical Indenters*

Johnson et al. (1971) suggested to calculate U_E as the difference between the stored elastic energy $(U_E)_1$ and accumulated by Hertz model on loading branch of the $P - \delta$ curve and the stored elastic energy $(U_E)_2$ spent by Boussinesq model on unloading branch. Therefore, one can calculate

$$(U_E)_1 = P_H \delta_H - \int_0^{P_H} \delta(P) dP. \quad (12.23)$$

Using the Boussinesq solution (12.14), we obtain for the unloading branch

$$(U_E)_2 = \int_P^{P_H} \frac{P}{2E^* a_1} dP = \frac{P_H^2 - P^2}{4E^* a_1}. \quad (12.24)$$

Thus, the stored elastic energy U_E is

$$U_E = (U_E)_1 - (U_E)_2. \quad (12.25)$$

The mechanical energy in the applied load

$$U_M = -P\delta = -P(\delta_H - \Delta\delta) \quad (12.26)$$

where $\Delta\delta = \delta_H - \delta$ is the change in the depth of penetration due to unloading. It can be found from the solution of the corresponding Boussinesq problem.

Since only the surface adhesive interactions within the contact region are taken into account (one neglects the adhesive forces acting outside the contact region), the surface energy can be written as

$$U_S = -w\pi a^2. \quad (12.27)$$

As it was argued by Tabor (1977) the JKR theory may be used if the distance between the free surface of the material and the indenter surface increases rapidly at the periphery of the contact region and the solutions of two contact problems having the same contact area may be superimposed on each other. Tabor introduced a dimensionless parameter that indicated when the JKR theory may be used and when the Derjaguin-Muller-Toporov (DMT) model should be employed. The DMT (Derjaguin et al. 1975) is an alternative theory of adhesive contact between spheres (see a discussion by Maugis 1992, 2000).

The total energy U_T can be obtained by (12.22) and the equilibrium at contact satisfies the equation

$$\frac{dU_T}{da} = 0, \quad \text{or} \quad \frac{dU_T}{dP_H} = 0. \quad (12.28)$$

Employing (12.13) and (12.14), Johnson et al. (1971) were able to write explicit expressions for U_T and the derivative (12.28). This enabled them to derive (12.20) and (12.21). These results were supported by experimental results for two rubber spheres.

4.2 *The JKR Formalism in Application to Frictionless Contact for Power-Law Shaped Indenters*

The above mentioned axisymmetric problems were developed for spherical indenters (or contact between two spheres). However, the shapes of indenters may often be described by more general functions.

Let the distances between the contacting solids be described as axisymmetric monomial functions of arbitrary degree $m \geq 1$

$$f(r) = B_d r^m, \quad (12.29)$$

where $m \geq 1$ is the degree of the monomial function and B_m is the constant of the shape.

According to the JKR formalism, we need to know a solution to a Hertz-type non-adhesive contact problem for the indenter. It is clear that the solution by Hertz (1882) cannot be used for $m \neq 2$. However, if the degree m is an even integer number, i.e. $m = 2n$ where $n = 1, 2, \dots$, then one can use the results presented by Shtaerman (1939)

$$P = 4n B_m E^* a^{2n+1} \frac{2 \cdot 4 \dots 2n}{1 \cdot 3 \dots 2n+1} = 4n B_m E^* a^{2n+1} \frac{(2n)!!}{(2n+1)!!} \quad (12.30)$$

and

$$\delta = B_m a^{2n} \frac{2 \cdot 4 \dots 2n}{1 \cdot 3 \dots 2n - 1}. \quad (12.31)$$

One can find these results in the classic book by Johnson (1985) (see Eqs. 5.20 and 5.22 in the book).

If $m = 1$, then the solution was presented by Love (1939). He used the same linearized formulation of the boundary-value problem as Hertz (1882). Using this formulation, he studied an indentation problem for a rigid blunt cone with semi-apex angle $\pi/2 - \alpha$. The cone is blunt; this means that $\tan \alpha = B_1 \approx \alpha$. In the linearized formulation, all boundary conditions are formulated for the $z = 0$ plane. In particular, the vertical displacements within the contact region are $u_3(r) = \delta - r \cot \alpha$. Love (1939) obtained the following solution

$$P = \frac{\pi}{2} E^* B_1 a^2 \cot \alpha, \quad \delta = \frac{\pi}{2} B_1 a. \quad (12.32)$$

Considering axi-symmetric frictionless Hertz-type contact problems for an elastic isotropic half-space and employing Kochin's harmonic function (Kochin 1940), Galin (1946) obtained expressions for the contacting force P , the depth of penetration δ and the pressure distribution under a convex, smooth in $\mathbb{R}^2 \setminus \{0\}$ punch of arbitrary shape $x_3 = -f(\rho)$, $f(0) = 0$. As an example, he gave explicit formulae for axisymmetric indenter whose shape is given by a monomial function of arbitrary degree m

$$P = E^* B_m \frac{m^2}{m+1} 2^{m-1} \frac{[\Gamma(m/2)]^2}{\Gamma(m)} a^{m+1}, \quad \delta = B_m m 2^{m-2} \frac{[\Gamma(m/2)]^2}{\Gamma(m)} a^m. \quad (12.33)$$

Using (12.33), he derived the following $P - \delta$ relation

$$P = E^* \left[B_m^{-\frac{1}{m}} 2^{2/m} m^{\frac{m-1}{m}} \frac{1}{m+1} [\Gamma(m/2)]^{-\frac{2}{m}} [\Gamma(m)]^{\frac{1}{m}} \right] \delta^{\frac{m+1}{m}}. \quad (12.34)$$

Here $\Gamma(m)$ is the Euler gamma function.

Let us denote

$$C(m) = \frac{m^2}{m+1} 2^{m-1} \frac{[\Gamma(m/2)]^2}{\Gamma(m)}.$$

Then the Galin solution can be represented in a compact form

$$a = \left(\frac{P}{C(m) E^* B_m} \right)^{1/(m+1)}, \quad \delta = \left[\frac{C(m) B_m}{(E^*)^m} \right]^{\frac{1}{m+1}} \left(\frac{m+1}{2m} \right) P^{m/(m+1)}. \quad (12.35)$$

Using the property of the Euler gamma functions $\Gamma(n+1) = n!$, it is easy to see that the Shtaerman (1939) solution (12.30) and (12.31) is a particular case $m = 2n$ of the Galin solution (12.33) and (12.34) or (12.35).

It follows from (12.33) that

$$P = \frac{2m}{m+1} \cdot E^* a \delta(a). \quad (12.36)$$

Taking a limit $m \rightarrow \infty$ in (12.36), one obtains the Boussinesq relation (12.14).

Using Galin's expressions (12.35), one can calculate the components of energy (12.22) and the following expression for the total energy U_T

$$U_T = \frac{1}{4} \left[\frac{C(m)B_m}{(E^*)^m} \right]^{\frac{1}{m+1}} \left[\frac{1}{2m+1} P_H^{\frac{2m+1}{m+1}} - P^2 P_H^{\frac{-1}{m+1}} - \frac{2}{m} P P_H^{\frac{m}{m+1}} \right] - w\pi \left(\frac{P_H}{C(m)E^*B_m} \right)^{\frac{2}{m+1}}. \quad (12.37)$$

Applying (12.28) to (12.37), one may obtain

$$P^2 - 2P(C(m)B_m E^*)a^{m+1} + (C(m)B_m E^*)^2 a^{2(m+1)} - 8w\pi E^* a^3 = 0.$$

Following the approach used by Johnson et al. (1971), one can solve this equation. Taking the stable solution, one obtains an exact formula giving a relation between the real load P and the real radius of the contact region a

$$P = P_H - \sqrt{8\pi w E^* a^3} = C(m)B_m E^* a^{m+1} - \sqrt{8\pi w E^* a^3}. \quad (12.38)$$

The real displacement of the punch is

$$\delta = (\delta_H - \Delta\delta), \quad (12.39)$$

i.e.

$$\delta = B_m C(m) \frac{m+1}{2m} a^m - \left(\frac{2\pi w a}{E^*} \right)^{1/2}. \quad (12.40)$$

These expressions were derived initially by Galanov (1993), then for $m = 2n$ independently by Carpick et al. (1996), and published first by Borodich and Galanov (2004), see also a discussion by Borodich (2008).

As one can get from (12.38), the radius of the contact region $a(0)$ at the external load $P = 0$ is

$$a(0) = \left[\frac{8\pi w}{E^* C^2(m) B_m^2} \right]^{1/(2m-1)}. \quad (12.41)$$

This value can be taken as a characteristic size that may be used for writing dimensionless equations.

Let us write the characteristic parameters of the adhesive contact problems as

$$a^* = a(0), \quad P^* = \left\{ \frac{(8\pi w)^{m+1} (E^*)^{m-2}}{[C(m)B_m]^3} \right\}^{\frac{1}{2m-1}}, \quad \delta^* = \left[\frac{2^{m+1}}{C(m)B_m} \left(\frac{\pi w}{E^*} \right)^m \right]^{\frac{1}{2m-1}}. \quad (12.42)$$

Then the solution to the frictionless JKR problem of adhesive contact (12.38) and (12.40) can be written as the following dimensionless equations

$$P/P^* = (a/a^*)^{m+1} - (a/a^*)^{3/2} \quad (12.43)$$

and

$$\frac{\delta}{\delta^*} = \frac{m+1}{m} \left(\frac{a}{a^*} \right)^m - \left(\frac{a}{a^*} \right)^{1/2}. \quad (12.44)$$

Originally, Galanov (1993) used another way for writing the dimensionless equations. However, these expressions are equivalent to each other. These expressions are also applicable to the case $m = 1$ (a conical indenter of semi-vertical angle $\pi/2 - \alpha$), that was independently studied by Maugis (2000). For the case $m = 1$, one has $f(r) = B_1 r$, $C(1) = \pi/2$, and $B_1 = \tan \alpha$. For a linearized treatment to be possible, α must be small compared with 1 and $\tan \alpha = B_1 \approx \alpha$. In fact, the solution presented by Carpick et al. (1996) may be obtained applying the JKR formalism to the Shtaerman (1939) expressions (12.30) and (12.31), while the solution presented by Maugis (2000) may be obtained applying the JKR formalism to the Love (1939) formulae (12.32), see a discussion by Borodich et al. (2012).

For a sphere of radius R , one has $m = 2$, $f(r) = B_2 r^2$, $B_2 = 1/(2R)$ and $C(2) = 8/3$. Substitution of these values into (12.38) and (12.40), obtains the classic JKRS expressions (12.20) and (12.21).

It is convenient to write the formula for the real displacement δ_2 in the case of frictionless boundary condition as

$$\delta_2 = \frac{B_m C(m)}{2m} a_1^m \left[1 + m \frac{P_0}{P_H} \right].$$

Comment In 1993 I received a letter from Prof. B.A. Galanov. He informed me that he could solve the JKR problem for monomial indenters. One of the final expressions of the solution was presented in the letter. Using the description of the JKR theory given in the book by Sviridenok et al. (1990) and employing the Galin solution for monomial indenters, I derived all expressions. Three days later I sent a letter to B.A. Galanov where I described the whole derivation. B.A. Galanov answered that he used another way for derivation, however, my approach is also correct. Unfortunately, my letter discouraged B.A. Galanov from publishing his

solution and it was included only in a Technical report (Galanov 1993) and a preprint dedicated to adhesive wear of diamond samples (Galanov and Grigorév 1994).

From December, 1997 to March, 1998, I spent four month as a visitor at the Centre de Reserca Matematica (Bellaterra, Barcelona, Spain). Being there I sent an email message to Prof. K.L. Johnson saying that Prof. Galanov and I are able to extend the JKR theory to power-law shaped indenters. Prof. Johnson answered that such a solution is known and gave a reference to Carpick et al. (1996). To my shame I did not record the reference. In 2001 I moved to Northwestern University where I attended a seminar by Prof. R. Carpick (at that time he worked at the University of Wisconsin-Madison). After the seminar I approached him saying it is my guess that Prof. Johnson gave me reference to his paper. Prof. Carpick went to my office and immediately showed the paper on my computer. Three years later I visited Madison to deliver a seminar about my rather skeptical views on fractal models of rough surfaces (for details about my fractal models see discussions by Borodich 2013, 2019). I had a nice conversation with Professors M. Plesha and R.W. Carpick, when I said that our solution is valid not only for even integers but also for arbitrary rational values of degree m . The solution was presented partially in Borodich and Galanov (2004) and the full solution was published ten years later by Borodich et al. (2014a).

4.3 Contact Problems for Polynomial Indenters

Let us represent the shape function of a smooth body of revolution in the form of the power series with fractional exponents

$$f(\rho) = \sum_{k=1}^{\infty} B_k \rho^{d_k}, \quad d_k > 0. \quad (12.45)$$

Using the Galin solution (12.33) and (12.34), the following result can be proved (Borodich 1990).

Let the indenter of shape (12.45) be pressed into an elastic half-space by a force P . Then the contact radius a , the contact load P and the depth of indentation δ in non-adhesive Hertz-type contact problem satisfy the following equations

$$P = E^* \sum_{k=1}^{\infty} A(B_k, d_k) a^{d_k+1}, \quad A(B_k, d_k) = B_k 2^{d_k-1} \frac{d_k^2}{d_k+1} \frac{[\Gamma(d_k/2)]^2}{\Gamma(d_k)},$$

$$\delta = \sum_{k=1}^{\infty} B_k d_k 2^{d_k-2} \frac{[\Gamma(d_k/2)]^2}{\Gamma(d_k)} a^{d_k}. \quad (12.46)$$

Indeed, it follows from (12.33) that if an indenter $f_k(\rho) = B_k \rho^{d_k}$ is pressed by the force

$$P_k = E^* A(B_k, d_k) a^{d_k+1}$$

then its contact radius with the half-space is equal to a .

If the indenter whose shape is described by (12.45), is pressed by the force

$$P_\Sigma = \sum_{k=1}^{\infty} P_k$$

then its contact radius is also a . This is because the Hertz-type contact problems with identical contact regions (in our case the contact regions having the same fixed contact radius a) can be superimposed on each other. Putting $P_\Sigma = P$ we obtain (12.46) as a superposition of solutions to linear Hertz-type contact problems.

The adhesive contact problem will not be considered for indenters of shape (12.45) because it will be shown below that the adhesive JKR-type contact problem may be solved for an axisymmetric indenter of arbitrary shape.

4.4 The JKR Formalism in Application to No-slip Contact for Power-Law Shaped Indenters

Non-adhesive contact problems with no-slip contact boundary condition (12.21) were studied in detail by Mossakovskii (1954, 1963) and Spence (1968). Although both authors used the term ‘adhesive contact’ in applications to their studies, they did not consider molecular adhesion. In fact, they considered problems with the no-slip contact boundary condition. These problems are of interest for the present study. Indeed, in contact problems with molecular adhesion, it is more natural to assume that a material point that came into contact with the indenter sticks to its surface, i.e. to assume that the non-slipping boundary conditions are valid, than to assume that the points of an adhesive material can move along the punch surface within the contact region without any friction. The schematic diagrams showing the trajectories of surface particles in an elastic material sample under normal loading by spherical and conical rigid indenters having the no-slip contact boundary condition, may be found in papers by Spence (1968) and Chaudhri (2017). It looks like the later paper attributed these trajectories to frictionless contact boundary condition of the Love problem, while in fact, these are for no-slip contact. This is because the radial displacements $u_r(r, 0, P)$ arise outside the contact region due to bounded contact stresses, then the radial displacements can be treated as the *frozen-in* displacements (Zhupanska 2009) and the radial strain at any given point of the contact zone does not change when the size of the contact region increases due to increase of the external parameter of the contact problem.

According to the JKR formalism, we need to obtain solutions for the Hertz-type and Boussinesq-type no-slip contact problems. Borodich and Keer (2004a,b) have derived formulae for contact of indenter with no-slip boundary conditions that are analogous to the Galin solution (12.35) of the frictionless contact problem. Let us use the following expressions C_{NS} and $I^*(m)$ introduced by Borodich and Keer (2004a,b)

$$C_{NS} = \frac{(1-\nu)\ln(3-4\nu)}{1-2\nu}, \quad I^*(m) = \int_0^1 t^{m-1} \cos \left[\frac{\ln(3-4\nu)}{2\pi} \ln \frac{1-t}{1+t} \right] dt.$$

Note that $I^*(m)$ can be found explicitly if $m = 1$ or $m = \infty$.

Mossakovskii (1954) solved the Boussinesq-type problem with the condition (12.12). For $m = \infty$, the solution can be written as

$$P = 2E^*C_{NS}a\delta. \quad (12.47)$$

This solution is similar to formula (12.14).

Spence (1968) solved the non-adhesive contact problem for a cone with no-slip boundary condition (12.12), i.e. for the case $m = 1$

$$P = E^*C_{NS}A_c a^2, \quad \delta = A_c a, \quad A_c = \frac{\pi B_1}{2I^*(1)}, \quad I^*(1) = \frac{\ln(3-4\nu)\sqrt{3-4\nu}}{2(1-2\nu)}. \quad (12.48)$$

Combining the Mossakovskii-Boussinesq solution (12.47) together with the Spence-Love (12.48) solution and applying the JKR formalism, one can get the following solution for the adhesive contact problem for a cone (Borodich et al. 2012)

$$P = A_c E^* C_{NS} a^2 E^* B_1 a^2 - (8\pi w E^* C_{NS} a^3)^{1/2}, \quad \delta = A_c a - \left(\frac{2\pi w a}{E^* C_{NS}} \right)^{1/2}. \quad (12.49)$$

For power-law indenter (12.21), the contact radius a of a punch and depth of indentation δ under the external load P could be found from the solution given by Borodich and Keer (2004b)

$$a = \left(\frac{m I^*(m) P}{E^* C_{NS} B_m C(m)} \right)^{\frac{1}{m+1}}, \quad \delta = \left[\frac{B_m C(m)}{m I^*(m) (E^* C_{NS})^m} \right]^{\frac{1}{m+1}} \left(\frac{m+1}{2m} \right) P^{\frac{m}{m+1}}. \quad (12.50)$$

In the case of $\nu = 0.5$, one has $I^*(m) = 1/m$ and $C_{NS} = 1$. Hence, for incompressible materials, the Borodich-Keer formulae (12.50) are identical to the corresponding formulae of the Galin solution (12.35).

Using (12.50) and (12.47) and employing the JKR formalism, one can solve the no-slip adhesive contact problem for the power-law shaped indenters (Borodich et al. 2014a).

$$P = P_H - \sqrt{8\pi w E^* C_{NS} a^3} = \frac{E^* C_{NS} C(m) B_m}{m I^*(m)} a^{m+1} - \sqrt{8\pi w E^* C_{NS} a^3}. \quad (12.51)$$

As in the above frictionless problem, the real displacement of the punch is $\delta = (\delta_H - \Delta\delta)$

$$\delta = B_m C(m) \frac{m+1}{2m} \frac{1}{m I^*(m)} a^m - \left(\frac{2\pi w a}{E^* C_{NS}} \right)^{1/2}. \quad (12.52)$$

In this case, the radius a of the contact region at $P = 0$ can be obtained from (12.51)

$$a(0) = \left[\sqrt{\frac{8\pi w}{E^* C_{NS}}} \frac{m I^*(m)}{C(m) B_m} \right]^{\frac{2}{2m-1}}.$$

Let us write the characteristic parameters of the non-slipping adhesive contact problems as

$$\begin{aligned} P^* &= \left\{ \frac{(8\pi w)^{m+1} (E^* C_{NS})^{m-2}}{[C(m) B_m / (m I^*(m))]^3} \right\}^{\frac{1}{2m-1}}, \quad a^* = a(0), \\ \delta^* &= \left[\frac{2^{m+1} d I^*(m)}{C(m) B_m} \left(\frac{\pi w}{E^* C_{NS}} \right)^m \right]^{\frac{1}{2m-1}}. \end{aligned} \quad (12.53)$$

Then the solution to the adhesive contact problem with no-slip boundary condition will have the same dimensionless form as the frictionless case, i.e. (12.43) and (12.44) are valid. One can see that these dimensionless relations are universal for the power-law shaped indenters. Indeed, they are valid for frictionless and no-slip boundary conditions, and as it will be shown below, they are also valid for transversely isotropic and elastic materials having homogeneously distributed initial stresses.

Spence (1968) suggested to use a decomposition of the integral $I^*(2)$ into a series. Using this decomposition, Borodich et al. (2014a) showed that the frictionless JKR model just slightly overestimates the adherence force for a sphere. The no-slip contact problems is not considered further.

4.5 The JKR Formalism in Application to Frictionless Contact for Arbitrary Shaped Axisymmetric Indenters

The above results were based on Galin solution for power-law shaped indenters. However, Galin (1946, 1953) solved frictionless axisymmetric contact problems for arbitrary blunt indenters. He derived the following expressions

$$P = \frac{2E}{1-\nu^2} \int_0^a \rho_1 \nabla^2 f(\rho_1) \sqrt{a^2 - \rho_1^2} d\rho_1, \quad (12.54)$$

$$\delta = \int_0^a \rho_1 \nabla^2 f(\rho_1) \operatorname{arctanh}(\sqrt{1 - \rho_1^2/a^2}) d\rho_1. \quad (12.55)$$

Here ∇^2 denotes the two-dimensional Laplace operator

$$\nabla^2 = \frac{\partial^2}{\partial x_1^2} + \frac{\partial^2}{\partial x_2^2} = \frac{\partial^2}{\partial r^2} + \frac{1}{r} \frac{\partial}{\partial r}. \quad (12.56)$$

Rostovtsev (1953) introduced a very elegant method based on the use of special harmonic functions of complex variables and using these functions, he derived another representation of Galin's expressions (12.54) and (12.55)

$$\frac{P}{2E^*} = \int_0^a \frac{r^2 f'(r) dr}{\sqrt{a^2 - r^2}}. \quad (12.57)$$

$$\delta(a) = \int_0^a \frac{f'(r)}{\sqrt{1 - r^2/a^2}} dr. \quad (12.58)$$

In fact, the representation by Rostovtsev may be obtained directly from the Galin solution, see a discussion by Borodich and Keer (2004b) and also by Argatov and Dmitriev (2003).

Using the solution (12.57) and (12.58), one can show that for a convex body of revolution $f(r)$, $f(0) = 0$, the JKR theory leads to the following expressions

$$P_H = P + \sqrt{8\pi w E^* a^3}, \quad \delta = \delta_H - \sqrt{\frac{2\pi w a}{E^*}} \quad (12.59)$$

or

$$P = P_H - \sqrt{8\pi w E^* a^3} = 2E^* \int_0^a \frac{r^2 f'(r) dr}{\sqrt{a^2 - r^2}} - \sqrt{8\pi w E^* a^3} \quad (12.60)$$

and

$$\delta = \int_0^a \frac{f'(r)}{\sqrt{1-r^2/a^2}} dr - \left(\frac{2\pi wa}{E^*} \right)^{1/2}. \quad (12.61)$$

It is interesting to discuss here the way the above equations were derived. In fact, there are two exact results that follow from the analysis of the force-displacement curves of the Hertz-type axisymmetric contact problems.

If the problem is considered assuming the validity of the no-slip boundary condition (12.12), then the slope of the $\delta - P$ curve at any point is

$$\frac{d\delta}{dP} = \frac{1}{2C_{NSa}E^*} \quad (12.62)$$

Let the elastic properties of contacting materials have rotational symmetry and their contact properties be characterized by the effective contact (reduced) modulus K^* . In particular, if the material is isotropic, linearly elastic then $K^* = E^*$. Then the slope of the $\delta - P$ curve of the Hertz-type frictionless contact problem at any point is

$$\frac{d\delta}{dP} = \frac{1}{2aK^*}. \quad (12.63)$$

The property (12.62) was proved by Borodich and Keer (2004b), the property (12.63) by Borodich (2014), however particular cases of this statement were considered earlier by Bulychev et al. (1975, 1976), Pharr et al. (1992), and Borodich and Keer (2004b).

For isotropic elastic-plastic materials, the formula (12.63) is the corner stone of modern depth-sensing indentation tests of samples by sharp pyramidal indenters. Indeed, the formula can be re-written as the BASH relation connecting the reduced contact modulus E^* of the material and the slope of the force-displacement curve according to the non-adhesive Hertz contact theory (see, e.g. Bulychev et al. 1975, Bulychev et al. 1976, Jin et al. 2022). Note, if one calculates the slope the force-displacement curve according to the adhesive JKR contact theory, then the BASH relation is not valid, and the relation should be corrected (Borodich and Galanov 2018). However, to evaluate not only elastic but also adhesive properties of materials, one can employ the depth-sensing indentation of spherical indenters and the method introduced by Borodich and Galanov (2008) as an alternative to the methods based on the use of sharp indenters. This method (the BG method) is based on the interpretation of the experimental force-displacement curves for spherical indenters by applying mechanics of adhesive contact, in particular the JKR theory. It was shown (Borodich et al. 2013) that the BG method is very robust. Recently the BG method was extended by Perepelkin and his colleagues (Perepelkin et al. 2019, 2020, 2021).

Note that the JKR formalism has been intentionally described in such a way that all expressions (12.23)–(12.28) do not depend on the shape of the indenter. In fact, if one substitutes E^* by K^* , then these expressions are also true for all materials having rotational symmetry and whose contact properties are characterized by the effective contact (reduced) modulus K^* .

Hence, the total energy U_T can be written as

$$U_T = (P_H - P)\delta_H - \int_0^{P_H} \delta(P)dP - \frac{(P_H - P)^2}{4K^*a} - w\pi a^2. \quad (12.64)$$

Applying the equilibrium condition (12.28) to (12.64), one obtains

$$\frac{dU_T}{dP_H} = (P_H - P)\frac{d\delta_H}{dP_H} - \frac{(P_H - P)}{2K^*a} + \left[\frac{(P_H - P)^2}{4K^*a^2} - 2w\pi a \right] \left(\frac{da}{dP_H} \right) = 0. \quad (12.65)$$

Here, one can see the essence of my ‘reinforcement’ of the JKR formalism that consists of two tricks: (1) the first two terms in (12.65) vanish due to the general property (12.63) of the slope of the $P - \delta$ curve; as a result, the equilibrium condition for the general JKR model is

$$\frac{dU_T}{dP_H} = \left[\frac{(P_H - P)^2}{4K^*a^2} - 2w\pi a \right] \frac{da}{dP_H} = 0; \quad (12.66)$$

(2) I do not need to calculate the derivative da/dP_H to write the final expression of the JKR theory

$$(P_H - P)^2 = 8\pi wK^*a^3. \quad (12.67)$$

Because it follows from the Boussinesq solution that

$$P_H - P = 2K^*a\Delta\delta,$$

one can get from (12.67) an expression for $\Delta\delta$. Substituting this expression into (12.39) and using the Galin solution, one obtains

$$\delta = \delta_H - \Delta\delta = \delta_H - \sqrt{\frac{2\pi wa}{K^*}} \quad (12.68)$$

It is evident that (12.59)–(12.61) are a particular case of (12.67) and (12.68) when $K^* = E^*$.

Thus, my derivation of the JKR theory for an axisymmetric indenter contacting without friction an elastic material based on employing the JKR formalism and properties of slopes of the $P - \delta$ curves, is even shorter than the derivation of the theory for adhesive contact of a spherical indenter by Johnson et al. (1971).

4.6 *The JKR Formalism in Application to Adhesive Contact with Transversely Isotropic and Homogeneously Prestressed Elastic Samples*

So far, I have discussed only isotropic linearly elastic materials. However, the JKR formalism is applicable to particular cases of anisotropic linearly elastic materials. Indeed, transverse isotropy is a very important case of anisotropy because many natural and artificial materials behave effectively as transversely isotropic elastic solids. If a solid is transversely isotropic then the contact region under an axisymmetric indenter is still a circle. In addition, Willis (1966) and independently Conway et al. (1967) presented an analytical expression for the solution to the Hertz frictionless contact between transversely isotropic solids using the Lekhnitskii (1940, 1981) results. They showed that the solution of the Boussinesq problem for a concentrated load P is

$$u_3(r, 0) = \frac{P}{\pi E_{TI} r} \quad (12.69)$$

where the coefficient E_{TI} is a contact (effective reduced) modulus for transversely isotropic material that can be expressed through its five elastic constants (see, e.g., Conway et al. 1967; Borodich et al. 2014b). Hence, if a rigid axisymmetric indenter contacts with a transversely isotropic half-space, then one needs to just replace E^* in all expressions of the Hertz-type problem solution by E_{TI} , i.e. $K^* = E_{TI}$. If there is contact between an isotropic indenter and a transversely isotropic solid then $(K^*)^{-1} = (E^*)^{-1} + (E_{TI})^{-1}$. The JKR problems for transversely isotropic elastic solids were presented by Espinasse et al. (2010) for spherical indenters, by Borodich et al. (2014b) for power-law shaped indenters and by Borodich (2014) for indenters of arbitrary profile.

Let us discuss now non-linear elastic materials having initial stresses. Again, the JKR formalism is applicable to particular cases of such materials. It is assumed in Hertz-type contact problems for such materials that the stress field arising during contact with a prestressed sample is just a small perturbation of the large initial stress field. If a non-linear elastic solid is initially isotropic or transversely isotropic and it has homogeneously distributed axisymmetric initial stresses, then the contact region under an axisymmetric indenter is still a circle.

Let us demonstrate the application of the JKR formalism on the example of neo-Hookean materials. The potential for hyperelastic material of neo-Hookean type may be written as

$$W = \frac{1}{2} G (\lambda_1^2 - 1 + \lambda_2^2 - 1 + \lambda_3^2 - 1), \quad (12.70)$$

where λ_i is the extension ratio in the x_i direction, G is the initial shear modulus of the material of the natural unstressed state.

It is assumed that the material in its natural unstressed state is isotropic and the shear modulus is $G = E/2(1 + \nu)$. For an incompressible material, one has $\nu = 0.5$ and

$$\lambda_1 \lambda_2 \lambda_3 = 1. \quad (12.71)$$

Because the initial prestress of the cell is homogeneous, there are the following conditions for a stretch λ of the material

$$\lambda_1 = \lambda_2 = \lambda, \quad \lambda_3 = \lambda^{-2}. \quad (12.72)$$

The full formulation of the Hertz-type contact problem for such a material can be found in Borodich (2014). Filippova (1978) and independently Dhaliwal and Singh (1978) presented an analytical expression for the solution to the Hertz frictionless contact between incompressible neo-Hookean isotropic solids. They showed that the solution of the Boussinesq problem for a concentrated load P acting on an elastic half-space whose properties and prestress are described by (12.70) and (12.72) respectively, may be written as

$$u_3(r, 0) = \frac{P}{4\pi Gr} N(\lambda) \quad (12.73)$$

where r is the radius of polar coordinates, u_3 is the vertical displacement of the surface, and the coefficient N is

$$N(\lambda) = \frac{2\lambda^4(1 + \lambda^3)}{\lambda^9 + \lambda^6 + 3\lambda^3 - 1}. \quad (12.74)$$

Because for incompressible solids $\nu = 0.5$, (12.73) can be written as

$$u_3(r, 0) = \frac{P}{E^* \pi r} N(\lambda) = \frac{P}{4G \pi r} N(\lambda). \quad (12.75)$$

Hence, the integral equation of an arbitrary contact problem for equally and uniformly prestressed solids differs from the integral equation of the corresponding classic contact problem only by a constant coefficient $N(\lambda)$.

A comprehensive review of current state of the art research in the area of contact problems for prestressed solids is presented by Babich et al. (2004). Babich and Guz (1984) showed that all Hertz-type problems of contact between an indenter and a non-linear elastic homogeneously prestressed half-space coincide with the mixed problem for the harmonic potential of the contact problem for an isotropic linear elastic half-space up to a constant multiplier $N(\lambda)$. The effective contact modulus E_{PS}^* for a non-linear elastic homogeneously prestressed incompressible half-space is

$$E_{PS}^* = E^*/N(\lambda) = 4G/N(\lambda) \quad (12.76)$$

where $N(\lambda)$ depends on the initial deformations λ within x_1x_2 plane and the non-linear strain potential of the material. For neo-Hookean materials, the expression of multiplier $N(\lambda)$ is given by (12.74). Babich et al. (2004) gave examples of the multipliers for other potentials of non-linear materials, e.g. (1) for a non-linear material with the harmonic potential

$$N(\lambda) = \frac{\lambda^2}{2 + \nu} \left(\lambda - \frac{1 + \nu}{2 + \nu} \right)^{-1},$$

(2) for a non-linear material with the Bartenev-Khazanovich potential

$$N(\lambda) = 2\lambda^{7/2} (3\lambda^3 - 1)^{-1}.$$

Thus, if a rigid axisymmetric indenter contacts with an elastic homogeneously prestressed half-space then one needs to just replace E^* in all expressions of the Hertz-type problem solution by E_{PS}^* , i.e. $K^* = E_{PS}^*$. If two isotropic linear elastic bodies contact each other than effective contact modulus $K^* = E_I^*$. If there is contact between the prestressed half-space and a transversely isotropic indenter then $(K^*)^{-1} = (E_{PS})^{-1} + (E_{TI})^{-1}$ Borodich (1990).

Problem of contact probing a biological cell whose membrane is modelled as a non-linear elastic homogeneously prestressed half-space has been studied by Borodich et al. (2021) (see also Borodich et al. 2022).

5 The JKR Formalism in Application to Non-Hertzian Contact Problems

So far, I have discussed only the application of the JKR formalism to Hertz-type contact problems when the contacting solids are replaced by corresponding elastic half-spaces and the problem is formulated on the boundary of these half-spaces. However, the JKR formalism is also applicable to non-Hertzian problems. In particular, to coated solids or to stretched membranes having monomolecular thickness. Indeed, thin solid films having layered structures have enormous areas of applications. In particular, many natural and artificial materials have coatings.

5.1 The JKR Formalism in Application to Elastic Layers

The assumptions of the classic Hertz contact theory are not applicable to coated solids, hence, these problems were studied using other formulations. Various methods were employed for the studies. In fact, it has been known for a long time that the problem of contact between an indenter and a thin elastic layer

(thickness h is much less than the characteristic dimension of the contact area a , i.e. $\epsilon = h/a \ll 1$) can be reduced to a contact problem for a Winkler-Fuss (Fus 1801) elastic foundation with stiffness coefficient K . In particular, this result was obtained by employing an integral formulation of the problem. However, as Johnson (1985) noted, the integrand in the integral formulation equation for contact problem of the layer has an awkward form and this has led to serious difficulties in the analysis of contact stresses in strips and layers.

On another hand, there are two effective asymptotic methods that can be employed for studying contact problems for layered structures: (1) the AM method (Argatov and Mishuris 2015) and (2) GKN (Goldenveizer-Kaplanov-Nolde) one (Goldenveizer et al. 1993). The GKN method is based on direct asymptotic integration; it was originally developed for applications in theory of plates and shells (Goldenveizer et al. 1993). Later it was shown that the GKN method may be applied to two-dimensional contact problems (Erbaş et al. 2011). Recently the GKN method has been applied directly to variables of the spatial contact problem formulation for a single elastic layer (Borodich et al. 2019) and to an elastic layer glued to a rigid substrate when the term ‘glue’ is used for any material layer (an interlayer) that connects the thin solid film and a rigid substrate, i.e. the interlayer is modelled as an elastic thin film (Erbaş et al. 2019). Employing any of these two asymptotic methods, one can show that the contact problem for a thin isotropic or transversely isotropic layer bonded or glued to a rigid support is reduced in leading order asymptotic approximation to the problem for a Winkler-Fuss layer.

Comment Nikolay Ivanovich Fuss also known as Nikolay Fus, and Nicolaus (Nicolas) von Fuß, is a Swiss-born Russian mathematician (1755–1826). He graduated from the University of Basel. He was recommended by Daniel Bernoulli to Leonhard Euler (1707–1783) as an able graduate who is able to serve as a mathematical assistant to blind Euler. In 1772 Fuss moved to Saint Petersburg where he lived in Euler’s house until 1783. In 1800–1826 Fuss served as the permanent secretary to the Saint Petersburg Academy of Sciences. As Fuss wrote: “the Academy has eight mathematicians who have enjoyed the instructions of Mr. Euler: MM. J.A. Euler, Kotelnikov, Rumovsky, Krafft, Lexell, Inokhodtsov, Golovine and I”. Although the main achievements of Fuss were in various areas of mathematics, he is also known as the author of various mechanical models. In particular, he studied the friction of coach wheels moved on “a crumbly surface having a rigid substrate” employing a model of “penetration of wheels into it by laws of hydrostatic” and using the friction coefficient μ introduced by another former Euler’s student S.K. Kotelnikov (in fact, Kotelnikov was the first author to have published a mathematical form to verbal formulation of Amontons law). The Fuss ‘hydrostatic’ foundation can be represented by a collection of independent springs attached to a rigid flat, it is known as the Fuss-Winkler, Fuss-Winkler-Zimmermann, Winkler-Fuss (see a discussion by Borodich et al. 2020) or an elastic ‘mattress’ model (Johnson 1985).

To explain the main features of the contact problem formulation, let us consider a single thin elastic layer. In this case, an elastic isotropic layer of thickness h

occupying the area $0 \leq x_3 \leq h$, bounded to a rigid half-space $x_3 \geq h$. The indenter is axisymmetric and blunt, hence the contact problem can be considered in a geometrically linear formulation. Then the formulation of the boundary value contact problem is very similar to the formulation of the Hertz-type contact problems. However, instead the conditions at infinity (12.6), one should write

$$u_1(r, h) = u_2(r, h) = u_3(r, h) = 0. \quad (12.77)$$

As it has been mentioned, the contact problem in the leading order of asymptotic expansion reduces to a problem of contact for a Winkler-Fuss spring layer whose stiffness K is (do not confuse with the effective contact modulus K^* used above in the Hertz-type contact problems)

$$K = \frac{E(1-\nu)}{h(1+\nu)(1-2\nu)} \quad (12.78)$$

In this case the contact region is a circle of radius a and the boundary conditions of the problem can be written as

$$\begin{aligned} u_3(r, 0) &= \delta - f(r), & \sigma_{33}(r, 0) &\leq 0, & r &\leq a, \\ u_3(r, 0) &> \delta - f(r), & \sigma_{33}(r, 0) &= 0, & (x_1, x_2) &\in \mathbb{R}^2 \setminus G, \\ \delta - f(a) &= 0, \end{aligned} \quad (12.79)$$

Because the foundation is bounded to the rigid support, the conditions at the bottom of the layer are

$$u_3(r, h) = 0. \quad (12.80)$$

The volume of the body under the cross-section of height $z = \delta$ is given by

$$V = 2\pi \int_0^\infty [\delta - f(r)]H[\delta - f(r)]rdr,$$

where H is the Heaviside step function. This expression can be presented as

$$V(\delta) = 2\pi \left[0.5\delta a^2 - \int_0^a f(r)rdr \right] = \pi \left[f(a)a^2 - 2 \int_0^a f(r)rdr \right].$$

Hence, for the contact force, we have

$$P = KV(\delta) = 2\pi K \left[0.5\delta a^2 - \int_0^a f(r)rdr \right]. \quad (12.81)$$

It has been shown by Borodich et al. (2019) that the slopes of the force-displacement curves for an axisymmetric indenter contacting (1) the Winkler-Fuss

foundation and (2) isotropic or transversely isotropic linear or linearized elastic layers in the leading term approximations of the solutions may be written as

$$S = \frac{dP}{d\delta} = \pi a^2 K. \quad (12.82)$$

Now we can employ the JKR formalism. Let us use now the notations P_H and δ_H for values of the load and the displacement of non-adhesive contact with the Winkler-Fuss that correspond to the true value of contact radius a of adhesive contact. Then the expressions (12.23), (12.25), (12.26) and (12.27) are valid for the problem under consideration. However, the expression (12.24) for unloading according to the Boussinesq problem should be replaced by the following one

$$(U_E)_2 = \int_P^{P_H} \frac{P}{\pi K a^2} dP = \frac{P_H^2 - P^2}{2\pi K a^2}. \quad (12.83)$$

According to the JKR formalism, one needs to calculate the total energy and apply (12.28). Using (12.82), one can apply the ‘reinforcement’ and obtain the following expressions for adhesive contact of an arbitrary convex body of revolution $f(r)$, $f(0) = 0$,

$$P_H = P + \sqrt{2wK}\pi a^2, \quad \delta = \delta_H - \sqrt{\frac{2w}{K}}. \quad (12.84)$$

Taking into account formula (12.81), the relations (12.84) can be written as

$$P = P_H - \sqrt{2wK}\pi a^2 = \pi K \left[f(a)a^2 - 2 \int_0^a f(r)r dr \right] - \sqrt{2wK}\pi a^2 \quad (12.85)$$

and

$$\delta = f(a) - \left(\frac{2w}{K} \right)^{1/2}. \quad (12.86)$$

These expressions may be written as

$$P = \pi K a^2 \left(f(a) - \sqrt{\frac{2w}{K}} \right) - 2\pi K \int_0^a f(r)r dr \quad (12.87)$$

and

$$\delta = f(a) - \sqrt{\frac{2w}{K}}. \quad (12.88)$$

Now we can apply these expressions to monomial indenters (12.29). In this case the JKR type expressions have the following form

$$P = \pi K \left(\frac{m}{m+2} B_m a^{m+2} - \sqrt{\frac{2w}{K}} a^2 \right) \quad (12.89)$$

and

$$\delta = B_m a^m - \sqrt{\frac{2w}{K}}. \quad (12.90)$$

It follows from (12.89) and (12.90) that the relation $P(\delta)$ can be expressed not only in a parametric form, i.e. as functions of contact radius a , but also as an explicit relation

$$P = \frac{\pi K}{m+2} \left[\frac{1}{B_m} \left(\delta + \sqrt{\frac{2w}{K}} \right) \right]^{2/m} \left(\delta m - 2\sqrt{\frac{2w}{K}} \right). \quad (12.91)$$

It follows from (12.89) that at $P = 0$ the radius a of the contact region and the corresponding displacement $\delta_c = \delta[a(0)]$ are

$$a(0) = \left(\frac{m+2}{m B_m} \sqrt{\frac{2w}{K}} \right)^{1/m}, \quad \delta_c = \delta[a(0)] = \frac{2}{m} \sqrt{\frac{2w}{K}}. \quad (12.92)$$

Further note that

$$\frac{dP}{d\delta} = \frac{dP}{da} / \frac{d\delta}{da}.$$

Therefore, the root (a_c) of the equation

$$\frac{dP}{da} = 0$$

is the critical radius of the contact region. It gives the maximum absolute value of the adherence force $P_c = -P(a_c)$. Taking the derivative of (12.89), we obtain

$$a_c = \left(\frac{2}{m B_m} \sqrt{\frac{2w}{K}} \right)^{1/m}. \quad (12.93)$$

Substituting (12.93) into (12.89), we obtain

$$P_c = -P(a_c) = \pi K \frac{m}{m+2} \left(\frac{2}{m B_m} \right)^{2/m} \left(\frac{2w}{K} \right)^{(2+m)/2m}. \quad (12.94)$$

Further details may be found in Borodich et al. (2019).

5.2 The JKR Formalism in Application to Adhesive Contact with a Thin Membrane

For many years there was a belief, that monomolecular thin two-dimensional ($2D$) materials could not exist in the free state due to their instability (see e.g., a discussion by Meyer et al. 2007). However, Geim, Novoselov and their coworkers (Novoselov et al. 2004) showed that atomically thin $2D$ carbon allotrope, named graphene, is stable. The term graphene denotes a carbon allotrope that can be described as an atom thick $2D$ sheet made of carbon atoms. Currently, there is a stream of papers dedicated to studies of $2D$ materials (see, e.g. Castro Neto and Novoselov 2011). In particular, various devices based on the use of graphene are often studied, including the circular drum resonators covered by graphene monomolecular membranes (Lee et al. 2008; Aguilera-Servin et al. 2015, see also a discussion by Borodich and Galanov 2016).

Because it was shown that graphene membranes are isotropic (Berinskii and Borodich 2013), it was argued by Borodich and Galanov (2016) that one may model the graphene drum as a stretched membrane made of a $2D$ material whose bending rigidity is negligible. This allowed them to use a geometrically linear formulation of the boundary-value problem like the classic contact problems have. Evidently, the Hertz-type and Boussinesq-type contact problems had to be reformulated to reflect the features of the $2D$ solid.

Mathematical problems related to stretched membranes have been studied by many researchers (see, e.g., Karman and Biot 1940; Le Dret and Lucquin 2016). Let us consider an elastic membrane Ω that is supported by a rigid frame in the horizontal plane \mathbb{R}^2 . Let the membrane be held under a uniform tension T , i.e. initially the membrane is stretched. Hence, each point (x, y) of the closure $\bar{\Omega}$ of Ω represents a material point of the membrane when it is stretched without any other applied force. If some external force of density $F(x, y)$ is applied perpendicularly to the membrane surface then vertical displacements of the membrane $u_3(x, y)$ appear. It is assumed that the internal forces lay in the tangent plane to the deformed surface. Thus, the shape of the deformed surface at equilibrium is presented as $(x, y, u_3(x, y))$ and the tension T does not depend on $u_3(x, y)$, i.e. T is constant. The function $u_3(x, y)$ satisfies the elastic membrane equation that actually is the following Poisson equation

$$T\nabla^2 u_3(x, y) = -F(x, y), \quad (x, y) \in \Omega, \quad \nabla^2 = \frac{1}{r} \frac{\partial}{\partial r} \left(r \frac{\partial}{\partial r} \right) + \frac{1}{r^2} \frac{\partial^2}{\partial \phi^2} = \frac{\partial^2}{\partial x^2} + \frac{\partial^2}{\partial y^2}. \quad (12.95)$$

Here ∇^2 is the Laplace operator.

If it is assumed additionally that the stretched membrane sticks to the border of the frame $\partial\Omega$, then one has a homogeneous Dirichlet boundary condition

$$u_3(x, y) = 0, \quad (x, y) \in \partial\Omega. \quad (12.96)$$

Because a circular drum of radius R is under consideration, one can use the explicit expression for the Green function $G(r, \phi, \rho, \psi)$ for a circular membrane having the Dirichlet boundary condition. Then the solution $u_3(r, \phi)$ to the elastic membrane equation (12.95) with homogeneous boundary condition (12.96) is presented in the form

$$\begin{aligned} u_3(r, \phi) &= \frac{1}{T} \int_{\Omega} G(r, \phi, \rho, \psi) F(\rho, \psi) \rho d\rho d\psi \\ &= \frac{1}{T} \int_0^{2\pi} \int_0^R G(r, \phi, \rho, \psi) F(\rho, \psi) \rho d\rho d\psi. \end{aligned} \quad (12.97)$$

To employ the JKR formalism, one needs to formulate analogies to Hertz-type and Boussinesq-type contact problems. An analogy to the axisymmetric Hertz-type contact problem states that a convex smooth indenter $f(r)$ pressed by a vertical load P into the membrane. One needs to find the radius a of unknown region D_C of contact between the punch and the graphene membrane and the displacement of the indenter nose δ . The problem has the following boundary conditions

$$u_3(r) = \delta - f(r), \quad r \leq a. \quad (12.98)$$

In the general case, the contact pressure $p(r)$ is acting along the z axis, i.e. it creates positive force density

$$p(r) = F(r) = -T \frac{1}{r} \frac{d}{dr} \left(r \frac{du_3}{dr} \right) = T \frac{1}{r} \frac{d}{dr} \left(r \frac{df(r)}{dr} \right), \quad r \leq a \quad (12.99)$$

because $u_3'(r) = -f'(r)$ for $r \leq a$; and $p(r) = 0$ for $r > a$. Note, the pressure may be negative due to the presence of adhesive interactions.

Borodich and Galanov (2016) derived a general relation for slopes S of the $\delta - P$ curves similar to the relations derived for frictionless Hertz-type contact problems. The following general statement for the slope of the force-displacement curve of a non-adhesive Hertz-type contact problem is valid: the slope of the $\delta_H - P_H$ curve at any point is

$$S = \frac{dP_H}{d\delta_H} = C_S, \quad C_S = \frac{2\pi T}{\ln(R/a)} \quad (12.100)$$

where a is the radius of the contact region.

An analogy to the Boussinesq-type contact problem: a flat-ended punch of radius a pressed by a vertical load P , then the pressure $p(r) = 0$ for $0 \leq r < a$ and

$$p(r) = C\delta(r - a)$$

where $\delta(r - a)$ is the Dirac delta-function having its support on the circle of radius a and the constant C is defined from the condition that the total vertical load acting on the membrane P satisfies the equation

$$P = \int_0^{2\pi} \int_0^R p(r)r dr d\phi = \int_0^{2\pi} \int_0^R C\delta(r - a)r dr d\phi = 2\pi aC. \quad (12.101)$$

Hence, $C = P/(2\pi a)$.

It is possible to show that the displacement δ_B of a flat-ended punch of radius a acting on an elastic membrane of radius R and stretched by the uniform tension T is a linear function of the external load P

$$\delta_B = u_3(r) = \frac{P}{C_S}, \quad C_S = \frac{2\pi T}{\ln(R/a)}, \quad 0 \leq r \leq a. \quad (12.102)$$

Applying the JKR formalism, one can see that only the expression for $(U_E)_2$ should be recalculated.

$$(U_E)_2 = \int_P^{P_H} \delta(P)dP = \int_P^{P_H} \frac{P}{C_S a} dP = \frac{P_H^2 - P^2}{2C_S a} \quad (12.103)$$

for a flat-ended indenter of radius a that is unloaded from P_H to the true contact load P . The solution for a flat-ended circular indenter was used to calculate (12.103). Thus, we have

$$U_E = (U_E)_1 - (U_E)_2 = P_H \delta_H - \int_0^{P_H} \delta(P)dP - \frac{P_H^2 - P^2}{2C_S a}.$$

The mechanical work of the applied load is calculated as

$$U_M = -P\delta = -P(\delta_H - \Delta\delta) \quad (12.104)$$

where $\Delta\delta = \delta_H - \delta$ is the change in the depth of penetration due to unloading. Because

$$\Delta\delta = \frac{P_H - P_0}{C_S a} = \frac{P_H - P_0}{S a},$$

one has

$$U_M = -P\delta = -P \left(\delta_H - \frac{P_H - P}{S a} \right).$$

Using the same trick (the ‘reinforcement’ of the JKR formalism) as I have used to derive the general expression of the adhesive contact problem for an elastic half-space (i.e. two terms in the expression for dU_T/dP_H vanish due to the use of the

slope S ; the final expression of the derivative is a product of the JKR-type expression and da/dP_H that is equal to zero, hence I do not need to calculate da/dP_H , one can obtain

$$P = P_H - \pi\sqrt{8wT}a, \quad \delta = \delta_H - \sqrt{\frac{2w}{T}}a \ln(R/a). \quad (12.105)$$

In particular, for a power-law indenter whose shape is described by (12.29), we have

$$P = 2\pi m T B_m a^m. \quad (12.106)$$

Substituting (12.106) into (12.105), one gets the expressions that solve the problem of adhesive contact between a membrane and a power-law indenter of degree m

$$P = 2\pi T \left(m B_m a^{m-1} - \sqrt{\frac{2w}{T}} \right) a, \quad (12.107)$$

$$\delta = m B_m a^m \left[\ln\left(\frac{R}{a}\right) + 1/m \right] - \sqrt{\frac{2w}{T}} a \ln(R/a). \quad (12.108)$$

Evidently, the expressions (12.107) and (12.108) reduce to the above non-adhesive contact problems (the analogy to the Hertz-type contact problems) in the case $w = 0$.

The $P - \delta$ curve describes the depth-sensing indentation of the system under consideration. It is clear that if the external compressive load is not reduced then the indenter and the membrane jump out of the contact at the point $dP/d\delta = 0$, i.e. at the point where the tangent line is horizontal in experiments at fixed load P (see, e.g. Borodich and Galanov 2016).

One can see that $a(0)$ does not depend on the radius of the drum R . If this value is taken as a characteristic size of the contact region in order to write dimensionless parameters, then the characteristic parameters of the adhesive contact problems may be taken as

$$a^* = a(0), \quad P^* = \left(\frac{\pi^{2(m-1)} 2^{3m-2} w^m T^{m-2}}{m^2 B_m^2} \right)^{\frac{1}{2(m-1)}}, \quad \delta^* = \left(\frac{2^m w^m}{m^2 T^m B_m^2} \right)^{\frac{1}{2(m-1)}}. \quad (12.109)$$

In this case (12.107) and (12.108) have the following expressions

$$P/P^* = (a/a^*)^m - (a/a^*) \quad (12.110)$$

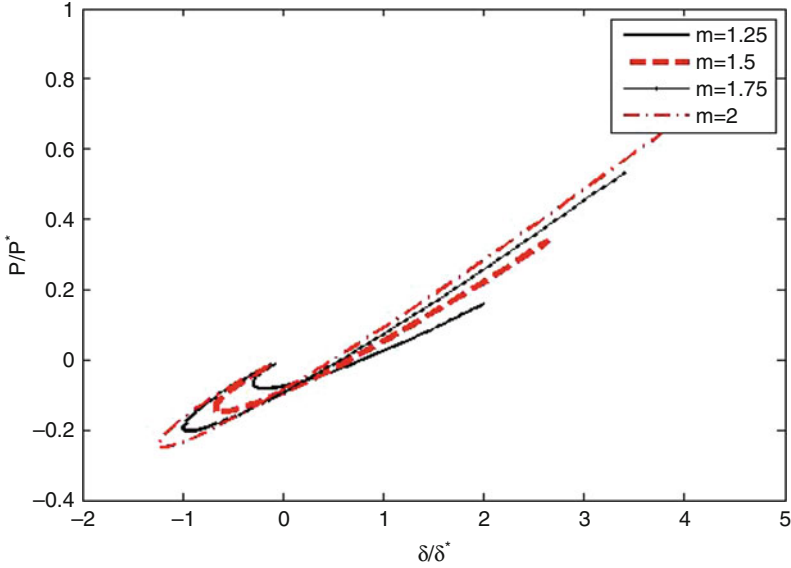


Fig. 12.2 The dimensionless $\bar{P} - \bar{\delta}$ relations for power-law indenters for m within the $0.25 \leq m \leq 2$ range

and

$$\frac{\delta_2}{\delta^*} = \left(\frac{a_1}{a^*}\right)^m \left[1/m - \ln\left(\frac{a_1/a^*}{R/a^*}\right)\right] + \frac{a_1}{a^*} \ln\left(\frac{a_1/a^*}{R/a^*}\right). \quad (12.111)$$

If we denote $\bar{P} = P_0/P^*$, $\bar{a} = a_1/a^*$ and $\bar{\delta} = \delta_2/\delta^*$, then (12.110) and (12.111) can be written as the following dimensionless relations

$$\bar{P} = \bar{a}^m - \bar{a} \quad (12.112)$$

and

$$\bar{\delta} = \bar{a}^m [1/m - \ln(\bar{a}/\bar{R})] + \bar{a} \ln(\bar{a}/\bar{R}), \quad \bar{R} = R/a^* \quad (12.113)$$

that are valid for arbitrary axisymmetric monomial punch of degree $m > 1$. The dimensionless $\bar{P} - \bar{\delta}$ relations for a membrane and power-law indenters are given in Fig. 12.2.

5.3 *The General Case of Explicit Transformation Between Non-adhesive and Adhesive Contact Problems*

The recent paper by Perepelkin and Borodich (2021) was dedicated to the accurate and clear formulation and derivation of the ‘reinforced’ JKR formalism. We have written the following expressions

$$P(a) = P_H(a) - \sqrt{\frac{4\pi waS^2(a)}{S'(a)}}, \quad \delta(a) = \delta_H(a) - \sqrt{\frac{4\pi wa}{S'(a)}}. \quad (12.114)$$

One can see that these expressions allow us to transform the force-displacement curves from non-adhesive (the Hertz-type and Boussinesq-type problems) to corresponding adhesive problems.

One can see that all considered cases are particular cases of (12.114). Indeed, in the adhesive contact for isotropic elastic solids assuming the no-slip boundary condition, one has $S = 2C_{NS}aE^*$ and $S'(a) = 2C_{NS}E^*$; in the adhesive contact for isotropic, transversely isotropic and homogeneously prestressed elastic solids assuming the frictionless boundary condition, one has $S = 2aK^*$ and $S'(a) = 2K^*$; in the adhesive contact for an isotropic elastic layer or a combination of a layer and an elastic interlayer, one has $S = \pi a^2K$ and $S' = 2\pi aK$ (see Sect. 5.1); and in the adhesive contact for a stretched membrane, one has $S = (2\pi T)/\ln(R/a)$ and $S' = (2\pi T)/[a \ln^2(R/a)]$. Substituting these values of S and S' into (12.114), one obtains correspondingly (12.49), (12.51), (12.52), (12.59), (12.67), (12.68), (12.84), and (12.105).

I have to note that particular cases of expressions (12.114) were discussed by Shull et al. (1998), however, the formulae were not applied to extend the JKR theory for arbitrary shaped solids and they were not suggested as a ‘reinforcement’ of the JKR formalism. The same is related to discussions by Maugis (2000), Sridhar et al. (1997), and Johnson and Sridhar (2001). As I have explained above, the ‘reinforcement’ of the JKR formalism with application to adhesive contact problem for the arbitrary axisymmetric shape of the indenter, was presented by Borodich (2014). The problems discussed there were restricted to the Hertzian approximation of contacting solids by half-spaces. I can say that the results related to thin elastic layer published by Borodich et al. (2019) were obtained during the visit of B.A. Galanov to Cardiff in 2006. One can see that these results contain the ‘reinforcement’ of the JKR formalism, while the paper by Argatov et al. (2016c) that was also devoted to the JKR problem for a thin elastic layer did not include the ‘reinforcement’. As one can see from the above discussion the ‘reinforcement’ was also used by Borodich and Galanov (2016) for problems of adhesive contact with mono-atomic thick membrane. This ‘reinforcement’ was also used by Argatov et al. (2016a) in problems of adhesive contact with a thick transversely isotropic layer.

I have to add that in my paper (Borodich 2014) I did not write explicitly these expressions (12.114) using the slope S . In fact, I wrote the formulae using $dP/d\delta$ in my calculations of the derivative of the total energy. However, I formulated

explicitly two theorems related to the slopes S in the case of frictionless and no-slip boundary conditions. My approach can be expressed using formulae (12.114) as it was eventually shown by Argatov et al. (2016a,b) and Popov (2018).

6 Discussion and Conclusion

I have presented a review of papers related to the JKR theory and applications of the JKR formalism to various problems of adhesive contact. The review reflected the development of the theory in historical order. Evidently, the review is not exhaustive.

I did not discuss in detail the fracture mechanics method in application to adhesive contact. Commenting the Boussinesq-Kendall adhesive contact problem (Kendall 1971) for a circular flat-ended indenter, Kendall (1973) noted that there is an analogy between the adherence of a flat punch and the fracture of a deeply notched bar. This comment gave Maugis a hint to apply the linear fracture mechanics method to adhesive contact (see discussions by Maugis and Barquins 1978, and Maugis 2000). Using this method, one can reformulate the JKR theory of adhesive contact using the Griffith energy balance and the Irvin concept of stress intensity factors. This approach is very popular. However, the Maugis approach is verified only for axisymmetric problems. There were attempts to use the Maugis approach to describe adhesive contact between not axi-symmetrical solids but rather the arbitrary 3D solids. One can find the first attempt to solve a 3D adhesive contact problem was made by Derjaguin (1934). This attempt was not successful. Johnson and Greenwood (2005) discussed adhesion between solids having elliptic contact region. Definitely, these approaches to arbitrary 3D indenters should be checked very carefully. Personally, I have very serious doubts that these attempts may be justified without additional assumptions and clear formulations of the approach restrictions.

I did not discuss in detail the problems when the contact region consists of an annulus or annuli. I would like to note that to check the validity of many statements related to fractal contact, I introduced the concept of parametric-homogeneity (PH) and developed the corresponding theory (Borodich 1993b, 1998a,b). In particular, I considered axi-symmetric indenters whose profiles are described by PH-functions. Borodich and Galanov (2002) presented results of numerical modelling of non-adhesive contact between a parabolic indenter with superimposed smooth log-periodic PH roughness and an elastic half-space. It was observed that the contact region consists of a central circular part and several annuli. It was proved that the contact problem obeys the law of discrete self-similarity and therefore, the geometry of the contact region that corresponds to any value of the external parameter \mathcal{P} of the problem may be obtained by a homothetic transformation from the geometry of the contact region for an appropriate value of the external parameter. The stress field has oscillations within the central circular part and non-constant values within the annuli. Evidently, adhesive contact problems for non-flat circular indenters, e.g. indenters having toroidal shape, are more complicated than non-adhesive contact

problems. The JKR problem for a toroidal indenter was studied by Argatov et al. (2016b). Then Willert et al. (2016) studied JKR-type problems for (1) an annular flat rigid punch; (2) an annular conical concave rigid punch, and (3) an annular spherically concave rigid punch. The last problem was also studied earlier by Kesari and Lew (2012). I believe that the JKR approach is not applicable to annular spherically concave rigid indenters because the distance between the free surface and the indenter surface does not increase rapidly at the periphery of the contact region, hence, one needs to consider the adhesive forces outside the contact region as Derjaguin et al. (1975) and Maugis (2000) argued.

In this review I have discussed only elastic solids, hence, I did not discuss the attempts to extend the JKR theory to elastic-plastic solids (see, e.g. Mesarovic and Johnson 2000; Tomas 2003; Gilabert et al. 2007). I did not discuss the attempts to ‘improve’ the JKR theory by considering the actual shape of the imprint under the indenter. These papers violate the main assumption of formulations of the Hertz, Boussinesq and JKR contact problems, namely the assumption of geometrically linear formulation of the contact problem. Please do not confuse these attempts with the so-called Galanov effect introduced by Galanov et al. (1983, 1984) for modelling of indentation of elastic-plastic solids.

I could also mention various attempts to apply the JKR theory to problems of contact between rough surfaces. As it was noted by Goryacheva (1998), the problem of the discrete contact between rough surfaces is a 3D boundary-value problem of contact mechanics for a system of coupled contacting spots. These problems are rather complicated. Galanov (1984, 1997) presented the results of his studies of non-adhesive indentation of a solid by coupled system of two paraboloids. It is clear that such system does not keep the rotational symmetry of the problem and, therefore, the JKR formalism is not applicable. However, one can assume that contact of each asperity does not depend on the contact of other asperities. There are statistical models of nominally flat rough surfaces consisting of independent spherical, elastic protuberances with a random height distribution introduced by Zhuravlev (1940), and Greenwood and Williamson (1966), see also my introduction in the English translation of Zhuravlev’s paper (Borodich 2007). Assuming that the protuberances have the same radii, but various heights (so that the protuberance number at a given height increases with depth), one can estimate the true contact area that is approximately proportional to the external load. One can try to apply the JKR theory to such statistical models. Although Johnson (1975) referred to both Zhuravlev (1940) and Greenwood and Williamson (1966) papers, he worked with the latter interpretation of the model of spherical asperities and introduced by these authors exponential distribution of heights of spherical summits. Fuller and Tabor (1975), Maugis (2000), Fuller (2011) and Galanov (2011) developed models of adhesion between rough surfaces assuming the Gaussian distribution of asperity heights. However, this topic is out of the scope of this review. Problems related to the description of surface roughness at both nano and microscales and possibilities for modelling of adhesion between rough surfaces were discussed by Borodich et al. (2016), Borodich and Savencu (2017), and Borodich et al. (2020).

Unfortunately, many papers dedicated to contact problems between rough surfaces employ models of surface roughness based on either fractal models of roughness or models based solely on properties of the auto-correlation function of surface heights or its Fourier transform, i.e. the power-spectral density function (PSDF). However, it has been demonstrated on many examples that neither models based solely on fractal dimensions of roughness nor on its PSDF are capable to reflect tribological properties of the surfaces (see, e.g. Borodich 2002, 2013; Borodich and Galanov 2002; Borodich et al. 2020). Therefore, papers based on fractal and PSDF models are often of rather limited scientific value (if any).

There were also attempts to solve adhesive contact problems for arbitrary anisotropic solids based on a claim that these contact problems are self-similar. Evidently, we cannot apply the JKR formalism to the case of arbitrary anisotropy, hence, the Maugis fracture mechanics approach is used to study problems for arbitrary anisotropic solids. I believe that these attempts are wrong. Non-adhesive Hertz-type contact problems for power-law shaped solids are self-similar as it was shown by Galanov (1981, 2009) and me (Borodich 1983, 1989, 1993a). However, it is evident that the JKR-type problems are not adhesive. It is very simple to show mathematically (see, e.g. Borodich 2014). One should realize that the contact region between a spherical indenter and arbitrary anisotropic half-space is not a circle. In addition, no proper verification of assumptions related to stress intensity factors on the periphery of the contact region have been published.

I have considered elastic systems where the surface of the indenter deforms in such a way that the separation between surfaces of the tested material and the indenter increases very rapidly with the distance from the contact edge. In this case one can neglect the adhesive interactions outside the contact region and the JKR formalism is applicable. A review is given of applications of the JKR formalism to axisymmetric indenters of various shapes, various materials, different conditions of contact, and some elastic structures. It is shown that the JKR formalism may be reinforced if one adds to it the properties of slopes of the force-displacement diagrams of non-adhesive indentation. The exact analytical expressions for the slopes are known in the case of isotropic and transversely isotropic elastic solids, Winkler-Fuss foundation, and stretched thin membranes. Evidently, the JKR formalism is applicable not only to thin and thick elastic layers and atomically thin stretched membranes, but also to many other structures that allow geometrical linear formulation of the boundary-value problem and superposition of solutions to contact problems having the same contact region.

Acknowledgments The author is grateful to Professor B.A. Galanov (Institute for Problems in Materials Science, National Academy of Sciences of Ukraine, Kiev) and Dr. N.V. Perepelkin (currently at Leeds Beckett University, UK) for stimulating discussions of various problems related to adhesive contact mechanics.

References

- Aguilera-Servin J, Miao T, Bockrath M (2015) Nanoscale pressure sensors realized from suspended graphene membrane devices. *Appl Phys Lett* 106:083103
- Adams GG, Nosonovsky M (2000) Contact modeling—forces. *Tribol Int* 33:431–442
- Argatov II, Dmitriev NN (2003) Fundamentals of theory of elastic discrete contact. Politekhnikha, St. Petersburg (Russian)
- Argatov I, Mishuris G (2015) Contact mechanics of articular cartilage layers. Asymptotic models. Springer, Berlin
- Argatov I, Mishuris G (2018) Indentation testing of biological materials. Springer, Berlin
- Argatov II, Borodich FM, Popov VL (2016a) JKR adhesive contact for a transversely isotropic layer of finite thickness. *J Phys D Appl Phys* 49:045307. <https://doi.org/10.1088/0022-3727/49/4/045307>
- Argatov I, Li Q, Pohrt R, Popov VL (2016b) Johnson-Kendall-Roberts adhesive contact for a toroidal indenter. *Proc R Soc A* 472:20160218. <https://doi.org/10.1098/rspa.2016.0218>
- Argatov II, Mishuris GS, Popov VL (2016c) Asymptotic modelling of the JKR adhesion contact for a thin elastic layer. *Q J Mech Appl Math* 69:161–179. <https://doi.org/10.1093/qjmam/hbw002>
- Babich SY, Guz AN (1984) Some spatial contact problems for a prestressed elastic half-space. *Soviet Appl Mech* 20:3–12
- Babich SY, Guz AN, Rudnitskii VB (2004) Contact problems for prestressed elastic bodies and rigid and elastic punches. *Int Appl Mech* 40:744–765
- Berinskii IE, Borodich FM (2013) On the isotropic elastic properties of graphene crystal lattice. *Surf Eff Solid Mech* 30:33–42
- Borodich FM (1983) Similarity in the problem of contact between elastic bodies. *PMM J Appl Math Mech* 47:440–442
- Borodich FM (1989) Hertz contact problems for an anisotropic physically nonlinear elastic medium. *Strength Mater* 21:1668–1676
- Borodich FM (1990) Hertz contact problems for an elastic anisotropic half-space with initial stresses. *Soviet Appl Mech* 26:126–132
- Borodich FM (1993a) The Hertz frictional contact between nonlinear elastic anisotropic bodies (the similarity approach). *Int J Solids Struct* 30:1513–1526
- Borodich FM (1993b) Similarity properties of discrete contact between a fractal punch and an elastic medium. *C R Acad Sci Paris Ser 2* 316:281–286
- Borodich FM (1998a) Parametric homogeneity and non-classical self-similarity. I. Mathematical background. *Acta Mech* 131:27–45
- Borodich FM (1998b) Parametric homogeneity and non-classical self-similarity. II. Some applications. *Acta Mech* 131:47–67
- Borodich FM (2002) Comment on “Elastoplastic contact between randomly rough surfaces”. *Phys Rev Lett* 88:069601
- Borodich FM (2007) Translation of historical paper. Introduction to VA Zhuravlev’s historical paper: ‘On the question of theoretical justification of the Amontons-Coulomb law for friction of unlubricated surfaces’. *Proc Inst Mech Eng Part J J Eng Tribol* 221(J8):893–898
- Borodich FM (2008) Hertz type contact problems for power-law shaped bodies. In: Gladwell G.M.L. (ed) L.A. Galin, Contact problems. The legacy of L.A. Galin. Springer, Cham, pp 261–292
- Borodich FM (2011) Contact problems at nano/microscale and depth sensing indentation techniques. *Mater Sci Forum* 662:53–76
- Borodich FM (2013) Fractal contact mechanics. In: Wang QJ, Chung Y-W (eds) Encyclopedia of tribology, vol 2. Springer, Berlin, pp 1249–1258
- Borodich FM (2014) The Hertz-type and adhesive contact problems for depth-sensing indentation. *Adv Appl Mech* 47:225–366
- Borodich FM (2019) Development of Barenblatt’s scaling approaches in solid mechanics and nanomechanics. *Phys Mesomech* 22:73–82. <https://doi.org/10.1134/S1029959919010119>

- Borodich FM, Galanov BA (2002) Self-similar problems of elastic contact for non-convex punches. *J Mech Phys Solids* 50:2441–2461
- Borodich FM, Galanov BA (2004) Molecular adhesive contact for indenters of nonideal shapes. In: ICTAM04, abstracts book and CD-Rom proceedings. IPPT PAN, Warsaw
- Borodich FM, Galanov BA (2008) Non-direct estimations of adhesive and elastic properties of materials by depth-sensing indentation. *Proc R Soc A* 464:2759–2776
- Borodich FM, Galanov BA (2016) Contact probing of stretched membranes and adhesive interactions: graphene and other two-dimensional materials. *Proc R Soc A* 472:2016.0550. <https://doi.org/10.1098/rspa.2016.0550>
- Borodich FM, Galanov BA (2018) Interpretation of nanoindentation tests using mechanics of adhesive contact. In: Abstracts of 10th European solid mechanics conference, Bologna, 2–6 July 2018
- Borodich FM, Keer LM (2004a) Evaluation of elastic modulus of materials by adhesive (no-slip) nanoindentation. *Proc R Soc Ser A* 460:507–514
- Borodich FM, Keer LM (2004b) Contact problems and depth-sensing nanoindentation for frictionless and frictional boundary conditions. *Int J Solids Struct* 41:2479–2499
- Borodich FM, Savencu O (2017) Hierarchical models of engineering rough surfaces and bioinspired adhesives. In: Heepe L, Xue L, Gorb SN (eds) *Bio-inspired structured adhesives: biological prototypes, fabrication, tribological properties, contact mechanics, and novel concepts*, chap 10. Springer International Publishing, Cham, pp 179–219. https://doi.org/10.1007/978-3-319-59114-8_10
- Borodich FM, Galanov BA, Prostov YI, Suarez-Alvarez MM (2012) Influence of the no-slip boundary condition on indentation of an elastic half-space by a rigid cone in presence of molecular adhesion. *PMM J Appl Math Mech* 76:744–753
- Borodich FM, Galanov BA, Gorb SN, Prostov MY, Prostov YI, Suarez-Alvarez MM (2013) Evaluation of adhesive and elastic properties of polymers by the BG method. *Macromol React Eng* 7:555–563
- Borodich FM, Galanov BA, Suarez-Alvarez MM (2014a) The JKR-type adhesive contact problems for power-law shaped axisymmetric punches. *J Mech Phys Solids* 68:14–32
- Borodich FM, Galanov BA, Keer LM, Suarez-Alvarez MM (2014b) The JKR-type adhesive contact problems for transversely isotropic elastic solids. *Mech Mater* 75:34–44
- Borodich FM, Pepelyshev A, Savencu O (2016) Statistical approaches to description of rough engineering surfaces at nano and microscales. *Tribol Int* 103:197–207. <https://doi.org/10.1016/j.triboint.2016.06.043>
- Borodich FM, Galanov BA, Perepelkin NV, Prikazchikov DA (2019) Adhesive contact problems for a thin elastic layer: asymptotic analysis and the JKR theory. *Math Mech Solids* 24:1405–1424. <https://doi.org/10.1177/1081286518797378>
- Borodich FM, Jin X, Pepelyshev A (2020) Probabilistic, fractal, and related techniques for analysis of engineering surfaces. *Front Mech Eng* 6:64. <https://doi.org/10.3389/fmech.2020.00064>
- Borodich FM, Galanov BA, Keer LM, Suarez-Alvarez MM (2021) Contact probing of prestressed adhesive membranes of living cells. *Philos Trans R Soc A* 379:20200289. <https://doi.org/10.1098/rsta.2020.0289>
- Borodich FM, Galanov BA, Keer LM, Suarez-Alvarez MM (2022) Adhesion of living cells: mechanisms of adhesion and contact models. In: Borodich FM, Jin X (eds) *Contact problems for Soft, Biological and Bioinspired Materials*, Ch. 1. Springer, Berlin, pp 1–30
- Boussinesq J (1885) *Applications des potentiels ‘a l’Étude de l’équilibrium et du Mouvement des Solides Élastique*. Gauthier-Villars, Paris
- Bryant MD, Keer LM (1982) Rough contact between elastically and geometrically identical curved bodies. *Trans ASME J Appl Mech* 49:345–352
- Bulychev SI, Alekhin VP, Shorshorov MK, Ternovskii AP, Shnyrev GD (1975) Determination of Young’s modulus according to indentation diagram. *Ind Lab* 41:1409–1412
- Bulychev SI, Alekhin VP, Shorshorov MKh, Ternovskii AP (1976) Mechanical properties of materials studied from kinetic diagrams of load versus depth of impression during microimpression. *Strength Mater* 8:1084–1089

- Carpick RW, Agraït N, Ogletree DF, Salmeron M (1996) Measurement of interfacial shear (friction) with an ultrahigh vacuum atomic force microscope. *J Vac Sci Technol B* 14:1289–1295
- Castro Neto A, Novoselov K (2011) Two-dimensional crystals: beyond graphene. *Mater Express* 1:10–17
- Chaudhri MM (2017) The Love equation for the normal loading of a rigid cone on an elastic half-space: no need for a modification. *Philos Mag Lett* 97:343–349
- Conway HD, Farnham KA, Ku TC (1967) The indentation of a transversely isotropic half space by a rigid sphere. *J Appl Mech Trans ASME Ser E* 34:491–492
- Derjaguin B (1934) Untersuchungen über die Reibung und Adhäsion, IV. Theorie des Anhaftens kleiner Teilchen. *Kolloid Z* 69:155–164
- Derjaguin BV, Abrikosova II, Livshitz EM (1958) Molecular attraction of condensed bodies. *Usp Fiz Nauk* 64:493–528. (English transl. Derjaguin BV, Abrikosova II, Livshitz EM (2015) Molecular attraction of condensed bodies. *Phys Usp* 58:906–924)
- Derjaguin BV, Muller VM, Toporov YP (1975) Effect of contact deformations on adhesion of particles. *J Colloid Interf Sci* 53:314–326
- Derjaguin BV, Churaev NV, Muller VM (1985) *Poverkhnostnye Sily*. Nauka, Moscow (Russian). (English transl. Derjaguin BV, Churaev NV, Muller VM (1987) *Surface forces*. Springer Science, New York)
- Dhaliwal RS, Singh BM (1978) The axisymmetric Boussinesq problems of an initially stressed neo-Hookean half-space for a punch of arbitrary profile. *Int J Eng Sci* 16:379–385
- Erbaş B, Yusufolu E, Kaplunov J (2011) A plane contact problem for an elastic orthotropic strip. *J Eng Math* 70:399–409
- Erbaş B, Aydın YE, Borodich FM (2019) Indentation of thin elastic films glued to rigid substrate: asymptotic solutions and effects of adhesion. *Thin Solid Films* 683:135–143. <https://doi.org/10.1016/j.tsf.2019.05.038>
- Espinasse L, Keer L, Borodich F, Yu H, Wang J (2010) A note on JKR and DMT theories of contact on a transversely isotropic half-space. *Mech Mater* 42:477–480
- Filippova LM (1978) Three-dimensional contact problem for a prestressed elastic body. *PMM J Appl Math Mech* 42:1183–1188
- Fuller K (2011) Effect of surface roughness on the adhesion of elastomers to hard surfaces. *Mater Sci Forum* 662:39–51
- Fuller KNG, Tabor D (1975) The effect of surface roughness on the adhesion of elastic solids. *Proc R Soc Lond A* 345:327–342
- Fus N (1801) An experience of theory on resistance by roads of various types to four-wheeled and two-wheeled carriages with definition of circumstances for which ones of these carriages are more useful than others. In: *Academic papers selected from the first volume of “Activities of Academy of Sciences” under title “Nova Acta Academiae Scientiarum Imperialis Petropolitanae”*, Part 1, Saint Petersburg, pp 373–422 (in Russian)
- Galanov BA (1981) Approximate solution to some problems of elastic contact of two bodies. *Mech Solids* 16:61–67
- Galanov BA (1984) Spatial contact problems for rough elastic bodies under elastoplastic deformations of the unevenness. *PMM J Appl Math Mech* 48:750–757
- Galanov BA (1993) Development of analytical and numerical methods for study of models of materials. Report for the Project 7.06.00/001-92, 7.06.00/015-92. Institute for Problems in Material Science, Kiev (Ukrainian)
- Galanov BA (1997) Boundary element method for contact problems with some applications to problems of materials science. In: J Ranachowski, J Raabe (eds) *Nowoczesne metody badan i technologicie materialow ceramiczych*. Międzynarodowa konferencja pod auspicjami E-MRS, Madralin, listopad 1996. Redakcja Naukowa, Warszawa, pp 125–146
- Galanov BA (2009) Similarity approach to Hertz type contact problems. In: Borodich FM (ed) *IUTAM symposium on scaling in solid mechanics*. Springer, Berlin
- Galanov BA (2011) Models of adhesive contact between rough elastic bodies. *Int J Mech Sci* 53:968–977

- Galanov BA, Grigor'ev ON (1994) Adhesion and wear of diamond. Part I. Modelling. Preprint. Institute for Problems in Materials Science, Nat. Ac. Sci. Ukraine, Kiev.
- Galanov BA, Grigorev ON, Milman YV, Ragozin IP (1983) Determination of the hardness and Youngs modulus from the depth of penetration of a pyramidal indenter. *Strength Mater* 15:1624–1628
- Galanov BA, Grigorev ON, Milman YuV, Ragozin IP, Trefilov VI (1984) Determination of the hardness and Young's modulus with elastoplastic penetration of indentors into materials. *Sov Phys Dokl* 29:146–147
- Galín LA (1945) Indentation of a punch in presence of friction and adhesion. *J Appl Math Mech (PMM)* 9:413–424 (Russian)
- Galín LA (1946) Spatial contact problems of the theory of elasticity for punches of circular shape in planar projection. *J Appl Math Mech (PMM)* 10:425–448 (Russian)
- Galín LA (1953) Contact problems in the theory of elasticity. Gostekhizdat, Moscow-Leningrad (Russian). (English transl. Galín LA (1961) Contact problems in the theory of elasticity. In: Sneddon IN (ed), North Carolina State College, Departments of Mathematics and Engineering Research, NSF Grant No. G16447)
- Gilabert FA, Quintanilla MAS, Castellanos A, Valverde JM (2007) Adhesive elastic plastic contact: theory and numerical simulation *Z Angew Math Mech* 87:128–138
- Goldenevizer AL, Kaplunov JD, Nolde EV (1993) On Timoshenko-Reissner type theories of plates and shells. *Int J Solids Struct* 30:675–694
- Goryacheva IG (1998) Contact mechanics in tribology. Kluwer Academic, Dordrecht
- Greenwood JA, Williamson JBP (1966) Contact of nominally flat surfaces. *Proc R Soc Lond A* 370:300–319
- Harkins WD (1919) Cohesion, internal pressure, adhesion, tensile strength, tensile energy, negative surface energy, and molecular attraction. *Proc Natl Acad Sci USA* 5:562–568
- Hertz H (1882) Ueber die Berührung fester elastischer Körper. *J Reine Angew Math* 92:156–171. (English transl. Hertz H (1896) On the contact of elastic solids. In: Jones DE, Schott GA (eds) *Miscellaneous papers by H. Hertz*. Macmillan, London, pp 146–162)
- Jin X, Li P, Borodich FM (2022) Chap. 9: Indentation tests of biological materials: theoretical aspects. In: Borodich FM, Jin X (eds) *Contact problems for soft, biological and bioinspired materials*, Springer, Berlin, pp 181–198
- Johnson KL (1958) A note on the adhesion of elastic solids. *Br J Appl Phys* 9:199–200
- Johnson KL (1975) Non-Hertzian contact of elastic spheres. The mechanics of the contact between deformable bodies. In: De Pater AD, Kalker JJ (eds) *Proceedings of the IUTAM symposium*. Delft University Press, Delft, pp 26–40
- Johnson KL (1985) *Contact mechanics*. Cambridge University Press, Cambridge
- Johnson KL (2003) The background to the JKR theory of adhesion of elastic spheres. In: Popov V (ed) *Kontaktmechanik und Reibungsphysik. Vorlesung 2. Qualitative Behandlung eines adhäsiven Kontaktes*. Berlin Technical University, Berlin
- Johnson KL, Greenwood JA (2005) An approximate JKR theory for elliptical contacts. *J Phys D Appl Phys* 38:1042–1046
- Johnson KL, Pollock HM (1994) The role of adhesion in the impact of elastic spheres. *J Adhesion Sci Technol* 8:1323–1332
- Johnson KL, Sridhar I (2001) Adhesion between a spherical indenter and an elastic solid with a compliant elastic coating. *J Phys D Appl Phys* 34:683. <https://doi.org/10.1088/0022-3727/34/5/304>
- Johnson KL, Kendall K, Roberts AD (1971) Surface energy and the contact of elastic solids. *Proc R Soc Lond A* 324:301–313
- Jung H (1950) Ein Beitrag zum Loveschen Verschiebungsfunktion. *Ing Arch* 18:178–190
- Karman TV, Biot MA (1940) *Mathematical methods in engineering. An introduction to the mathematical treatment of engineering problems*. McGraw Hill, New York
- Kendall K (1971) The adhesion and surface energy of elastic solids. *J Phys D Appl Phys* 4:1186–1195

- Kendall K (1973) An adhesion paradox. *J Adhes* 5:77–79. <https://doi.org/10.1080/00218467308078440>
- Kendall K (2001) *Molecular adhesion and its applications*. Kluwer Academic/Plenum Publishers, New York
- Kendall K, Kendall M, Rehfeldt F (2011) *Adhesion of cells, viruses and nanoparticles*. Springer, Dordrecht
- Kesari H, Lew AJ (2012) Adhesive frictionless contact between an elastic isotropic half-space and a rigid axi-symmetric punch. *J Elast* 106:203–224
- Kochin NE (1940) Theory of a wing of finite span with circular form in plane. *J Appl Math Mech (PMM)* 4:3–32 (Russian)
- Krupp H (1967) Particle adhesion - theory and experiment. *Adv Colloid Interface Sci* 1:111–239
- Krupp H, Sperling G (1965) Haftung kleiner Teilchen an Feststoffen. Teil II: Theorie. *Z Angew Phys* 19:259–265
- Krupp H, Sperling G (1966) Theory of adhesion of small particles. *J Appl Phys* 37:4176–4180
- Le Dret H, Lucquin B (2016) *Partial differential equations: modeling, analysis and numerical approximation*. Birkhauser, Basel
- Lee C, Wei X, Kysar JW, Hone J (2008) Measurement of the elastic properties and intrinsic strength of monolayer graphene. *Science* 321(5887):385–388
- Lekhnitskii SG (1940) Symmetrical deformation and torsion of a body of revolution with a special kind of anisotropy. *PMM J Appl Math Mech* 4:43–60. (Russian)
- Lekhnitskii SG (1981) *Theory of Elasticity of an Anisotropic Body*. Moscow, Mir
- Love AEH (1939) Boussinesq's problem for a rigid cone. *Q J Math* 10:161–175
- Maugis D (1992) Adhesion of spheres: the JKR–DMT transition using a Dugdale model. *J Colloid Interface Sci* 150:243–269
- Maugis D (2000) *Contact, adhesion and rupture of elastic solids*. Springer, Berlin
- Maugis D, Barquins M (1978) Fracture mechanics and the adherence of viscoelastic bodies. *J Phys D Appl Phys* 11:1989–2023
- Meyer JC, Geim AK, Katsnelson MI, Novoselov KS, Booth TJ, Roth S (2007) The structure of suspended graphene sheets. *Nature* 446:60–63
- Mesarovic SD, Johnson KL (2000) Adhesive contact of elastic-plastic spheres. *J Mech Phys Solids* 48:2009–2033
- Mossakovskii VI (1954) The fundamental mixed problem of the theory of elasticity for a half-space with a circular line separating the boundary conditions. *PMM J Appl Math Mech* 18:187–196 (Russian)
- Mossakovskii VI (1963) Compression of elastic bodies under conditions of adhesion (axisymmetric case). *PMM J Appl Math Mech* 27:630–643
- Novoselov KS, Geim AK, Morozov SV, Jiang D, Zhang Y, Dubonos SV, Grigorieva IV, Firsov AA (2004) Electric field effect in atomically thin carbon films. *Science* 306:666–669
- Pepelyshev A, Borodich FM, Galanov BA, Gorb EV, Gorb SN (2018) Adhesion of soft materials to rough surfaces: experimental studies, statistical analysis and modelling. *Coatings* 8(10):350
- Perepelkin NV, Borodich FM (2021) Explicit transition between solutions to non-adhesive and adhesive contact problems by means of the classical Johnson-Kendall-Roberts formalism. *Philos Trans R Soc A* 379(2203):20200374
- Perepelkin NV, Kovalev AE, Gorb SN, Borodich FM (2019) Estimation of the elastic modulus and the work of adhesion of soft materials using the extended Borodich-Galanov (BG) method and depth sensing indentation. *Mech Mater* 129:198–213
- Perepelkin NV, Borodich FM, Kovalev AE, Gorb SN (2020) Depth-sensing indentation as a micro- and nanomechanical approach to characterisation of mechanical properties of soft, biological, and biomimetic materials. *Nanomaterials* 10:15. <https://doi.org/10.3390/nano10010015>
- Perepelkin NV, Argatov II, Borodich FM (2021) Evaluation of elastic and adhesive properties of solids by depth-sensing indentation. *J Adhes* 97:569–610. <https://doi.org/10.1080/00218464.2019.1686981>
- Pharr GM, Oliver WC, Brotzen FR (1992) On the generality of the relationship among contact stiffness, contact area, and elastic modulus during indentation. *J Mater Res* 7:613–617

- Popov VL (2010) Contact mechanics and friction. Springer, Heidelberg
- Popov VL (2018) Solution of adhesive contact problem on the basis of the known solution for non-adhesive one. *FU Mech Eng* 49:93–98. <https://doi.org/10.22190/FUME180105009P>
- Purto J, Gorb EV, Steinhart M, Gorb SN (2013) Measuring of the hardly measurable: adhesion properties of anti-adhesive surfaces. *Appl Phys A* 111:183–189
- Rostovtsev NA (1953) Complex stress functions in the axisymmetric contact problem of elasticity theory. *PMM J Appl Math Mech* 17:611–614
- Rvachev VL, Protsenko VS (1977) Contact Problems of the Theory of Elasticity for Non-Classical Regions. Kiev, Naukova Dumka. (Russian)
- Scherge M, Gorb SN (2001) Biological micro- and nanotribology nature's solutions. Springer, Berlin
- Shtaerman IYa (1939) On the Hertz theory of local deformations resulting from the pressure of elastic solids. *Dokl Akad Nauk SSSR* 25:360–362 (Russian)
- Shtaerman IYa (Steuermann EJ) (1949) Contact problem of elasticity theory. Gostekhizdat, Moscow (Russian)
- Shull KR (2002) Contact mechanics and the adhesion of soft solids. *Mater Sci Eng R Rep* 36:1–45. [https://doi.org/10.1016/S0927-796X\(01\)00039-0](https://doi.org/10.1016/S0927-796X(01)00039-0)
- Shull KR, Ahn D, Chen WL, Flanigan CM, Crosby AJ (1998) Axisymmetric adhesion tests of soft materials. *Macromol Chem Phys* 199:489–511. [https://doi.org/10.1002/\(sici\)1521-3935\(19980401\)](https://doi.org/10.1002/(sici)1521-3935(19980401)199:489-511::AID-MACP19980401)
- Spence DA (1968) Self similar solutions to adhesive contact problems with incremental loading. *Proc R Soc Lond A* 305:55–80
- Sperling G (1964) Eine Theorie der Haftung von Feststoffteilchen an festen Körpern. Unpublished doctoral dissertation, Technische Hochschule Karlsruhe
- Sridhar I, Johnson KL, Fleck NA (1997) Adhesion mechanics of the surface force apparatus. *J Phys D Appl Phys* 30:1710–1719. <https://doi.org/10.1088/0022-3727/30/12/004>
- Sviridenok AI, Chizhik SA, Petrokovets MI (1990) Mechanics of discrete frictional contact. Navuka i Tekhnika, Minsk
- Tabor D (1977) Surface forces and surface interactions. *J Colloid Interface Sci* 58:2–13
- Tomas J (2003) Mechanics of nanoparticles adhesion – a continuum approach. In: Mittal KL (ed) Particles and surfaces 8: detection, adhesion and removal. VSP, Utrecht
- Willert E, Li Q, Popov VL (2016) The JKR-adhesive normal contact problem of axisymmetric rigid punches with a flat annular shape or concave profiles. *Facta Univ Mech Eng* 14:281–292. <https://doi.org/10.22190/FUME1603281W>
- Willis JR (1966) Hertzian contact of anisotropic bodies. *J Mech Phys Solids* 14:163–176
- Zhupanska OI (2009) Axisymmetric contact with friction of a rigid sphere with an elastic half-space. *Proc R Soc A* 465:2565–2588
- Zhuravlev VA (1940) On question of theoretical justification of the AmontonsCoulomb law for friction of unlubricated surfaces. *Zh Tekh Fiz* 10:1447–1452. (English transl. Zhuravlev VA (2007) On question of theoretical justification of the Amontons-Coulomb law for friction of unlubricated surfaces. *Proc Inst Mech Eng Part J J Eng Trib* 221:397–404)